Effects of surface heating on stability and transition in a supersonic nozzle boundary layer
by Torence Patrick Brogan

A thesis submitted in partial fulfillment of the requirements for the degree of Doctor of Philosophy in Engineering (Applied Mechanics)
Montana State University

Abstract:
Acoustic fluctuations that originate from transitional and turbulent boundary layers in a supersonic wind tunnel limit the capabilities of ground test facilities for boundary layer transition research and testing. The present work explores boundary layer stability and transition with and without surface heating on one contoured wall of a low-disturbance Mach 3 two-dimensional wind tunnel at Montana State University.

The throat area of the lower contoured surface was heated to a steady state temperature of 13% and 22% over the stagnation temperature at unit Reynolds numbers of 5.2xl0^6/m and 6.2x10^6/m, respectively. Boundary layer measurements with a small, fast-response, pitot probe were used to characterize fluctuation magnitude, frequency content, and the rate of amplification with and without surface heating. The effect of surface heating was to reduce the amplitude of a low frequency disturbance at all streamwise positions. Suppressing this low frequency activity caused turbulent bursting to be moved downstream, thereby increasing the extent of laminar flow to nearly the entire nozzle length. Predictions with linear stability theory showed that heat has a mild stabilizing effect on Gortler vortices, and first-mode Tollmien-Schlichting waves could be suppressed with a proper heating distribution by moving the neutral point downstream and reducing the subsequent amplification rates. However, the e^N method with linear stability theory completely failed to predict the observed transition in the nozzle boundary layer due to unsteady oscillations, even in the case without surface heating.

Calculations of the mean-flow also showed that natural cooling (heat followed by cooling) and roughness arguments do not appear to explain the observed stability events.

The experiment and theory show at least two different paths to turbulence suppression by heating the surface of a supersonic nozzle. (1) The experiment demonstrates that heat suppresses a bypass mechanism triggered by receptivity events near and possibly upstream of the nozzle throat. (2) The computations show that a proper heating distribution can also be used to suppress the growth of linear instabilities in the nozzle if bypass were not present.

EFFECTS OF SURFACE HEATING ON STABILITY AND TRANSITION IN A SUPERSONIC NOZZLE BOUNDARY LAYER

by

Torence Patrick Brogan

A thesis submitted in partial fulfillment of the
requirements for the degree

of

Doctor of Philosophy

in

Engineering (Applied Mechanics)

MONTANA STATE UNIVERSITY
Bozeman, Montana

January 1999

APPROVAL

of a thesis submitted by

Torence Patrick Brogan

This thesis has been read by each member of the thesis committee and has been found to be satisfactory regarding content, English usage, format, citations, bibliographic style, and consistency, and is ready for submission to the College of Graduate Studies.

Dr. Anthony Demetriades _____ (Signature) 1/14/99 (Date)

Approved for the Department of Mechanical and Industrial Engineering

Dr. Vic Cundy _____ (Signature) 1/14/99 (Date)

Approved for the College of Graduate Studies

Dr. Bruce McLeod _____ (Signature) 1-20-99 (Date)

STATEMENT OF PERMISSION TO USE

In presenting this thesis in partial fulfillment of the requirements for a doctoral degree at Montana State University-Bozeman, I agree that the Library shall make it available to borrowers under the rules of the Library. I further agree that copying of this thesis is allowable only for scholarly purposes, consistent with "fair use" as prescribed in the U.S. Copyright Law. Requests for extensive copying or reproduction of this thesis should be referred to University Microfilms International, 300 North Zeeb Road, Ann Arbor, Michigan 48106, to whom I have granted "the exclusive right to reproduce and distribute my dissertation in and from microform along with the non-exclusive right to reproduce and distribute my abstract, in whole or in part."

Signature Torenee R. Brogan

Date 1/7/99

ACKNOWLEDGEMENTS

I would first like to thank my advisor, Dr. Anthony Demetriades, for his encouragement and guidance over the last 6 years. His often subtle suggestions have provoked my technical imagination, desire to learn, and determination for understanding to a level far beyond what I could have achieved on my own. Through my graduate program, I have gained both a colleague and friend.

I have enjoyed the many enlightening technical discussions with members of the Fluid Mechanics Laboratory at NASA Ames Research Center. In particular, I would like to thank Jim Laub for his moral support and the encouragement to pursue a Ph.D., as well as Lyn King for the invaluable assistance with the numerical calculations (and general understanding of Fluid Mechanics!).

The members of my graduate committee, Drs. Frank Albini, Jay Conant, Alan George, Ken Bowers, and Anthony Demetriades, have all had a profound influence on my ability to reason, both mathematically and physically, in the Engineering Sciences. The helpful comments they have provided to the manuscript are also acknowledged. Many thanks to Terry Kennedy, Dana Aughney, and Barbara Valdez in the Mechanical Engineering office, who have kept things smooth, even when they were not.

Last, and most important, I would like to thank my wife, RaKyel, for her unwavering love and support. While giving up countless weekends, evenings, and vacations, she has always encouraged me to strive for excellence. Words could not describe the amount of effort, which was often unrecognized, that she has invested into my education. This work is as much hers as it is mine.

This work has been funded by a GSRP Fellowship from NASA-AMES, thanks in large part to the efforts of Sanford Davis and Jim Laub.

TABLE OF CONTENTS

LIST OF TABLES

APPENDIX TABLES

LIST OF FIGURES

APPENDIX FIGURES

NOMENCLATURE

Symbol	Description
A	amplitude of an instability
A_o	amplitude of an instability at the neutral stability point
c_r	phase speed of an instability wave
e	voltage -or- exponential
f	physical frequency of disturbance (kHz)
F	Dimensionless disturbance frequency (normalized on a convective scale) $F=(2\pi\nu_e/U_e^2)f$
G	Görtler number based on a generic reference length
G_θ	Görtler number based on momentum thickness, θ. $G_\theta = \frac{U_e\theta}{\nu_e}\left(\frac{\theta}{r_c}\right)^{1/2}$
h	height of the nozzle throat h=1.799 cm
H_{12}	Shape factor, $H_{12}=\delta^*/\theta$
i	$(-1)^{1/2}$
j	grid index in the streamwise direction
k	maximum peak-to-valley roughness height, *or* grid index normal to the wall
L	nozzle length (throat to test section entrance) L=38.48 cm.
l^*	viscous length scale, $l^*=(\nu_e s/U_e)^{1/2}$
M	Mach number
n	time-stepping index
N	N-factor, $N\equiv\ln(A/A_o)$
P	static pressure

p'	disturbance state static pressure
P_o	stagnation pressure
P_p	pitot pressure: total pressure behind a normal shock
p_p'	disturbance state pitot pressure
Q	vector of unknowns in the Navier-Stokes solution –or– a general basic state flow quantity
q'	general disturbance state quantity
q_w	heat flux at the wall (+ into the boundary layer)
r_c	local radius of curvature
Re	Reynolds number
Re_k	roughness Reynolds number based on local conditions from a smooth-wall solution at the tip of the roughness element, $Re_k=U_k k/\nu_k$
Re_θ	Reynolds number based on momentum thickness θ
$Re_{\Delta x}$	Reynolds number based on length of quiet flow: Quiet-flow Reynolds number
Re'_∞	Unit Reynolds number based on free-stream conditions at Mach 3, $Re'_\infty=U_\infty/\nu_\infty$
s	arc-length, (s=0 @ start of boundary layer computation)
S_u	velocity sensitivity coefficient of the dynamic pitot probe
t	time
T	mean temperature
T'	disturbance state temperature
T_o	stagnation temperature

T_o'	disturbance state stagnation temperature
U,V,W	mean velocity in the x, y, z directions, respectively
u',v',w'	disturbance velocity in the x, y, z directions, respectively
x	streamwise coordinate (x=0 @ nozzle throat)
y	vertical distance from the wall (y=0 @ wall)
y^+	turbulent law-of-the-wall variable
z	spanwise distance from the nozzle centerline (z=0 @ centerline)
α	dimensionless streamwise component of the wavenumber
β	dimensionless spanwise component of the wavenumber
β^*	spanwise component of the wavenumber ($=l^*\beta$)
β_H	pressure gradient parameter
δ	boundary layer thickness, $\delta=y$ @ $U/U_e=0.99$
δ^*	displacement thickness, $\delta^* = \int_0^\infty \frac{\rho}{\rho_e}\left(\frac{U}{U_e}-1\right)dy$
λ	disturbance wavelength
λ_z	disturbance wavelength in spanwise direction, $\lambda_z=2\pi/\beta$
θ	momentum thickness, $\theta = \int_0^\infty \frac{\rho U}{\rho_e U_e}\left(\frac{U}{U_e}-1\right)dy$
γ	turbulent intermittency *or* ratio of specific heats
ϕ	disturbance wave-angle, $\phi=\tan^{-1}(\alpha_r/\beta)$
ρ	density
σ	amplification rate of steady Görtler instability
μ	dynamic viscosity

ν	kinematic viscosity, $\nu=\mu/\rho$
ω	dimensionless circular frequency of the disturbance, $\omega=2\pi f(l^*/U_e)$
ξ	transformed streamwise coordinate in the computational plane
η	dimensionless normal coordinate, $\eta=y/l^*$
η_{BL}	transformed normal coordinate for boundary layer solution

Subscripts

Symbol	Description
$()_{aw}$	local adiabatic conditions at the nozzle block surface
$()_e$	conditions at the edge of the boundary layer; represents a local free-stream quantity
$()_i$	imaginary component of a complex number
$()_N$	value at neutral point ($\alpha_i=0$)
$()_r$	real component of a complex number.
$()_T$	value at transition onset
$()_w$	local wall conditions
$()_\infty$	conditions based on tunnel core flow Mach number
$()_{rms}$	root-mean-square value

Superscripts

$\bar{()}$	instantaneous flow quantity (basic state + disturbance state)
$()'$	disturbance state quantity

(^)	disturbance eigenfunction

Acronyms

BW	Beam-Warming
DAC	digital to analog conversion
CFD	computational fluid dynamics
LFC	laminar flow control
LST	linear stability theory
MEP	maximum energy point
MSU	Montana State University
PSE	parabolized stability equations
SWT	Supersonic wind tunnel
TS	Tollmien-Schlichting

ABSTRACT

Acoustic fluctuations that originate from transitional and turbulent boundary layers in a supersonic wind tunnel limit the capabilities of ground test facilities for boundary layer transition research and testing. The present work explores boundary layer stability and transition with and without surface heating on one contoured wall of a low-disturbance Mach 3 two-dimensional wind tunnel at Montana State University.

The throat area of the lower contoured surface was heated to a steady state temperature of 13% and 22% over the stagnation temperature at unit Reynolds numbers of 5.2×10^6/m and 6.2×10^6/m, respectively. Boundary layer measurements with a small, fast-response, pitot probe were used to characterize fluctuation magnitude, frequency content, and the rate of amplification with and without surface heating. The effect of surface heating was to reduce the amplitude of a low frequency disturbance at all streamwise positions. Suppressing this low frequency activity caused turbulent bursting to be moved downstream, thereby increasing the extent of laminar flow to nearly the entire nozzle length. Predictions with linear stability theory showed that heat has a mild stabilizing effect on Görtler vortices, and first-mode Tollmien-Schlichting waves could be suppressed with a proper heating distribution by moving the neutral point downstream and reducing the subsequent amplification rates. However, the e^N method with linear stability theory completely failed to predict the observed transition in the nozzle boundary layer due to unsteady oscillations, even in the case without surface heating. Calculations of the mean-flow also showed that natural cooling (heat followed by cooling) and roughness arguments do not appear to explain the observed stability events.

The experiment and theory show at least two different paths to turbulence suppression by heating the surface of a supersonic nozzle. (1) The experiment demonstrates that heat suppresses a bypass mechanism triggered by receptivity events near and possibly upstream of the nozzle throat. (2) The computations show that a proper heating distribution can also be used to suppress the growth of linear instabilities in the nozzle if bypass were not present.

CHAPTER 1

INTRODUCTION

1.1 Background

As design margins for modern supersonic and hypersonic flight vehicles become tighter, the fidelity of engineering predictions for thermal and aerodynamic loading become increasingly important. Since the magnitudes of skin friction and heat transfer depend heavily on whether the boundary layer is laminar or turbulent, the natural state of the boundary layer over the vehicle surface becomes a "first-order" variable in the design process. Yet, the location and extent over which boundary layer transition occurs is often the largest source of uncertainty in sub-system performance. Furthermore, if the physics of the boundary layer transition process are well understood, then control becomes a reality, with potentially high pay-off.

1.1.1 Applications of Transition Experiments

Some estimates have indicated that if laminar flow can be maintained on the wings of a large commercial transport, the reduction in skin-friction drag would give as much as 25% savings in fuel (Reed et al. 1996). This has obvious implications for transport range, payload economy, and emissions control to the environment. A recent numerical study by King et al. (1998) has also shown that the location and extent of boundary layer

transition has a significant influence on both lift and drag of supercritical airfoils by changing the location of the shock-wave, and the subsequent shock-boundary layer interaction. This is an important finding, since the transition location is usually prescribed a priori, rather than computed from physical principles with the flow-field solution. Perhaps the most severe consequences for accurate transition prediction are found in the heating requirements for thermal protection systems (TPS) on hypersonic re-entry vehicles like the Space Shuttle (Olynick and Tam 1997) and the Lockheed X-33 technology demonstrator. If the current design predictions for boundary layer transition on the X-33 were to be exceeded, "the increased heating would exceed the TPS limits." (Thompson et al. 1998) An overly conservative design increases the vehicle weight, decreases payload capacity, and changes the allowable flight trajectories. The goal of single-stage to orbit also becomes more difficult.

Although there has been much progress in modeling boundary layer transition (Reshotko 1997a), there are still many shortcomings that prevent transition prediction and control based on first-principles, particularly for three-dimensional flows, and elevated disturbance environments; the problem is magnified at supersonic and hypersonic speeds. Further progress can only be achieved with wind tunnel experiments of sufficient quality to use for model validation (Haynes et al. 1996), and the conclusive identification of relevant flow physics. The basic component to these experiments is a wind tunnel that has a high-quality flow field in which disturbances are below various threshold values similar to free-flight conditions. These low-disturbance wind tunnels in the supersonic

and hypersonic regime are termed "quiet" wind tunnels for their low levels of free-stream noise.

1.1.2 Sources of Free-stream Noise in a Supersonic Wind Tunnel

A review by Morkovin (1959) discusses the various sources of disturbances found in wind tunnels (Figure 1-1)[1]. The unsteady disturbances can be categorized into three unique modes that can exist independent of one another in a compressible flow. Vorticity (turbulence) and entropy (temperature spottiness) modes are convected disturbances that propagate along streamlines, and are traceable to conditions upstream of the nozzle throat. The third type of disturbance is an acoustic mode, whose intensity radiates across streamlines along local Mach lines. Vorticity and entropy modes can be mitigated with proper stilling tank design and screen arrangements located downstream of the classic disturbance generators listed in the left of Figure 1-1, and just upstream of the contraction. Additionally, Laufer (1961) showed that above about Mach 2.5, the acoustic disturbances dominate the free-stream flow field and the convected disturbances are damped due to the high accelerations and flow-stretching through the nozzle.

The acoustic disturbances are composed of fluctuations that originate at the wall due to a localized "effective" displacement of the boundary layer. In the case of wall roughness and waviness, the surface geometry produces a local pressure perturbation (Mach-wave) that emanates from a fixed location, and any unsteadiness in the boundary layer causes the Mach-wave to shiver, so that this wrinkled Mach-wave displaces back

---

[1] Figures and tables are located at the end of each chapter.

and forth relative to a fixed observer. As boundary layer transition sets in, discrete turbulent eddies form that protrude above the surface of the boundary layer. Each of these eddies is capped by a weak, unsteady, conical shock wave that moves with the speed of the eddy (Laufer 1964). As one approaches hypersonic speeds discrete turbulent bursts are even observed in the free-stream as eddy-Mach-waves convect past a stationary probe (Stainback et al. 1974, Wilkinson et al. 1994, Schnieder and Haven 1995). Recently, Wilkinson (1997), and Brogan and Demetriades (1998) have also shown that unstable activity in the boundary layer can interact with the stream to produce pressure perturbations before the formation of turbulent bursting in the wall boundary layer. As the Mach number increases in the core flow, the effect of perturbations in the inviscid surface are amplified proportional to M^2 (Laufer 1961).

1.1.3 Effects of Free-stream Noise on Transition

Pate and Schueler (1969) and Pate (1980) clearly demonstrated that the transition process on a model can occur at lower Reynolds numbers when acoustic disturbances originating from eddy-Mach-waves in a transitional and turbulent boundary layer impinge on a model. These acoustic waves act as a forcing function (Mack 1975) that, at the proper frequencies, can prematurely excite instabilities within the model boundary layer causing the layer to break down to turbulence. The leading edge region is particularly susceptible to the adverse effects of wind tunnel noise.

Dougherty and Fisher (1982) also made a direct comparison of the Reynolds number at transition onset (Re_T) in wind tunnel and flight experiments at identical conditions with the same 10° sharp cone. Figure 1-2 shows the results of Dougherty and Fisher,

supplemented by flight data at higher Mach numbers as reported in Beckwith et al. (1983)[2]. With increasing Mach number, Figure 1-2 graphically illustrates the large disparity between supersonic transition experiments conducted in conventional wind tunnels and those of free flight. The noise characteristics of these conventional supersonic wind tunnels are typically more than an order of magnitude above that found in free-flight, primarily because of the acoustic radiation from the turbulent boundary layer on the tunnel walls (recall radiated noise increases with M^2). Moreover, when the same experiment is conducted in a quiet wind tunnel with laminar wall boundary layers, noise levels approach those of free-flight, and Re_T increases to flight-values. The "quiet tunnel data" (Beckwith et al. 1983, Creel et al. 1985, Chen 1993) in Figure 1-2 was acquired again on a 10° cone in the two-dimensional Langley Mach 3.5 Pilot Quiet Tunnel (cone M_e=3.33) with only the apex of the cone subject to a low noise environment. Higher Re_T values were limited by the model size and tunnel conditions; it is still possible that if larger runs of low-noise flow were permitted on the model, Re_T would continue to increase.

It is also important to realize that the increased noise levels not only move transition forward in general, but they also modify parametric effects so that the transition test in the conventional tunnel has no relevance to free-flight conditions.

---

[2] This flight data is only about half of a larger data set also reported by Beckwith (1975). The reason for omitting these points is not known, although the latter is far outside the general cluster of data for M_e<5. The conditions and Re_T values of the complete data set are documented in (Schneider 1998b).

Therefore, if one is to conduct meaningful experiments dealing with boundary-layer transition on a wind tunnel model it is essential that the boundary layer growing along the wind tunnel nozzle itself remains laminar, to the extent that Mach waves emanating downstream of transition in the latter boundary layer do not impinge on the model. Because of this linkage between the boundary-layer turbulence and the free-stream disturbances, understanding the nozzle boundary layer is a prerequisite for attacking the free-stream disturbance problem systematically, and for designing "quiet" wind tunnels.

1.1.4 Organization of the Literature Review

The purpose of this thesis is to first, to understand more fully the mechanism(s) of boundary layer instability and transition on the wind tunnel walls and second, to explore how surface heating can be used as a design technique for delaying those instability mechanism(s) which cause transition in the nozzle boundary layer. In the remainder of this chapter, the elements of the transition process are first reviewed, emphasizing the mechanisms preceding transition. Then the current state of the art in quiet wind tunnels is discussed. Finally, the objectives of the present research are presented.

1.2 Supersonic Boundary Layer Transition Mechanisms

The evolution from a laminar to turbulent boundary layer is a process that begins with disturbances at the boundaries (i.e. surface and free-stream edge) of the layer. The Navier-Stokes equations dictate that with a proper match in scale and frequency, these disturbances will be ingested into the layer, then be naturally amplified by the conditions in the layer without the aid of external forcing. When disturbances *in the boundary layer*

grow to a certain point, a localized region of turbulence appears. With increasing distance, more turbulent "spots" appear and merge together, until a fully turbulent layer is achieved; that is, the production of turbulence is self-sustained, stable, and statistically stationary. Morkovin (1991) developed a "system portrait of roads to wall turbulence" reproduced here as Figure 1-3. The details of this schematic are still not complete, and some still poorly understood, but the portrait covers the major categories of the transition problem.

The mechanism(s) by which the disturbances like sound, vorticity, and roughness can be converted to free-waves in the boundary layer ("eigenmodes") is termed receptivity, and, as illustrated in Figure 1-3, it encompasses and influences the entire transition process. First, receptivity provides the crucial information for the initial amplitude, phase, and frequency at the inception of the primary instability. Second, distributed receptivity recognizes the boundary layer as a truly open system, to provide the boundary conditions for the disturbance equations as the instability grows. The character of the initial conditions and boundary conditions in turn controls the path of non-linear break down of the laminar flow. However, the non-homogeneous boundary conditions are often unimportant because of the disparity in scales between the free-stream and boundary layer disturbances.

Since the unsteady free-stream disturbances generally have much larger wavelengths than those of the boundary layer eigenmodes, a mechanism to re-scale the free-stream disturbances is required for a strong coupling between the external and internal perturbations of the boundary layer. These mechanisms are found in rapid, localized

adjustments of the basic state. Thus, the classic receptivity sites are near surface roughness, and the model leading edge or stagnation point where a strong local pressure gradient exists and rapid boundary layer growth occurs. The stationary disturbances (i.e. Görtler and crossflow) apparently respond to streamwise vorticity generated at the leading edge or discrete roughness elements (Reibert and Saric 1997, Saric et al. 1998) so that this re-scaling is not necessarily required.

In a low-disturbance environment, the initial growth of the instability can be described by a set of linear disturbance equations (derived from the unsteady Navier-Stokes equations) valid in the limit of small disturbance amplitudes. As the amplitude increases, non-linear interactions occur that give rise to new secondary instabilities. The boundary layer becomes highly three-dimensional, instability growth is very rapid, and breakdown to turbulence occurs quickly. The final mechanism that leads directly to the chaotic and random fluctuations of turbulence is appropriately named the tertiary instability. However, the latter occurs over such a short distance, that there is usually no distinction made between the secondary and tertiary instabilities.

At times, the initial amplitude of the instability can be so strong that one or more stages of instability growth is "bypassed" (Morkovin 1984). Non-linear mechanisms lead to turbulence prematurely. The bypass mechanisms are poorly understood, but have been repeatedly observed in cases of high disturbance environment, including free-stream turbulence, sound (e.g. the conventional wind tunnel), sufficient roughness, and wall-waviness.

1.2.1 Boundary Layer Stability Prediction

1.2.1.1 Instability types

At the heart of the transition process is the presence of an instability within the boundary layer whose characteristics are governed by the basic state, free-stream conditions, disturbance environment, and surface geometry. The instability mechanisms that initiate the transition process (primary instability of Figure 1-3) are categorized by their physical mechanisms of instability growth as Tollmien-Schlichting (TS) and Mack-modes, Görtler vortices, crossflow vortices, and Rayleigh instabilities. Under enabling conditions, each instability can exist as a "natural" oscillation, whose growth is driven by a conversion of energy from the boundary layer basic state to the instability. Many applications will have more than one instability that co-exist, in which case, the more unstable disturbance will dominate over the others, and/or strong non-linear interactions between instabilities will occur.

The TS mode is a general description of a vorticity wave propagating through the layer in the streamwise direction (two-dimensional wave), or at an angle inclined to the streamwise direction (oblique wave). Mack (1969, 1984) has given a complete account of these waves for the compressible layer at supersonic and hypersonic speeds. In particular, he showed that (1) the oblique "first-mode" waves are more unstable than their two-dimensional counterpart, and (2) with increasing Mach number (M_e>4), a second-mode and additional "Mack-modes" with an acoustic nature become more unstable than the first-mode instability. The TS and Mack-modes are traditionally responsible for transition in flat plate and conical flows with a low-disturbance environment.

In the boundary layer on a concave wall (the general case is treated with streamline curvature rather than geometry curvature), the Görtler instability develops due to an imbalance between centrifugal forces and the pressure gradient normal to the wall. The outer regions of the boundary layer have a higher radial acceleration than the inner regions. Hence, the boundary layer exchanges fluid between the inner and outer regions with counter-rotating vortices whose axes are parallel to the streamwise coordinate.

A three-dimensional boundary layer provides the possibility for a crossflow instability associated with the inflection point in the lateral velocity profile. The inflection point is highly unstable and gives rise to spanwise modulations in the form of co-rotating vortex structures with their axes aligned with the inviscid streamlines. The vortex structure provides many similarities to the Görtler instability.

1.2.1.2 Linearized theory

The initial development of the primary instability can be described with linear stability theory (LST) in the limit of small amplitude disturbances. A harmonic perturbation is superimposed onto the undisturbed boundary layer state. If that perturbation grows, the layer is said to be unstable, and if all disturbances decay, the layer is stable. The LST has its roots in the unsteady Navier-Stokes equations linearized about the basic state. But the major simplifications in the theory come about by locally ignoring all boundary layer growth terms, and imposing homogeneous boundary conditions at the wall (smooth wall) and in the free-stream (no external disturbances). The resulting set of equations can be solved at any streamwise location with a given basic

state, and represents the correct zeroth-order approximation – formally justified with a complete nonparallel analysis.

Reed, Saric and Arnal (1996) have most recently reviewed linear stability theory. Mack (1969) still provides the most complete account of incompressible and compressible stability theory. Later he condensed this discussion and updated some of the issues in three-dimensional boundary layers and three-dimensional instabilities in (Mack 1984).

1.2.1.3 Non-linear methods

More sophisticated methods of stability prediction are the Parabolized Stability Equations (PSE) (Herbert 1997) and direct numerical solutions (DNS) of the Navier-Stokes equations (Reed 1993). The new PSE approach treats the boundary layer as a weakly non-parallel flow by including boundary layer growth terms, but neglecting streamwise diffusion in the disturbance equations. The result is a set of parabolic disturbance equations that are marched in the streamwise direction to analyze the evolution of single or interacting Fourier modes. Initial conditions are prescribed, presumably from experiment or a receptivity analysis. The DNS techniques remove all constraints of the stability problem, with an arbitrary spectrum of unsteady free-stream and surface conditions as input.

1.2.2 Boundary Layer Transition Prediction

Traditional engineering methods predict the onset of transition (defined by the first appearance of turbulent bursts) with empirical correlations. The simplest of these are

based on integral boundary layer parameters. Examples include the shape factor correlation of Wazzan (1981), or transition based on a momentum thickness Reynolds number Re_θ. However, the physics of the instability growth, and receptivity are completely removed.

The most common method for transition prediction used in industry involves LST coupled with an e^N transition prediction scheme (Smith and Gamberoni 1956, Van Ingen 1956, Arnal 1993). Growth rates of the linear disturbance are calculated on the body with LST for a given frequency, wavelength, and disturbance orientation. Integrating the growth rates from the first unstable point to some downstream location gives the disturbance amplitude A relative to the initial disturbance amplitude A_o. Transition is said to occur when the initial disturbance A_o has been amplified to a certain threshold, e^N, where N is the so-called N-factor is defined by

$$N \equiv \ln\left(\frac{A_T}{A_o}\right) \qquad \textbf{(1-1)}$$

The quantity A_T is the disturbance amplitude at transition. Since the e^N method can only correlate transition to the amplitude ratio, the role of receptivity in defining A_o is ignored entirely, and any effect of the disturbance environment must be included in the "calibrated" value of N. The primary utility in the e^N method is in comparing transition induced by the same primary instability between two similar disturbance environments. The N-factor can also be used as a stability index for parametric studies using the local amplitude A in place of A_T. At a given location, a lower value of N would indicate a more stable flow, and a longer run of laminar flow would be expected.

In low-disturbance environments, such as that found in quiet wind tunnels and free-flight, transition has been correlated to $N \approx 9$-11 for a wide variety of two-dimensional bodies with TS instabilities in subsonic through hypersonic conditions (Malik 1989a, Arnal 1993). Computations by Malik (1989a) showed that transition on a flat plate and cone (recall Figure 1-2) at Mach 3.5 occur near $N=10$. Transition on the Dougherty and Fisher 10° sharp cone in flight also correlated $9<N<11$.

As a correlation, the method is equally applicable to compressible and incompressible boundary layers with steady Görtler, or crossflow instabilities. However, the vortex motion of these instabilities quickly causes non-linear distortion of the basic state; the use of LST all the way to the point of transition is highly questionable (Arnal 1993, Reed et al. 1996). For Görtler vortices, Floryan (1991) reports that about 50% of the total distance from the neutral point to transition onset is dominated by non-linear development, whereas TS instabilities have a linear development that covers 75% to 85% of the unstable region (Arnal 1993). Accordingly, the N-factor for stationary vortical disturbances implicitly includes a large extrapolation of the linear region to the location of transition onset, as well as the receptivity effects on A_o. It is not surprising that the e^N method shows a high-degree of scatter for Görtler and crossflow disturbances.

The PSE and DNS techniques allow transition prediction directly from the instability amplitude, since the value of A_o is required in the solution. The inclusion of non-linear effects also allows transition prediction methods more closely related to physical conditions in aircraft design like the point of minimum shear stress or minimum heat transfer – but at considerable computational expense.

1.2.3 Heat-Transfer Mechanisms in Stability and Transition

1.2.3.1 Uniform heating

The hydrodynamic stability of a boundary layer is strongly controlled by the shape of the mean velocity profile in the boundary layer. It has been shown (Mack 1969) that the more negative the velocity second derivative is at the wall, $(\partial^2 U/\partial y^2)|_{y=0}$, the "fuller" and more stable the velocity profile becomes. This result applies to both inviscid and viscous instabilities. With an understanding of how $(\partial^2 U/\partial y^2)|_{y=0}$ affects hydrodynamic stability, a class of stability modifiers (Gad-el-Hak 1990, see also section 3.7 of Reed et al. 1996) has been developed from the compressible stream-wise momentum equation applied at the wall,

$$\left[\rho V \frac{\partial U}{\partial y}\right]_{y=0} + \frac{dP}{dx} - \frac{d\mu}{dT}\left[\frac{\partial T}{\partial y}\frac{\partial U}{\partial y}\right]_{y=0} = \left[\mu \frac{\partial^2 U}{\partial y^2}\right]_{y=0}. \qquad \textbf{(1-2)}$$

Note that differentiation has been performed on the viscous dissipation term to obtain the last term on the left hand side (LHS) and the term on the right in equation 1-2.

Among other modifiers (suction, controlled pressure gradient, etc.) the last term on the LHS is positive or negative depending on the direction of heat transfer. In air, the dynamic viscosity, μ, always increases with temperature, therefore, $d\mu/dT>0$ and $\partial U/\partial y|_{y=0} > 0$ for non-separating flows. If heat is removed from the fluid (wall cooling), $\partial T/\partial y>0$, and the last term of the LHS is negative. The second derivative $(\partial^2 U/\partial y^2)|_{y=0}$ becomes more negative showing a fuller and thus more stable velocity profile. Similarly, wall heating produces $\partial T/\partial y<0$, bringing the second derivative closer to zero, and

destabilizing the boundary layer. This heating effect has been verified in a number of experiments on cones and flat plates. In fact, Lees (1946), and later Reshotko (1963) showed the possibility that at low supersonic Mach numbers, a boundary layer can be completely stabilized with cooling below some threshold ratio of cooled wall to adiabatic wall temperature.

However, the arguments related to equation 1-2 (the "classical heat transfer effect") apply to the boundary layer stability governed by first-mode TS waves. Other modes of instability, such as the Mack modes (Mack 1984), Görtler vortices (Floryan 1991), and crossflow instabilities (Reed et al. 1996) do not respond to the heat transfer effect in the same way as discussed above, and may show an opposite heat transfer effect.

Analysis of Görtler vortices for incompressible and compressible flows shows a mixed response to surface heating. At supersonic speeds, El-Hady and Verma (1983, 1984) used a normal mode solution to show that the stabilizing or destabilizing effects is dependent upon the choice of parameters in the problem. Spall and Malik (1989) solved the full Görtler problem with a marching procedure (linear PSE) to improve the solution of El-Hady and Verma, explore the effect of pressure gradient, and extend the results to wall heating at supersonic and hypersonic Mach numbers. At Mach 3.5, Spall and Malik show that heating has a mild stabilizing effect (doubling the wall temperature gave a 15% increase in Re_T at N=10) and cooling is slightly destabilizing – an apparent monotonic trend. Growth rates with and without heating at other Mach numbers were not presented.

The stability trends with surface heating or cooling for the compressible Görtler problem are rationalized against the relative dominance of viscous dissipation

(stabilizing) and centrifugal forces (destabilizing) (El-Hady and Verma 1984, Kabayashi and Kohoma 1977).

1.2.3.2 Localized Heating

Recently, the possibilities of stabilizing first-mode TS waves in a boundary layer by localized heating have been explored in subsonic flows. There are relatively few papers on the subject (most in Russian), but the reported effects are all consistent.

Masad and Nayfeh (1992) demonstrated, theoretically, that the boundary layer over a flat plate could be notably stabilized when the heating strips are properly placed ahead of the neutral stability point. Heating the boundary layer upstream causes the boundary layer to be "cooled" upon entering the region of instability. Therefore, by the classical cooling effect of equation 1-2, the velocity profile instead becomes more stable, thus moving transition onset downstream. Placing the heat transfer strips inside the unstable region (i.e. downstream of the neutral point), increased the growth rates at and downstream of the strip – again showing the relevance of equation 1-2. Masad and Nayfeh calculated the opposite behavior when cooling strips were used in place of the heating strips. Both incompressible and compressible flows (up to M=0.8) were included in the study.

The same "natural cooling" effect has also been confirmed in several flat-plate experiments (Dovgal et al. 1990, Maestrello and Nagabushana 1989). Dovgal et al. showed by experiment that when heat was concentrated at and near the leading edge, the growth of unstable waves was reduced. If heat was placed in the unstable region, the boundary layer became more unstable. With proper location of the heating, transition

Reynolds number could be increased by as much as 70% over the adiabatic case, with only a 28% increase in the local wall temperature. Transition could even be delayed with heating at the leading edge in even the presence of a three-dimensional square roughness element.

Kazakov et al. (1995) have also applied the localized heating technique to the leading edge of a two-dimensional airfoil to show substantial increases in the transition Reynolds number in the chord-wise direction. When intense heating was used, transition delay could even be demonstrated with a thermally insulated surface downstream of the initial heating. These results were in qualitative agreement with the experiments of McCroskey (1961, quoted in Maestrello 1990) whose results were again attributed to natural cooling.

Maestrello (1990) also reports the local surface heating as a means for re-laminarizing a turbulent boundary layer proceeding a concave surface with Görtler vortices. With an initially turbulent boundary layer heat is applied in the appropriate location, and the relaminarization produces the famous Blasius profile. Relaminarization is again attributed to natural cooling downstream of the heater, according to the stability arguments of equation 1-2.

1.3 State of the Art in Quiet Wind Tunnels

As described in Section 1.1, the natural state of the boundary layer on the nozzle walls is the most common cause of a noisy environment which in turn causes poor results from transition experiments conducted in wind tunnels. Figure 1-5 shows a schematic of how transition on the nozzle walls defines the low-disturbance test core of the quiet

tunnel. The forward region of the test rhombus is defined by the Mach lines that extend forward from the nozzle exit, while the back of the test core is limited by the Mach lines that emanate from an acoustic source at the wall – e.g. the onset of boundary layer transition. If the distance between the apex of the opposing wedges (or cones in an axisymmetric tunnel) is Δx, then the Reynolds number at the free-stream conditions in the test rhombus, based on Δx ($Re_{\Delta x}$) represents the largest Reynolds number that can be tested within the quiet test core. The primary objective in quiet tunnel design is to maximize $Re_{\Delta x}$ by maintaining laminar flow on the nozzle walls as long as possible. The largest "quiet-flow Reynolds number" achieved in practice to date has been $Re_{\Delta x} = 9 \times 10^6$ in the Langley Mach 3.5 pilot tunnel (Chen and Malik 1990).

Before discussing the LFC techniques employed to maximize $Re_{\Delta x}$, we must address the question: What constitutes quiet flow? The database of atmospheric disturbances in the flight environment is sparse, and cannot be used for a quantitative comparison to the wind tunnel environment. In the absence of these direct measurements, the best working definition of "quiet-flow" would be derived from a comparison of Re_T in the wind tunnel and flight. Beckwith et al. (1983) have used the Dougherty and Fisher 10° cone data and corresponding low-disturbance wind tunnel tests (Figure 1-2) to suggest a level of static pressure fluctuations less than 0.05% of the mean for quiet flow. Another common threshold is pitot pressure (i.e. total pressure behind a normal shock wave) fluctuations that are less than 0.1% of the mean (Beckwith et al. 1983, Wolf et al. 1994, Wolf and Laub 1996). In either case, the disturbance spectra should also be monotonic decreasing with increasing frequency (Reshotko 1997b).

1.3.1 Boundary Layer Development on a Supersonic Nozzle

To achieve "quiet" operation, a solid understanding is needed of transition in the boundary layers growing on the interior surfaces of the wind tunnel nozzle and test section. A necessary element in this understanding is the behavior of the nozzle laminar boundary layer, on the basis of which stability calculations and accompanying transition predictions can be made.

Most nozzle designs are either of the two-dimensional type or axisymmetric, each with its inherent advantages. The two-dimensional nozzle consists of two opposing contoured nozzle blocks enclosed within two flat sidewalls. Flow sections are rectangular, with expansion taking place in a direction parallel to the sidewalls. At any given distance from the nozzle throat, the inviscid flow is therefore laterally uniform on the contoured surfaces, but is strongly variable on the sidewalls. Specifically, pressure gradients appear on the sidewalls in a direction normal to the main flow vector, inducing crossflows which distort the sidewall boundary layers and generate appreciable three-dimensionalities in the corners (King and Demetriades 1993, Ostrander et al. 1989). The resultant laminar boundary layer profiles around the periphery of any given cross-section are thus non-uniform, also leading to potential non-uniformities in the boundary layer stability and transition to turbulence. The laminar boundary layer development of the two-dimensional nozzles has been most recently addressed with experimental and theoretical analyses by Demetriades et al. (1998). Axisymmetric tunnels enjoy some simplicity in the boundary layer development, since the inviscid flow and boundary layer development at any given distance from the throat are independent of the angular coordinate. Boundary layer stability and transition are also

expected to be nominally axisymmetric. However, the fabrication and visual access of axisymmetric tunnels are more difficult to achieve than with a two-dimensional shape.

1.3.2 Nozzle Design Features for Laminar Flow Control and Noise Reduction

To summarize the history of quiet nozzle development (Beckwith and Miller 1990), the primary causes of nozzle wall turbulence have been found to be roughness in the nozzle throat, continuation of the turbulent boundary layer in the settling chamber and contraction into the nozzle, and destabilization of the nozzle wall laminar boundary layer by the formation and amplification of instabilities which subsequently grow and cause a turbulent wall boundary layer. These issues are addressed by providing a highly polished nozzle, suction slot upstream of the throat to remove the turbulent boundary layer (i.e. "bleed slots"), and a slow-expansion axisymmetric nozzle to reduce the strength of Görtler vortices, and increase the axial distance of the quiet test core based on Mach lines from the "acoustic origin" of the turbulent boundary layer.

It would appear that the techniques for maintaining natural laminar flow by optimizing the nozzle geometry have been exhausted. Yet, the present achievable transition Reynolds numbers on nozzle walls (and hence quiet test core size) still impose severe limitations for studying natural transition at flight conditions in the wind tunnel. It therefore remains to explore other LFC methods to further increase $Re_{\Delta x}$. One such method appears to be a controlled temperature distribution on the nozzle surface.

1.3.3 Observed Temperature Effects on Nozzle Boundary Layers

In 1975, Harvey et al. investigated the effect of heating the surface in a Mach 5 pilot supersonic nozzle as part of a quiet wind tunnel design. Strip heaters were placed around the outside of the nozzle surface and subsonic approach. The results showed the transition Reynolds number increased by approximately 20%. The heating in these experiments, however, was not applied locally, as in the work of Masad and Nayfeh (1992), but uniformly over the nozzle surface. The probable mechanism of transition delay was explained as a result of an increased boundary layer thickness with heating that, in turn, reduced the relative height of surface roughness (Harvey et al. 1975a). Thus, the surface heating produced a "smoother" surface. The finding that heat could delay transition was apparently overshadowed by the two-fold increase in Re_T produced by boundary layer bleed-slots, and was not pursued further.

Through the 1978-1981 period, Demetriades (1978, 1981a, 1981b, 1992a) studied the effect of surface roughness and wall temperature on the boundary layer in the throat of the MSU Mach 3 supersonic wind tunnel. Liquid nitrogen was circulated through ducts in the nozzle throat region located approximately 1 cm below the exposed surface of the aluminum nozzle block. Transition Reynolds numbers were seen to monotonically decrease with decreasing wall temperature (Figure 1-4). This result was again in opposition to the simpler theory for flat plate flows.

In 1993, Demetriades (1996) returned to the nozzle heating effect to confirm the observations of Harvey et al. (1975) and Demetriades (1981a, 1992a) and explain why heating or cooling delays or promotes transition, respectively. A uniform heat flux was

applied with a film heater that began upstream of the throat, and extended to 70% of the nozzle length. With surface temperatures only about 12% above the adiabatic wall temperature, the boundary layer state could be reduced from turbulent to laminar (Demetriades 1996). It was hypothesized that the heat concentrated near the nozzle throat caused a natural cooling of the boundary layer downstream, and thus a more stable boundary layer by the classical cooling effect.

Very recently, similar trends have been observed with a cold wall promoting transition in the Purdue Mach 4 Ludwieg Tube (Munro 1996, Schneider 1997).

1.4 Purpose of This Investigation

If the apparent heating effect can be optimized (e.g. heating level, location) and transferred to other wind tunnel facilities, implications on quiet wind tunnel technology can be far reaching. Moreover, if instability growth, and thus transition, can be substantially delayed by local heating in a wind tunnel, the acoustic origin of noise produced by the transitional and turbulent boundary layer will be moved down-stream, and the quiet test core will be enlarged for a given set of stagnation conditions.

The review of the current literature clearly shows that the heating effect on the nozzle boundary layer has remained largely unexplained from either an experimental or theoretical viewpoint. And furthermore, direct measurements of boundary layer transition, even without surface heating, on the interior surfaces of a wind tunnel nozzle are scarce. The objectives of the present investigation have been to explore physical mechanisms responsible for the observed delay in transition on the wind tunnel nozzle when heat is applied.

(1) Linear stability theory was applied to the boundary layer of a quiet supersonic nozzle to identify linear stability mechanisms associated with and without surface heating on the wind tunnel nozzle.

(2) The unsteady oscillations preceding the onset of boundary layer transition on a wind tunnel nozzle were measured both with and without surface heating.

(3) The results of the experiment and those of linear stability theory were compared.

With a favorable comparison between the theory and experiment, surface heating techniques could be applied to new and existing low-disturbance facilities with confidence using a rational design approach. However, if the theory could not predict the experimental observations with acceptable accuracy, the measurements themselves could provide more insight into the physics of the surface heating and guide the way for further study.

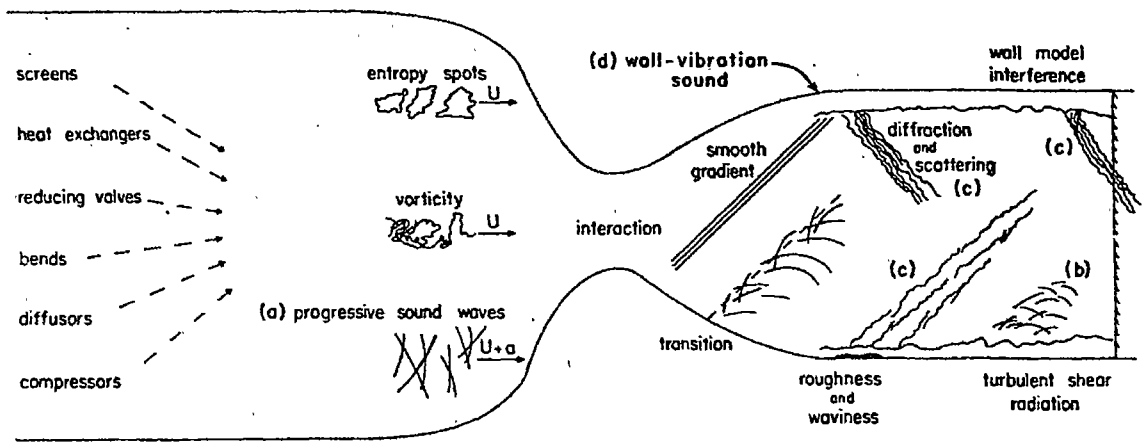

Figure 1-1. Unsteady disturbances found in a supersonic wind tunnel. Acoustic radiation from group (c) is the most common cause of premature transition in a supersonic wind tunnel model. Adapted from (Morkovin 1959).

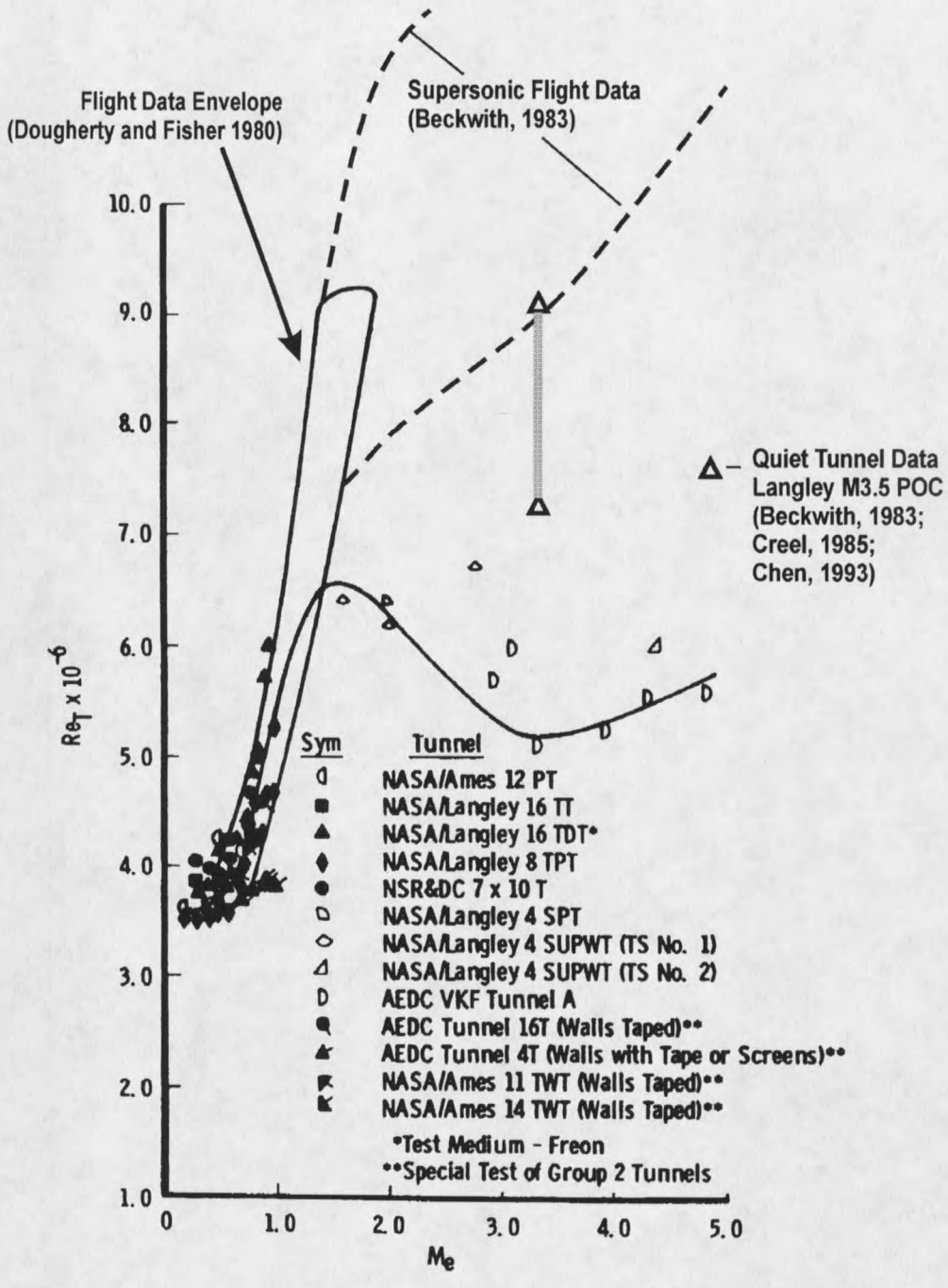

Figure 1-2. Disparity of transition experiments on a 10° cone between the best "conventional" wind tunnels, and flight-data. Quiet wind tunnel data is shown for comparison. Graph adapted from (Dougherty and Fisher 1982).

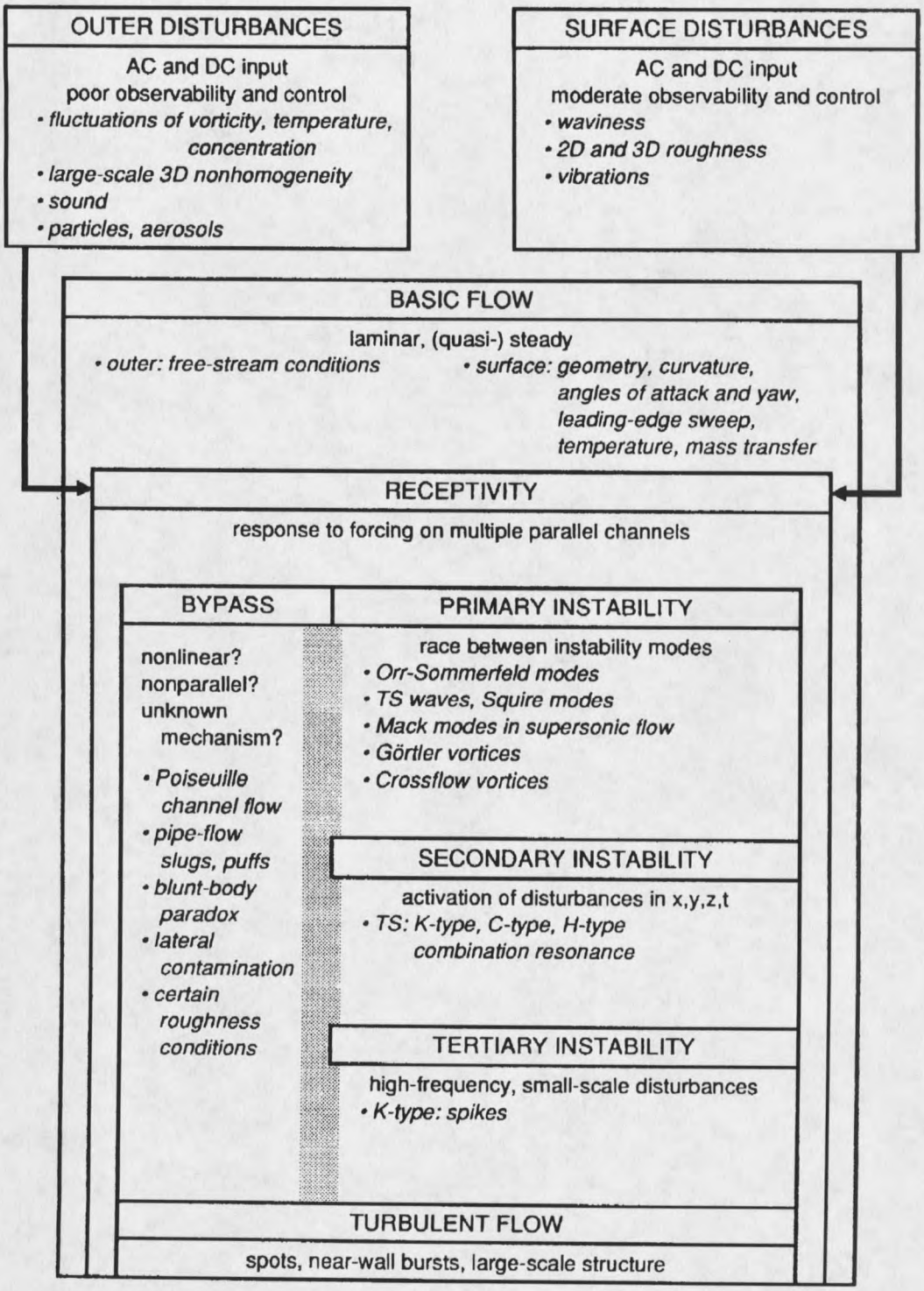

Figure 1-3. System portrait of roads to wall turbulence. Reproduced from (Morkovin 1991)

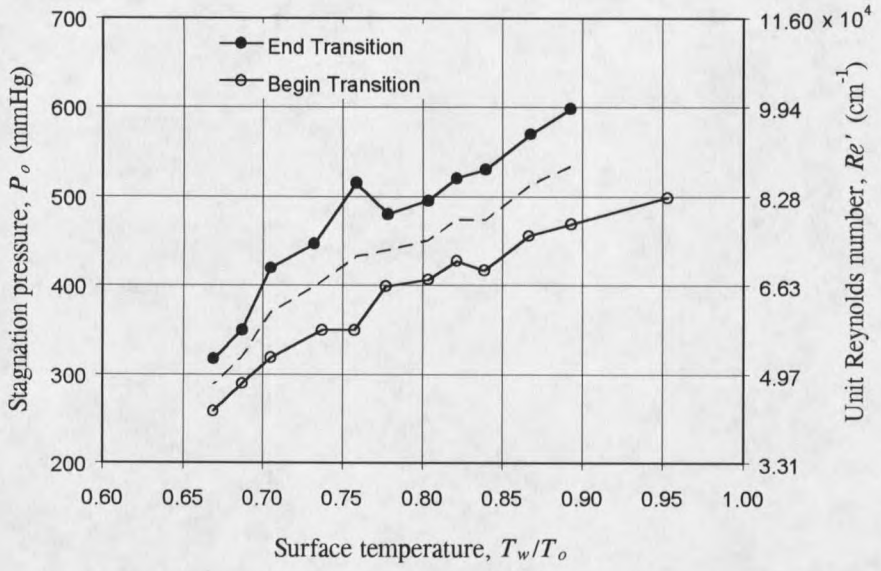

Figure 1-4. Effect of wall temperature on transition near the throat. Adapted from (Demetriades 1981a, Demetriades 1992a).

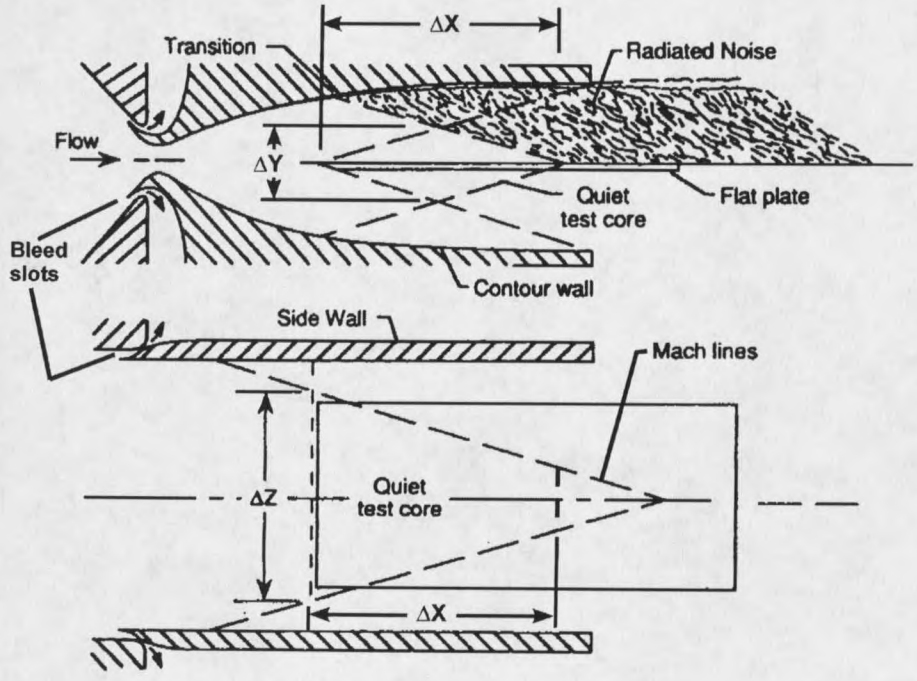

Figure 1-5. Illustration of the "quiet test core" in a low-disturbance supersonic wind tunnel. Picture of Mach 3.5 Quiet tunnel at NASA-Langley adapted from (Beckwith and Miller 1990).

CHAPTER 2

APPROACH

The facility chosen for this investigation was the two-dimensional Mach 3 Supersonic wind tunnel at MSU (MSU-SWT). Prior surface heating investigations involved observing fluctuations within the boundary layer at a single streamwise position (Demetriades 1992a, 1996), the present investigation has explored the streamwise development of instabilities and transition on the nozzle lower surface.

2.1 Wind tunnel and Nozzle Configuration

2.1.1 Wind tunnel

The Mach 3 wind tunnel at MSU is an open-circuit, continuous flow facility with run times as long as 12 hours. A low-disturbance flow is achieved by the absence any moving parts upstream of the test section, and by the two-stage contraction and screen arrangement upstream of the nozzle throat (see Figure 2-1). The first 3-dimensional contraction is approximately 56:1, and after the air goes through a flow-straightener and a series of screens, the air is accelerated to the nozzle throat in a 2-dimensional contraction with an area ratio of 8.5:1. The two dimensional nozzle and test section are shown in Figure 2-2. The nozzle interior is formed by two contoured upper and lower nozzle blocks bounded on each side with optical quality glass windows. The contour is a

conventional type (Chen et al. 1985) with the inflection point located at 9.8 cm from the nozzle throat and a maximum slope of 9.84°. The radius of curvature at the throat is 29.8 cm. Stagnation conditions can be controlled to obtain total pressures from 300-620 mmHg, and total temperatures of 21°C to 67°C. The range of unit Reynolds number from 2.1×10^6 to 6.7×10^6/m can cause a quiescent laminar, transitional, or a fully turbulent boundary layer to naturally occur on the nozzle surface.

The wind tunnel is also equipped with a two- or three-axis programmable traverse that is interfaced to a personal computer for automated experiments. The present experiments were conducted with only the x- and y- components of the traverse active. The optical access that extends from the contraction to the diffuser entrance allows the user to have un-obstructed view of the experiment at all times when moving diagnostic sensors in the flow.

2.1.2 Nozzle Modifications

The present investigations used the modified lower nozzle block of Demetriades (1992a, 1996). The aluminum nozzle block contains ducting located 1.0 cm beneath the nozzle surface (Figure 2-3) from $-9<x<9$ cm that spans the width of the nozzle. The present experiments used a circulating bath heater to pump hot ethylene glycol through the ducting that allowed a maximum surface temperature of 100°C. The temperature was maintained at a set-point value to within +/- 1°C with a closed loop controller. The details of the heater arrangement are given in (Brogan 1995).

A thin 0.023 cm overlay was instrumented with thermocouples as shown in Figure 2-3, and installed to cover the entire length of the two-dimensional contraction and nozzle.

The outer skin was a sheet of 0.013 cm stainless steel shim. After the overlay was installed, the entire upper surface of the nozzle block was hand-polished to a mirror-like surface. The measured surface roughness of the overlay showed a 0.05mm average roughness acquired with a stylus-type indicator.

The continuous glass sidewalls allowed the experimenters to observe the entire overlay throughout all data acquisition. Initially, waviness (0.002 cm peak-to-valley over 1 cm) was noted in the overlay, but after a few extended heating cycles, no defects could be observed. Furthermore, the polished surface optically amplified any defects present so that waviness of several microns was easily noticed. Measurements of the core mean-flow also showed no perturbations introduced by the overlay.

2.2 State of the Unheated Nozzle Boundary Layer

Figure 2-3 shows a qualitative "map" of instability growth and transition for the MSU-SWT Mach 3 nozzle. The transition map was created for the unheated nozzle condition using hot-wire and pitot pressure fluctuation data (Kulite measurements) collected over the past 20-odd years of tunnel operation. Though a number of detection techniques are represented in the transition map, the region boundaries were constructed primarily by viewing filtered rms activity as P_o was varied at a given streamwise position. The combination of wideband rms, the high-pass (>200kHz) rms, and visual inspection of time-series waveforms allowed a qualitative determination of the region boundaries (King and Demetriades 1993).

Under adiabatic conditions, Mueller observed that transition on the unheated nozzle appears to occur as a result of a low frequency disturbance (2-3 kHz) which grows and

gradually breaks down to turbulence with bursts appearing at the peaks and valleys of the base waveform. Mueller's findings also showed that the transition process in the MSU-SWT nozzle occurred at nominally the same streamwise position around the perimeter of the tunnel, with a slight preference for the sidewalls to become transitional before the contoured surface. Symmetry about the horizontal and vertical center-planes of the tunnel was also confirmed.

2.3 Scope of the Surface Heating Investigation

Since transition delay with surface heating had been observed on the lower nozzle block, the present study was focussed toward analyzing the stability of the boundary layer over the contoured surface with and without surface heating. The problem was approached with both theoretical predictions using LST and with experimental measurements on the centerline of the lower contoured surface of the MSU-SWT nozzle. Boundary layer stability was computed over the supersonic region of the nozzle both with and without surface heating. Measurements of unsteady fluctuations preceding and during transition were acquired over the latter half of the nozzle at conditions identical to the numerical analysis.

Table 2-1 shows the matrix of conditions for the present investigation. The low-pressure case (500 mmHg, 21°C) was selected to capture the unsteady fluctuations leading to turbulence and compute growth through a linear regime with and without surface heating. At 595 mmHg, the boundary layer without surface heating has a large turbulent content and cannot be discussed in the context of stability theory, or a pre-transitional phenomenon. However, the high-pressure case demonstrated the worst

condition (highest Re'_∞) in the MSU-SWT for which surface heating could be used to delay boundary layer transition. The measurements at P_o=595 mmHg also afforded an opportunity to extend the earlier measurements by Demetriades (1996) who also recorded a transition delay at 595 mmHg.

The "unheated" condition of Table 2-1 refers to the condition that no fluid was circulated beneath the nozzle throat. As will be discussed later, the unheated and adiabatic conditions showed different surface temperature distributions. The theoretical predictions were conducted for both "unheated" conditions and an adiabatic surface for comparison.

P_o mmHg	T_o °C	Re'_∞ m^{-1}	Nozzle surface condition*	Measurement Range x/L
500	21	5.20×10^6	Adiabatic Wall	---
500	21	5.20×10^6	Unheated, $(T_w)_{x=0}$ = 15 °C	0.54 - 0.95
500	21	5.20×10^6	Heated, $(T_w)_{x=0}$ = 60 °C	0.54 - 0.95
595	16	6.23×10^6	Adiabatic Wall	---
595	16	6.23×10^6	Unheated, $(T_w)_{x=0}$ = 12 °C	0.54 - 0.95
595	16	6.23×10^6	Heated, $(T_w)_{x=0}$ = 80 °C	0.54 - 0.95

*$(T_w)_{x=0}$ is the throat temperature only. Although the heated nozzle has a non-uniform surface temperature, the throat temperature, nozzle geometry, and stagnation conditions are sufficient to establish a unique temperature profile on the nozzle surface.

Table 2-1. Matrix of flow conditions for the surface heating investigation. Theoretical predictions are executed for the same.

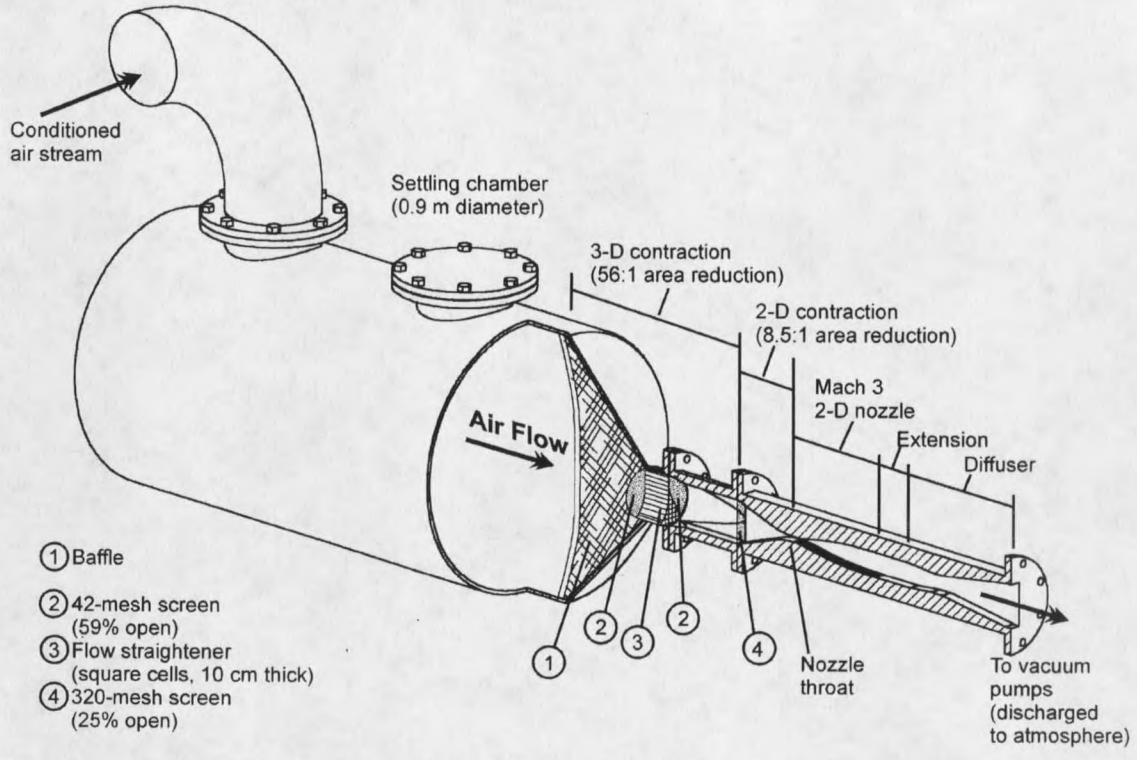

Figure 2-1. Section view of the MSU-SWT Mach 3 wind tunnel showing components of the settling chamber, contraction, and nozzle.

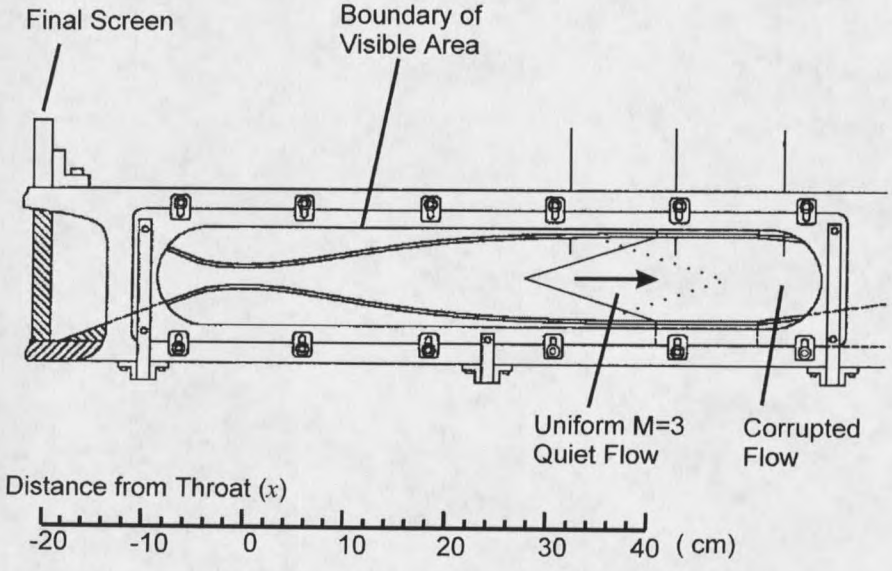

Figure 2-2. Schematic of the MSU-SWT 2-D Mach 3 Nozzle. (Nozzle length is L=38.48 cm)

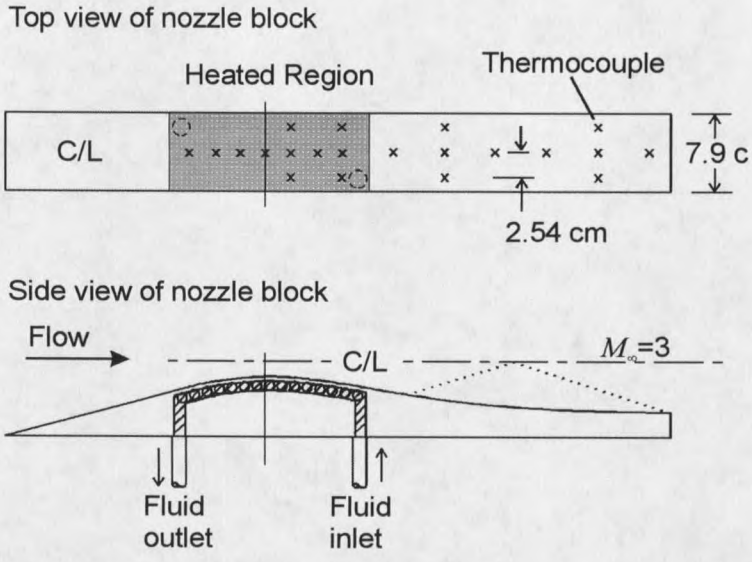

Figure 2-3. Heater configuration and thermocouple locations

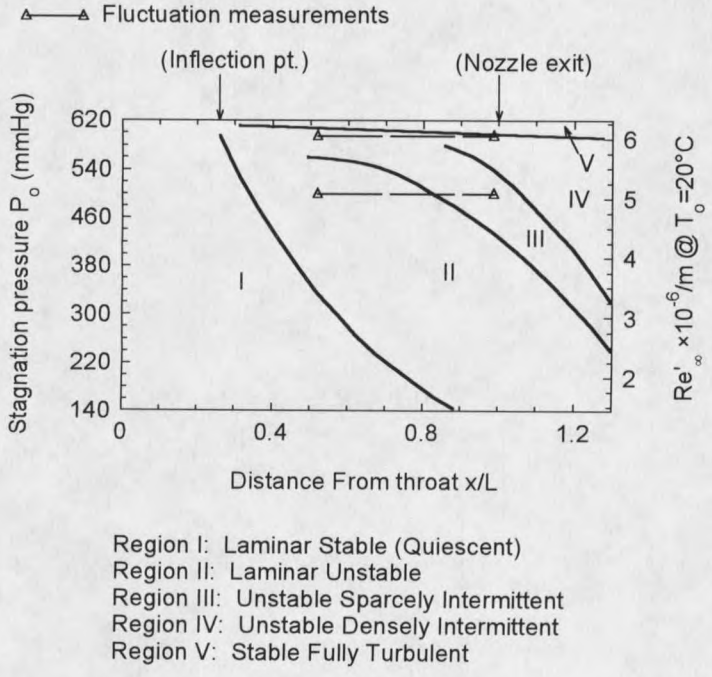

Region I: Laminar Stable (Quiescent)
Region II: Laminar Unstable
Region III: Unstable Sparcely Intermittent
Region IV: Unstable Densely Intermittent
Region V: Stable Fully Turbulent

Figure 2-4. Transition map in the MSU-SWT nozzle @ 20 °C with data range of the present fluctuation measurements.

CHAPTER 3

COMPUTATIONAL METHODS

Computations for the theoretical predictions followed a similar three-step pattern to that reported by King and Demetriades (1993). A streamwise pressure gradient was first computed with a viscous Navier-Stokes solver beginning upstream of the two-dimensional contraction and continuing to the test section exit. The pressure gradient from the Navier-Stokes solution, along with a thermal boundary condition at the wall was then used as input to a two-dimensional viscous gas boundary layer code. Boundary layer profile quantities and subsequent derivatives could be calculated at a much higher resolution with the boundary layer code than that afforded by the Navier-Stokes solution. Last, the basic state computed with the boundary layer code was used as input to a third program to compute linear stability predictions for first-mode Tollmien-Schlichting instabilities, and Görtler vortices.

All solutions were executed on the CRAY YMP at NASA-Ames for speed and precision. The Navier-Stokes solutions typically required less than 15 minutes of CPU time, and the boundary layer solver and stability code usually required less than 1 minute. Tabular summary files were also generated for each step of the solution (using custom programs and modifications to the source code) for interpreting the results graphically with plotting software. The combination of rapid solution times and convenient graphics

visualization allowed detailed parametric studies that could be performed interactively. Executing the codes on the CRAY also provided 64-bit arithmetic to minimize the effects of round-off error in the solutions. This is particularly important for the boundary layer and stability computations where 32-bit single-precision arithmetic often produces totally unusable results with wild oscillations.

3.1 Navier-Stokes Solution

3.1.1 OVERFLOW Description

The Navier-Stokes solver, OVERFLOW, was used to compute the adiabatic steady flow through the nozzle including the inviscid core and viscous boundary layer growth on the tunnel walls. The compressible Navier-Stokes equations are solved with a finite difference code in conservation form. OVERFLOW uses implicit differencing in time with options for central or upwind differencing in space, artificial dissipation, multigrid, and other convergence acceleration features for steady-state solutions. Certain of the code's features are presented here to acquaint the reader with the options used in the solutions presented below. A more complete description of the code and its basic algorithms can be found in (Buning et al. 1997, Jespersen et al. 1997, and Pulliam 1986).

Consider the time dependent Navier-Stokes equations written as

$$\frac{\partial Q}{\partial t} + L(Q) = 0, \qquad \textbf{3-1}$$

where Q is the vector of unknowns and $L(Q)$ is the spatial difference operator for the steady Navier-Stokes equations. The non-linear flux terms in the steady Navier-Stokes

equations ($L(Q)$) are linearized with Taylor series expansions. Then the discretized equations are cast into a delta form, such that

$$\left(I + \Delta t A(Q^n)\right)\Delta Q = \Delta t RHS^n \qquad \textbf{3-2}$$

where n denotes the previous time level and the solution is updated to the present time level n+1 with

$$Q^{n+1} = Q^n + \Delta Q \qquad \textbf{3-3}$$

The right-hand side term RHS in equation 3-2 is composed of $L(Q)$ plus some possible artificial dissipation. The matrix $A(Q)$ is the Jacobian of $L(Q)$ also with artificial dissipation. The matrix pre-multiplying ΔQ is referred to as the left-hand side term LHS.

Options in OVERFLOW for treating the LHS and RHS of equation 3-2 were chosen to resemble the diagonalized, implicit Beam-Warming (BW) algorithm (Pulliam 1986). This includes central difference operators in LHS and RHS, and approximate factorization with diagonalization in the LHS matrix.

In order to initiate a computation with approximate starting data as well as to suppress high frequency oscillations in the solution of the non-linear Euler and Navier-Stokes equations, it is necessary to add artificial dissipation to the BW scheme. This is accomplished by using a blend of second- and fourth-order dissipation terms with a "switch" that is sensitive to the pressure gradient. The fourth-order dissipation is active in the smooth portions of the flow field to damp high frequency waves, while the second-order dissipation is much more effective for shock capturing. The magnitude of dissipation is controlled by a multiplying factor set by the user. This factor can be a scalar that controls the amount of dissipation uniformly for all flow variables, or a matrix

that scales the dissipation appropriately for each individual characteristic field. The scalar dissipation has faster convergence and works well for most problems. However, it often gives excessive dissipation in boundary layer regions, which in turn produces a velocity overshoot at the edge of the boundary layer (for example see Figure 21, Jespersen et al. 1997). This behavior was confirmed in the present studies and would cause errors in the boundary layer edge detection, and boundary layer integral properties. As such, matrix dissipation was used for all final results.

In steady-state computations, convergence can be accelerated with multigrid and full-multigrid (FMG) techniques (Wesseling 1995). The benefit of multigrid is to combine the inherent advantages of solving a problem on a fine grid and on a coarse grid. On the finest level, high frequency error components are smoothed by the viscous dissipation in the scheme (real or artificial), and on the coarse level, solutions are quick and low frequency components convect out of the domain faster than on the fine level. Though multigrid increases computational overhead for each iteration (one multigrid cycle), fewer iterations are required to convergence. The net result with the multigrid implementation in OVERFLOW is a typical reduction in CPU time by a factor of two or three (Jespersen et al. 1997). The multigrid algorithm in OVERFLOW uses a saw-tooth cycle. For a single multigrid cycle, an approximate solution is obtained on the finest level, then interpolated or "restricted" to the next level, solved again, restricted to the next level, and so on until the coarse grid is reached. The solution is then successively interpolated or "prolongated" back to the fine level, thus completing a multigrid cycle. The maximum efficiency is achieved with "full-multigrid", or FMG. Here, one begins on

the coarse level, and gradually works up to the finest level, using the multigrid algorithm at any intermediate level. The number of iterations spent at each intermediate level is specified by the user and is optimized by numerical experimentation for a given problem.

Convergence to steady-state can also be accelerated with a spatially varying time step. A global time step is usually limited by only a small region in the solution domain for time accuracy and stability of the scheme (typically governed by the smallest cell dimensions). A variable time step can be viewed as a way to condition the iteration matrix of the relaxation scheme so that each cell has a time step proportional to the local CFL number. This allows much larger CFL numbers in the outer flow that accelerates the process of setting up the inviscid portion of the flow field. The inviscid flow in turn drives the boundary layer development and time to convergence for the overall solution is substantially improved. OVERFLOW implements a variable time step either with local time stepping (Δt is proportional to the cell volume) or with a constant CFL number over the entire flow-field (Buning et al. 1997). The present computations have used a mixture of both techniques: local time stepping was specified, and a minimum CFL number (typically 2 for initial start-up, and 5 thereafter) was enforced.

3.1.2 Grids

The nozzle geometry was modeled in two dimensions using a constant section plenum and the design coordinates for the nozzle block. The "plenum" replaced the three-dimensional contraction of the wind tunnel, and extended far upstream in order to minimize the influence of the numerical inflow condition. The plenum joined the two-dimensional contraction with a constant-curvature arc whose end points were tangent to

each surface. Beyond the throat, the nozzle design coordinates were first smoothed then refined to define the nozzle surface on arbitrary streamwise grid spacing.

Three different grids for the two-dimensional Navier-Stokes computation with dimensions 140×41, 169×65, 201×97 were used to explore the solution convergence. As an example, Figure 3-1 graphically shows the coarse grid. Each grid was algebraically determined through the lower half of the nozzle (allowed by symmetry) using body fitted coordinates.

First, grid spacing in the y-direction at the throat was generated with a simple geometric progression to cluster grid points near the solid surface for good resolution in the boundary layer. Then, the grid at the throat was projected through the contraction and nozzle, requiring the mesh to be orthogonal at the boundary surfaces and approximately orthogonal through the interior of the solution domain. The y-coordinates normalized by the throat height h (=1.799 cm) of the grid points at the throat are plotted in Figure 3-2 for the coarse, medium, and fine grids.

The streamwise mesh spacing for all three grids is shown in Figure 3-3. The largest streamwise gradients occur through the throat region where the flow is quickly accelerated from subsonic to supersonic speeds. The streamwise grid was established by first specifying a minimum Δx at the throat (x=0). In the contraction (x<0), an approximate potential flow was used to provide a grid spacing proportional to the estimated velocity potential, which led to a hyperbolic progression. Grid points in the nozzle (x>0) were biased toward the throat with a geometric progression.

As shown in Figures 3-2 and 3-3, the primary effect of increasing the number of grid points in both normal and streamwise directions was to increase the resolution in regions of high gradient. Table 3-1 summarizes the important grid parameters for the coarse, medium, and fine grids.

3.1.3 Initial Conditions and Boundary Conditions

The nozzle symmetry was enforced by specifying the upper boundary (tunnel centerline) as a flat inviscid wall with an extrapolation of the normal momentum equation and an adiabatic wall. The lower contoured boundary used a no-slip viscous condition with viscous terms started at the 5^{th} grid point. A pressure extrapolation was used to compute the solution at the wall. Flow variables at the inflow boundary were computed by using a constant P_o and T_o, then calculating the other flow variables based on the local Riemann invariants. In this way, characteristics propagating upstream were allowed to pass through the upstream boundary rather than reflect and introduce numerical oscillations into the solution. At the downstream boundary, all flow variables were extrapolated to the exit plane.

The computation was initiated by starting with a stagnant flow field and specifying a low pressure uniformly across the nozzle exit. Physically, this produced a rarefaction that propagated upstream then established the supersonic flow through the diverging portion of the nozzle. After the entire inviscid core was supersonic at the nozzle exit, the downstream boundary was changed to an outflow condition so that all flow variables were extrapolated to the exit plane, and the solution was marched to convergence.

In a supersonic nozzle the mass flow is uniquely determined by the nozzle throat and the stagnation conditions, and is a part of the solution. The mass flow in the solution was first estimated based on uniform sonic flow at the nozzle throat, and the effective throat area (corrected for the boundary layer displacement thickness). This guess was supplied to the code by specifying a uniform Reynolds number, Mach number and static temperature across the flow-field inlet. The elliptic nature of the subsonic flow upstream of the nozzle throat then allowed the mass-flow restriction condition to propagate upstream and adjust the inlet conditions as the solution developed (requiring P_o and T_o to be constant).

3.2 Two-dimensional Boundary Layer Solution

The boundary layer mean-flow over the contoured surface was computed with the two-dimensional (and axisymmetric) boundary layer code of Harris and Blanchard (1982), applicable to compressible, viscous, ideal gases. Since the boundary layer code can easily accommodate many more points in the surface normal direction than the Navier-Stokes code, it is the program of choice to provide detailed boundary layer quantities and derivatives for use by the stability code. Furthermore, the code was used by Brogan (1995) to explore the effects of surface heating on the mean-flow development in the MSU-SWT, and provided a natural extension to the present work.

The boundary layer code solves the system of governing equations with a coupled implicit finite difference procedure in the wall normal direction. The first streamwise station is solved with a locally self-similar solution, then marches in the streamwise direction at variable increments of the arc-length s specified by the user. Probstein-Elliot

and Levy-Lees transformations are employed to remove the classic boundary layer singularity at the starting location (s=0), and reduce the layer growth in the streamwise direction. The grid in the wall-normal direction is generated for all s with a geometric progression in the transformed normal coordinate, η_{BL}. As input, the user specifies $\eta_{BL,max}$, the number of grid points N, and the geometric progression constant ($=\Delta\eta_{BL,k+1}/\Delta\eta_{BL,k}$). Note that the subscript "BL" is included to distinguish the Levy-Lees variable from the wall-normal coordinate η used in the stability calculations, and in the solutions presented later.

As input, the boundary layer code required the edge pressure distribution (P_e/P_o), and wall thermal condition (q_w or T_w) as a tabulated function of arc-length s. Here, the Navier-Stokes solution was used to calculate P_e/P_o, and surface temperature distributions were obtained from experimental measurements. The stagnation conditions, surface geometry, solution and output control parameters were also specified as input. Output was in the form of boundary layer profiles and station summaries.

The boundary layer code had been modified to generate an input file (including profile derivatives) for the basic state used in the stability computations. First and second derivatives for velocity and temperature in η were computed in the Harris and Blanchard code using finite differences. Through the interior, 3-point centered differences were used to give second- and first-order accuracy on the first and second derivatives, respectively. Derivatives at the wall were computed with forward differences that maintained the same order of accuracy as in the interior domain.

3.3 Stability Computations

Theoretical predictions for the stability of the boundary layer were explored with the e^{MALIK} spatial linear stability code (Malik 1989b). This program has been used by a number of investigators for engineering predictions of boundary layer stability and transition in quiet nozzle design. This section describes the underlying theory of the code for stability predictions as it applies to the present computations.

3.3.1 General method

The formulation of the stability equations begins by expressing the instantaneous quantities $\overline{q} = [\overline{u}, \overline{v}, \overline{w}, \overline{p}, \overline{T}]^T$ as the sum of a mean-flow component Q and a disturbance q' so that

$$\overline{q}(x, y, z, t) = Q(x, y, z) + q'(x, y, z, t). \qquad \textbf{3-4}$$

The instantaneous quantities are substituted in to the full compressible Navier-Stokes equations, the basic state is subtracted out, and terms which are quadratic in the disturbance are dropped to leave a set of linear partial differential equations describing the behavior of small perturbations in a boundary layer. This set of stability equations is difficult to solve in general, and further assumptions are required for a tractable solution.

The boundary layer growth is assumed small over one wavelength of the disturbance, so that all of the "non-parallel" terms can be neglected in the disturbance equations. Physically, this can be interpreted as the local wave motion of the instability being governed by the local mean-flow with a negligible influence of local boundary layer growth. Accordingly, the mean-flow at a given streamwise position is expressed as

a two-dimensional parallel flow with $[U,V,W] = [U(y),0,0]$. The resulting linear disturbance equations formally represent a zeroth-order formulation of the instability, but they allow separation of variables that leads to an eigenvalue problem in the wall-normal direction y. The correct zeroth-order statement of the stability problem can be formally justified with a nonparallel analysis (see, for example, Gaster 1974)

The disturbance is modeled with a small amplitude harmonic waveform (i.e. single Fourier component) so that

$$q'(x,y,z,t) = \hat{q}(y)e^{i(\alpha x+\beta z-\omega t)}, \qquad \textbf{3-5}$$

where $\hat{q}(y) = [\hat{u},\hat{v},\hat{w},\hat{p},\hat{T}]^T$ is the vector of eigenfunctions that describes the mode structure through the boundary layer. To compute the growth of the waves in a spatial frame of reference, the wavenumbers α and β are complex and the disturbance frequency ω is real; a temporal formulation is achieved with α and β real, and ω complex. The two frames of reference lead to approximately the same physical description and are related through group velocity of the wave packets using Gaster's transformation (Mack 1984).

Separating the real and imaginary components of the exponent,

$$q(x,y,z,t) = \hat{q}(y)e^{-\alpha_i x}e^{i(\alpha_r x+\beta_r z-\omega t)}. \qquad \textbf{3-6}$$

The first exponential describes the growth of a single Fourier component, and the second exponential describes the waveform. Accordingly, a wave will be "unstable" and grow in the streamwise direction if $-\alpha_i > 0$, will be "neutral" for $\alpha_i = 0$, or will be "stable" for $-\alpha_i < 0$. Here we are principally concerned with the growth of the instability in the streamwise direction, so growth in the spanwise direction has been ignored by setting $\beta_i = 0$ (as is

customarily done) and considering β to be only a real number. The wave-angle ϕ of the traveling disturbance is defined by

$$\phi = \tan^{-1}\left(\beta_r / \alpha_r\right) \qquad \textbf{3-7}$$

Substituting equation 3-6 into the linearized disturbance equations, separation of variables allows the partial differential equations to be reduced to an 8th-order system of ordinary differential equations in the wall normal direction. The disturbance velocity and temperature perturbations are required to go to zero at y=0 and y=∞, for the set of 8 boundary conditions

$$\begin{aligned} y = 0: &\quad u' = v' = w' = T' = 0 \\ y \to \infty: &\quad u', v', w', T' \to 0 \end{aligned} \qquad \textbf{3-8}$$

The homogeneous disturbance equations and 3-8 constitute an eigenvalue problem for α, with parameters β and ω. There are a number of techniques for choosing values of β and ω, but, typically they are chosen in combination to either match experimental values, or to determine the largest growth rates (α_i) within a given basic state. The full set of equations for the eigenvalue problem in compressible LST can be found in (Mack 1984) or (Malik 1990a).

Equation 3-6 is the general description (in LST) for the TS instability, including first-mode (i.e. the first unstable eigenvalue), and the higher "Mack" modes. In the Mach number range of the present work, oblique first-mode instabilities with ϕ between 50-70° are dominant over other modes (Mack 1984).

When solving the stability problem, the disturbance equations are made dimensionless with the local edge conditions of the mean-flow (U_e, T_e, ρ_e) and a characteristic length,

$$l^* = \sqrt{\frac{\nu_e s}{U_e}}$$

where ν_e is the kinematic viscosity at the boundary layer edge, and s is the arc-length of the boundary layer solution. When the distance from the wall y is scaled by l^*, the familiar boundary layer coordinate

$$\eta = y/l^* = y\sqrt{\frac{U_e}{\nu_e s}}$$

is obtained. Combining the length and velocity scales leads to a dimensionless circular frequency

$$\omega = \frac{2\pi l^*}{U_e} f ,$$

where f is the physical frequency of the disturbance. However, for a given Fourier mode (constant physical frequency f), ω will change with streamwise distance. Consequently, it has become almost standard to use

$$F = \frac{2\pi\nu_e}{(U_e)^2} f$$

as the dimensionless frequency for the disturbance, which depends only upon the local edge conditions.

3.3.2 Görtler instability

Centrifugal instabilities of the steady Görtler type have been found to be a principal cause of transition on the concave portion of a supersonic nozzle, and are therefore critical to any investigation of stability in the nozzle boundary layer. The e^{MALIK} spatial linear stability code also computes the growth of Görtler vortices within the framework of equations 3-4, 3-5, and the quasi-parallel boundary layer approximations. The disturbance equations in e^{MALIK} retain all curvature terms in the leading order of approximation so that a steady centrifugal instability can be approximated with the limit of equation 3-6 as $\alpha_r \rightarrow 0$, and $\omega \rightarrow 0$.

The classical formulation of the Görtler problem describes steady counter rotating vortices by a perturbation the spanwise direction so that

$$\begin{bmatrix} u'(x,y,z) \\ v'(x,y,z) \\ w'(x,y,z) \\ p'(x,y,z) \\ T'(x,y,z) \end{bmatrix} = \begin{bmatrix} \hat{u}(x,y)\cos(\beta z) \\ \hat{v}(x,y)\cos(\beta z) \\ \hat{w}(x,y)\sin(\beta z) \\ \hat{p}(x,y)\cos(\beta z) \\ \hat{T}(x,y)\cos(\beta z) \end{bmatrix} \qquad \textbf{3-9}$$

where β is again the spanwise wavenumber (real). The Görtler solutions employed here also use the local reference scales presented in the previous section. The steady Görtler vortices modeled by equation 3-9 are illustrated in Figure 3-4. The $[x,y,z]$ coordinate system is positioned with z=0 in between the vortex pair. The wavelength of the disturbance λ_z is related to the nondimensional spanwise wavenumber β ($=\beta^* l^*$) by

$$\lambda_z = \frac{2\pi l^*}{\beta}$$

Substituting equation 3-9 into the Navier-Stokes equations, and linearizing, results in a set of linear partial differential equations in x and y that can be solved with a marching procedure in the streamwise direction.

The derivation of the Görtler disturbance equations, as first presented by Floryan and Saric (1981), also shows formally that the mean-flow components of the boundary layer can be properly described with first-order boundary layer theory. That is, curvature effects in the mean-flow are second-order so that a "standard" first-order boundary layer solver like that of Harris and Blanchard can be used to compute the basic state. However, curvature appears in the leading order of approximation for the disturbance equations. El-Hady and Verma (1983) first presented the appropriate formulation of the compressible Görtler problem with a set of partial differential equations. Spall and Malik (1989) later solved the system of equations directly with a finite difference procedure.

The e$^{\text{MALIK}}$ code invokes the quasi-parallel flow assumption and separates the amplitude functions with[3]

$$\hat{q}(x,y) = \hat{q}(y)e^{-\sigma x}. \qquad \textbf{3-10}$$

Boundary conditions from equation 3-8 lead to an eigenvalue problem for σ with parameters β and the Görtler number $G = \mathrm{Re}_{\delta_r}\left(\delta_r / r_c\right)^{1/2}$, where δ_r is some reference length. The Görtler number appearing in the disturbance equations plays a similar role to the Reynolds number of flat-plate and conical flows; it is essentially the ratio of viscous

to curvature length scales. Equation 3-10 is referred to as the normal-mode solution of the Görtler problem.

Hall (1983, 1988) and Saric (1994) have criticized the quasi-parallel flow approach since this approximation is only formally valid for vortices with an infinitesimal wavelength, while the most amplified wavelengths and those observed experimentally are typically $O(1)$ relative to the boundary layer thickness. This same issue is encountered in predicting TS disturbances, but the Görtler disturbance is apparently more sensitive to the boundary layer growth terms. Day et al. (1990) compared normal-mode solutions (without parallel flow) to the marching solution of the full PDE formulation for incompressible flows and found moderate agreement at $O(1)$ wavenumbers. They concluded that the normal-mode solution would be adequate for engineering predictions of growth rates, while one could only expect a qualitative description of the eigenfunctions. As expected, the differences increased dramatically for smaller wavenumbers (i.e. large, weak vortices) and converged for larger wavenumbers (small vortices). Spall and Malik (1989) solved the compressible flow problem for a Mach 3.5 boundary layer. They found that growth rates from the normal-mode solution were about 5% higher than those from the marching solution. Thus, the normal-mode solution again showed conservative estimates of the disturbance growth with sufficient accuracy for engineering purposes. A comparison of the eigenfunctions was not presented.

---

[3] Comparison of equation 3-9 to equation 3-6 shows that the growth rate σ for the Görtler problem plays the same role as $-\alpha_i$ of the general harmonic disturbance. However, the notation σ is maintained here for consistency with the literature, and to emphasize the intrinsic difference between the steady Görtler instability and TS instabilities.

3.3.3 Transition prediction

In addition to computing the stability characteristics, the e^{MALIK} code can be used for transition prediction with an N-factor. The N-factor is a measure of the relative amplitude growth (A/A_o) of the instability, defined by

$$N = \ln\left(\frac{A}{A_o}\right) = \int_{x_o}^{x} -\alpha_i dx \qquad \textbf{3-11}$$

where A_o is the initial amplitude of some disturbance quantity $q'(x,y,z,t)$ at the neutral point x_o (i.e. x=x_o at $-\alpha_i$=0).

The eigenvalue problem is solved at each streamwise station, and the amplification rate varies as the boundary layer changes with streamwise position x. The "path of integration" in equation 3-11 uses a fixed value of the physical frequency f, along with a scheme for specifying β as a function of x. The e^{MALIK} code allows the user to either (1) specify a fixed *dimensional* value of the spanwise wavenumber β^* for all x, (2) specify a fixed wave-angle ϕ for all x, or (3) employ an envelope method by allowing β to vary with x such that the growth rate $-\alpha_i$ is maximized. This is achieved by enforcing the condition

$$\left(\frac{\partial \alpha_i}{\partial \beta}\right)_{f,R} = 0 \qquad \textbf{3-12}$$

at each x-station.

Mack uses non-conservative wave theory to argue that the physically relevant procedure is to choose β^* as constant with streamwise position (Mack 1984, page 3-11). However, in practice, using equation 3-12 produces only small variations in β^* for first-

mode TS solutions, and it adds considerable simplification by reducing the number of free parameters in the eigenvalue solution to only one (i.e. frequency). Furthermore, the resulting solution with equation 3-12 provides an upper limit on the most unstable condition for a given physical frequency f.

3.3.4 Numerical method

The e^{MALIK} code solves the eigenvalue problem with either a global or local method depending on whether or not a guess for the eigenvalue is available. If no guess is available, all eigenvalues of the discretized system are computed with a QR or QZ algorithm (Wilkinson 1965). This is computationally expensive, so the streamwise diffusion terms are neglected in the global solution and a coarse grid is used. Eigenvalues from this global search are then filtered for physically reasonable values, and supplied to a local method as a "guess." The local method solves the complete dispersion relation as a system of 8 first-order ordinary differential equations with a Newton-Ralphson iteration procedure. The user can also supply a guess for the local eigenvalue search and the code skips the global computation.

To execute the code, the user chooses the disturbance frequency, and a method for computing β, along with a number of control parameters for the solution algorithm. A separate input file contains a complete specification (numerically tabulated in an unformatted FORTRAN file) of the basic state, including profile derivatives at all streamwise locations of the stability calculation. Output options can be specified for station summaries of the disturbance variables and an N-factor for transition prediction.

Eigenfunctions are also output at requested stations to identify the structure of the disturbance through the boundary layer.

Grid	Dimensions ($N_x \times N_y$)	j-Grid pt. @ throat	Streamwise stretching constant	Minimum $\Delta x/L$	Wall-normal stretching constant	Minimum $\Delta y/h$
Coarse	140×41	48	1.025	3.12×10^{-3}	1.12	6.43×10^{-4}
Medium	169×65	60	1.025	2.00×10^{-3}	1.12	4.21×10^{-5}
Fine	201×97	70	1.022	1.51×10^{-3}	1.083	1.94×10^{-5}

Table 3-1. Geometric grid parameters of the Navier-Stokes solution for the MSU-SWT nozzle.

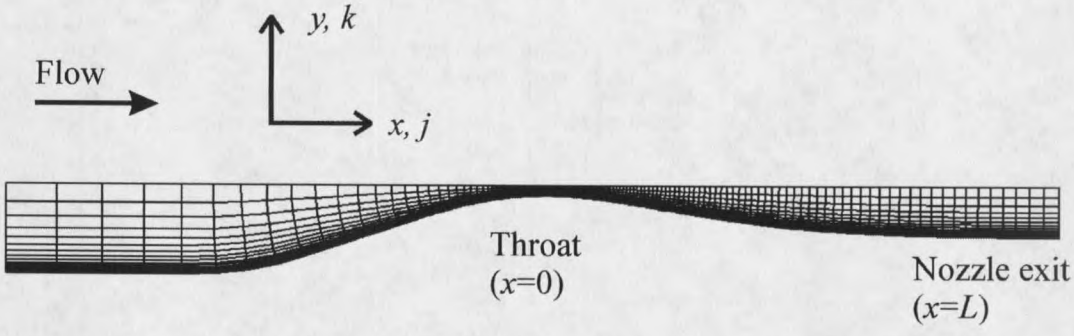

Figure 3-1. Grid used in the two-dimensional Navier-Stokes computations: coarse-grid shown (140×41), every grid line in j-direction, and every other grid line in k-direction.

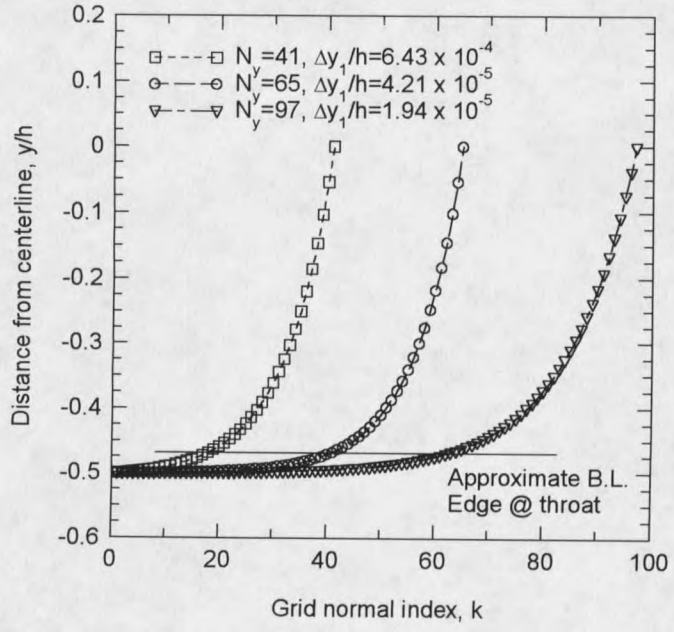

Figure 3-2. Grid spacing in the wall-normal direction (k) at the nozzle throat (x=0).

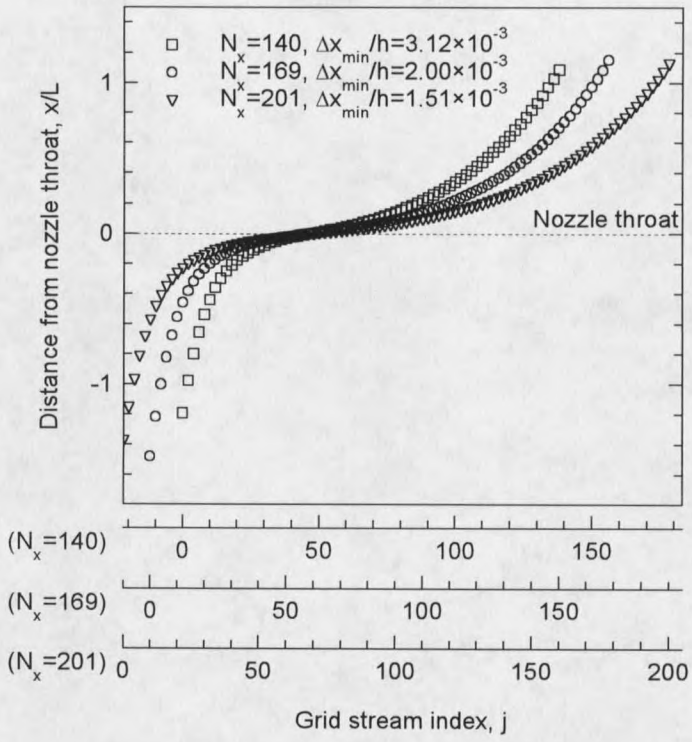

Figure 3-3. Grid spacing in the streamwise direction (*j*) on the nozzle surface.

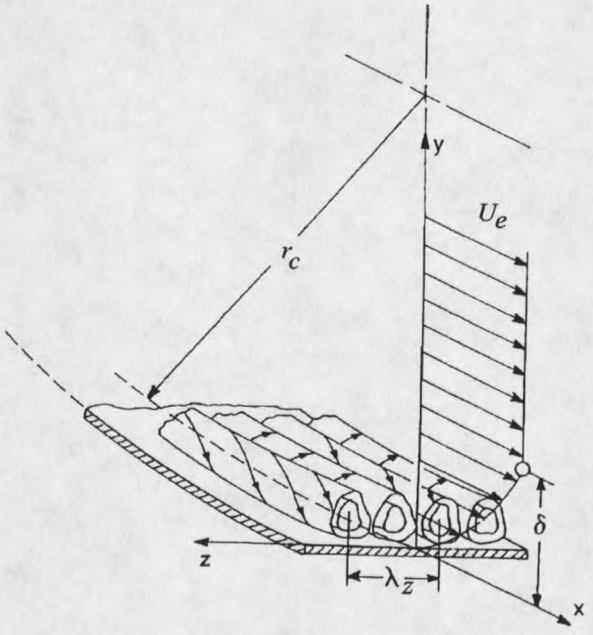

Figure 3-4. Görtler vortices in the boundary layer of a concave wall. Adapted from (Saric 1994).

CHAPTER 4

NUMERICAL RESULTS

4.1 Mean-flow Results

4.1.1 Navier-Stokes Solution

Following the procedure outlined in Chapter 3, Section 1, the Navier-Stokes solutions were solved with the diagonalized implicit Beam-Warming algorithm, full multigrid, and matrix dissipation. In accordance with the thin-layer Navier-Stokes approximation, viscous terms in the streamwise direction were turned off. Solutions were obtained for the two sets of stagnation conditions in Table 2-1, with an adiabatic wall in all cases. Changes in the core flow from heat flux at the wall would be felt through a change in the displacement thickness, which will be shown later to have only a minor effect on the boundary layer edge conditions. The results presented below were solved on the medium grid (169×65). After presenting the numerical results, solution accuracy and convergence will be discussed in Section 4.3 in terms of the parameters that affect the stability predictions.

4.1.1.1 Boundary layer edge definition

The identification of the boundary layer edge is somewhat arbitrary in a Navier-Stokes computation. The velocity varies continuously through the viscous and inviscid

regions, and no single "free-stream" velocity exists as in boundary layer theory. However, in an isentropic nozzle, the total pressure remains constant through the inviscid region and decreases with viscous dissipation. Therefore, a criterion suggested by King and Demetriades (1993) is to define the total pressure at the boundary layer edge $P_{o,e}$ to be

$$P_{o,e} = P_{o,w} + 0.98\left(P_{o,\max} - P_{o,w}\right) \qquad \textbf{4-1}$$

The "free-stream" conditions are taken at the point where the local total pressure is equal to $P_{o,e}$, then the boundary layer thickness δ is defined by the distance normal to the wall at which U=0.99U_e. This was the criterion used for the present computations.

Alcenius (1994) also compared the King criterion, its approximate equivalent $P_{o,e}$=0.98$P_{o,\max}$, and $P_{o,e}$=0.90$P_{o,\max}$, using velocity and total pressure profiles from a Navier-Stokes solution. The results showed the King criterion and the 0.98$P_{o,\max}$ threshold both worked well to objectively extract the boundary layer edge conditions from the Navier-Stokes solution.

4.1.1.2 Edge Pressure Distribution

The distribution of P_e/P_o shown in Figure 4-1 is the principal result of the Navier-Stokes computations in this study. The edge pressure distribution P_e/P_o and Mach number M_e change by about 1% from the lowest Reynolds number case (Re'_∞=3.28×10^6/m) computed by King (King and Demetriades 1993), to the highest Reynolds number case (Re'_∞=6.23×10^6/m) of the present work. The core flow is expected to change somewhat with Re'_∞ due to the change in the displacement thickness

of the boundary layer. However, the net change produced by δ^* is a second-order effect on the boundary layer edge conditions.

4.1.2 Mean-flow on Nozzle Contoured Surface

Brogan (1995) gives a complete discussion of the effects of surface heating on the laminar boundary layer of the MSU-SWT nozzle. The principal result was that for surface heating levels near $(T_w/T_o)\approx 1.1$, changes in the velocity profiles (U/U_e) were small, approximately 2-3%. Changes in temperature and density profiles were much larger. In this section, the results of boundary layer mean-flow solution with and without surface heating are presented for the cases of Table 2-1. Emphasis is placed on those parameters that have been correlated to boundary layer instability and transition.

The boundary layer mean-flow was computed with the Harris and Blanchard code using the edge pressure distributions of Figure 4-1 and a measured temperature distribution. Solutions were obtained on a grid with 101 points in the direction normal to the wall, geometric stretching $\eta_{BL,k+1}/\eta_{BL,k}=1.04$, and a constant streamwise spacing of $\Delta s=0.15$ cm. The nozzle geometry and edge pressure distributions were mapped onto the streamwise coordinate with second-order Lagrangian interpolation. Wall temperatures were mapped with a simple linear interpolation between the measurement locations. Higher order interpolation was not justified given the error-bars associated with temperature readings from the embedded thermocouples. Starting at $x/L=-0.3$ ($M_e=0.137$), the boundary layer solution was marched through the nozzle past $x/L=1$.

The pressure gradient parameter β_H (akin to the Hartree pressure gradient parameter in self-similar Falkner-Skan flows) is plotted in Figure 4-2 to demonstrate the integrity of the "input" pressure data to the boundary layer solution, where

$$\beta_H = \frac{2\xi}{U_e}\frac{dU_e}{d\xi}$$

and ξ is the transformed streamwise coordinate of the boundary layer solution (ξ is defined in equation 22 of Harris and Blanchard 1982). The calculation of pressure gradient is extremely sensitive to variations in the edge pressure that can be generated either by the interpolation from the input data to the computational grid, or by small perturbations in the P_e/P_o distribution. (For example, a 10 μm perturbation in the design coordinates was found to cause a steady pressure wave that would produce a 10% variation in the pressure gradient parameter. This illustrates the requirement for using *smoothed* nozzle coordinates.)

The streamwise temperature distributions with and without surface heating are plotted in Figure 4-3, where the symbols indicate measurement locations. The data in Figure 4-3 was used as input to the boundary layer solutions. The computed adiabatic wall temperature is included for comparison to the "unheated" wall condition. The wall temperature, in the absence of heat transfer, drops rapidly as the Mach number increases. However, axial conduction in the upper and lower aluminum nozzle blocks and heat transfer to the surroundings, prevent large gradients in the surface temperature, resulting in a near isothermal temperature distribution. At higher stagnation temperatures (e.g. T_o=70 °C), wall temperatures increase slightly (T_w=42 °C), but a uniform distribution

($\Delta T_w \approx 0.01 T_o$) persists. This is a significant result in itself, because a constant T_w is usually associated only with blow-down facilities with short run times.

In the heated cases, although circulating fluid was confined to the throat area, the surface temperature over the entire nozzle block rose. A uniform distribution was observed in the streamwise direction at the throat, with a gradual decrease toward the nozzle exit. Off-axis surface temperature measurements at $z=\pm 2.5$cm (Figure 4-4) varied by 1% (3°C) across the span at the throat, and were uniform across the width within 0.3% (1°C) thereafter. The small non-uniformities at the throat were most likely due to the path of the circulating fluid through the nozzle ducting, and heat conduction to the sidewalls.

4.1.2.1 Heat Transfer

The heat flux prediction (Figure 4-5) shows a maximum at the throat where the boundary layer is thinnest, and a diminishing *positive* heat flux in the basic state toward the nozzle exit. Beyond $x/L=0.5$, curves for all cases merge, indicating that the majority of the thermal energy for the heated cases is put into the boundary layer through the contraction and throat area. The low heat flux levels near the nozzle exit also indicate that the broad temperature rise of Figure 4-3 is strongly influenced by heat convected in the boundary layer. Heat exchange with the nozzle wall may also be affected by instabilities within the boundary layer. In particular, the fluid exchange of steady Görtler vortices can increase the heat transfer by as much as 100% to 150% (McCormack et al. 1970). The integrated heat flux distribution in Figure 4-5 only accounts for about 25% of

the total heat input to the nozzle. The majority of the heat loss is expected to come through natural convection to the surroundings.

Even with low heat transfer in the latter half of the nozzle, a principal feature of Figure 4-5 is that heat is directed *into* the boundary layer along the entire nozzle length. In previous work (Demetriades 1996), it was hypothesized that the boundary layer was heated near the throat, then cooled in the latter regions of the nozzle, and thus, transition delay with heat would be explainable by simple stability predictions. However, according to the present calculations, this "natural cooling" cannot explain the observed transition delay in the MSU-SWT.

4.1.2.2 Mean-Flow Profiles

Figures 4-6 and 4-7 show typical mean-flow profiles for temperature and velocity with and without surface heating. The static temperature through the heated boundary layer is higher than that of the unheated boundary layer as would be expected; variations in the normalized density (ρ/ρ_e) follow the inverse of the normalized temperature profile. The velocity profiles exhibit a more complex behavior. Near the wall, higher temperatures increase the viscosity to produce a velocity profile that is "less-full" through the inner region of the boundary layer. In the outer layer, the effect of decreasing the density overshadows the increase in viscosity. In spite of the viscous retardation, the pressure gradient imposed by the free-stream produces a greater acceleration on this region of lower density fluid, causing the upper region of the boundary layer to bulge (Cohen and Reshotko 1956). In fact, near the nozzle exit (x/L=1), the profiles with surface heating show edge velocities that exceed the free-stream velocity.. A comparison

of Figures 4-6 and 4-7 show that both trends of slower velocities near the wall, and faster velocities of the outer region of the boundary layer are amplified as the surface heating is increased.

The consequences of this momentum shift on the integral properties of the boundary layer are shown in Figure 4-8. When heat is applied, the boundary layer thickness does not change, and may even become thinner, the displacement thickness increases, and the momentum thickness decreases. These trends are consistent with the experimental and theoretical findings of Brogan (1995).

The shape factor H_{12}, as computed with the boundary layer code (Figure 4-9), increases with surface heating by as much as 60% in the low Reynolds number case and practically doubles (93%) in the high Reynolds number case. The difference in shape factor increases rapidly until x/L=0.3, which is shortly downstream of the peak surface heating (see Figure 4-5). The profiles then appear to be permanently altered as the difference in shape factor is maintained through the remainder of the nozzle. Changes in H_{12} are primarily due to density changes through the layer, since velocities show a smaller response to heat.

Empirical correlations for boundary layer stability with the shape-factor identify an increase in H_{12} with a decrease in the critical Reynolds number based on δ^* (Wazzan et al. 1979). Wazzan's correlation was constructed with a diverse set of low-speed data for first-mode TS instability. However, the extrapolation from the low speed flows to the compressible flow on the nozzle involves a high degree of speculation.

4.1.2.3 Roughness

The mean-flow results can also be used to investigate the plausibility of transition controlled by surface roughness. Transition on the forward region of blunt bodies, to which the nozzle throat has many similarities, correlates with a roughness Reynolds number Re_k, based on a roughness height, k, and the local conditions from a smooth wall solution at $y=k$.

$$Re_k = \frac{\rho_k U_k k}{\mu_k} \qquad \textbf{5-12}$$

Many of the lower transition Reynolds numbers observed in the Langley quiet tunnels have been identified with roughness particularly in the throat region where the nozzle boundary layer is thinnest. Beckwith et al. (1988) suggest $Re_k<12$ is required for a boundary layer transition process on the nozzle that is independent of the surface roughness. Roughness heights for these nozzles were measured with scanning microvideo equipment to find a maximum peak-to-valley defect over a sample area. The largest roughness elements were found to be between 1μm and 5μm depending on the condition of the nozzle, machining practices, and polishing technique. These maximum defects were typically 15-20 times the rms roughness values.

Surface roughness of the MSU-SWT nozzle was characterized with a stylus-type digital surface roughness tester (Mitutoyo Surftest 211) with resolution to 0.01 μm peak-to-peak. The maximum peak-to-valley height over a set of samples, each 4mm in length, was 1.2 μm, and the typical maximum near 0.8 μm. The arithmetic average of the absolute roughness profile about the mean was 0.05 μm to 0.07 μm. Measurements were

recorded at several locations on the contoured nozzle block, including the throat. The tester had been factory calibrated, but was verified again after the nozzle roughness measurements to within 2% against a precision roughness specimen supplied by the manufacturer.

Figure 4-10 shows the local Re_k over the nozzle surface with and without surface heating. A reduction in Re_k comes by increasing the kinematic viscosity ν_k, which is proportional to $T_w^{1.7}$ in the vicinity of the roughness. However, all Re_k are less than 0.2, which is far below the current design criterion for quiet nozzles. Therefore, based on the Re_k<12 criterion, the present results would indicate that (1) roughness does not appear to influence the transition process on the MSU-SWT nozzle, and (2) roughness arguments do not explain the observed transition delay with heating.

4.2 Boundary Layer Stability on the Nozzle Floor

The amplification and growth of unstable Görtler vortices and first-mode TS waves were calculated for each case of the test matrix (Table 2-1) using LST. For each type of instability, the e^{MALIK} code was executed at various streamwise locations along the nozzle length to first identify approximate locations of neutral stability. Then, beginning upstream of the neutral point, the instability was followed downstream at increments of Δx=0.3 cm, to provide stability characteristics as a function of streamwise distance. The procedure was repeated for different choices of the disturbance frequency f, and spanwise wavenumber, β.

4.2.1 Görtler Instability

4.2.1.1 Mean-Flow (Görtler Number)

Numerous LST predictions for supersonic nozzles indicate that the Görtler instability is usually the dominant transition mechanism on supersonic nozzles. Early oil-flow experiments in two Langley Mach 5 (Beckwith and Holley 1981) axi-symmetric nozzles and a Mach 3.5 two-dimensional nozzle in 1985 showed a shear pattern induced by Görtler vortices that began shortly downstream of the inflection point. The oil collected at regions of low shear in between the vortex pairs and extended in parallel rows to the nozzle exit. Measured vortex spacing was in agreement with the most amplified wavelength from LST, as in subsonic flows (Floryan 1991).

At high enough Reynolds numbers, the streak pattern was obliterated near the nozzle exit, indicating transition to turbulence. It was thus assumed that transition was caused by breakdown of the Görtler instability. Transition over the concave portion of supersonic nozzles has been observed with a Görtler number G_θ ranging from 5 to 10 (Beckwith and Holley 1981, Chen et al. 1985, Beckwith and Miller 1990). The amplitude growth of the vortices has also been correlated to transition with N-factors ranging from 5 to 12 in a variety of conditions and nozzles.

As with most boundary layer stability and transition parameters, the growth and wavelength selection of Görtler vortices are strongly affected by the disturbance environment to which the boundary layer is exposed. This environment includes both surface roughness and free-stream turbulence levels upstream and downstream of the

inception of centrifugal instability. Thus, variation between facilities could be expected regardless of geometry similarities.

Figure 4-11 shows G_θ over the contoured surface of the MSU-SWT nozzle as a function of streamwise distance x/L with and without heating for the high and low Re'_∞ cases. The maximum Görtler number is near 7 then decays as the curvature goes to zero at the nozzle exit. Thus, in the case without heating, the values of G_θ suggest that vortex development may be sufficient to influence or cause transition near the nozzle exit.

A strong effect of the surface heating is seen in both the low and high Reynolds number cases. In the low Reynolds number case, G_θ is reduced by 25% with surface heating, while the higher heating levels of the high Reynolds number case cause a 42% reduction in the peak G_θ. As mentioned in the description of the mean-flow, the surface heating causes a reduction in the momentum thickness, which is the sole contributor to the reduction of G_θ displayed in Figure 4-11 (all other parameters are based on the edge conditions and geometry which do not change with surface heating).

4.2.1.2 Linearized Growth: N-factor

The Görtler number is only a mean-flow variable and cannot include the amplification history of the instability. Therefore, integrated growth from stability predictions provides a better comparison between facilities (Chen et al. 1991).

Chen et al. (1985) surveyed transition on supersonic nozzles in 4 quiet tunnels from Mach 3 to 5 with a range of $9.8\times10^6/\text{m}<Re'_\infty<59\times10^6/\text{m}$. Within this data set, and for "ideal conditions", transition onset correlated well with N-factors ranging from 9 to 11,

with the instability growth modeled by LST. Much lower N-factors were observed, but were attributed to roughness effects (Re_k>12), residual vorticity (due to the absence of boundary layer removal slots in the subsonic approach), and a wavy wall. An N-factor at transition onset (N_T) of 9 was also confirmed in a later nozzle design at Mach 3.5 (Chen et al., 1990). Recent measurements with a new Mach 6 hypersonic quiet nozzle (Chen et al., 1991) have indicated transition at N_T=7.5, as computed by LST for the Görtler problem. As a conservative measure, the latest quiet nozzle design has used N_T=7.5 (Schneider 1998a).

Figure 4-12 shows the spectra of amplification rates at the streamwise distance of peak amplification (x/L=0.5). The "spectra" of wavelengths is very narrow with the most amplified wavelengths on the order of the boundary layer thickness. Arrows indicate the respective wavelength corresponding to $\lambda_z=2\delta$ for the heated (solid arrow) and unheated (dash-arrow) surface conditions. When surface heating is applied, only a small reduction in the local amplification rate is observed. Though the changes are small, Figure 4-12 also shows that the peak amplification with and without surface heating does not scale with the boundary layer thickness.

Maximum N-factors were computed for each case of the test matrix (Table 2-1) by choosing the most unstable wavelength, holding β fixed, and integrating the growth rate in the streamwise direction with equation 3-11. The results are plotted in Figure 4-13. The ratio of the vortex wavelengths λ_z to the boundary layer thickness δ_N at the neutral point are also included for each curve. The selection of the most amplified wavelength

agrees with the typical value $\lambda_z/\delta_N = 3$ reported by Chen et al. (1985) for other supersonic nozzles.

Predicted maximum N-factors for both the low and high pressure cases show that the Görtler instability is not sufficient to cause transition in itself, based on the N_T=7.5 criterion. Furthermore, when heating is applied, there is less than 5% difference in the maximum N-factor at the nozzle trailing edge. Spall and Malik (1989) also found a small effect of heating/cooling on the Görtler instability at Mach 3.5. They computed a 15% decrease in the N-factor when the wall temperature was increased by a factor of 2 over the adiabatic wall temperature. Wall cooling showed a small, but destabilizing effect. The linear stability predictions for Schneider's Mach 6 nozzle also support the minimal effect of surface heating on the growth of Görtler vortices (Schneider 1998a).

The eigenfunctions of the disturbance (an example shown in Figure 4-14) show a general movement of disturbance energy toward the edge of the boundary layer with heating. As reported by Day et al. (1990), the disturbance energy starts near the edge of the boundary layer and moves toward the wall as the strength of the vortices increase. The eigenfunctions in Figure 4-14 can only provide a qualitative description of the disturbance structure at best since boundary layer growth terms are neglected in the e^{MALIK} solution.

4.2.1.3 Unsteady Görtler Instability

Since the e^{MALIK} code includes curvature terms with a general harmonic disturbance of the form in equation 3-6, unsteady centrifugal instabilities can also be computed. Figure 4-15 shows the amplification rates as a function of disturbance frequency F, at the

location where the vortices are the least stable (x/L=0.5). The steady vortices are less stable than their unsteady counterpart, in agreement with (Garg and Diprima 1984, Hall 1982).

The inset of Figure 4-15 also shows how the wave-angle ϕ approaches 90° as the frequency goes to zero. In the limit as $F \rightarrow 0$, the wavenumber $\alpha_r \rightarrow 0$ also, such that the phase speed of the wave in the streamwise direction $(c_r)_x = \omega/\alpha_r$ remains less than unity. The phase speed in the spanwise direction approaches zero since $(c_r)_z = \omega/\beta_r$. The physical picture that emerges is waves of vorticity that are traveling almost perpendicular to the free-stream velocity, so that to the fixed observer, streaks of streamwise vorticity appear to be slowly moving across the span of the boundary layer. Borrowing from the literature on steady and unsteady crossflow vortices, we may call these "traveling" Görtler modes.

Examination of the eigenfunctions with $F \rightarrow 0$ further shows that the unsteady disturbance of equation 3-6 approaches the simplified form of the disturbance with a single spanwise perturbation of equation 3-9. Conversely, as F increases from zero, both symmetric and antisymmetric components of the harmonic function become similar in magnitude. The result is that the clean cellular shape of the "vortices" (Figure 3-4) is no longer present. In fact, for values of $\beta \sim O(10^{-1})$, the results of the e$^{\text{MALIK}}$ code are difficult to distinguish from oblique TS modes ($\phi \sim 65°–75°$, $(c_r)_x \sim 0.6–0.7$). The only distinguishing feature to classify this computed instability is that the latter is gone when curvature is eliminated. Therefore, the instability is related to centrifugal effects in the disturbance equations, which is the defining trait of the Görtler problem.

Figure 4-15 also shows that when heat is applied to the nozzle surface, the unsteady disturbances increase. This is interpreted as the general destabilizing effect of viscosity to unsteady disturbances. More will be said regarding this point in Chapter 6. The relative characteristics between the steady and unsteady Görtler instability in Figure 4-15 are representative of all choices of β and x through the unstable range. While heat shows a destabilizing effect as frequency increases, the principal feature of Figure 4-15 concerning transition prediction is still that the steady vortices are more stable than unsteady "vortices", and would therefore be expected to dominate in a low-disturbance environment.

4.2.2 First-mode Tollmien-Schlichting Instability

The strong pressure gradient in a supersonic nozzle usually suppresses TS waves, except in the case of longer, slow-expansion nozzles. Yet, there is no formal reason to expect a priori that TS modes cannot exist in any region of the nozzle. And, though there is no direct experimental evidence, predictions of the interaction between TS and Görtler modes indicate that the Görtler vortices could have a destabilizing effect on the growth of oblique TS modes under certain enabling conditions (see Floryan 1991 for a review). As such, even weak TS growth may be significant.

After identifying the neutral points, the maximum instability growth can be examined with streamwise distance using an envelope method (equation 3-12).

Calculations showed that amplification does not occur until near the nozzle exit where the favorable pressure gradient decreases. The neutral stability point for the most unstable frequency is at x/L=0.90 for the unheated cases and x/L=0.93 for both heated

cases. Figure 4-16 shows the spectra of amplification rates at the nozzle exit. The peak frequency occurs at low values relative to those typically found in a Mach 3 flow. At Re'_∞=5.2×10^6/m the peak occurs at F×10^4=0.1 at the nozzle exit, and decreases as the boundary layer grows downstream. In a Mach 3 flat-plate stability experiment, Demetriades found the most amplified frequencies to be substantially higher between F×10^4=0.5 and F×10^4=1.5 (Demetriades 1989). The principal difference in the nozzle boundary layer is that the strong pressure gradient in the nozzle has allowed the boundary layer to become thicker without amplifying the TS instabilities. The thicker boundary layer leads to lower frequencies. Wave-angles in the nozzle typically varied between 60° and 75°. The disturbance wavelengths were on the order of 10-15δ.

Both the wave-angle and disturbance wavelengths decrease with surface heating. Figure 4-17 shows the eigenfunctions for the TS instability in adiabatic and heated conditions at the most amplified wave-angle ϕ=68° at the nozzle exit. As with the Görtler modes, surface heating pushes the disturbance energy further toward the boundary layer edge. It is interesting that this shift is occurring while the boundary layer thickness decreases with surface heating (recall Figure 4-8).

Maximum N-factors at the nozzle trailing edge of only 0.8 and 0.2-0.3 were found for the unheated and heated cases, respectively.

4.2.2.1 Post-Nozzle Development

Even though the growth of TS waves are negligible for transition in the nozzle, surface heating was found to both move the neutral point downstream, and reduce the

rate of amplification. To further explore this heating effect, the computational domain in the boundary layer solver was extended past the nozzle exit with a uniformly flat, adiabatic surface, and zero pressure gradient. The adiabatic condition was justified in all cases in view of the heat-flux plots which asymptote to zero at the nozzle trailing edge (Figure 4-5).

Beyond the nozzle exit, amplification of the first-mode disturbances increases for all frequencies. Figure 4-18 shows the amplification rates at x/L of 1.0, 1:5, and 2.0 for the heated and unheated cases. It is immediately clear that the surface heating reduces amplification rates at all streamwise positions, particularly at the higher frequencies. The higher heating levels of $(T_w/T_o)_{x=0}$=1.22 produce a somewhat stronger damping effect than that observed with $(T_w/T_o)_{x=0}$=1.13. The peak frequency does not change with heating, since the boundary layer thickness is nearly the same with and without heat. Apparently, the surface temperature distribution in the nozzle has a strong, and lasting effect on the boundary layer. Even the small amount of heating from the ambient conditions has a visible influence on the stability downstream of the nozzle (Figure 4-19). For compressible flows, a sufficient condition for the existence of an unstable wave is that,

$$D(\rho DU) = 0 \quad @\ \eta_s > \eta_o \qquad \textbf{4-2}$$

in the boundary layer where η_s is located at the point of inflection, η_o is the point at which U/U_e=1-1/($M_e\cos\phi$), and $D(\ )$=d($\ $)/d$\eta$. Equation 4-2 is also both a necessary and sufficient condition for a neutral wave to exist. Equation 4-2 is the "general inflection point" criterion, and reduces to the Rayleigh criterion (Schlichting 1979) for

incompressible flows when ρ is constant. The sufficiency of equation 4-2 is only mathematically rigorous for inviscid instability (i.e. in the limit of infinite Reynolds number). However, it is often taken as a qualitative measure of stability in viscous layers as well; as η_s moves further out into the layer, a more unstable boundary layer is observed. This behavior is illustrated on a neutral stability diagram by a larger neutral curve that opens up at high Reynolds numbers (typical of inviscid instabilities), and moves forward to lower Reynolds numbers. The magnitude of $D(\rho DU)$ near the critical layer (where the mean velocity equals the phase speed of the instability wave) is also related to the amount of energy production driving an inviscid instability wave.

Figure 4-20 shows profiles of $D(\rho DU)$ with heating applied in the nozzle, and an adiabatic condition at $x/L>1$. In the nozzle, no general inflection point is observed owing to the strong pressure gradient. Two points of general inflection first appear near the nozzle exit (close to the neutral points of the first-mode TS instability). Beyond the nozzle exit the adiabatic wall condition and zero pressure gradient lead to $D(\rho DU)=0$ at the wall, while a single inflection point gradually moves out into the layer with increasing streamwise distance. When heat is applied, the magnitude of $D(\rho DU)$ at the wall decreases by a factor of 2 in the nozzle. But, for $x/L>1$, the location of the inflection point is unchanged, and the magnitude of $D(\rho DU)$ for $\eta<\eta_s$ is actually less than the adiabatic case near the wall.

Before the present work, the stabilizing effect of upstream heating has been rationalized by explaining the improved stability as a natural cooling effect. As in the case of Masad and Nayfeh (1992), when a heat transfer "strip" was placed upstream of

the neutral stability point, the boundary layer would pass over a relatively cooler surface, shifting the neutral curve downstream, and reducing the amplification rates at all subsequent streamwise locations. The relation of natural cooling to boundary layer stability is summarized with stability modifier theory (equation 1-2) that relates the direction and magnitude of heat-flux ($\propto \partial T/\partial y|_w$) to the velocity second derivative at the wall (described in Chapter 1). The latter controls the location of η_s in equation 4-2 to provide a link to the qualitative description of stability in a boundary layer.

Since $D(\rho DU)$ is identically zero past the nozzle exit, stability modifier theory and the natural cooling do not predict the stabilizing effect of upstream heating observed in Figures 4-18 and 4-19. This failure may have been expected since stability modifier theory can only describe the effect of heat flux in non-similar boundary layers as a local condition, and cannot include any effects of upstream heating. In that respect, stability modifier theory is only capable of describing gross effects of the wall conditions on boundary layer stability. The important point here is that natural cooling at or beyond the neutral point need not be present to produce a more stable boundary layer. Even the proper heating (q_w into the boundary layer) distribution can produce changes in the boundary layer which enforce a more stable condition for all streamwise distances beyond the neutral point.

Mack (1969) gives a more complete description of the relation between the mean-flow structure and stability variables. The complete discussion is intricate and uses results of stability theory that are far beyond the scope of this text. Here, it will suffice to say that the stability of oblique first-mode waves is more rigorously related to the value

of U_s relative to U_o. As $U_s \rightarrow U_o$, the boundary layer becomes more stable. The location of the inflection point does not change with heating, so U_s is the nearly the same with and without surface heating. However, the surface heating reduces the wave-angle of the most amplified waves, which increases the value of U_o (equation 4-2), bringing it closer to U_s. At $Re'_\infty=6.2\times10^6$/m, $x/L=1.5$, the difference between U_s and U_o is reduced by 25%, and the peak amplification rate decreases by 20%. Thus, by Mack's account of heating and cooling effects on the first-mode instability, the stabilization at a given streamwise position x comes by keeping the inflection point fixed, and decreasing the wave-angle of the most amplified wave.

4.3 Numerical Accuracy of the Solutions

The computation of boundary layer stability involves a three-step process, with each part having its own source of error that can propagate and/or amplify through each step. This is particularly true of the boundary layer and stability computations. Therefore, the numerical accuracy of the solutions described above is evaluated emphasizing those parameters relevant to boundary layer stability.

4.3.1 Navier-Stokes Solution

Throughout the Navier-Stokes solution, the boundary layer development was used as the primary measure of accuracy in the final solution. The inviscid core converges rapidly, and in turn, drives the development of the boundary layer through viscous shearing. Furthermore, the boundary layer has, by definition, slow-moving fluid which physically requires more time to convect through the solution domain. Therefore, the

boundary layer as a whole is considered the most sensitive region for measuring solution convergence.

4.3.1.1 Convergence

Iteration convergence to steady-state was examined in all solutions with the residual history measured by the RHS l_2-norm ($=\sum_{j,k}(RHS_{j,k})^2$). Recall from equation 3-2, that RHS is essentially the unsteady term of the Navier-Stokes equations and will therefore go to zero as the marching solution approaches steady-state ($L(Q)=0$). Other residual information such as the location and magnitude of the RHS l_∞-norm was available to identify the locations of slow convergence.

Residual histories for solutions on the coarse grid with different options in OVERFLOW are shown in Figure 4-21. Using FMG provides a considerable reduction in CPU time to eliminate the initial transients, and for convergence to machine zero. At low values of the residual, matrix dissipation causes slow convergence, with 5 times as much CPU time to reach machine-zero (10^{-14}) than the case with scalar dissipation.

The relation between the l_2-norm and the boundary layer convergence is illustrated in Figure 4-22 using the same conditions as Figure 4-21 with FMG and matrix dissipation. After the residual has reached $O(10^{-8})$, the displacement thickness of the boundary layer δ^*, and the shape factor H_{12}, are within 4 significant digits of the final solution at machine-zero. Therefore, all subsequent solutions were marched until the residual was reduced by at least 6 orders of magnitude. For all grids, this condition corresponded to about 3000 iterations, and the final residual less than $O(10^{-9})$. The

solution presented by King and Demetriades (1993), found with a different Navier-Stokes solver (ARC2D), at identical stagnation conditions is within 1% of the present solution.

Inspection of the l_∞-norm showed that with matrix dissipation the residual maximum occurred near the center of the contraction with slowly decreasing low frequency oscillations – possibly caused by the inflow boundary condition, or the application of the compressible flow solver to a near incompressible flow (M=0.07). No attempt was made to improve the convergence further since acceptable accuracy was achieved in the boundary layer long before reaching machine-zero.

4.3.1.2 Grid Dependence

The grid dependence of the Navier-Stokes solution is illustrated in Figure 4-23 with the boundary layer displacement thickness, δ^* and shape factor H_{12} computed on the coarse, medium, and fine grids of Table 3-1. Clearly, the boundary layer is not adequately resolved with the coarse grid. While the displacement thickness computed on the coarse grid is close to that on the fine grid, the shape factor differs by 10%. The medium and fine grid show shape factors that are within 0.1% of each other, illustrating a converged solution with the medium grid.

Table 4-1 summarizes the convergence parameters for the Navier-Stokes calculation at Re'_∞=5.2×10^6/m. All convergence parameters in the boundary layer indicate that the medium grid provided a converged solution for the viscous and inviscid flow through the nozzle. Therefore, all final results from the Navier-Stokes solution used the medium grid.

Table 4-1 also lists minimum and maximum values of the turbulent similarity variable y^+ at the first point off the wall, where

$$y^+ = y\sqrt{\frac{1}{\nu}\left(\frac{\partial U}{\partial y}\right)_w}$$

Here, y^+ is recast from its usual form (Schlichting 1979) to show the relation between grid spacing and the velocity gradient near the wall. Typically, the first grid point off the wall should be well within the inner layer at a y^+ of about 1 or less (Buning et al. 1997). Consistent with Figure 4-23, the y^+ values at the first grid point indicate that boundary layer is resolved well with the medium and fine grids. At a higher unit Reynolds number case, with P_o=600 mmHg where the boundary layer is thinner, y^+ increases by about 15%.

The relation between the core flow and the boundary layer resolution is illustrated in Figure 4-24 with the edge Mach number and displacement thickness. The small changes in displacement thickness with increasing resolution or Re'_∞ produce less than 1% change in the edge Mach number. Measurements by Brogan (1995) at the boundary layer edge showed a difference of 4% with a similar range in Re'_∞. The larger variations observed in the experiment are most likely the influence of the sidewall boundary layer on the core flow – which is not accounted for in the two-dimensional computations.

4.3.2 Boundary Layer Solutions

Two different grids were used in the boundary layer computations to establish a grid-independent solution. The coarse grid used 60-points in the wall-normal direction,

and the solution was marched at streamwise increments of Δs=0.3 cm. The fine grid used 101-points in η_{BL}, and streamwise increments of Δs=0.15 cm. Both grids employed geometric stretching (k=1.04) in η_{BL}, and an $\eta_{BL,max}$=10, which was near 2δ for all stations. Since the Navier-Stokes solution showed no grid dependence in H_{12} and δ^* with more than 35 points in the boundary layer one would expect more than sufficient resolution for both boundary layer grids. Indeed, the fine and coarse grids gave a maximum difference of 0.5% in the second derivative profiles of U/U_e and T/T_e (Figure 4-25) at x/L=1.0. Thus, both grids were adequate for both solving the boundary layer equations, *and* computing the derivatives for stability computations. In view of the minimal resources required to run the code on the CRAY, the 101-point grid was used for all calculations.

The streamwise marching procedure in the boundary layer computations was started at x/L=-0.3 (M_e=0.137). Starting the calculations at x/L<-0.3 (>500δ_{throat}) produced no effect on the boundary layer development downstream of the nozzle throat. Presumably, the high pressure gradient, and flow stretching through the throat region dominated over any upstream history in the mean-flow boundary layer. The same cannot be said for unsteady activity in the boundary layer.

The solution grid for stability calculations was also varied. The eigenvalues were the same to 3 significant figures with 80 points (the default) or 120 points in the wall-normal direction. All results presented herein use the 80-point grid for the local eigenvalue search.

Interpolation errors incurred by passing the solution from one stage to the next (e.g. pressure from the Navier-Stokes solution to the boundary layer solution) were not observed. The grid requirements for a converged solution imposed a more severe constraint than did those for accurate interpolation.

Grid	$\log\left(\frac{l_{2\,start}}{l_{2\,stop}}\right)$	$l_{2\,stop}$	Grid points in Boundary Layer	min y+/max y+ (@ k=1)
140×41	6.4	1×10^{-9}	> 18	1.2 / 4.8
169×65	7.0	2×10^{-10}	> 35	.083 / .34
201×97	7.2	7×10^{-11}	> 55	.042 / .15

Table 4-1. Convergence parameters in two-dimensional Navier-Stokes computation. Re'_∞=5.2×10^6/m, All solutions stopped at 3500 iterations.

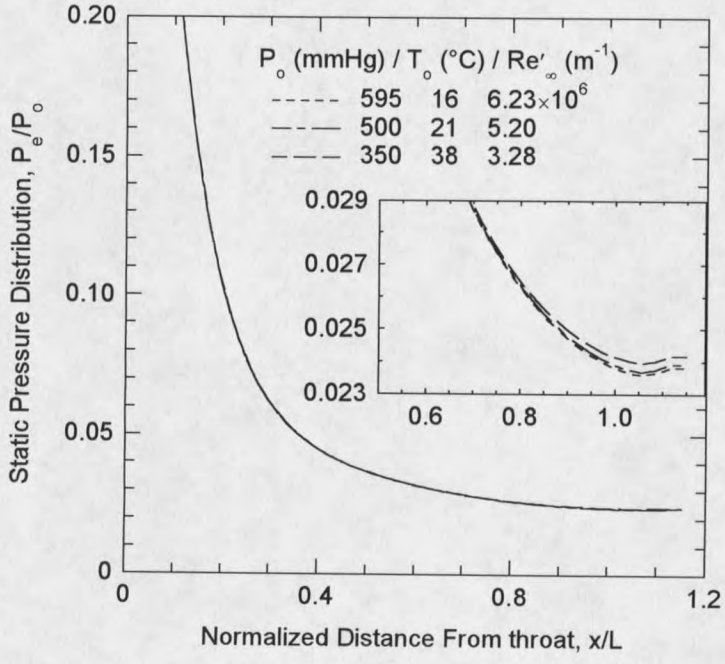

Figure 4-1. Normalized static pressure at boundary layer edge predicted by the Navier-Stokes code.

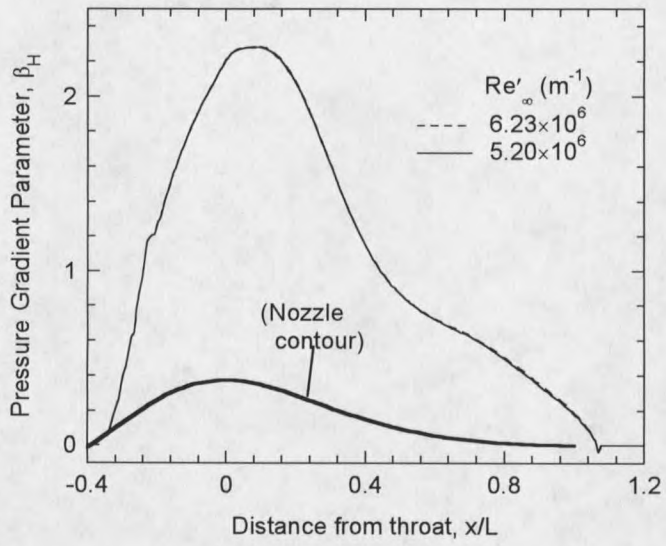

Figure 4-2. Pressure gradient parameter computed in the boundary layer solution.

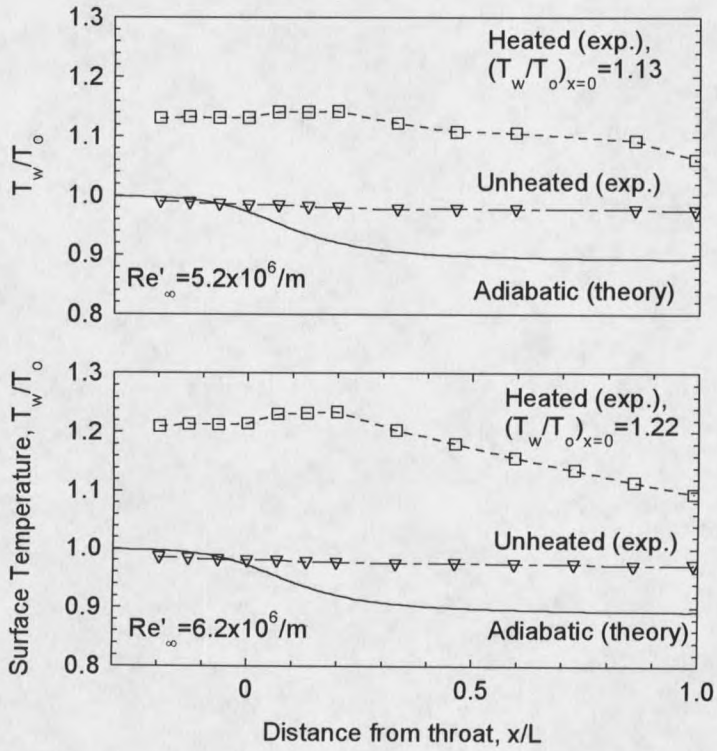

Figure 4-3. Streamwise surface temperature distribution for heated and unheated nozzle condition. Symbols indicate thermocouple measurements.

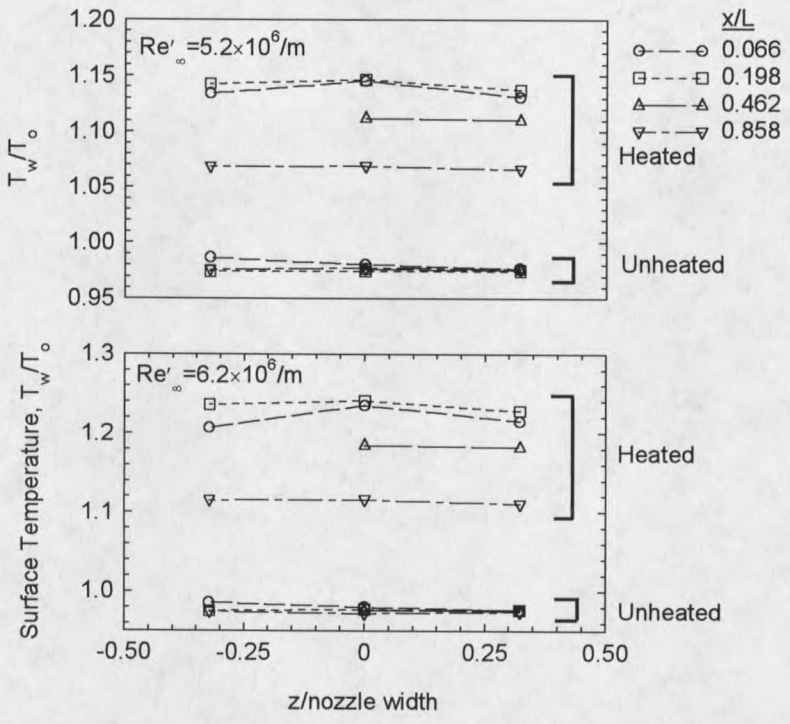

Figure 4-4. Spanwise uniformity of surface temperatures. Symbols indicate thermocouple measurements.

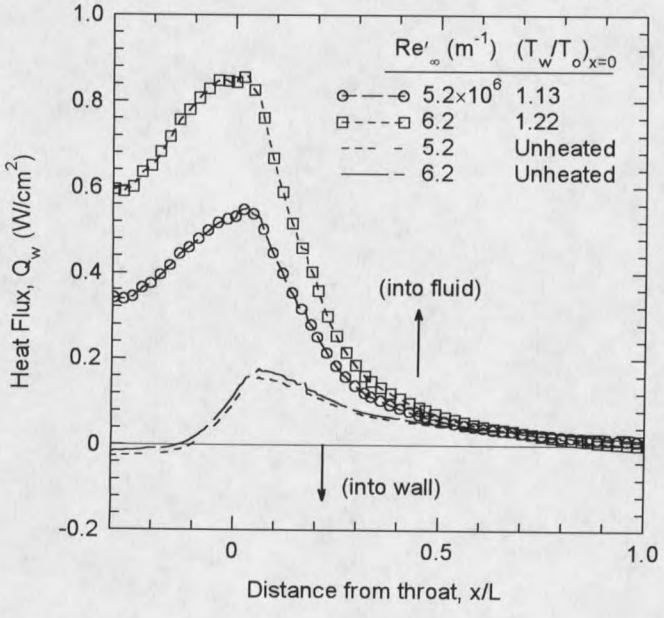

Figure 4-5. Calculated heat flux from 2D boundary layer code using measured temperature distributions.

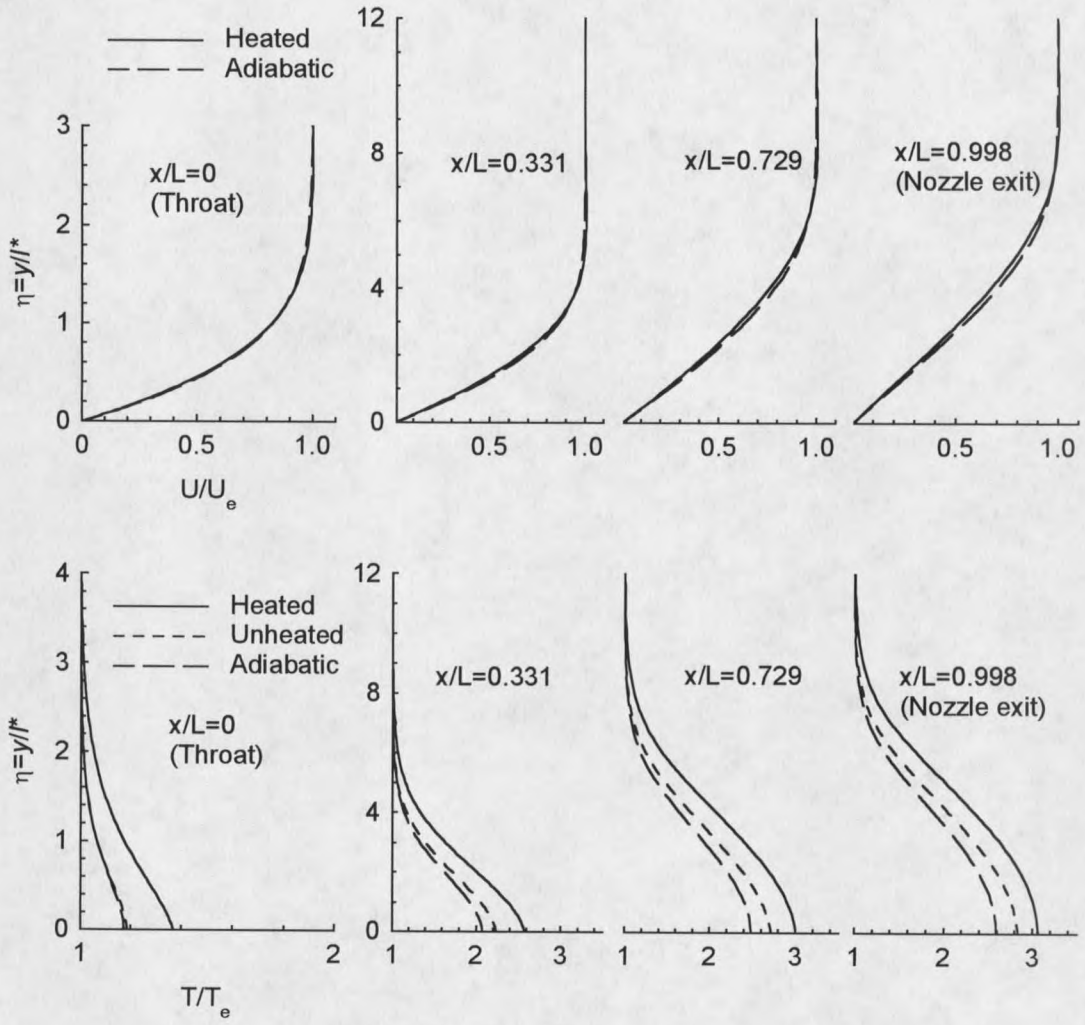

Figure 4-6. Mean-flow profiles for normalized velocity U/U_e and static temperature T/T_e. Re'_∞=5.2×10^6/m, heated condition is $(T_w/T_o)_{x=0}$=1.13

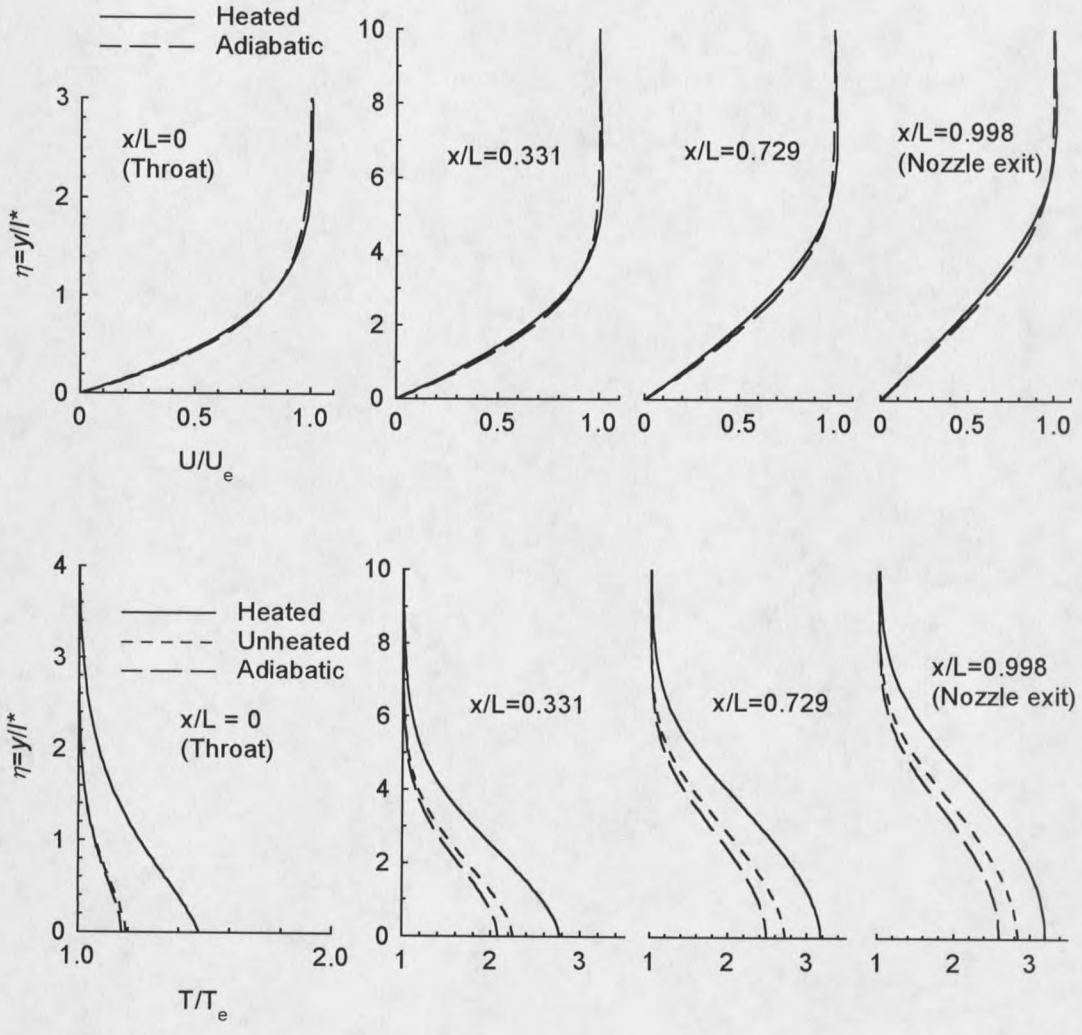

Figure 4-7. Mean-flow profiles for normalized velocity U/U_e and static temperature T/T_e. Re'_∞=6.2×10^6/m, heated condition is $(T_w/T_o)_{x=0}$=1.22.

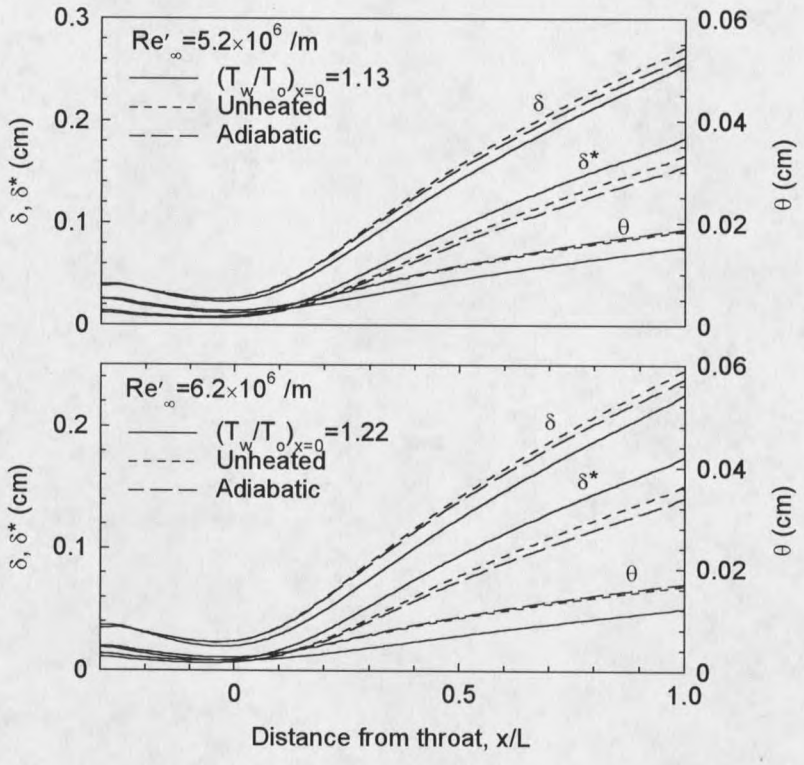

Figure 4-8. Boundary layer thickness and integral properties with and without surface heating.

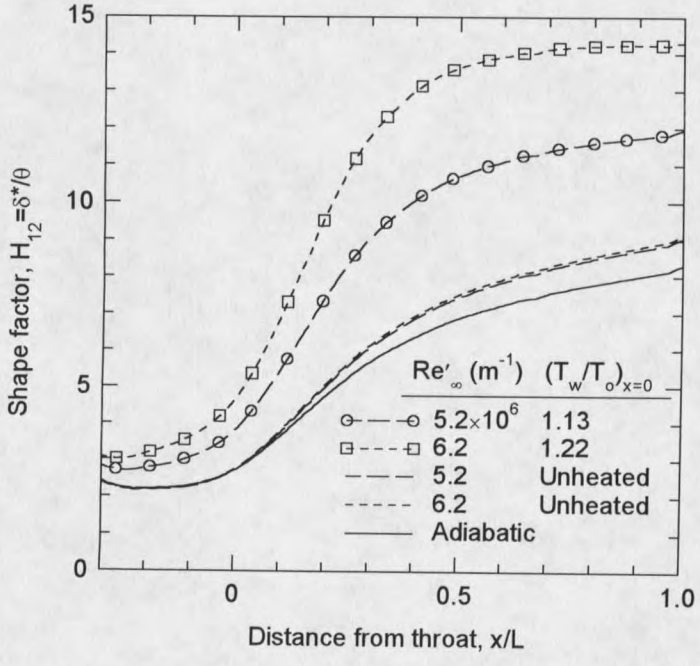

Figure 4-9. Shape factor H_{12} progression with and without surface heating.

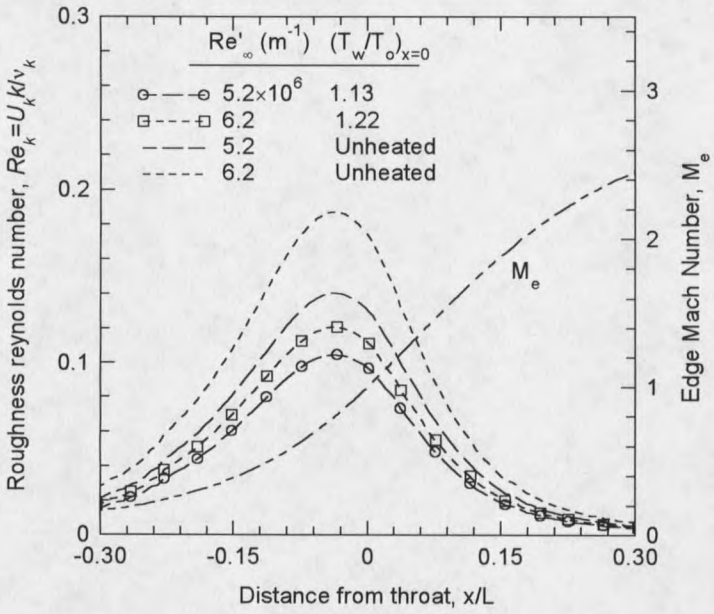

Figure 4-10. Local roughness Reynolds number through the throat region using the maximum peak to valley differential (PVD) for roughness height. k=1.2μm.

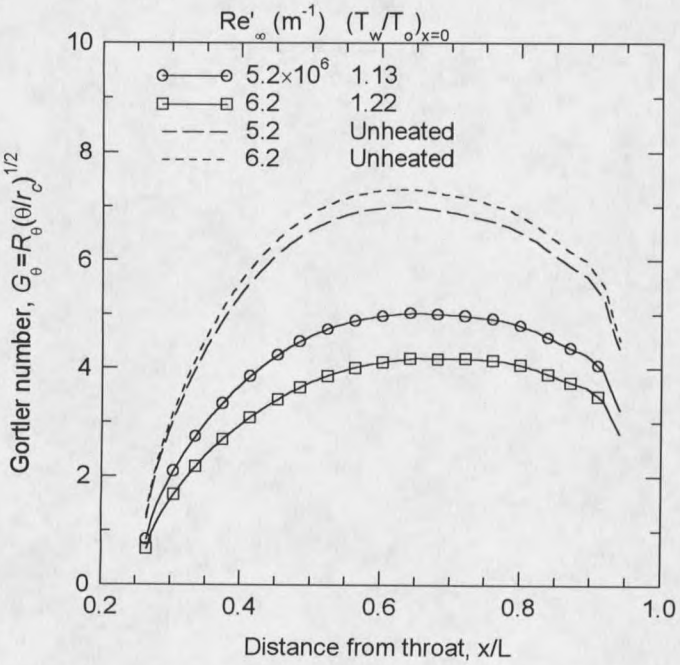

Figure 4-11. Variation in Görtler number based on momentum thickness with and without surface heating.

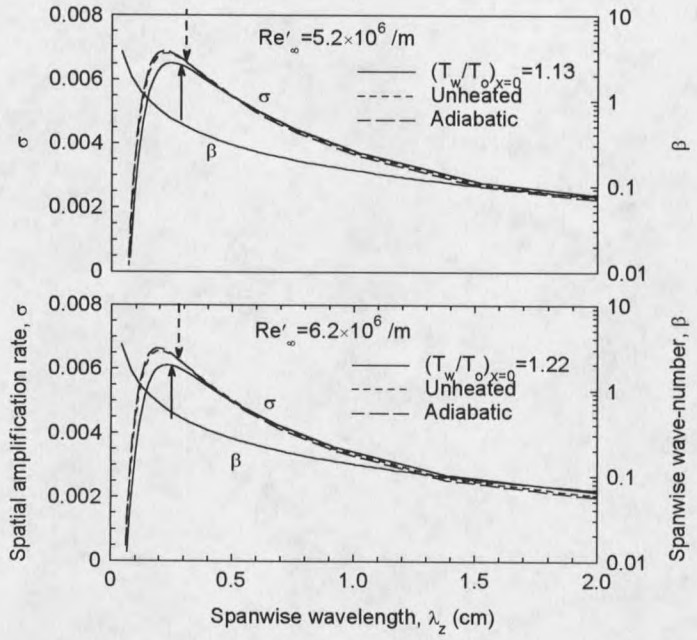

Figure 4-12. Amplification rate σ of the steady Görtler instability as a function of spanwise wavelength, λ_z. Arrows indicate the point at which $\lambda_z=2\delta$ with heat (solid) and without heat (dash). Streamwise position near most unstable point (x/L=0.500).

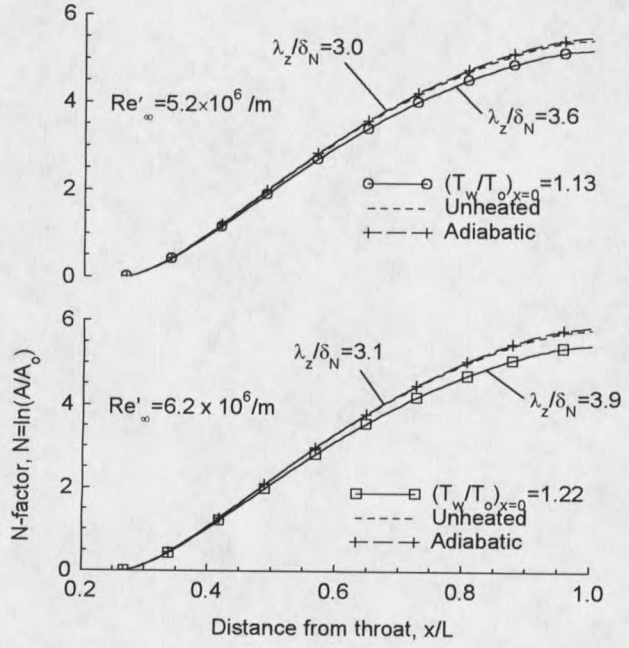

Figure 4-13. Computed *N*-factors of the steady Görtler instability for the spanwise wavelength of largest growth at nozzle exit.

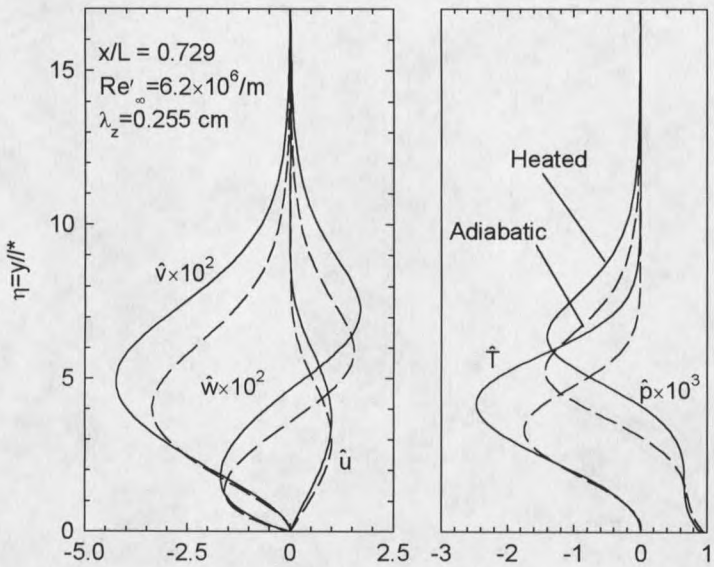

Figure 4-14. Eigenfunctions of the Görtler instability. Re'_∞=6.2×10^6/m, x/L=0.729, λ_z=0.255 cm. All eigenfunctions are normalized by $\hat{u}_{max}$.

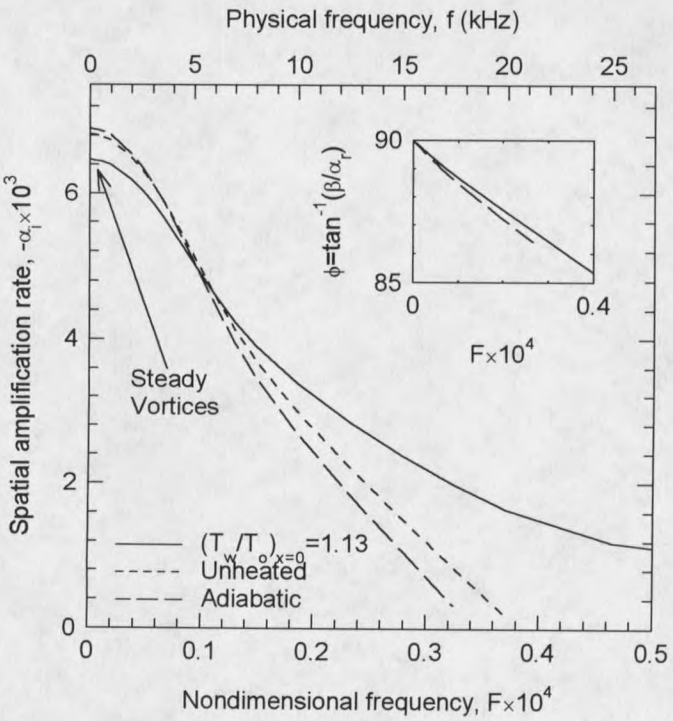

Figure 4-15. Amplification rate $-\alpha_i$, of the unsteady Görtler instability, as a function of dimensionless frequency, F. Near most unstable wavelength, β=0.7 (see Figure 4-12).

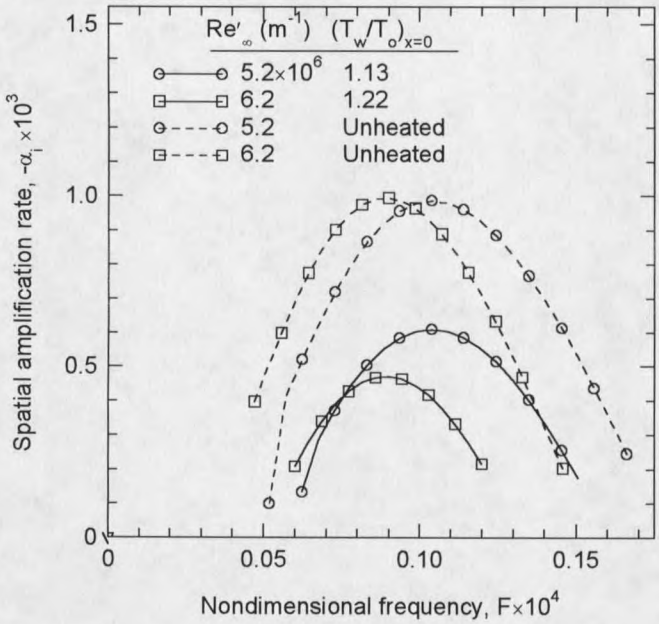

Figure 4-16. Spectra of "maximum" amplification rates $-\alpha_i$ for first-mode instability with and without surface heating. Nozzle exit (x/L=1), wave-angle varied to maximize $-\alpha_i$ for each frequency.

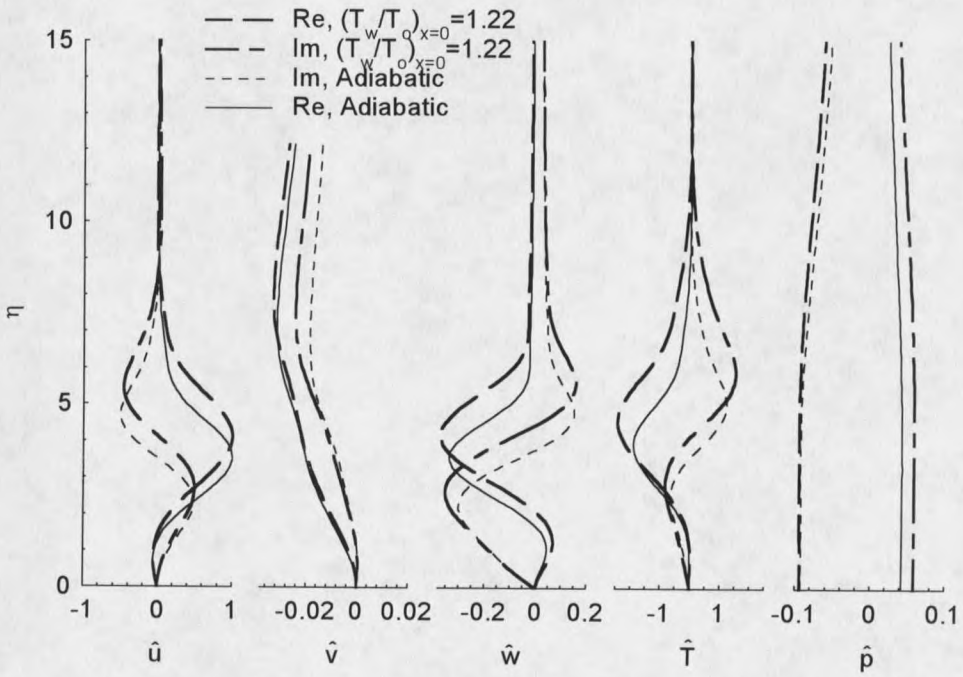

Figure 4-17. Eigenfunctions of the first-mode TS instability with and without surface heating. Re'_∞=6.2×10^6/m, x/L=1.0, f=5 kHz, ϕ=68°. All eigenfunctions are normalized by $|\hat{u}|_{max}$

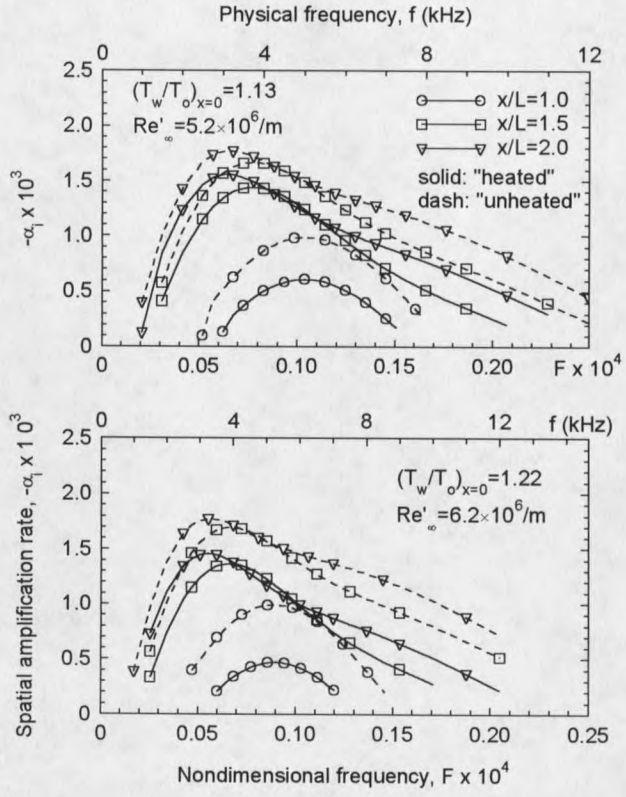

Figure 4-18. Effect of heating on amplification rate $-\alpha_i$ beyond nozzle exit. Adiabatic wall specified for $x/L>1$, wave-angle varied to maximize $-\alpha_i$ for each frequency.

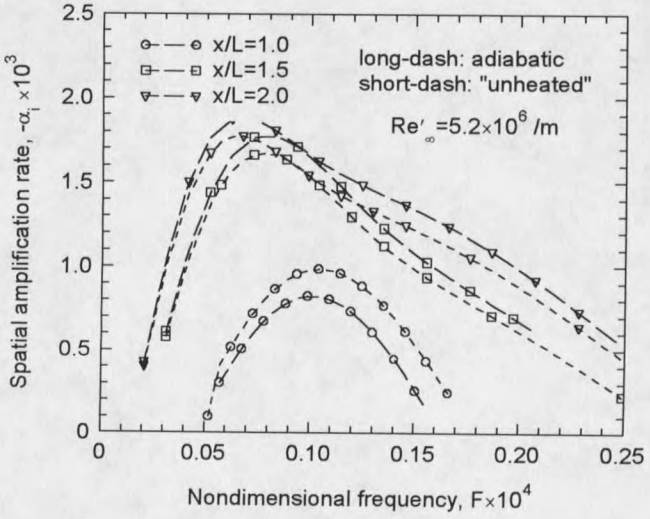

Figure 4-19. Comparison of adiabatic and unheated conditions on amplification rate $-\alpha_i$ beyond nozzle exit. Adiabatic wall specified for $x/L>1$, wave-angle varied to maximize $-\alpha_i$ for each frequency.

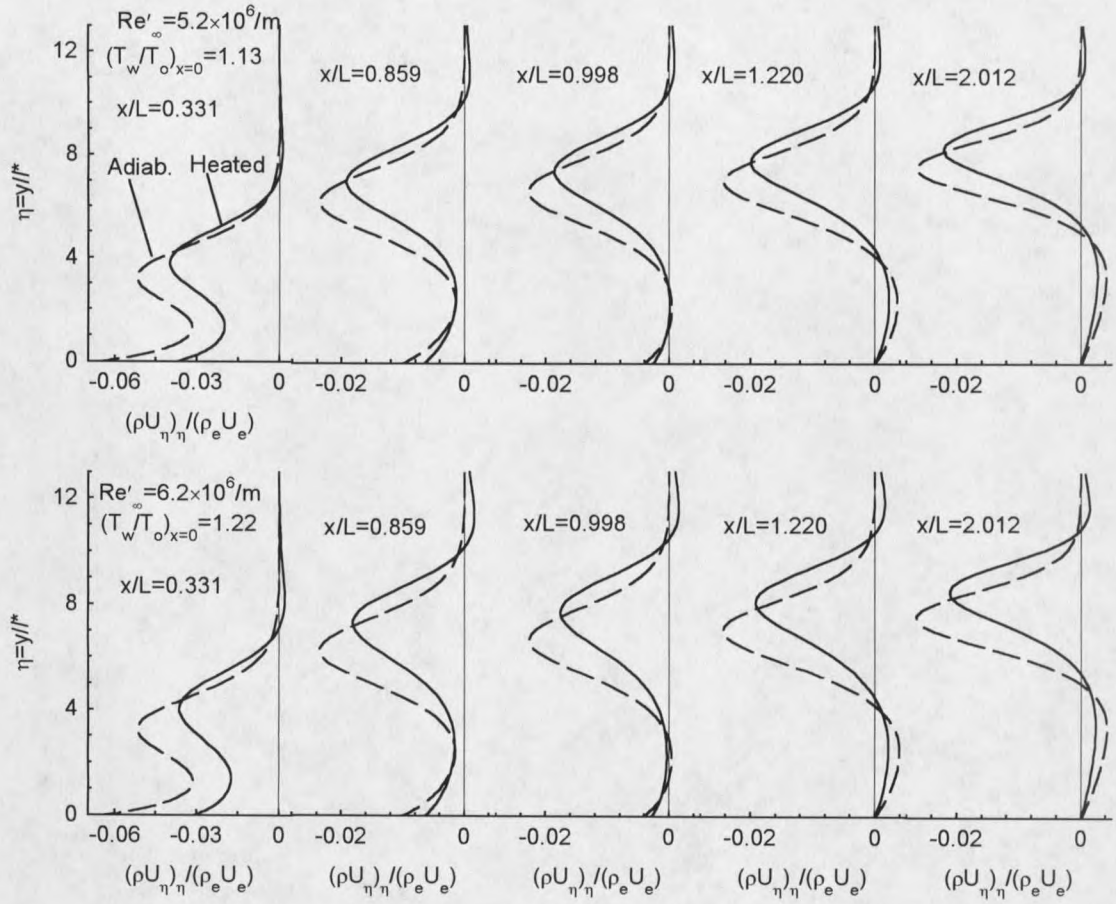

Figure 4-20. Progression of D(ρDU) profiles with and without surface heating in the nozzle. Adiabatic wall specified for $x/L>1$. Subscript $(\,)_\eta$ denotes derivative with respect to normal coordinate η. Subscript $(\,)_e$ denotes edge quantity.

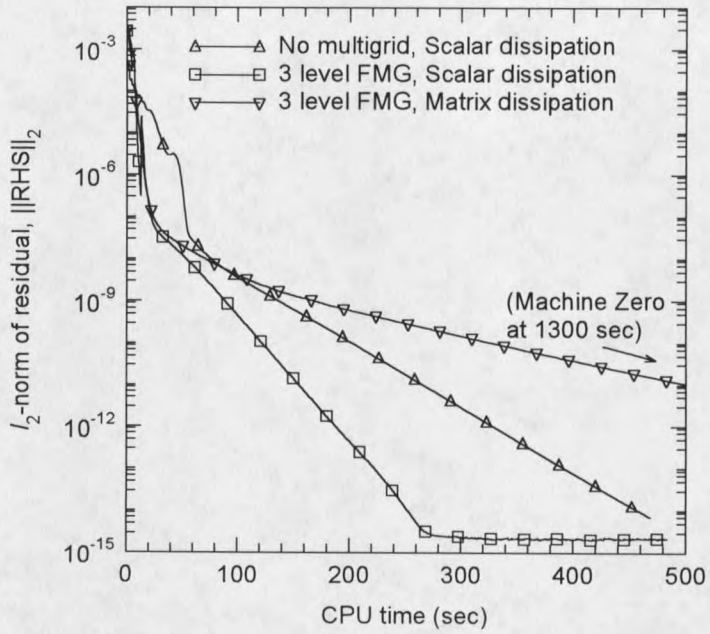

Figure 4-21. Residual history for 2D Navier-Stokes computation, P_o=350 mmHg, T_o=38°C, Re'_∞=3.28×10^6/m, 140×41 grid, Δt=1, CFL$_{min}$ = 5.

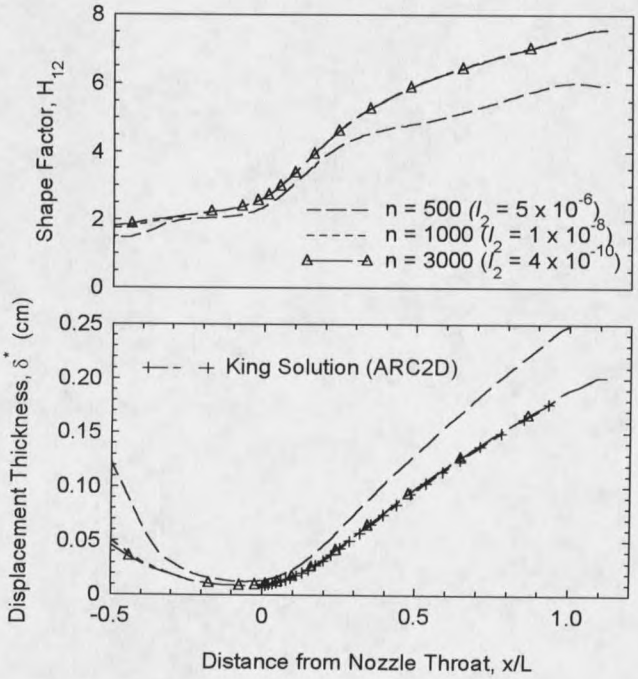

Figure 4-22. Iteration convergence of floor boundary layer in 2D Navier-Stokes computation. Conditions of Figure 4-21, matrix dissipation, 3 levels FMG.

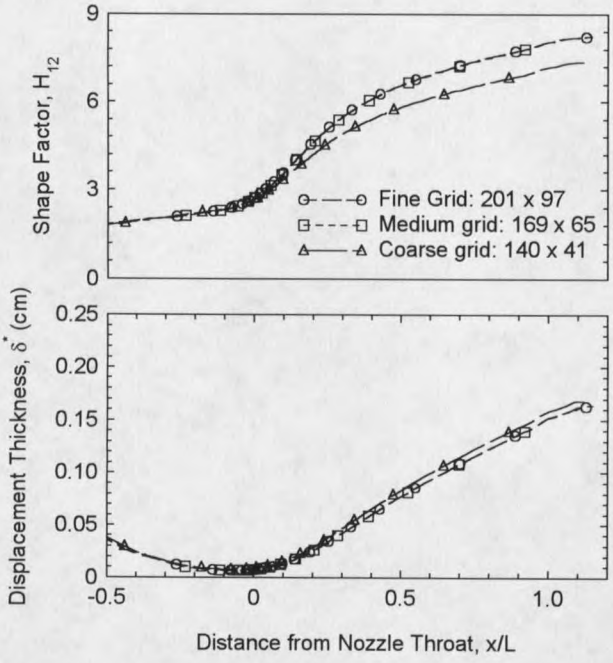

Figure 4-23. Grid dependence of boundary layer on contoured surface: 2D Navier-Stokes computation. P_o=500 mmHg, T_o=21°C, Re'_∞=5.2×10^6/m.

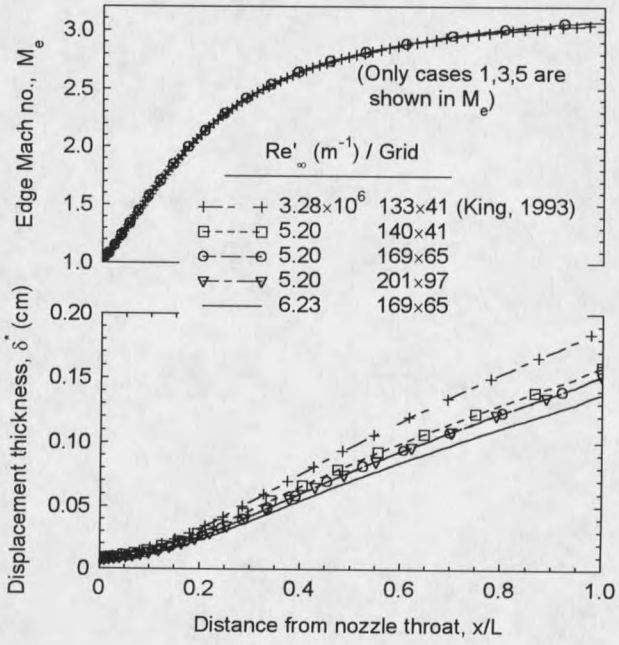

Figure 4-24. Boundary layer conditions from Navier-Stokes solution (top) Edge Mach number, (bottom) displacement thickness.

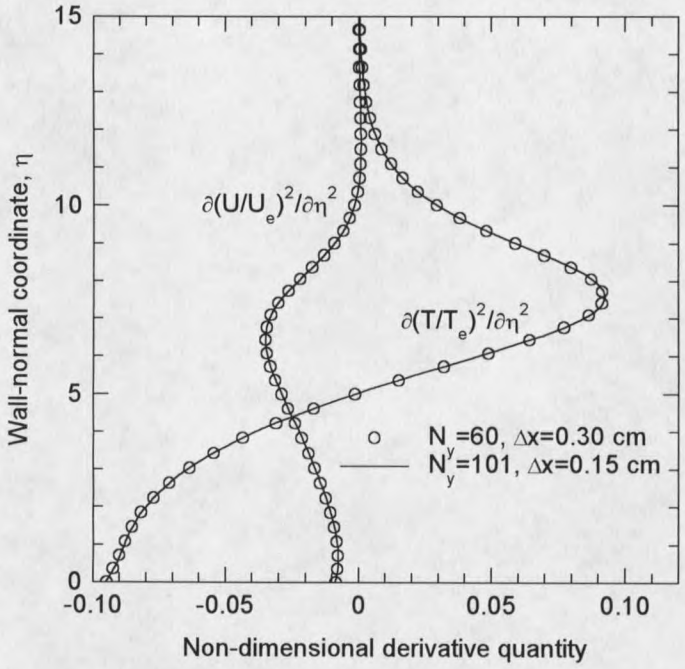

Figure 4-25. Convergence of boundary layer solution for derivative computations. Re'_{∞}**=5.2×10^6/m,** $(T_w/T_o)_{x=0}$**=1.13,** x/L**=1.0**

CHAPTER 5

EXPERIMENTAL MEASUREMENTS

Unsteady fluctuations were experimentally observed in the boundary layer growing on the lower nozzle block for the same conditions as the theoretical predictions of Chapter 4. As discussed briefly in Chapter 2 (Approach), previous experience in the MSU-SWT has shown that two fundamentally different states of the unheated nozzle boundary layer naturally occur at P_o=500 mmHg (Re'_∞=5.2×10^6/m) and P_o=595 mmHg (Re'_∞=6.2×10^6/m). Recall the transition map illustrated in Figure 2-3. At P_o=500 mmHg, low frequency oscillations are present over the majority of the nozzle that break down to turbulence near the nozzle exit. At P_o=595 mmHg, the boundary layer has densely intermittent turbulence for the entire nozzle length. The goal of the present experiment was to observe what effect heating the nozzle surface (concentrated at the nozzle throat) had on the unsteady boundary layer developing on the nozzle contoured surface specifically for the conditions listed in Table 2-1. Each test case consisted of measuring peak pitot pressure fluctuations p_p' in the boundary layer at 25 uniformly spaced points along the nozzle block centerline from x/L=0.54 (x=21 cm) to x/L=0.94 (x=36.3 cm) for a total of 100 data records. Recall that the temperature distributions for the heated and unheated conditions were shown above in Figure 4-3.

5.1 Unsteady Measurement Techniques

5.1.1 Sensor

The pitot pressure fluctuations p_p' were measured using a dynamic pitot probe (DPP) that consisted of a micro-miniature Kulite (CQ-030-100D) mounted on a probe sting as shown in Figure 5-1. This style of sensor had been successfully used by researchers in the MSU-SWT in the past (Berger 1988, Tritz 1990, Demetriades et al. 1994), primarily for turbulence measurement. Comparisons between hot-wire and DPP measurements in the turbulent boundary layer have shown good agreement (for example, Figure 48 in Berger 1988). The previous heated nozzle measurements by Demetriades also used the DPP.

The Kulite had a 0.76 mm diameter body with a 0.25 mm active diameter that was maintained normal to the x-axis ±2°. The Kulite had a 0-5170 mmHg range with a 1.50 $\mu V/mmHg/e_{excit}$ sensitivity and a 1.5 MHz resonant frequency reported by the manufacturer. The Kulite used in the present experiments was chosen based on its size and frequency response to afford the maximum resolution within the boundary layer, at a compromise in the Kulite output voltage strength. The probe resolution relative to the laminar boundary layer thickness (Figure 4-8) was about 1:5 based on the OD of the Kulite body and 1:15 based on the probe active diameter. In the present experiments, the Kulite was operated over about 3% of the transducer full scale range, which led to signal to noise ratios that ranged from about 3 in a turbulent boundary layer to unity for the quiescent layer and free-stream.

The DPP was operated to provide an AC signal only, since the manufacturer reported that DC measurements with the CQ-030-100D would be unreliable due to offset drift with temperature and time. Pitot pressure fluctuations were obtained from the AC signal using the sensitivity reported by the manufacturer, which had been previously verified to within 15% (Tritz 1990, Berger 1988). In situ calibrations had proven cumbersome and error-prone.

5.1.2 Electronic Circuit

The amplified DPP signal was recorded to analog tape during the experiment using a Honeywell 7900 FM Recorder so that the data could be played back and analyzed later. Figure 5-2 shows the recording circuit used for all DPP measurements. The Kulite was excited with a 3.1 Vdc (nominal) source using two D-size dry-cell batteries in series for a low-noise power source. The DPP signal was augmented by the differential amplifier resident in a Tektronix 502A oscilloscope, along with a HP 465A amplifier for a total AC gain of 3640 V/V (amplified DPP signal is 5.46 mV/mmHg/e_{excit}). The amplified DPP output signal was then fed to a wide-band rms meter, a spectrum analyzer to monitor the signal spectrum (averaged) in real-time, and to a digital storage oscilloscope to monitor discrete wave-forms as the amplified DPP signal was being recorded. The DC output voltage of the *y*-position actuator was recorded to channel 5 and a 20 kHz tone was recorded to channel 7 during intervals of valid data (i.e. recorder locked at proper tape speed). All recording was performed at a tape speed of 120 ips and a playback speed of 3 3/4 ips.

The components of the recording circuit (except the DPP) were verified by measurement to confirm a frequency response flat from 0.1 to 300 kHz, and a 3-dB point at 1 MHz. While the turbulent boundary layer contains frequencies exceeding 1 MHz (Tritz 1990), Mueller (1993) demonstrated that the *unstable* activity was concentrated in frequencies less than 15 kHz. Since the present study concentrated on the instabilities preceding the onset of turbulence, a 300 kHz frequency response was more than adequate.

5.1.3 Data Reduction

The playback signal was digitized at a sampling rate of 20 kHz, which corresponds to a real-time frequency of 640 kHz. The high sampling rate provided good resolution to capture turbulent bursting activity in the time-series waveforms. The weak signal at high frequencies also diminished aliasing in the digitized signal.

Digital signals were acquired using a 12-bit National Instruments Lab-PC+ A/D conversion card installed in a 386-20 computer. The Lab-PC+ card has a maximum sampling frequency of 80 kHz. Figure 5-2 also shows the playback arrangement used to digitize the data. Each digital waveform recorded to disk was 6.4 msec in length. To save on storage requirements, information regarding the acquisition speed, playback to real-time speed ratio, digital-to-analog conversion (DAC) voltage range, etc. were stored as a header in each file, then only a single 12-bit integer DAC value was stored for each digital sample. During data reduction, software logic was used to convert DAC values to voltages in terms of floating point numbers. All data reduction was done with MATLAB

routines written by this author, with frequent use of functions in the Signal Processing Toolbox.

Power spectra were computed for the MEP measurements by averaging periodograms from 512 independent 6.4 msec waveform snapshots (4096 points), with a Hamming window and frequency resolution of 156 Hz per spectrum point. Increasing the number of averages increased the accuracy and smoothness of the spectra, but only slightly better spectra were achieved beyond 512 waveforms. The lower and upper frequency bounds within which oscillations could be accurately captured were about 500 Hz to 320 kHz, respectively. Below 500 Hz the low frequency spectrum was dominated by electronic noise and revealed no useful information. At the Nyquist frequency of 320 kHz, the spectrum typically tapered down by at least an order of magnitude below the peak rms value associated with the dominant boundary layer activity, preventing appreciable aliasing in the signal. Figure 5-3 shows typical spectra for a strong and weak signal within the boundary layer. Note that the spectra are plotted on a linear rms scale, to facilitate a more direct comparison with results presented later in this chapter.

Electronic noise measurements were recorded for "wind-off" conditions with all electronic instruments on and running, as they would be during the experiment. As displayed in Figure 5-3, the electronic noise is most prevalent in frequencies below 1 kHz, and masks much of the measured activity for weak signals. In order to isolate the boundary layer activity for further data reduction, the averaged spectra of the electronic noise was routinely subtracted in the square from the averaged spectra of the total signal

at each streamwise location. Unless otherwise stated, all spectra discussed here have the wind-off electronic noise subtracted in the square.

A typical free-stream spectrum from the present experiments is shown in Figure 5-3 for comparison. The free-stream rms voltage readings add almost no content to the total spectrum, and below about 1 kHz free-stream measurements are actually less than the wind-off conditions. Since the wind-off measurements were recorded within a closed test section with no air-movement, any wind-on signal is physically required to be greater than the electronic noise (assuming the electronic noise is uncorrelated to the signal). Apparently then, the electronic noise characteristics of the Kulite change slightly between the wind-off and wind-on conditions. Other researchers (Munro 1996) have also noted this Kulite behavior. Higher frequencies of the FS measurements do show an increased rms amplitude over that of the wind-off conditions. Nevertheless, differences between the FS and wind-off values are very small, making the present free-stream noise measurements un-useable. Additionally, the results with weak boundary layer activity below 1.5kHz must be viewed with reservation.

5.2 Interpretation of the DPP Signal

5.2.1 Thermodynamic Relations

In a supersonic flow, small fluctuations in pitot pressure (p_p') can be translated through the normal shock that stands in front of the probe to small perturbations in the static variables (temperature, velocity, and pressure). A quasi-static analysis (Morkovin 1956) applied to the Rayleigh Supersonic Pitot formula (Ames Research Staff 1953)

provides a linearized equation that depends only upon the local Mach number M and ratio of specific heats γ (Tritz 1990, Demetriades 1991):

$$\frac{p'_p}{P_p} = \frac{p'}{P} + \left[\frac{2M^2 - 1}{M^2 - \frac{\gamma - 1}{2\gamma}}\right]\left(\frac{u'}{U} - \frac{1}{2}\frac{T'}{T}\right). \qquad \textbf{5-1}$$

If total temperature fluctuations (T_o'/T_o) can be neglected in the analysis, the one-dimensional adiabatic energy equation gives a form of the so-called Strong Reynolds Analogy

$$\frac{T'}{T} = -(\gamma - 1)M^2\frac{u'}{U}. \qquad \textbf{5-2}$$

Substituting equation (5-2) into (5-1) and neglecting the acoustic modes ($p'/P << u'/U$) leads to

$$\frac{p'_p}{P_p} = S_u\frac{u'}{U} \qquad \textbf{5-3}$$

with

$$S_u(M) \equiv \left[\gamma M^2 - \frac{(M^2 - 1)^2}{\left(M^2 - \frac{\gamma - 1}{2\gamma}\right)}\right] \qquad \textbf{5-4}$$

for $M>1$. When the transducer sensitivity ($S_{transducer}$) is included in the formula, then the fluctuating output voltage from the probe (e'_{out}) can be related directly to normalized velocity fluctuations (u'/U_e) by

$$\frac{u'}{U_e} = \frac{(U/U_e)}{S_u P_p}\frac{e'_{out}}{S_{transducer}}, \qquad \textbf{5-5}$$

where S_u and P_p are determined from the mean boundary layer profile. Equation 5-5 makes the DPP a convenient instrument for directly measuring velocity fluctuations if the mean-flow is known.

Quantitative use of the DPP relies on the assumptions that total temperature and pressure fluctuations can be neglected, as is commonly done in hot-wire analysis. Extensive hot-wire measurements show a velocity-temperature relation that agrees very well with equation 5-2 in adiabatic boundary layers at supersonic speeds (see, for example, Smits and Dessauge 1996).[4] Though the present experiments do not have an adiabatic condition, wall to total temperature ratios are still small enough that equation 5-2 is a good approximation *at the probe tip*.

Since $S_u>1$ at supersonic speeds, it is reasonable to neglect the pressure fluctuations with $p'/P << S_u u'/U$ in the turbulent boundary layer where $p'/P \sim (u'/U)^2$. In the unstable boundary layer, the eigenfunctions for TS or Görtler instabilities (Figures 4-17 and 4-14) also show that pressure fluctuations are an order of magnitude less than the velocity fluctuations, at the peak value of u'/U. Figure 5-4 shows the amplitude envelope for pitot pressure fluctuations induced by a TS wave computed with the complex eigenfunctions of Figure 4-17. The agreement between curves from equation 5-1 and 5-3 is good (3%

---

[4] This agreement does not necessarily come by "small" values of T_o'/T_o. For example, Debieve et. al. (1996) show $T_o'/T_o \sim 4\%$ in an adiabatic flat-plate boundary layer at M=2.3. With a wall temperature ratio near 1.5, T_o'/T_o increases to a maximum of 6% near the wall. Instead, the actual solutions to the full equations of motion do not depend strongly on the total temperature fluctuations as long as the mixed Prandtl number is close to unity. This is the case for adiabatic flows or nearly adiabatic flows with small wall-to-total temperature ratios.

difference) at the peak fluctuation amplitude in the layer. This peak is the so-called maximum energy point (MEP) in the boundary layer and ranges from y/δ=0.5 to y/δ=0.65 for TS modes at the most amplified conditions according to the theoretical predictions presented in Chapter 4 (Theoretical Results). Fluctuation measurements at the MEP are particularly useful for computing amplification rates of an instability. A larger signal input to the probe also reduces errors in measuring p_p' or u'.

5.2.2 Treatment of Boundary Layer Mean-Flow

Brogan (1995) measured profiles of the boundary layer mean-flow from $0.264<x/L<0.594$ at conditions of the low-Re'_∞ case in the present work both with and without surface heating. A comparison of the measured profiles to laminar boundary layer theory (computed with the Harris and Blanchard code), in general, showed thicker profiles by about 15%. But, when vertically scaled with the boundary layer thickness, profiles compared well. Shape factors were typically within 5% to 10% of each other for both heated and unheated wall conditions. Despite only moderate agreement in the profiles, all trends present (including those due to surface heating) in the experiments were predicted well in the theory. Mean-flow profile measurements by Brogan (1995), and by King and Demetriades (1993) at lower Re'_∞ showed somewhat better agreement with the theory.

Originally, mean-flow measurements were also planned to accompany the fluctuation data. However, the wind tunnel facility was temporarily decommissioned (3 ½ years) and dismantled immediately following the fluctuation measurements, and the

test-matrix had to be curtailed. The facility has only recently come on-line, but the heated nozzle experiments have not been repeated. The approach taken here is to present the data in the more precise terms of pitot pressure fluctuations (p_p'/P_o) and then make inferences, where appropriate, to the corresponding magnitude in velocity fluctuations (u'/U_e) via equation 5-5 with a computed mean-flow, rather than a measured mean-flow.

5.3 MEP Recordings

At any given streamwise location, the MEP based on $p_p'_{rms}$ was found by traversing the dynamic pitot probe (DPP) vertically away from the wall through the boundary layer, while monitoring the amplified wide-band rms output produced by the DPP. The MEP would then be determined by examining a plot of the wide-band rms and visually choosing the probe position at the maximum rms output. For every traverse through the layer to find the MEP, the DPP output was monitored on a digital storage oscilloscope displaying waveforms one at a time with 1-second updates, and a dual-display spectrum analyzer showing the Fourier components of both the free-stream signal and the current reading. A complete record of the analog maximum energy recordings, including tabulated values of the MEP location, can be found in Appendix A.

Figure 5-5 shows a set of typical wide-band rms traverses through a predominantly laminar boundary layer with unstable activity in the layer and a small amount of turbulent bursting. The horizontal tic-mark locates the MEP at each streamwise location, where a 7-second real-time signal (3.7 minutes playback) was recorded to analog tape. The oscillations in the wide-band rms signal were due to very low frequency noise (<10 Hz)

in the electronic circuit that was later filtered out in the digitizing process. Appendix A also reports the raw rms voltages through each of the stage of data reduction.

In all cases, measurements were acquired at the most downstream location first (x/L=0.942, x=36.3 cm), then marched forward at increments of approximately 0.6 cm ($\Delta x/L$=0.0156) to x=21 cm (x/L=0.545). By marching upstream, the shock wave from the probe and the associated wake did not alter the local surface temperature at the measurement location of each MEP recording. The absolute locations in the streamwise direction were known within ±0.3 mm, and distance from the wall to within ±0.1 mm. Relative distances in both axes were accurate to within ±0.05 mm.

5.3.1 Location of MEP

Figure 5-6 shows the location of the MEP identified by the peak $p_p'_{rms}$ signal within the boundary layer for Re'_∞=5.2×10^6/m with and without surface heating. The computed laminar boundary layer thickness from the Harris and Blanchard code (Figure 4-8) is included for comparison.[5] However, mean-flow profile measurements by Brogan (1995) at these same conditions indicate that the measured boundary layer thickness is slightly larger than the calculated value. Since the mean-flow measurements were only available for x/L<0.6, the solid curve in Figure 5-6 is an extrapolation of that data. Mean-flow measurements of the laminar boundary layer at other conditions confirm this thickness trend for x/L>0.6 (Brogan 1995).

In the unheated case, the MEP based on $p_p'_{rms}$ remains near y/δ=0.7 with reference to the measured thickness until about x/L=0.7 where the peak fluctuations slowly begin moving deeper into the boundary layer. Near the nozzle exit, the MEP is located at about y/δ=0.6. With surface heating, the MEP starts slightly higher at y/δ=0.8 then quickly tracks the same pattern as the unheated case. The flagged symbol at x/L=0.64 is a data point from Demetriades (1996) at the same stagnation conditions with an unheated nozzle. The repeatability of the two data sets (Demetriades 1996 and the present) is remarkable, considering that the two experiments were conducted by two different experimenters some two years apart with two different overlays installed on the nozzle block. The vertical error band in Figure 5-6 corresponds to the error in the actuator, not the subjective error of determining the location of the MEP.

The MEP location at Re'_∞=6.2×10^6/m is shown in Figure 5-7 with the computed (Chapter 4) laminar boundary layer thickness for the unheated condition included for comparison. Without surface heating, the boundary layer is densely intermittent, and δ from a laminar boundary layer theory has little relevance. But, when surface heating is applied, the layer is reduced to a laminar condition over the measurement range (as will be shown below). One would expect the MEP to be less than the computed boundary layer thickness as in Figure 5-6. The experiment shows that in fact the MEP based on $p_p'_{rms}$ moves away from the wall at x/L<0.7 with surface heating. The signal for these

---

[5] In view of the minute changes in δ with surface heating found by experiment (Brogan 1995) and theory (Chapter 4), no distinction is made between δ from the heated or unheated conditions.

measurements was very weak, and a MEP was difficult to precisely locate which led to the scatter in the data at $x/L<0.7$.

Again, the MEP locations in the present experiment are in agreement with Demetriades' measurements (1996) at $Re'_\infty=6.2\times10^6$/m. At a uniform throat temperature of $(T_w/T_o)_{x=0}=1.18$, Demetriades located the MEP from a $p_p'_{rms}$ traverse at 0.20 cm, which also lies outside the computed laminar boundary layer thickness, with disturbance energy continuing out to 0.5 cm. The mean-flow pitot traverse in Figure 5 of (Demetriades 1996) shows a boundary layer thickness near 0.3 cm at $x/L=0.660$, which is considerably higher than the laminar prediction. Therefore, it is not clear that the MEP at $x/L<0.7$ was diverging into the free-stream as originally suspected (Brogan and Demetriades 1998a). Detailed mean-flow measurements at this Reynolds number are required to resolve this discrepancy.

5.3.2 RMS progression

Figure 5-8 shows the wide-band pitot pressure fluctuations at the MEP. The rms values were computed by integrating the averaged spectra in the square from 0.156 to 320 kHz. In the unheated configuration with $Re'_\infty=6.2\times10^6$/m, the rms level is flat at $p_p'_{rms}/P_o=3.4\%$ due to the turbulent state of the boundary layer illustrated in Figure 2-3 (Transition map). At $Re'_\infty=5.2\times10^6$/m, the rms levels rise as the amplitude of the instability increases. When heating is applied, the reduction in $p_p'_{rms}$ fluctuations is apparent.

The magnitude of u'_{rms}/U_e can also be estimated from the $p_p'_{rms}/P_o$ levels in Figure 5-8 using equation 5-5 and a computed mean-flow. Since accurate mean-flow are not available by theory or previous measurements at Re'_∞=6.2×10^6/m, the application of equation 5-5 is limited to the measurements at Re'_∞=5.2×10^6/m. The mean-flow terms of equation 5-5 were computed at two y-locations to provide a range of probable u'/U_e magnitudes to account for the differences between the measured and computed mean-flow at Re'_∞=5.2×10^6/m (recall the discussion in Section 5.2.2). The first solution was obtained with the physical y-location of the MEP plotted in Figure 5-6 (i.e. $y_{MEP,\ BL\ CODE}$=$y_{MEP,\ PHYSICAL}$). The second solution employed a y-location that was first scaled by 15% (i.e. $y_{MEP,\ BL\ CODE}$=$y_{MEP,\ PHYSICAL}$/1.15). This variation in distance from the wall was equivalent to a 15% variation in the y/δ location of the MEP. The resulting velocity fluctuations are plotted in Figure 5-9. The curves are stopped at the location where turbulence appears in the MEP signal since the laminar boundary layer solution would no longer be applicable. The error bars in Figure 5-9 indicate the range of predicted magnitudes, and the symbols are located at the corresponding average. Since errors in the mean-flow term are multiplied by the magnitude of $p_p'_{rms}/P_o$, the error in u'_{rms}/U_e grows with $p_p'_{rms}/P_o$.

A comparison of Figures 5-8 and 5-9 show that the disturbance growth with streamwise distance in terms of u'/U_e is larger than the growth viewed by p_p'/P_o. As the MEP moves to smaller y/δ, the mean-flow terms S_u and P_p decrease faster than U/U_e, and the probe's "sensitivity" to velocity fluctuations decreases. That is, for a given

magnitude of u', the measured p_p' will be smaller as the probe moves toward the wall. A similar pattern occurs between heated and unheated profiles; at a given physical distance from the wall, the heated boundary layer has a lower P_p and S_u than does the unheated profile, which also causes a decrease in the sensitivity to velocity fluctuations.

At the first measurement station (x/L=0.56), the velocity fluctuations are reduced from u'_{rms}/U_e=0.66% without heating to u'_{rms}/U_e=0.45% at $(T_w/T_o)_{x=0}$=1.13. Transition occurs at u'_{rms}/U_e between 2-3% without surface heating and at a slightly larger magnitude near 4% when the layer is heated. At the nozzle exit, rms velocity fluctuations are estimated to be near 8% both with and without surface heating, which is close to the u'_{rms}/U_e magnitudes found by Tritz (1990) in the turbulent nozzle boundary layer at the same y/δ location.

5.3.3 Time Series

The progressions of waveforms at the MEP shows increasing activity with streamwise distance (Figures 5-10 to 5-13) for all cases. At Re'_∞=5.2×10^6/m without surface heating, the signal at x/L=0.57 has no discernable unsteadiness over the electronic noise. Gradually, a low frequency oscillation emerges with a period of about 0.25 msec. At high p_p'/P_o levels near 5% to 7% bursts of turbulence appear at the peaks and valleys of the base waveform. Using equation 5-5, this corresponds to high instantaneous velocity fluctuations of u'/U_e~10% in the base instability. When surface heating is applied, the reduction of activity both in the low frequency base waveform, and turbulence activity is immediately apparent. The Re'_∞=6.2×10^6/m waveforms show the

most dramatic decrease, which supports the absence of activity in the boundary layer at upstream locations referred to in Figures 5-7 to 5-9. Some spontaneous bursts appear at $Re'_\infty=6.2\times10^6$/m with surface heating (for example at $x/L=0.613$ in Figure 5-13). This is indicative of bypass events, possibly due to the very high noise levels in the free-stream from the acoustic radiation produced by the turbulence on the three remaining un-altered walls. When the waveforms are analyzed statistically, the occurrence of these bursts is found to be so infrequent that the percentage of turbulence is considered to be zero, as will be shown in the next section.

5.3.4 Turbulent Intermittency

Statistical techniques were next applied to the digital waveforms to characterize the turbulent intermittency (i.e. the percentage of time that the flow is turbulent as viewed by a stationary probe) of the MEP signal. A complete description of the technique to compute intermittency, along with a comparison to other intermittency methods is given in Appendix C. The method is briefly summarized here.

Figure 5-14 shows an example of the technique applied to a waveform from the present work. The raw signal is high-pass filtered at 20 kHz with an 8^{th}-order elliptic filter, then a mean-square value is computed over some short time-span, and a threshold criterion applied. The result is a square wave carried along with the original signal that can be integrated in time to provide the intermittency γ for that waveform.

The intermittency results are shown in Figure 5-15, computed with an ensemble average of 100 waveform records, each 6.4 msec in length. The plotted curves indicate the average value of the intermittency with ± one standard deviation for the error bars.

The turbulent intermittency shows the onset and progression of transition apart from the boundary layer stability. In the case of Re'_∞=5.2×10^6/m without surface heating, transition begins at approximately x/L=0.78, and the turbulent intermittency increases to about 20% at x/L=0.95. This is consistent with the original transition map presented in Figure 2-3. At the higher Reynolds number (Re'_∞=6.2×10^6/m) in the unheated condition, the signal shows significant bursting with a turbulent content that ranges from 50% to 80% over the entire range of measurement – also consistent with previous data in the MSU-SWT. Measurements by Demetriades have shown that turbulent bursting first appears 1–3 cm downstream of the throat ($0.026 \le x/L \le 0.078$) for P_o=600 mmHg (Re'_∞=6.3×10^6/m) (Demetriades 1981b, Figure 7).

Heating the boundary layer causes the turbulent bursting to be delayed for both the high and low Re'_∞ cases until the last two MEP recordings at x/L>0.92. When considering this transition delay, it must be remembered that the sidewalls were not altered, and were still turbulent or transitional when the lower nozzle block was heated. Therefore, the transition location (x/L=0.92) observed with heating may be influenced by unsteadiness that feeds from the sidewall boundary layers and/or by the acoustic radiation generated by the latter. It is possible, that if transition on all four walls were delayed, more laminar flow would be observed than with heating only one wall as reported here.

5.3.5 Fourier Spectrum Analysis

Figures 5-16 and 5-17 show the progression of the power spectral density in the physical frequency range 0-16 kHz. Beyond about 5 kHz, the spectrum was monotonically decreasing to nearly zero at 320 kHz for all maximum energy recordings (recall Figure 5-3). The boundary layer edge conditions change slightly from $0.54<x/L<0.94$ which causes a corresponding 8% change in the local time scale. For consistency with the theory (Chapter 3 and 4), the dimensionless frequency F is referenced to the local edge conditions. However, it should be noted that all discussions of a single "Fourier component" refer to a fixed physical frequency f, as in the theory.

In the unheated low Re'_∞ case, the spectrum progression shows the instability growing at first with a dominant peak around $F\times10^4=0.05$ ($f\approx3$ kHz) and decreasing to $F\times10^4=0.03$ ($f\approx1.5$ kHz) as the boundary layer thickens. Close inspection of Figure 5-16 reveals that near $x/L=0.8$, the low frequency components begin to decay while a mode centered near $F\times10^4=0.08$ ($f=4$ kHz) becomes dominant. The disturbance growth at $F\times10^4=0.08$ then slows as the disturbance saturates, energy diffuses into higher frequencies, and turbulent bursting appears regularly at the peaks and valleys of the base waveform. The movement of the "center frequency" located at the peak Fourier component for each streamwise position is shown in Figure 5-18.

At the higher Reynolds number, the layer without surface heating still shows a saturated peak near $F\times10^4=0.035$ ($f\approx2$ kHz), possibly as a signature of an instability preceding the break-down to turbulence.

When surface heating is applied, the frequencies of the dominant oscillations stay approximately the same, but disturbance amplitudes are reduced. (The "peak" frequency selected for $x/L<0.64$ at $Re'_\infty=5.2\times10^6$/m with heating in Figure 5-18—first 5 open circles in the top graph—is an artifact of a very weak signal, where no discernable center frequency can be associated with an instability.) The low Reynolds number case is particularly important in regard to the boundary layer stability since it shows the unstable activity before transition onset (defined as the first appearance of turbulent bursts in Figure 5-15) both with and without surface heating. Comparing the progression of power spectra to the change in turbulent intermittency with heating also shows that the delay in transition to turbulence is accompanied by a reduction in the amplitude of the peak disturbance(s) in the frequency range of 2-4 kHz. This is consistent with previous findings in the MSU-SWT (Mueller 1993, Demetriades 1996). Therefore, at $Re'_\infty=5.2\times10^6$/m, it appears that transition to turbulence is suppressed with heating through a decrease in the strength of the base waveform (2-4 kHz wave).

In the higher Reynolds number case, the intermittency computations (Figure 5-15) and waveform pictures (Figures 5-12 and 5-13) have already shown that heating quenches the turbulent bursting and unsteadiness in the layer. Now, the power spectra show that heating has simultaneously reduced the low frequency oscillations dramatically so that the instability growth resembles that of the low Reynolds number case with heating (in terms of $p_p'_{rms}$ magnitudes). Clearly, the heating has already had a strong effect in the first half of the nozzle. Though the conditions leading to turbulence at $Re'_\infty=6.2\times10^6$/m without surface heating have not been observed directly as in the low-

Re'_∞ case, it is inferred that turbulence has been prevented by suppressing the instability amplitude in the throat region.

The upstream effect of surface heating is further quantified in Figure 5-19 with a plot of the disturbance amplitude spectrum at the first measurement station. With surface heating at Re'_∞=5.2×10^6/m, the fluctuations at x/L=0.582 has been reduced by 25% at the peak Fourier component (F×10^4=0.05), and a factor of 2 or more at higher frequencies. This comparison is also similar in terms of velocity fluctuations, using equation 5-5 and measured velocity profiles from (Brogan 1995) near this x-position. A much more dramatic effect is observed at Re'_∞=6.2×10^6/m with a reduction in the peak fluctuations by an order of magnitude when the nozzle is heated. The higher heating level of $(T_w/T_o)_{x=0}$=1.22 has even reduced the $p_p'_{rms}$ amplitudes to less than the heated case at Re'_∞=5.2×10^6/m, and $(T_w/T_o)_{x=0}$=1.13 – despite the profound differences in the layer condition with an unheated nozzle.

5.3.6 Amplification Rates

The distribution of MEP spectra can be used to calculate the spatial amplification of small disturbances for each Fourier component, in accordance with boundary layer stability theory. Since the description of instabilities leading to transition only has relevance when turbulence is not present, comparison of the spatial amplification rates is limited to Re'_∞=5.2×10^6/m with and without surface heating where the turbulent intermittency is zero.

Though no formal connection has been made between the present experiments and linearized stability theory for two-dimensional boundary layers, the spatial amplification rate $-\alpha_i$ can be computed from the separable form of the disturbance in equation 3-6. If the local rms amplitude of a single Fourier component (fixed physical frequency) in the boundary layer is given by A, then the spatial amplification rate can be computed from the experiment with

$$-\alpha_i = \frac{1}{A}\frac{\partial A}{\partial x} \qquad \textbf{5-6}$$

In the framework of linear stability theory, all disturbance quantities are amplified by the same amount (see equation 3-6) so that pitot pressure fluctuations are just as suitable as any other quantity. However, the quasi-parallel (Mack 1984) and non-parallel linear theories (Herbert 1993) implicitly or explicitly use the velocity fluctuations at the MEP for measuring the disturbance growth, and thus growth rates. Therefore, using the velocity fluctuations at the MEP in equation 5-6 represents a slightly improved result over that of the pitot pressure fluctuations. Using the relation for velocity fluctuations from the DPP output (equation 5-5) in equation 5-6 yields

$$\left(-\alpha_i\right)_{u'} = \frac{1}{e'_{out}}\frac{\partial e'_{out}}{\partial x} - \frac{U}{S_u P_p}\frac{\partial (S_u P_p / U)}{\partial x} \qquad \textbf{5-7}$$

where $(-\alpha_i)_{u'}$ indicates amplification rates based on velocity fluctuations. The first term in equation 5-7 is the local amplification rate based on the probe output e'_{out} (or p_p'), while the second term represents streamwise changes in the local mean-flow at the probe tip. The latter gives a positive contribution to $(-\alpha_i)_{u'}$ so that amplification rates based on

p_p' quantitatively understate the amplification rate based on u'. However, the MEP follows approximately the same path with or without surface heating (Figure 5-6), so that the mean-flow contribution in equation 5-7 *due to a variation in* y/δ *with streamwise position* is quantitatively similar with and without surface heating. Therefore, a qualitative comparison in the change with and without surface heating reveals the same features based on e'_{out} (or p_p') as those based on u'.

Accurate calculations of $-\alpha_i$ by equation 5-6 first require a smoothing procedure. The spatial derivatives ($\partial A/\partial x$) are computed from the "smooth" spectrum at a fixed dimensional frequency f, then divided by the local rms magnitude, A. In the present work, a polynomial smoothing procedure along the lines of (Demetriades 1992b) in both space (x) and frequency (f) was employed with some improvements. The smoothing procedure worked well as demonstrated by a comparison of Figure 5-20 with Figure 5-16. Appendix B provides further details and an evaluation of the smoothing procedure used here.

Figure 5-21 shows the amplification rates based on $p_p'_{rms}$ of selected Fourier components as a function of streamwise distance x/L. Note that the amplification rates have been made dimensionless with the viscous length scale l^*, consistent with the calculations in Chapter 4. The corresponding dimensionless frequency F is listed as an approximate value since the edge conditions are changing slightly over the measurement range. The amplification rates based on u'_{rms} are shown in Figure 5-22. The amplification rate curves for Figures 5-21 and 5-22 are truncated at the location where turbulent bursting begins, as identified by Figure 5-16.

As discussed above, the magnitude $(-\alpha_i)_{u'}$ is numerically larger than $(-\alpha_i)_{e'}$, but the primary features with and without surface heating are the same. The principal difference occurs at $x/L<0.65$ where the curves for the heated case show larger values in the amplification rate of u' than in e'_{out} (or p_p'). Given the uncertainties in the measurements and the transformation from p_p' to u', it is not wise to emphasize this difference.

In the unheated case, the growth is a maximum at $x/L\approx0.7$ for all frequencies and then decays with increasing distance from the throat. When surface heating is applied to the boundary layer, the peak amplification shifts downstream to $x/L\approx0.8$ (i.e. higher Reynolds number). The fact that the amplification rates increase at all frequencies is indicative of non-linear processes.

It is also important to note that positive amplification rates are observed for all frequencies and all x/L investigated. Thus, neutral points defined by $-\alpha_i=0$, and their subsequent relation to surface heating could not be evaluated experimentally.

5.4 Free-stream Disturbance Environment

The disturbances in the free-stream are vital to understanding and interpreting the boundary layer transition process. As mentioned above in Section 5.1, the DPP and electronic circuit used in the present measurements were not suitable for low-disturbance measurements in the free-stream. However, recent and previous data reported by Brogan and Demetriades (1998b) can be used to estimate the disturbance environment impinging on the nozzle boundary layer for the present experiments. Brogan and Demetriades used sensors with much better signal-to-noise ratios to measure p_p' in the free-stream. The

noise characteristics and spectral content in the Mach 3 test-volume were determined as a function of Re'_∞ and x.

It must be emphasized that these noise measurements were recorded with the unheated nozzle block only *and* include all 4 walls as acoustic sources. The external acoustic environment impinging on the heated and unheated layers of the lower surface will be composed of radiation from the remaining 3 walls since any given wall in a rectangular nozzle can only "see" the other three walls. Since these three other walls (top and sidewalls) are unaltered when heating the lower nozzle block, the acoustic environment of the latter will be the same with and without surface heating.

Static pressure fluctuations (p'/P) along the tunnel centerline range from 0.1% at low pressures when the nozzle wall boundary layers are laminar and stable to 0.3-0.5% when the layers are transitional or turbulent. Mach lines can be traced from noise measurement locations on the tunnel centerline and an estimate of the disturbance magnitudes impinging on the developing nozzle boundary layer can be obtained. At $Re'_\infty=5.2\times10^6$/m (500 mmHg), disturbances are 0.3-0.4% at the nozzle trailing edge, and estimated at 0.1% at $x/L=0.6$ near the edge of the boundary layer where the MEP recordings begin. At $Re'_\infty=6.2\times10^6$/m the boundary layer on the tunnel walls is densely intermittent, and has a measured $p'/P=0.4$-0.5% at the layer edge over the entire region of MEP recordings.

Spectral content of the free-stream disturbances rolls off near 50 kHz, and the low frequency oscillations in the boundary layer are clearly reflected in the free-stream. Fluctuations at the tunnel centerline increase gradually with streamwise distance corresponding to the long wall boundary layer transition region.

In addition to considering the external disturbances over the measurement range, the disturbances at the "inception" of the boundary layer even upstream of the nozzle throat should be addressed. Here, the inception of the boundary layer is considered to be the exit of the final screen, upstream of the two-dimensional contraction since the conditions will be identical at this point with or without surface heating. Unfortunately, direct measurements have not yet been acquired. However, some comments can be offered as to the source and type of disturbances that could be found.

The boundary layer on the nozzle walls is a continuous system beginning in the settling chamber at M_e~0, passing through two screens, a three-dimensional contraction, and a final screen before arriving to the two-dimensional contraction formed by the sidewalls and nozzle blocks (see Figure 2-1). Through each of these stages, the boundary layer is assumed to be laminar due to the low Reynolds numbers (Re_θ<100) and short length of the three-dimensional contraction. However, even in a laminar state, the layer cannot be free of disturbances. In the three-dimensional contraction, the intersection of the conical shape to a rectangular shape forms sharp convex corners with turning angles near 10° that are likely to produce steady and/or unsteady separation. The turbulence screens, which break-up and dissipate turbulence in the free-stream, will also leave some streamwise vorticity in the free-stream and the boundary layer (Watmuff 1997, Böttcher and Wedemeyer 1989, Bradshaw 1965). In particular, the final 320 mesh screen has very low open area ratio of 25% which enhances spanwise variations in vorticity with small jets that randomly coalesce to form steady longitudinal vortices (Bradshaw 1965).

The measurements by Brogan and Demetriades have indicated that the noise levels appear to asymptote to about 0.1% in the test core, when all of the walls are laminar. The composition of these remaining disturbances is unknown. It is assumed that in the absence of any disturbance generators through the nozzle (with laminar wall boundary layers) this 0.1% represents the disturbances from the settling chamber that could have both acoustic and vorticity content.

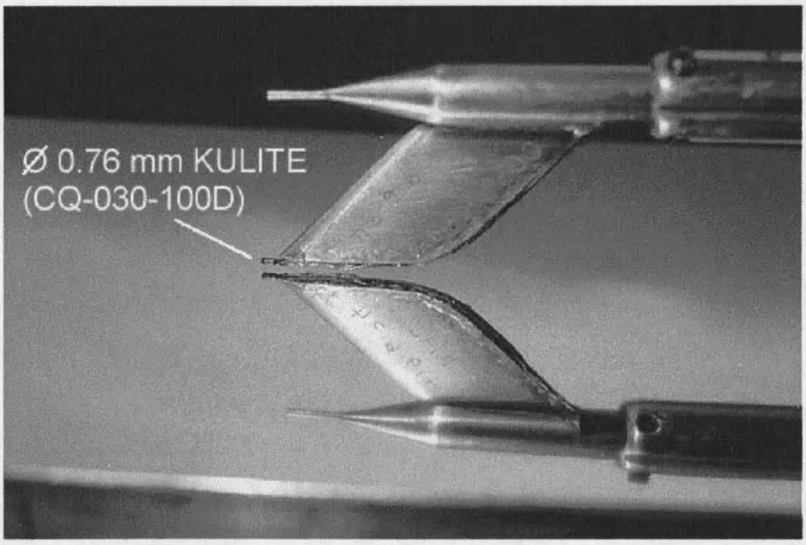

Figure 5-1. Schematic of the dynamic pitot probe (DPP) consisting of an ultraminiature Kulite mounted on a probe sting. (Probe reflection off of nozzle surface shows polishing quality)

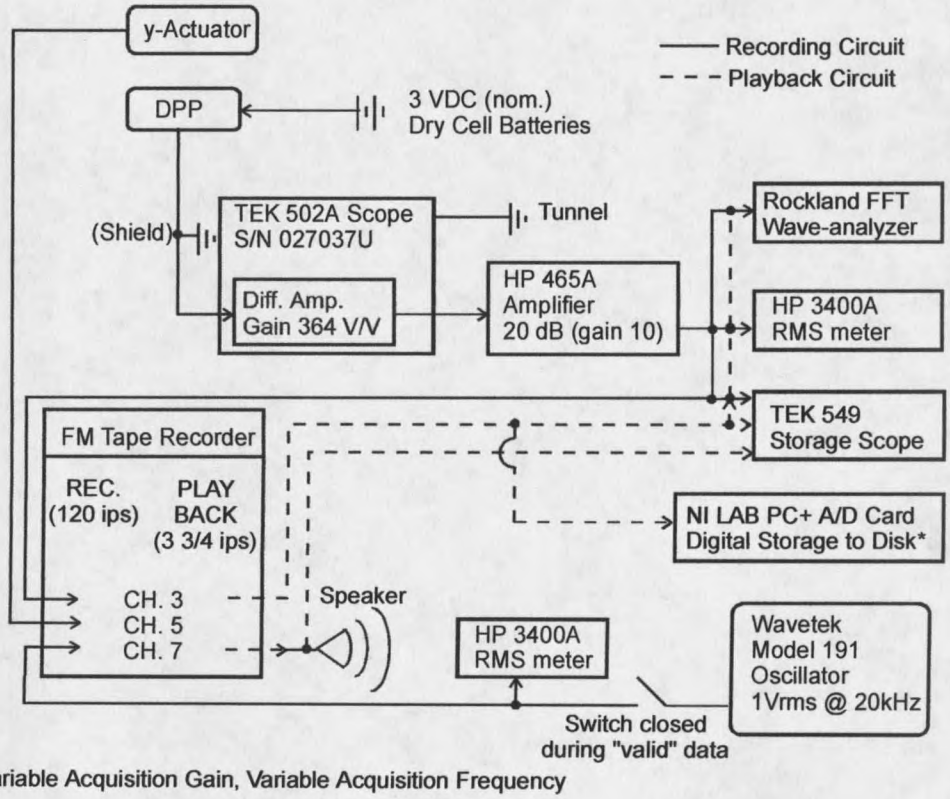

Figure 5-2. Recording and playback circuit for unsteady measurements with the dynamic pitot probe (DPP).

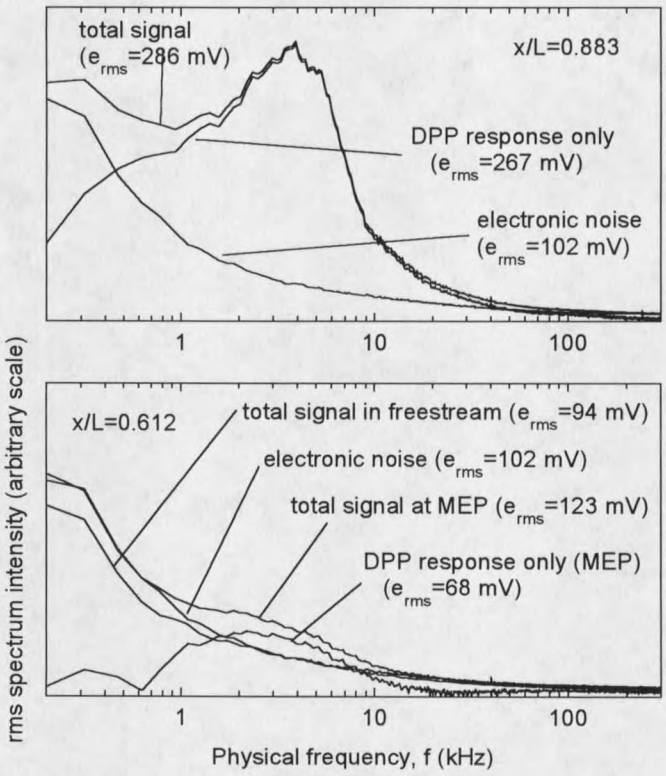

Figure 5-3. Typical power spectra with and without electronic noise. Conditions are from $Re'_{\infty}=5.2\times10^{6}$/m, Unheated. (top) "robust" signal, (bottom) "weak" signal with low signal to noise ratio.

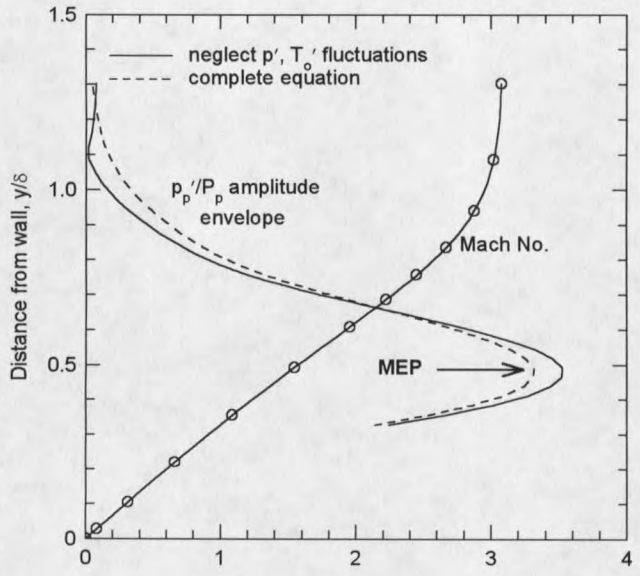

Figure 5-4. Amplitude envelope for fluctuations sensed by a dynamic pitot probe in a supersonic boundary layer.

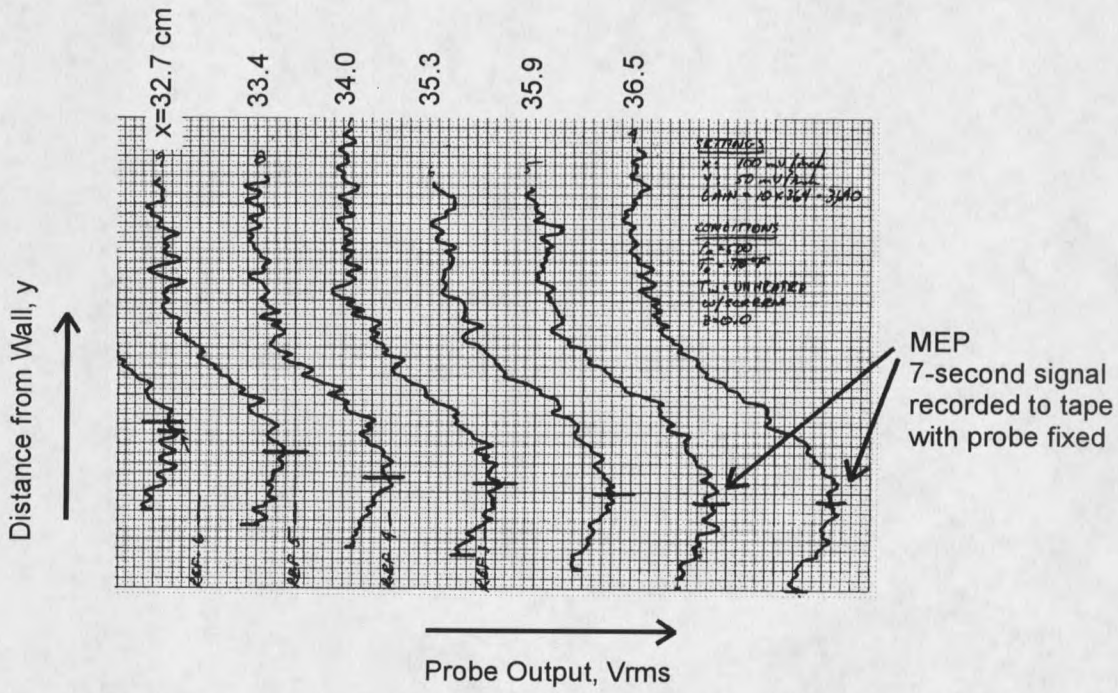

Figure 5-5. Technique to determine maximum energy point (MEP) within the boundary layer. Tic-marks indicate the MEP. Each trace is a different streamwise (x) position on the nozzle.

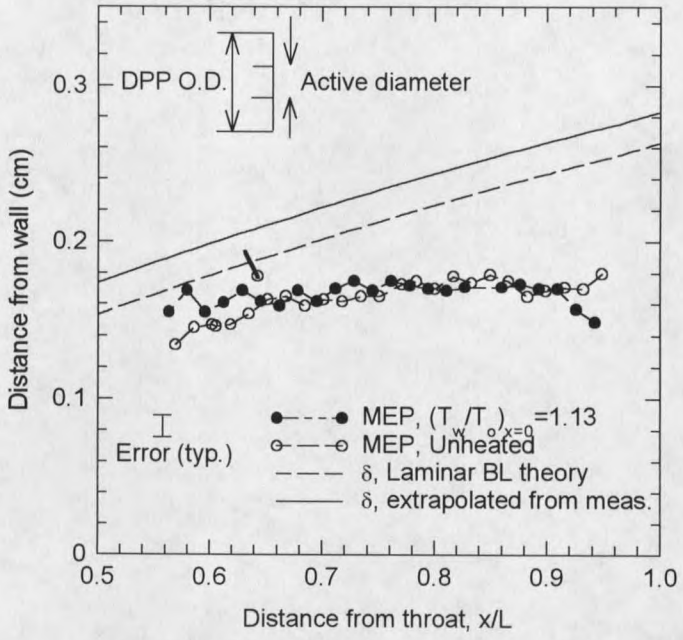

Figure 5-6. Location of maximum energy point (MEP) within the boundary layer at Re'_∞=5.2×10^6/m with and without surface heating. Flagged symbol indicates measurements by Demetriades (1996) at the same stagnation conditions.

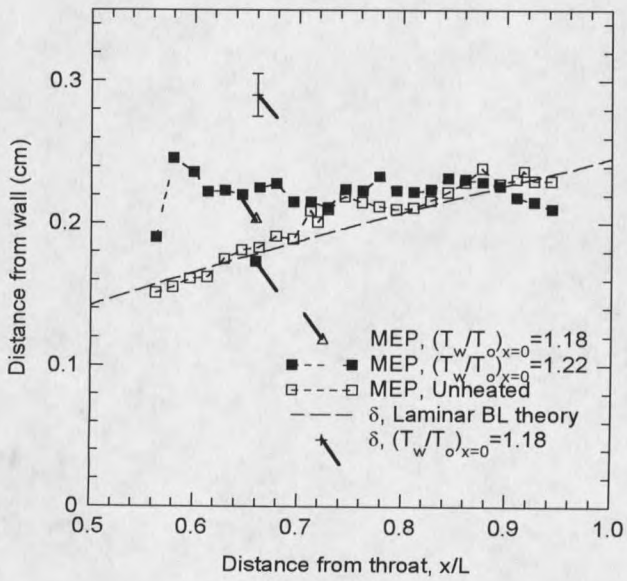

Figure 5-7. Location of maximum energy point (MEP) within the boundary layer at Re'_∞=6.2×10^6/m with and without surface heating. Flagged symbols indicate measurements by Demetriades (1996) at the same stagnation conditions.

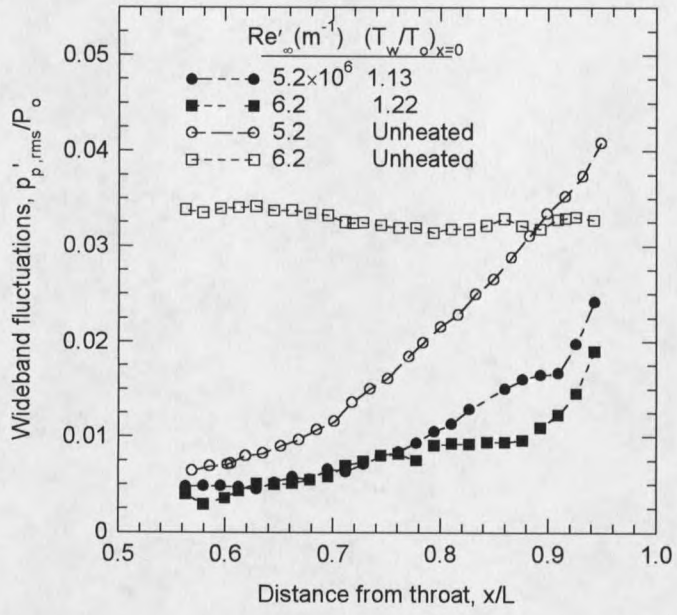

Figure 5-8. Wideband pitot pressure fluctuations at the maximum energy point (MEP) with and without surface heating. Computed by integrating averaged power spectra from 156 Hz to 320 kHz. Electronic noise subtracted in the square.

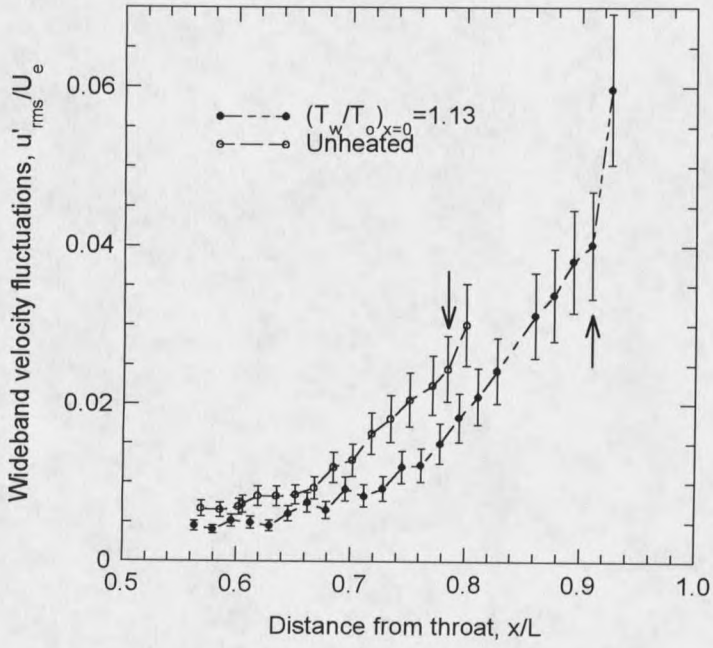

Figure 5-9. Wideband velocity fluctuations for Re'_∞=5.2×10^6/m. Calculated with equation 5-5 using mean-flow computed from boundary layer theory. Error bars based on total variation in MEP location (y/δ) of 15%.

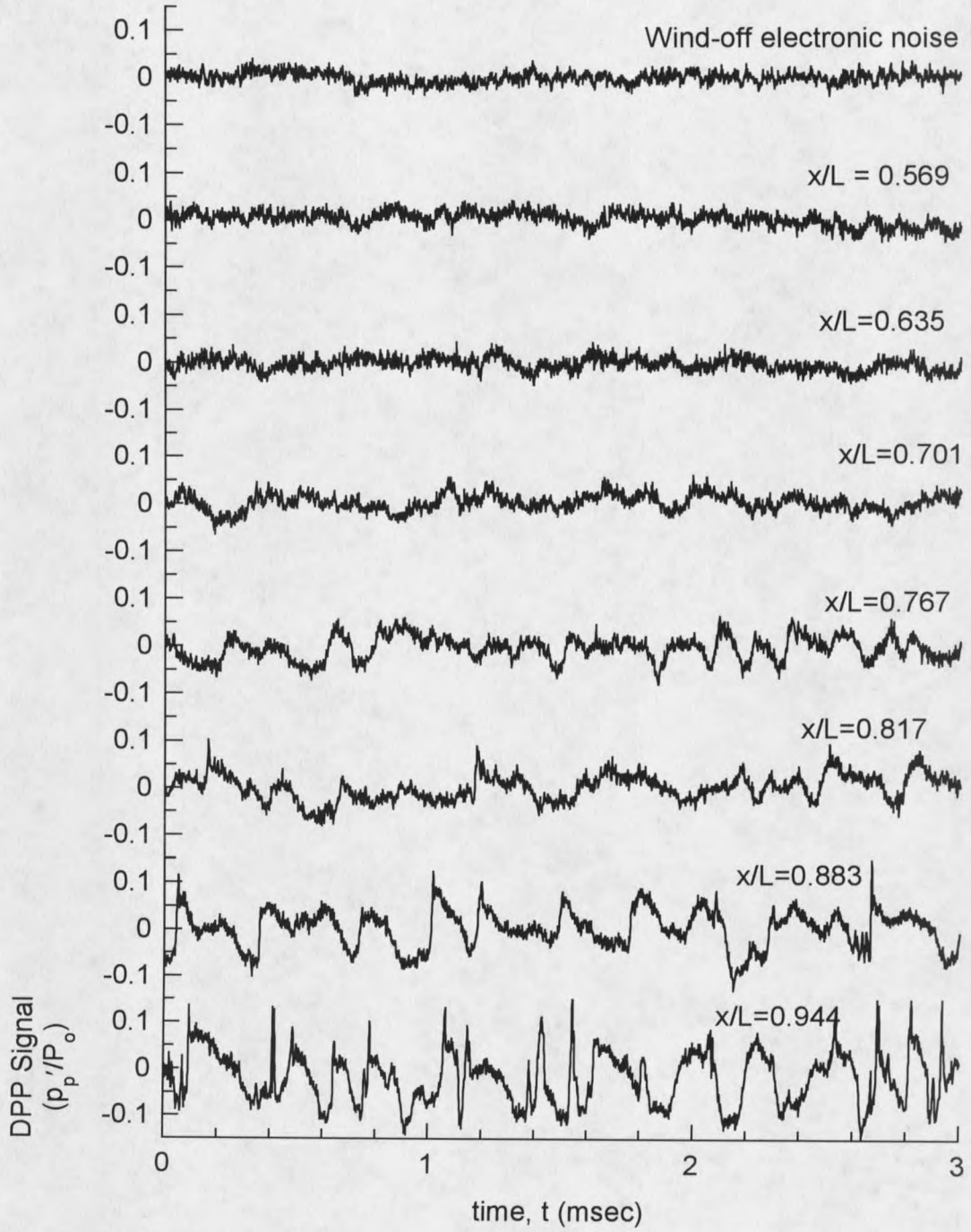

Figure 5-10. Progression of sample waveforms at maximum energy point (MEP). Re'_{∞}=5.2×10^6/m, Unheated.

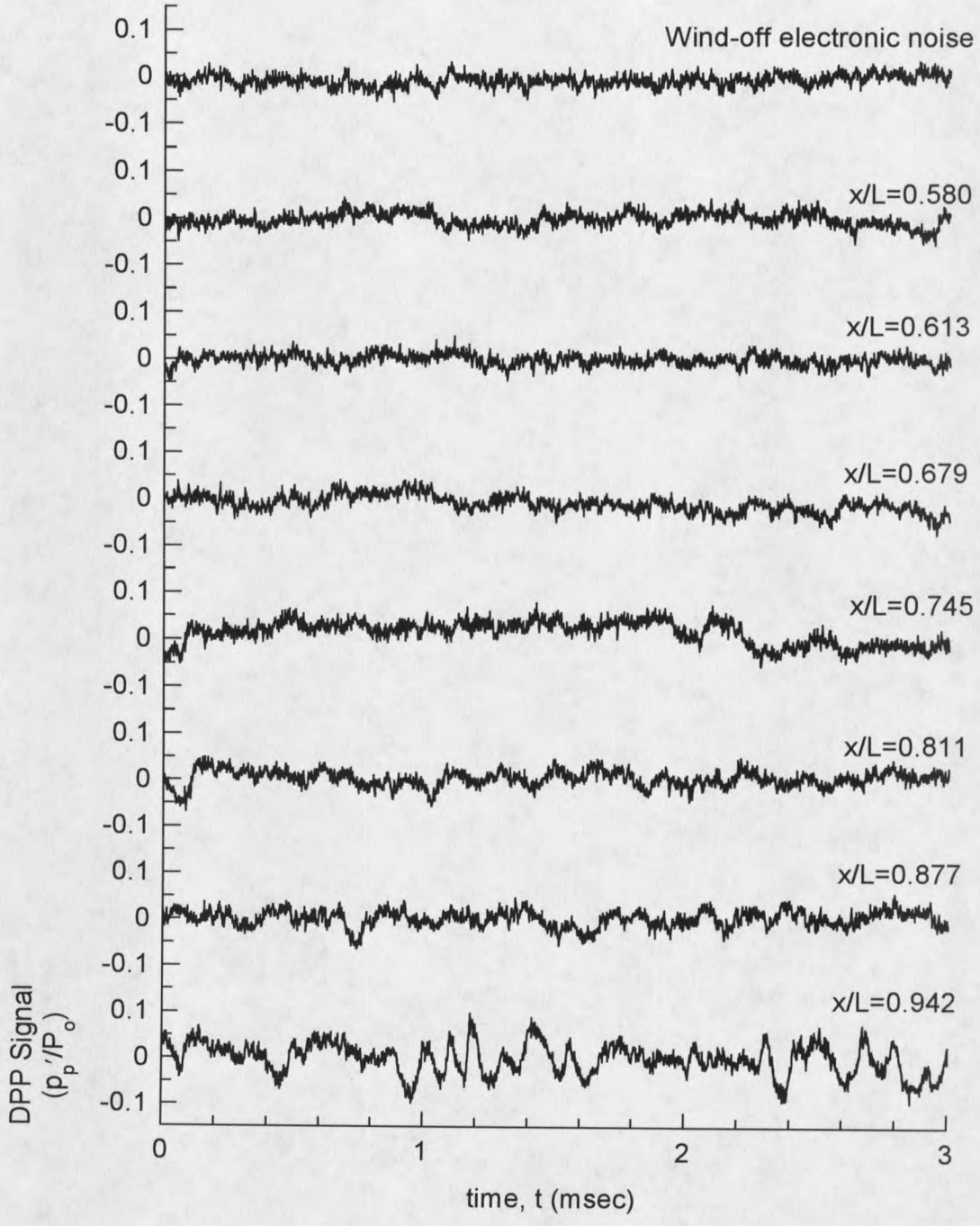

Figure 5-11. Progression of sample waveforms at maximum energy point (MEP). Re'_{∞}**=5.2×10^6/m, Heated** $(T_w/T_o)_{x=0}$**=1.13.**

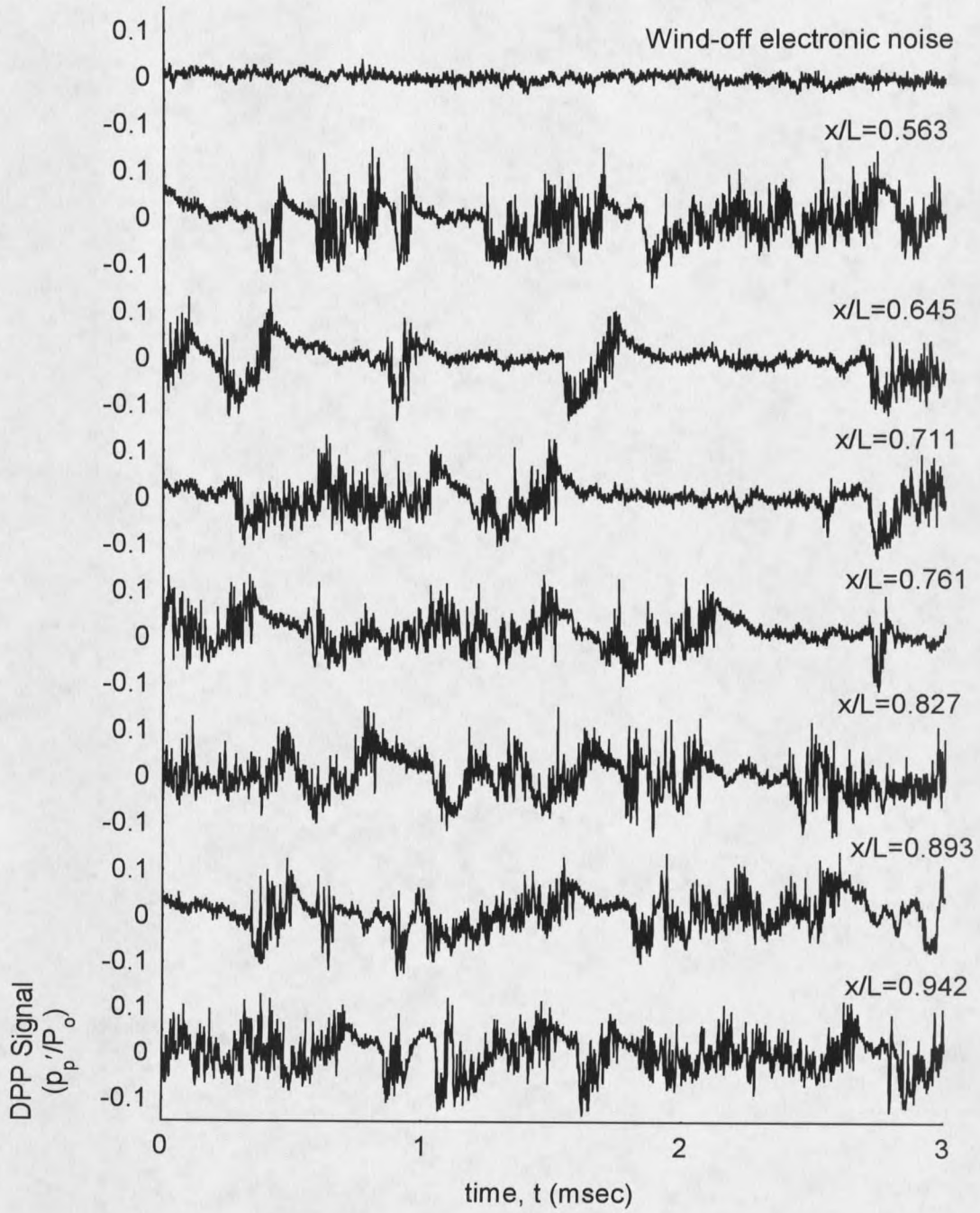

Figure 5-12. Progression of sample waveforms at maximum energy point (MEP). Re'_{∞}=6.2×10^6/m, Unheated.

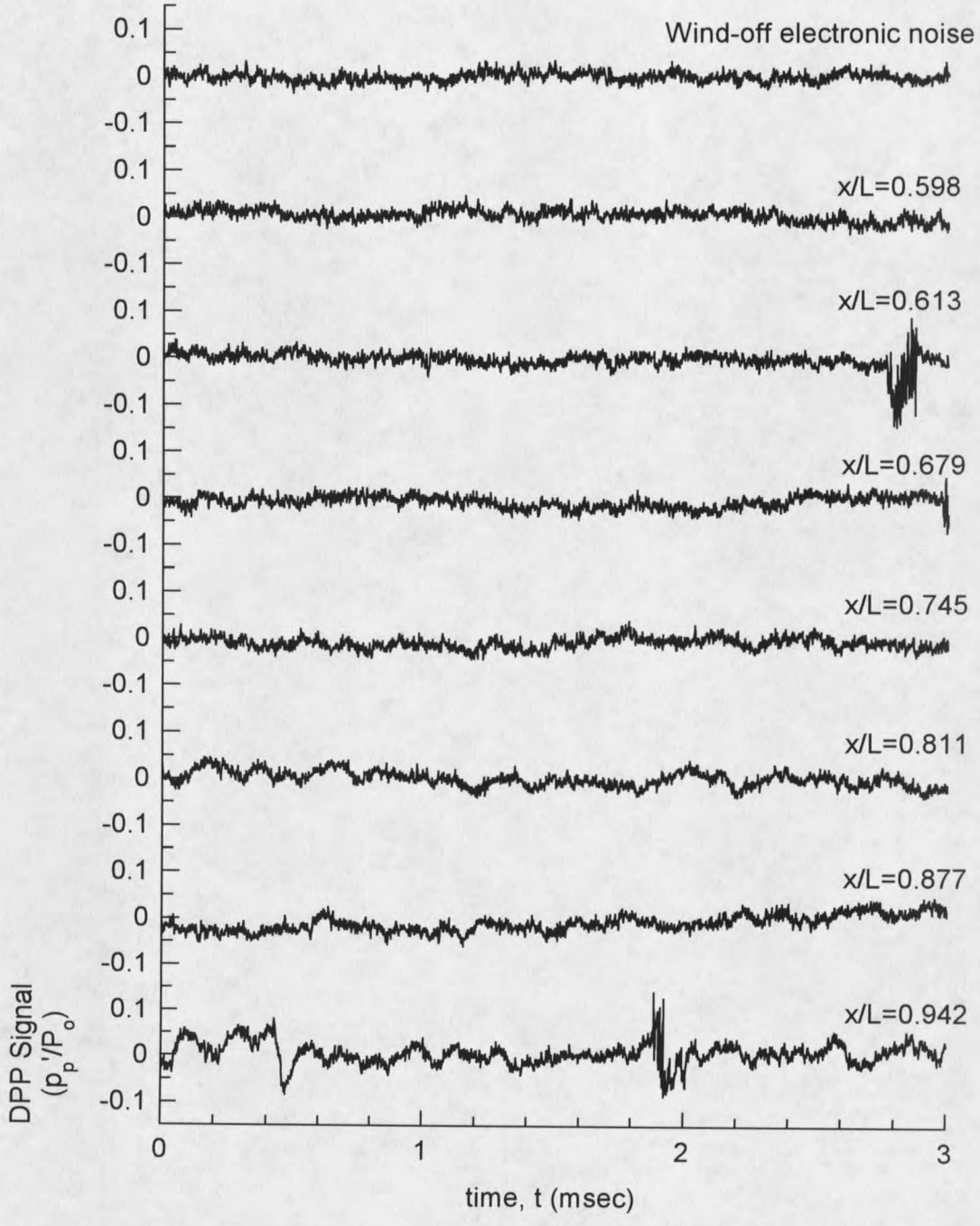

Figure 5-13. Progression of sample waveforms at maximum energy point (MEP). Re'_{∞}=6.2×10^6/m, Heated $(T_w/T_o)_{x=0}$=1.22.

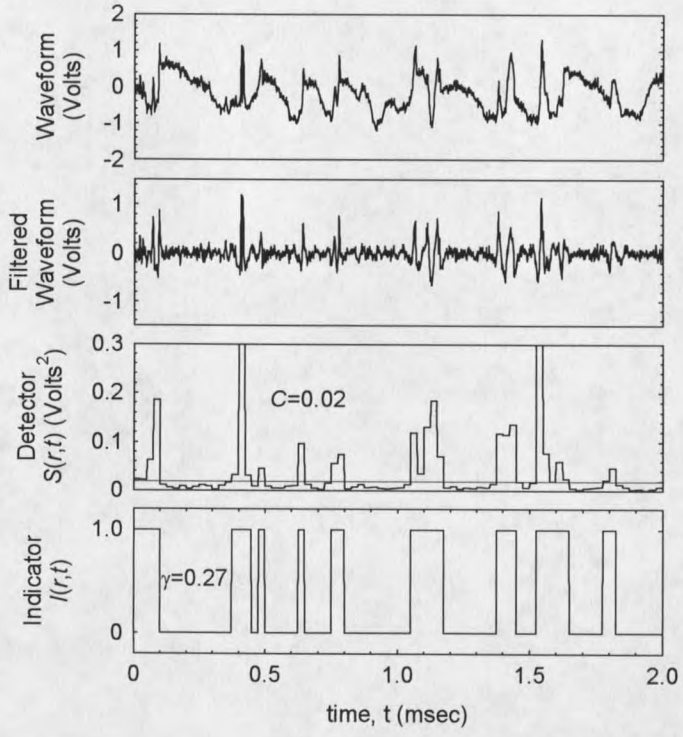

Figure 5-14.Intermittency technique applied to sample waveform (Re'_∞=5.2×10^6/m, Unheated, x/L=0.949); γ=Intermittency; C=Threshold criterion.

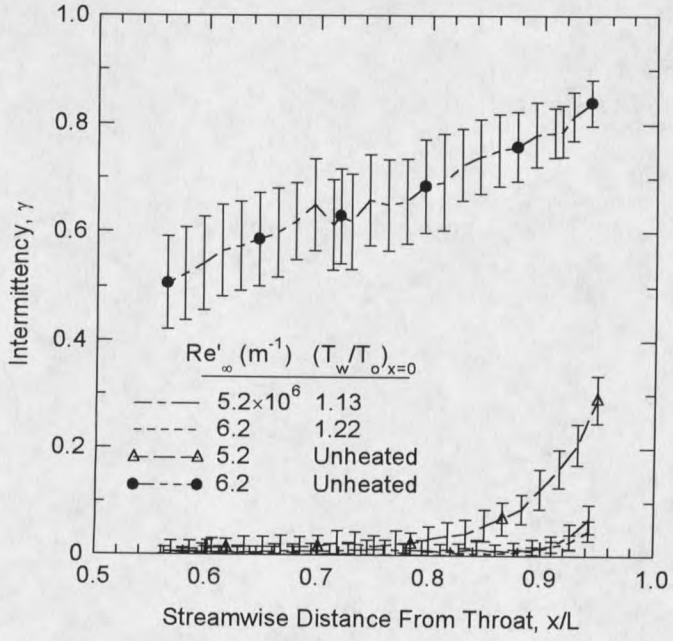

Figure 5-15.Streamwise progression of intermittency with and without surface heating.

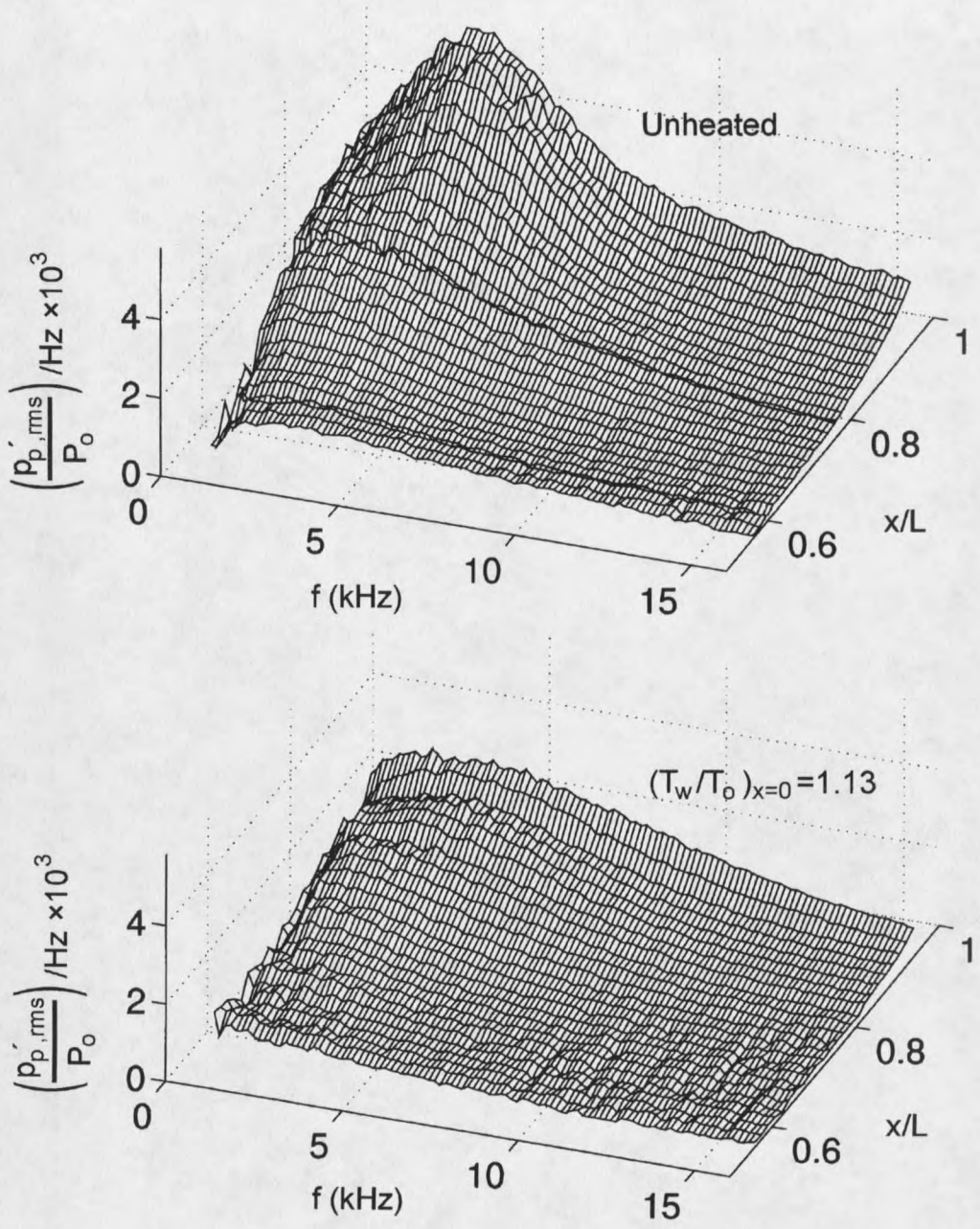

Figure 5-16. Streamwise progression of power spectral density at the maximum energy point with and without surface heating. Re'_∞=5.2×10^6/m. Electronic noise subtracted in the square.

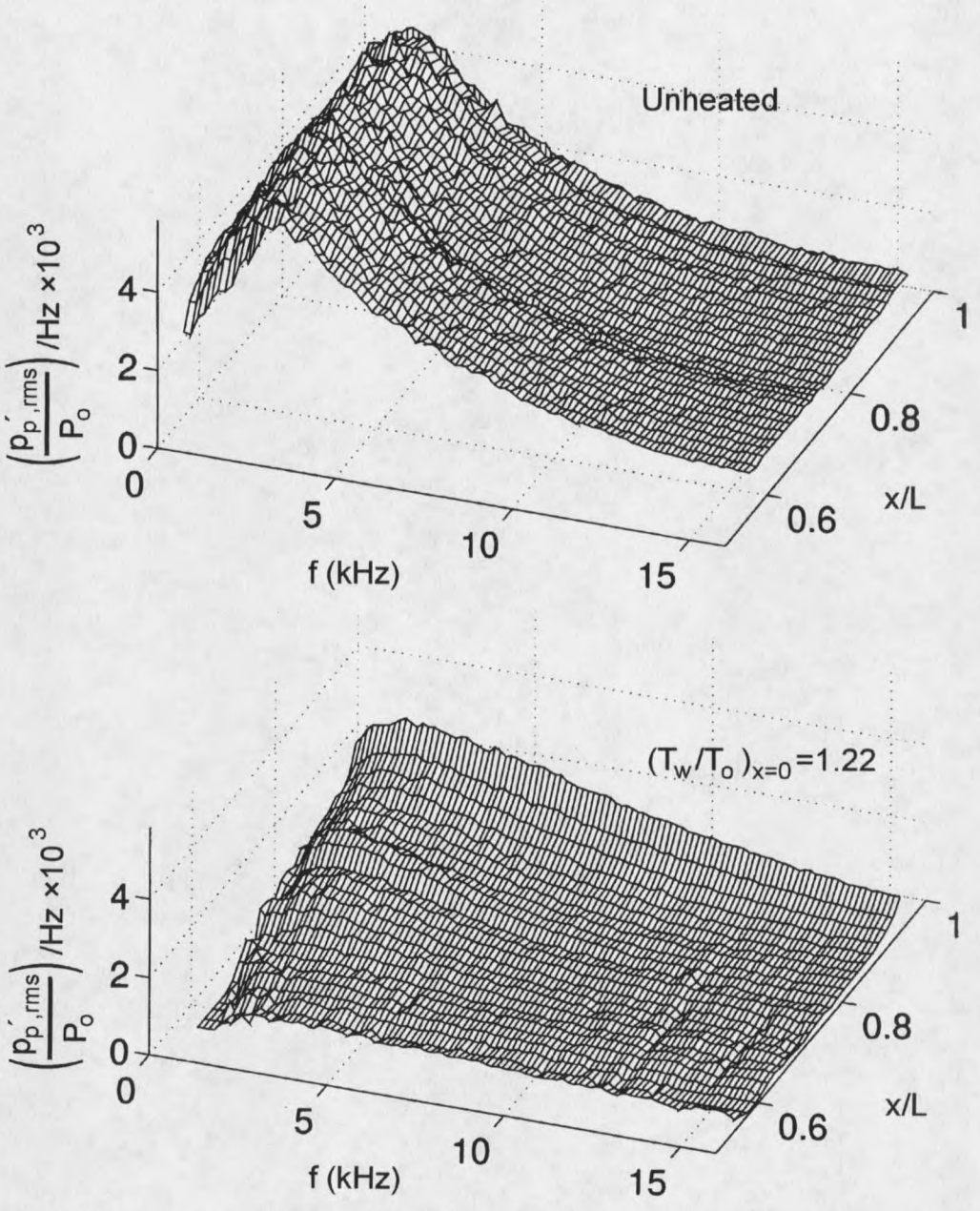

Figure 5-17. Streamwise progression of power spectral density at the maximum energy point with and without surface heating. Re'_∞=6.2×10^6/m. Electronic noise subtracted in the square.

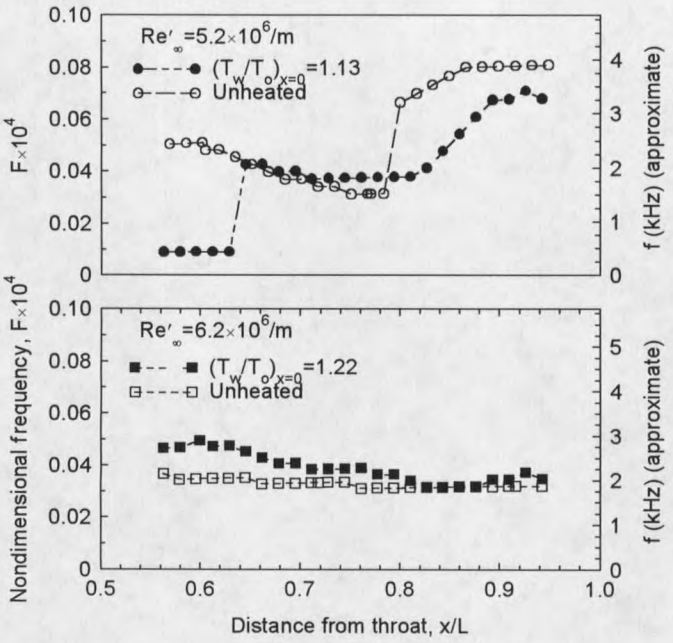

Figure 5-18. Dimensionless frequency at the maximum spectral intensity. Maxima computed from smoothed spectra.

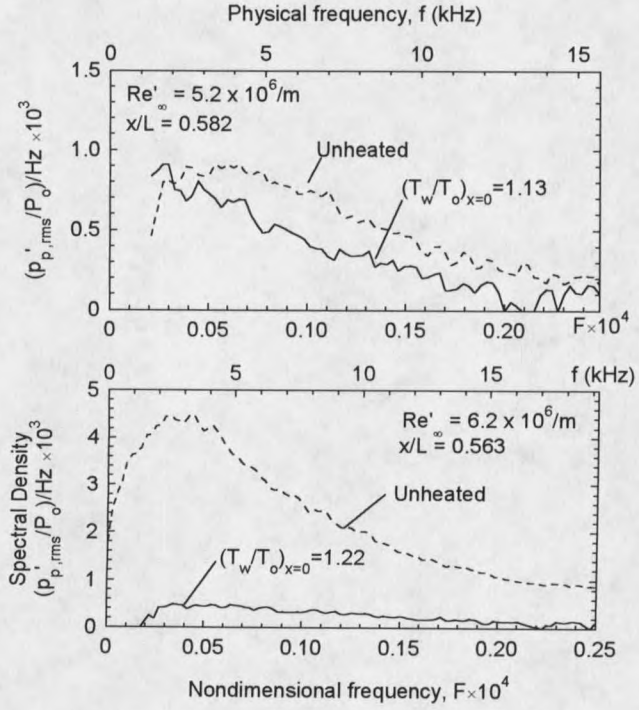

Figure 5-19. Comparison of fluctuation rms amplitude spectrum with and without surface heating at the first measurement location.

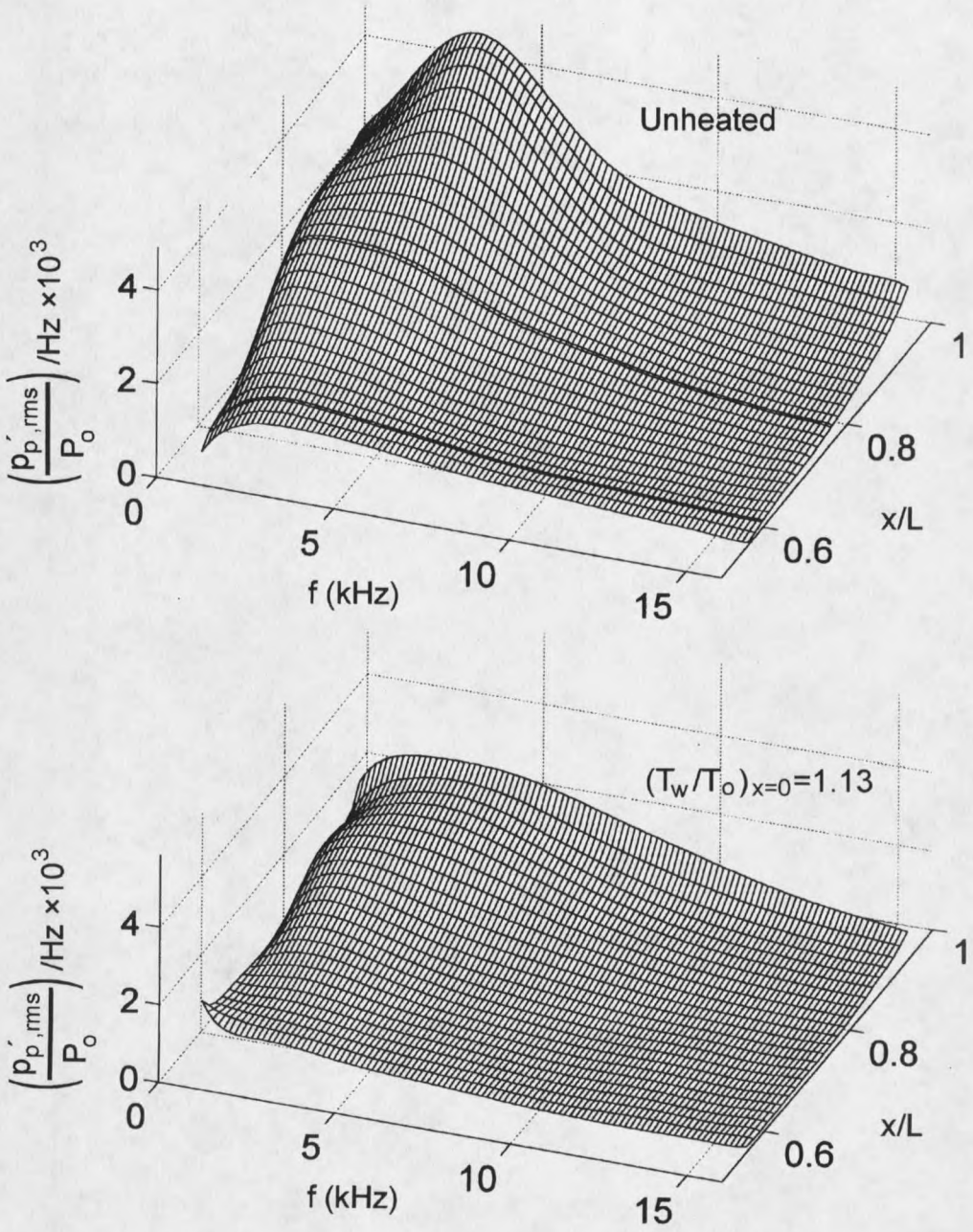

Figure 5-20. Smoothed power spectral density of Figure 5-16. Re'_∞=5.2×10^6/m. Polynomial smoothing procedure used with 10th-order polynomial in frequency and 7th-order polynomial in the streamwise direction.

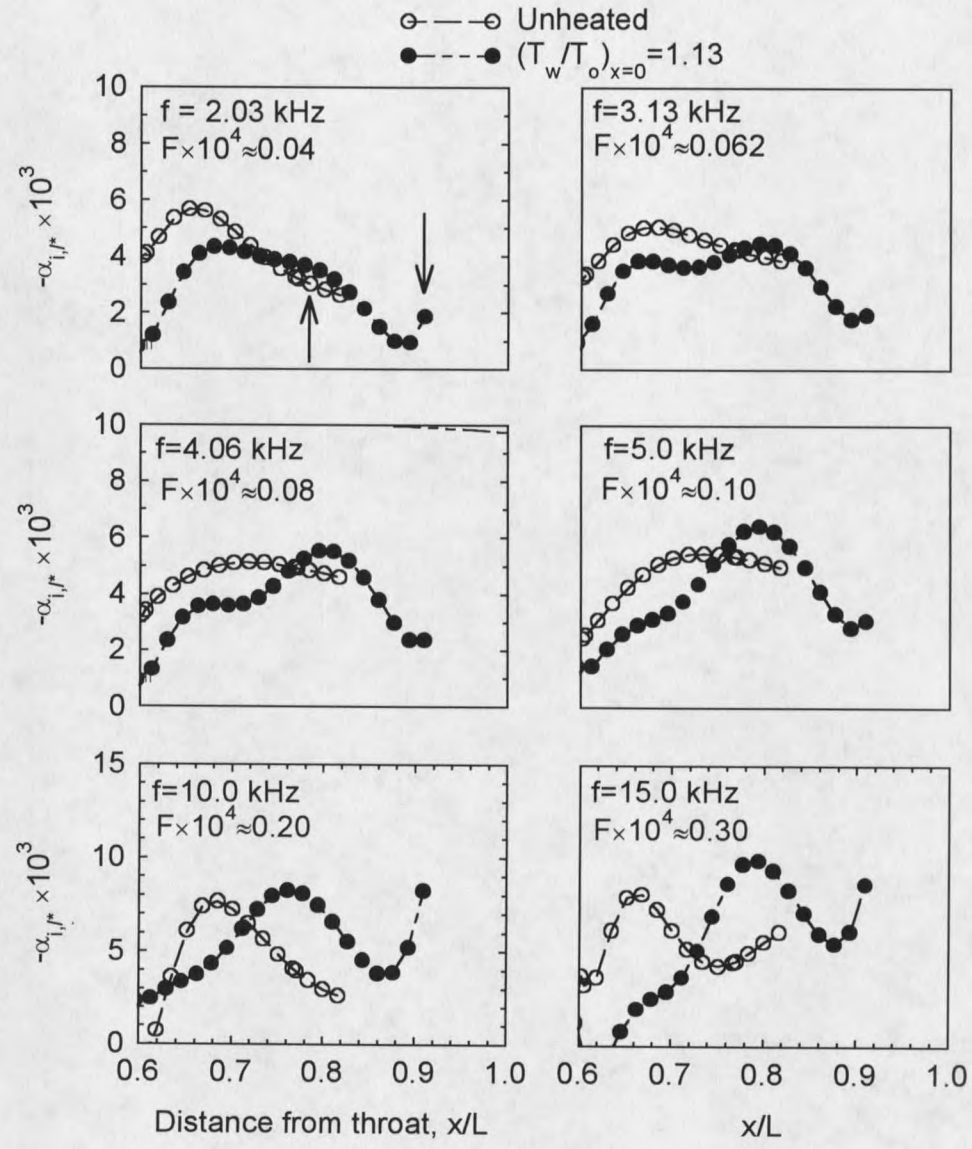

Figure 5-21. Comparison of spatial amplification rates based on $p_p{}'_{rms}$ at selected Fourier components. Re'_∞=5.2×10^6/m with and without surface heating. Spatial amplification rates nondimensionalized with viscous length scale l^*.

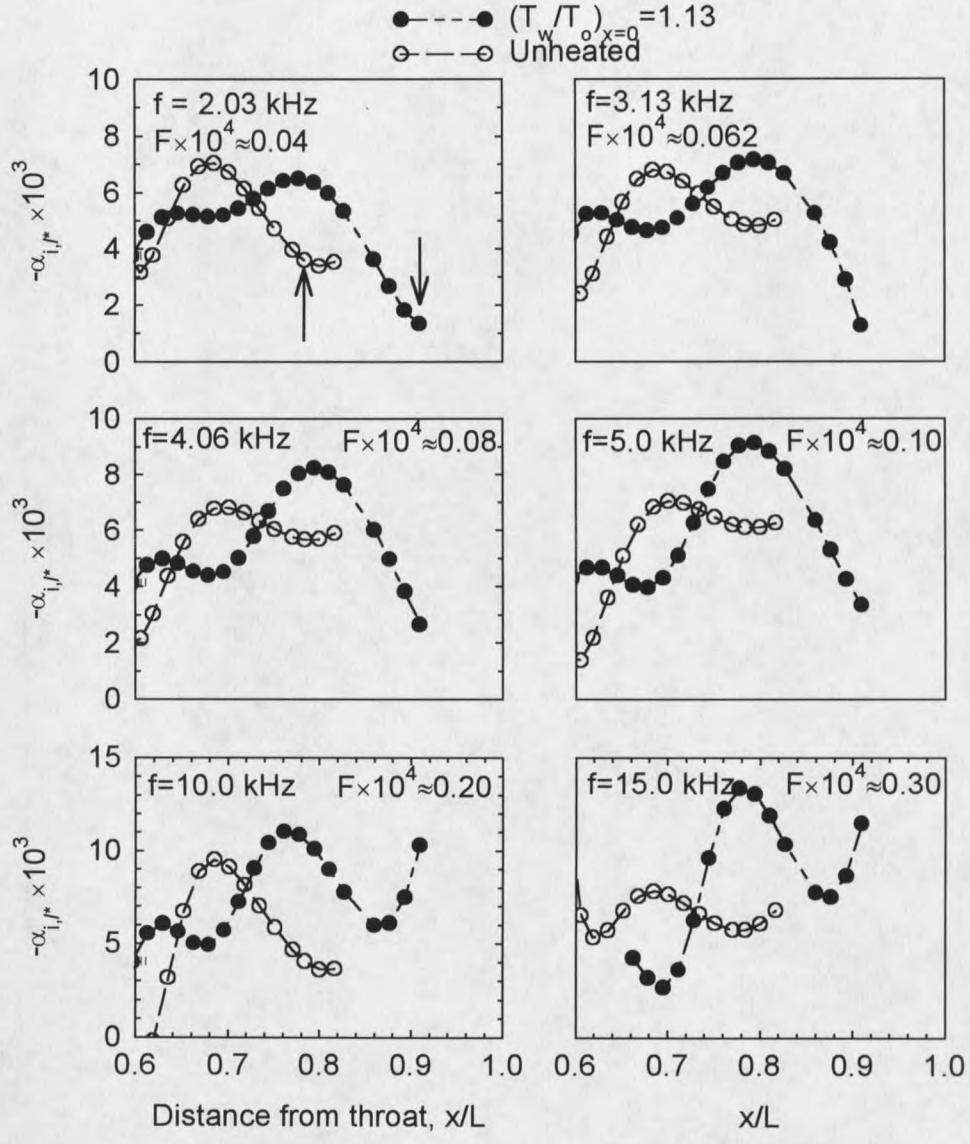

Figure 5-22. Comparison of spatial amplification rates based on u'_{rms} at selected Fourier components. $Re'_{\infty}=5.2\times10^6$/m with and without surface heating. Spatial amplification rates nondimensionalized with viscous length scale l^*.

CHAPTER 6

DISCUSSION

6.1 Comparison of Theory and Experiment

The approach to understanding the mechanisms by which surface heating influences the MSU-SWT supersonic nozzle boundary layer has been to explore the effects of heating at two different Re'_{∞}, and wall heating levels, characterized by the throat temperature, $(T_w/T_o)_{x=0}$. In the unheated condition, the transition map (shown in Figure 2-3) illustrates two fundamentally different states of the boundary layer on the contoured surface for P_o=500 mmHg, and P_o=595 mmHg. At P_o=500 mmHg, "the map" describes a transition process occupying a majority of the nozzle that involves the inception, growth, and break-down of unstable waves. At P_o=595 mmHg, these instability events are not present *in the nozzle*; turbulent bursting is initiated at the throat, and the boundary layer is "densely intermittent" over the entire nozzle length.

6.1.1 Unheated Nozzle Surface

The present measurements with an unheated surface condition also confirm the events of Figure 2-3 and add quantitative details.

The LST calculations, which describe the tendency of isolated infinitesimal disturbances of a prescribed form to grow or decay, do not portray this same picture.

Corresponding to the small (20%) change in Re'_∞ (or P_o) over the range $5.2\times10^6<Re'_\infty<6.2\times10^6$/m, relatively small changes in the stability of the nozzle boundary layer on the contoured surface are predicted. Linear stability theory shows a Görtler instability that forms in the concave region of the nozzle and TS modes that first become unstable near the nozzle exit. Obviously, this cannot explain the observed transition at $Re'_\infty=6.2\times10^6$/m that begins at the throat, far upstream of the nozzle inflection point. The conclusion that follows is that transition on the nozzle at $Re'_\infty=6.2\times10^6$/m (i.e. P_o=595 mmHg) "bypasses" the linear regime altogether, and follows directly from non-linear events and/or spontaneous bursts of turbulence. These "non-linear events" can include a response of the boundary layer to finite amplitude disturbances, roughness, mode interactions, small three-dimensionalities in the mean-flow, and influence of unsteadiness in the corner flow and the boundary layer on the sidewalls. None of these features are modeled in the linear theory. We will return to the discussion of bypass transition later in Section 6.2.1.

At $Re'_\infty=5.2\times10^6$/m, the linear stability theory does not appear to explain *transition* events through an N-factor correlation based on a low-disturbance environment. Correlating the present LST predictions for steady Görtler vortices (Figure 4-13) to the measured transition location, $x_T/L=0.8$ (x_T=30.8 cm) produces a maximum N-factor at transition of $N_T=4.84$. This value falls in the range of $3.5<N_T<7.2$ (with Re'_∞ from 15×10^6/m to 10×10^6/m) determined by Chen et al. (1985) for the Langley Mach 5 slow-expansion nozzle used in the nozzle heating experiments of Harvey et al. (1975a). Correlations were based on LST for Görtler vortices correlated to boundary layer

transition data determined with mean-flow sensors (Harvey et al. 1975a, Stainback et al. 1974, Harvey et al. 1975b) for the unheated nozzle surface condition. The N-factors in this Mach 5 nozzle and the MSU nozzle are below the generally accepted N-factor criteria of N_T=7.5 (Schneider 1998a, Chen et al. 1991) for modern quiet nozzle design. Chen et al. (1985) argue that the low N_T correlations for the slow expansion Mach 5 nozzle are biased by the presence of "finite" disturbances in the boundary layer past the nozzle throat, and are therefore not appropriate for correlations in a low-disturbance environment. The finite disturbances were assumed to exist because the nozzle did not have boundary layer bleed slots to provide a "clean" boundary layer at the nozzle throat. The MSU nozzle also does not have boundary layer bleed slots.

Another feature of the Re'_∞=5.2×10^6/m case that has not been predicted by LST is the observed unsteady wave-form growth at 2-4 kHz that is apparently responsible for the observed transition on the contoured nozzle surface. The steady Görtler vortices, by definition, do not have a fluctuating component, and TS modes are not predicted to occur in the nozzle. Thus, within the framework of LST, the only means by which a fluctuating component could be generated is with the unsteady Görtler instability. But, Figure 4-15 shows that the growth of steady vortices would be predicted to dominate over the unsteady vortices. Moreover, the 2-4 kHz "center-frequency" would not be expected by LST, given a white-noise background of sufficiently low amplitude. Otherwise, unsteadiness would be required to come by non-linear processes, such as the break-down of Görtler vortices (Swearingen and Blackwelder 1987), or mode interaction between TS and Görtler vortices (for example Herbert & Morkovin 1980, Nayfeh 1981, Nayfeh and

Al-Maaitah 1987, Malik and Hussaini 1990), neither of which can be predicted by a linear theory.

6.1.2 Heated Nozzle

When surface heating is applied, concentrated at the nozzle throat, the observations of boundary layer instability and transition change dramatically. At Re'_∞=6.2×10^6/m, a heating level of $(T_w/T_o)_{x=0}$=1.22 suppresses both the turbulence and the 2 kHz unstable waveform; at the first measurement station (x/L=0.56), the peak Fourier component is reduced by an order of magnitude, and the wide-band rms signal in the layer approaches that of the free-stream. With the lower heating levels at $(T_w/T_o)_{x=0}$=1.13 and Re'_∞=5.2×10^6/m, a reduction of unsteady activity is also apparent. However, Figure 5-19 illustrates that the peak Fourier component at the first measurement station (x/L=0.56) is only reduced by 25% (in p_p'). A 35% reduction in the velocity fluctuations is estimated. The lower p_p' fluctuations near the nozzle exit also reflect the slightly lower amplification rates from 0.56<x/L<0.72 (recall Figure 5-21). The velocity fluctuations show a similar trend (Figure 5-22), but the decrease in amplification rates at x/L<0.72 is smaller. Collectively, the results at Re'_∞=5.2×10^6/m, show that (1) the disturbance amplitude has been reduced by some mechanism at x/L<0.5, and (2) changes due to events in the latter half of the nozzle with surface heating are not dramatic i.e. the reduction in the initial amplitude propagates through the entire nozzle.

The LST predictions, in comparison to the experiment, show only small changes in the Görtler instability on the nozzle boundary layer with surface heating, primarily due to

the large differences between the experiment and theory in the unheated cases. Indeed, the progression of power spectra with surface heating at Re'_∞=5.2×10^6/m in Figure 5-16 and Re'_∞=6.2×10^6/m in Figure 5-17, are qualitatively very similar.

As in the unheated cases, the only mechanism in the framework of LST, that could produce the unsteady fluctuations are the traveling Görtler vortices. Figure 6-1 compares some selected Fourier modes from the experiment (Figure 5-21), and the theory for the traveling Görtler vortices with and without surface heating. The theoretical curves were computed with the e^{MALIK} code by specifying a fixed dimensional spanwise wavelength λ_z*=0.255 cm (i.e. spanwise wave-number β*=24.6 cm^{-1}), fixed dimensional frequency f, and marching the quasi-parallel flow solution in the streamwise direction. The neutral point occurs shortly after the nozzle inflection point at x/L=0.25 (illustrated with an arrow), amplification peaks near the point of maximum curvature then decays as the surface flattens out with decreasing curvature. As the frequency increases, the amplification rates computed with the theory decrease monotonically, as demonstrated earlier in the "spectrum" of unsteady Görtler modes (Figure 4-15). The amplification rates determined from the MEP recordings show a trend that is very similar to the theory at low frequencies. However, this similarity is inconclusive and may be fortuitous, since the Görtler instability is inherently non-linear. The fact that amplification rates start low at x/L=0.6 and rapidly increase suggests that a mechanism not included in the linear theory has initiated the measured unsteadiness.

The linear theory also cannot offer any indication as to why there is a clear "center-frequency" at F×10^4=0.04 (f=2 kHz), since the LST shows the steady modes should be

more amplified than unsteady modes. The answers from theoretical predictions regarding the 2 kHz center frequency lie in the receptivity problem and non-linear processes.

6.1.3 Steady Disturbances

It should also be noted that the neither the presence of *steady* Görtler vortices nor their response to heating have been established in the present experiments. Though steady vortices have been observed on supersonic nozzles (Beckwith and Holley 1981), there is no reason to preclude traveling modes from being superimposed on the steady flow-field. For example, Deyhle and Bippes (1996) show measurements from crossflow vortices, (which have similarities to the Görtler problem) that show both steady and unsteady modes. The relation between steady and unsteady modes is ultimately related to the initial conditions, and external disturbances. However, very little work has been done on the receptivity problem (numerically or by experiment) for Görtler vortices in either compressible or incompressible flow. In the crossflow instability, the traveling modes appear to be related to higher free-stream turbulence, whereas the stationary modes are strongly dependent upon streamwise vorticity (e.g. induced by three-dimensional roughness) (Reibert and Saric 1997, Saric 1998). The streamwise vorticity pattern of the steady and unsteady Klebanoff modes also share similar properties (Goldstein et al. 1992, Westin et al. 1994).

6.2 The Relation of Heat-Transfer to Instability and Transition Suppression

The experiment and theory collectively demonstrate that there are two paths to delaying transition in the boundary layer developing over the contoured surface of a

supersonic nozzle. Referring back to Morkovin's "Roads to Wall Turbulence" (shown Figure 1-1), transition can follow from a process that begins with the growth of small disturbances described by linear stability theory, or from a "bypass" mechanism that skips over the linear development. The boundary layer receptivity and disturbance environment will dictate the path of transition from a laminar to turbulent flow. The receptivity and environment also influence the extent of linear growth and the non-linear processes prior to breakdown to turbulence. This section presents physical arguments to demonstrate mechanisms that could be responsible for delayed transition by surface heating. Mechanisms related to the disturbance environment are first considered, followed by mechanisms related to linear stability theory.

6.2.1 Effect on Receptivity and Bypass

Receptivity and bypass are concerned with how the disturbance environment interacts with the boundary layer upstream of the neutral point of some instability. Here, the disturbance environment is taken to include input from all boundaries: surface roughness at the wall, initial disturbances at the inception of the boundary layer, and unsteady fluctuations at the boundary layer edge. At Re'_∞=5.2×10^6/m, the region of interest for discussing receptivity and bypass is upstream of the nozzle inflection point since disturbances are stable prior to this point according to both experimental measurements and LST predictions. The observed transition at Re'_∞=6.2×10^6/m shows the bypass region is in the subsonic approach upstream of the nozzle throat.

The spatial extent of surface heating is limited only to the nozzle block, so that the heating cannot have an effect upstream of the two-dimensional contraction. In addition,

since the heat penetrates the fluid from the wall, the observed differences in stability and transition must be due to changes only in the boundary layer, not the external disturbance environment. The mean-flow calculations have shown (in Figure 4-6 and 4-7) that surface heating changes the hydrodynamic (U/U_e) profile by a small amount in comparison to the thermal profile (T/T_e). This strongly suggests that changes through the layer can be confined to those properties related to the static temperature T, i.e. density $\rho \sim T^{-1}$, and viscosity $\mu \sim T^{0.7}$.

As already illustrated in Figure 4-10, the increase in kinematic viscosity at the wall ν_w ($=\mu/\rho$, proportional to $T_w^{1.7}$) reduces the roughness Reynolds number Re_k. In roughness controlled (i.e. bypass) transition on the windward side of blunt bodies, Reda (1981) has shown that transition can be correlated to a single value of $Re_k \sim 150$.[6] For transition that is controlled by surface roughness, one would therefore expect wall heating to move transition onset downstream commensurate with a decrease in the local influence of surface roughness characterized by Re_k. Demetriades (1981b, 1992a) has shown the convincing similarities in the flow through the nozzle throat and that over the windward side of a blunt body, in regard to both roughness and wall cooling.

Here, it is relevant to note that the blunt body correlation described by Reda (1981), for example, and the Langley $Re_k < 12$ criteria involve different physics. The former follows from *bypass* transition that occurs via turbulence generated at the tips of the

---

[6] Correct application of Reda's correlation requires that k is based on the arithmetic average of the physical peak-to-valley roughness height. This is a different definition for k than is used in the rest of the text but all qualitative features discussed herein are the same.

roughness elements. The latter describes a *receptivity* process that introduces small, but finite disturbances into the layer. These disturbances provide the "initial conditions" for some primary instability that becomes unstable downstream, without the input disturbances associated with the roughness being unstable themselves. The steady instabilities (crossflow, Görtler, Klebanoff modes) appear to show an extreme sensitivity to roughness since the steady streamwise vorticity generated by the roughness elements has a direct input to the disturbance. For example, Saric et al. (1998) have shown, at low-speeds, that the linear and non-linear growth of steady crossflow vortices (which have many similarities to the Görtler vortices) can be controlled with micron-sized roughness elements on the order of $Re_k \sim 0.1$. The receptivity problem at high-speeds is poorly understood, especially for a complex boundary layer like that of the supersonic nozzle. What is important to note for instability and transition in the MSU-SWT, is that while there is still a great deal of uncertainty for any threshold value of Re_k, the measured roughness yields a maximum $Re_k < 0.2$, even without surface heating. This is nearly two orders of magnitude below the Langley criterion. We will return to this point again in a moment.

The density variations over the heated convex surface can also produce a stabilizing effect. By the same arguments that concave curvature is destabilizing, convex curvature is considered to have a stabilizing effect (Van Driest 1975, Malik and Poll 1985). When variations in density ρ, are neglected, the centrifugal stability or instability of an inviscid parallel flow can be described by the well-known Rayleigh circulation criterion, which is:

$$\frac{d(rU)^2}{dr} \begin{cases} < 0 & unstable \\ > 0 & stable \end{cases} \qquad \textbf{6-1}$$

where r is the radial coordinate. Lees (1958) first derived the corresponding condition for compressible flows to show that density variations can be properly included by replacing $(rU)^2$ by $\rho(rU)^2$ in equation 6-1. Upon dividing by $\rho(rU)^2$, the result is:

$$\left[\frac{1}{\rho}\frac{d\rho}{dr} + \frac{1}{(rU)^2}\frac{d(rU)^2}{dr}\right] \begin{cases} < 0 & unstable \\ > 0 & stable \end{cases} \qquad \textbf{6-2}$$

If we consider that (rU) is the angular momentum at a point (per unit mass), equation 6-1 states that the flow over a convex surface will be stable if the angular momentum increases in the radial direction. Equation 6-2 adds the result that additional stability will be achieved if the density increases with radial direction (i.e. the "heavier" fluid is at the edge of the layer). Considering that $\rho \sim 1/T$, Figures 4-6 and 4-7, illustrate the increase in the density gradient through the layer with a heated wall, as expected.

The increased stability due to the larger positive density gradient is interpreted as a stronger damping effect on disturbances in the layer as they travel through the throat region; most notably the damping effect acts on streamwise vorticity either due to surface roughness, or due to disturbances introduced or not fully damped upstream of the nozzle throat. The magnitude, modal composition, and streamwise dissipation of these disturbances in the free-stream and boundary layer upstream of the nozzle throat is not known. Beckwith et al. (1973) discuss some issues of this "residual vorticity", but, most

quiet wind tunnels avoid the issue altogether by placing suction-slots (i.e. bleed slots) upstream of the nozzle throat to remove the boundary layer initiated in the contraction.

Last, the general increase of dynamic viscosity ($\mu \sim T^{0.7}$) through the throat region will also increase the viscous dissipation of both steady and unsteady disturbances. Beckwith et al. (1973) consider this point through the "acceleration parameter" [$=(\nu_w/U_e^2)(dU_e/ds)$], which combines the damping effects of both pressure gradient and viscosity.

It is also significant that the damping effect of both the density gradient and viscosity have the strongest effect at the throat. There, the boundary layer is the thinnest, so that density gradients are enhanced, and the static temperature is much higher than in the supersonic region. Also, the thermal conductivity ($\sim T^{0.7}$) will be larger at the throat, so that the heat can penetrate the layer much more effectively in the throat region, than in the supersonic region.

6.2.2 Effect on Growth of Infinitesimal Disturbances

Linear stability theory coupled with the e^N method for transition prediction has been the method of choice for quiet nozzle design. Despite the lack of detailed and direct measurements of the steady and/or unsteady disturbances in the boundary layer that actually lead to the onset of transition on a nozzle wall, the LST/N-factor approach to quiet nozzle design has been successful in most instances. Relevant parametric studies with surface heating rely heavily on the (interdependent) assumptions that (1) LST correctly models the physics leading to transition in a particular nozzle, and (2) a single calibrated value of N for a given nozzle geometry applies equally with and without

surface heating. In the MSU-SWT, direct measurements show that neither of these assumptions strictly hold for the boundary layer on the nozzle contoured surface. However, since the LST/*N*-factor approach with surface heating may work well in other facilities, the calculations for the MSU-SWT nozzle may provide some guidance for future nozzle design, optimized heating patterns, and adaptation of existing facilities. To this end, the reader is also referred to the recent Mach 6 nozzle design by Schneider (1998a), where a much more complete parametric study of surface heating with LST in an axisymmetric geometry is provided.

In the MSU-SWT, steady Görtler vortices showed very small effects of increased wall temperature on the vortex growth rates. This is in agreement with the findings of Spall and Malik (1989) who also concluded that "for all practical purposes, wall heat transfer has a negligible effect on the growth of Görtler vortices..." (Spall and Malik 1989, p. 1829).

The effect of heat on the "traveling" Görtler modes ($F\neq0$) at higher frequencies ($F\times10^4>0.1$) was found to be destabilizing, in opposition to the trend computed for steady vortices (i.e. $F=0$). This result illustrates the very different mechanisms driving instability growth for steady and unsteady instabilities. The steady vortex pattern arises from the dynamical effect of rotation, therefore viscosity does not contribute to the instability itself, but acts as a source of dissipation. For a temporal instability, however, the production of disturbance energy is proportional to viscosity by the integral of the Reynolds stress through the layer (Prandtl 1934; quoted in Mack 1984). The result, in a

simplified view, is that viscosity has a general destabilizing influence that outweighs the viscous dissipation.

While the subtle relations between the steady and unsteady Görtler modes is interesting, the LST/*N*-factor approach uses only the most amplified mode to compute the *N*-factor. Therefore, in terms of nozzle design, the steady Görtler vortices are considered more important than their unsteady counterpart. When non-linear effects are considered, with mode interactions, the same relative importance of steady and unsteady Görtler modes may not hold.

The heating relation on the first-mode TS instability is somewhat more complicated with variable wall temperature. It is possible to have a temperature distribution with heating concentrated in the nozzle throat that notably stabilizes TS modes near the nozzle exit. The calculations of Chapter 4 showed that this was even possible over an adiabatic surface that followed the upstream heating. In the $Re'_\infty=6.2\times10^6$/m case, the *N*-factor was reduced by 28% at almost two times the nozzle length ($x/L=1.94$). In much larger, slow-expansion nozzles, this could have a major impact on the nozzle design if a fixed value of N_T is used as the transition criterion.

6.3 Comparison to other facilities

6.3.1 Summary of Transition Delay

Table 6-1 shows a comparison of results for the three facilities which have published transition data for nozzle-wall boundary layers in connection with surface heating or cooling. The overall measure of the effect of surface heating or cooling is characterized

by the ratio of transition Reynolds number based distance from the throat and conditions at the design Mach number with and without surface heating. Two primary methods for determining transition on the nozzle walls have been employed. Either (1) the probe is held at a fixed x-position and the unit Reynolds number Re'_∞ is varied with P_o and/or T_o, or (2) the stagnation conditions are fixed and the streamwise position x is varied. Since transition on the nozzle walls cannot be described uniquely by the length Reynolds number (or any single parameter for that matter) some quantitative differences between the two techniques are expected.

All observations of the increase or decrease of $Re_{x,T}$ with surface heating or cooling in supersonic and hypersonic nozzles known to the present author are consistent. In the present work with $Re'_\infty=6.2\times10^6$/m, the ratio of $Re_{x,T}$ with and without surface heating is difficult to define precisely because heating transformed the nozzle boundary layer from all "transitional" to laminar until the first appearance of turbulence bursting at $x_T/L=0.92$. At $Re'_\infty=5.2\times10^6$/m, transition onset was moved from $x_T/L=0.78$ to $x_T/L=0.92$ (Note that $x_T/L=0.92$ may not be representative of the full effect of delaying transition by surface heating at these conditions; the turbulence on the sidewalls may have affected the transition location with surface heating.). In the original throat cooling experiment by Demetriades, the unit Reynolds number Re'_∞ at transition onset was decreased by half when the wall temperature relative to the stagnation temperature (T_w/T_o) was reduced from 0.95 to 0.67. The experiments of Harvey et al. in the Langley Mach 5 slow-expansion nozzle required somewhat higher temperatures at 40% to achieve an increased unit Reynolds number at transition of 20%. The most recent independent observation has

come from the Mach 4 Purdue Ludwieg tube; transition delay is observed when the supply air is heated, thus making the nozzle surface (which is at room temperature) appear cool. The fact all of these measurements point to a consistent trend is especially significant when one considers the differences in geometry and operating conditions between the three facilities.

It is evident that only a small amount of surface heating is required to produce a significant effect on the transition location of the wall boundary layers. None of the experiments summarized in Table 6-1 have attempted to optimize the heating configuration, or surface temperature distribution. If an appropriate theoretical model was available to predict the observed heating effect, the surface temperature distribution could be optimized, and even higher transition Reynolds numbers could be possible on the nozzle walls.

6.3.2 Postulated Mechanisms

The present work has shown (as originally concluded by King and Demetriades 1993), that LST fails to predict the unstable activity in the layer that apparently leads to transition in the MSU-SWT.

In section 6.1, it was argued that transition in the unheated nozzle state was controlled with bypass events at the high-Reynolds number case, and influenced by receptivity events in the low-Reynolds number case. Then, in Section 6.2 physical arguments were presented for those mechanisms by which heating in the nozzle throat could suppress instability and transition in the nozzle wall boundary layer. Now, some

comments are offered on the relevance of those mechanisms to the observed transition delay with surface heating discussed in section 6.1 and summarized in Table 6-1.

The observation of Harvey et al (1975a) at NASA-Langley that transition could be delayed in a supersonic nozzle by heating the walls was rationalized on the basis of surface roughness arguments. First, they concluded that transition was predominantly controlled by three-dimensional roughness in the throat region (i.e. bypass). Then, in view of the transition delay with heating, they postulated that increasing the thickness of the laminar boundary layer effectively made the height of the roughness smaller, thereby decreasing the effectiveness of such roughness in promoting transition. Clearly, this argument cannot explain the transition delay with wall heating observed in the MSU-SWT. Both the computed boundary layer thickness (Figure 4-8), and the measurements by Brogan (1995) show that the boundary layer thickness decreases with surface heating, due to the strong pressure gradient in the nozzle. However, it is noted that the boundary layer thickness can only provide a crude description of the effectiveness of roughness to influence transition. The boundary layer thickness δ is measured at the outer edge of the boundary layer, while the physics of roughness-modified transition appear to be confined to the conditions in the vicinity of the roughness element (Morkovin 1990).

A much stronger statement of the roughness influence in the boundary layer is given by the roughness Reynolds number Re_k, as described earlier in Section 6.2.1. The nozzle roughness studies at Langley (Beckwith et al. 1988, Chen and Malik 1990) imply that transition on supersonic nozzles is independent of surface roughness when $Re_k<12$ in the nozzle throat. But, again, transition in the MSU-SWT does not appear to be roughness

related since the magnitudes of Re_k are less than 0.2 for all conditions tested (recall Figure 4-10).

Measurements during the 1978-1981 time-frame in the MSU-SWT by Demetriades (1978, 1981a, 1981b, 1992a) had also shown that transition in the throat had a very weak sensitivity to small roughness. Therefore, in the absence of a plausible argument by roughness effects, the nozzle heating experiments by Demetriades in 1992 (published 1996) were rationalized with a "natural cooling" argument along the lines of Masad and Nayfeh (1992) (recall Section 1.2.3 and 4.2.2). However, the calculations in the present work show that with a similar setup, the measured temperature distributions predict a positive heat-flux (Figure 4-5) into the boundary layer at all streamwise locations. Therefore, the natural cooling mechanisms are not operating in the MSU-SWT. Furthermore, by the arguments of Section 6.1, the primary effect of surface heating appears to occur in the throat region, where the boundary layer is without question subject to strong heating. Also, it is significant that a uniform temperature distribution was used to heat the Mach 5 Langley nozzle, which would eliminate the possibility of natural cooling. Harvey et al describe the arrangement: "The nozzle wall was heated by strip-type heaters wrapped around the exterior surface of the nozzle. A layer of insulation was then applied to the whole strip heater assembly. Wall temperatures up to about 860 °R (478 °K) could be obtained. The interior wall temperature was measured at several locations near the exit and assumed uniform along the entire nozzle for each test." (Stainback et al. 1974, p.16)

In the apparent absence of an explanation by roughness arguments, and given the failure of LST to predict transition even in the unheated cases, a likely mechanism for transition delay with surface heating is the damping of initial disturbances ingested into the layer through the subsonic approach. In this connection, it is also noteworthy that none of the nozzles represented in Table 6-1 have bleed-slots to remove the boundary layer which forms in the approach section to the nozzle throat. A discussion of the disturbances at the inception of the layer was provided in Chapter 5, Section 4. The stabilizing effects discussed in Section 6.2.2 associated with viscous dissipation, the density gradient, and curvature through the throat region provide a means by which surface heating can damp the "residual vorticity" within the boundary layer. By reducing the disturbance level in the boundary layer prior to the neutral point, instabilities are not prematurely excited and bypass mechanisms are avoided. The linear theory completely ignores the role of initial conditions and the external environment on the transition process. Yet, both theoretically and experimentally, the evidence is overwhelming that the non-linear stages of the instability leading to turbulence are highly dependent upon the initial conditions.

Other possibilities of the surface heating mechanism could be found in non-linear processes related to the steady Görtler instability (e.g. interaction with TS waves). The MEP and frequency band of the measured dominant instability (particularly at Re'_{∞}=5.2×10^6/m) show similarities to first-mode TS waves which are predicted to occur near the nozzle exit. However, there is simply not enough information in the present data set to identify this relation as any more than coincidence.

The corner flows also represent a possible source of instability that has not been specifically addressed in any of the MSU-SWT nozzle studies. When the lower nozzle block is heated, the corner flow will be bounded by a hot wall on the horizontal surface, and by a cold wall on the vertical surface. There are no studies known to date (i.e. 1998) that describe the mean-flow or stability of such a flow either experimentally or theoretically.

As a final note, this same perplexity of delaying transition by surface heating has been observed in the transition over blunt bodies (whose wind-ward flow has common points to nozzle flow). The most relevant of these studies seems to be that of Cooper and Mayo (1960). Some 38 years ago, they commented on this finding that heat, rather than cooling, was experimentally observed to delay transition in the forward region on a blunt body traveling at supersonic speeds:

> "This idea has been postulated before, and each time the suggestion of such a phenomenon has been sufficient to initiate discussion pro and con. The primary objection is usually an intuitive one – such an occurrence is contrary to the cooling effect in the classical flat-plate stability theory. Furthermore, there is no satisfying theoretical basis to prove that such a phenomenon should occur on blunt bodies. In each experimental case a plausible argument can be advanced that roughness effects, rather than a new transition phenomenon, cause the observed occurrences.... Yet [the results] indicate that roughness does not appear to be a dominant factor in causing transition from turbulent flow to laminar flow as the body is warmed..." (Cooper and Mayo 1960)

It would appear that we have progressed only a small amount in this matter, which serves to illustrate the extreme complexity in transition from laminar to turbulent flows and the need for more study.

6.4 Suggestions for Future Work

6.4.1 Theoretical Predictions

The linear stability predictions for the nozzle contoured surface are complete as they stand. Convergence and numerical accuracy of the solutions have been thoroughly addressed.

Predictions for the Görtler instability have used the "normal-mode" solution, neglecting the terms due to boundary layer growth. Several researchers have shown that these assumptions can lead to large errors at the low growth-rates encountered near the neutral stability point (El-Hady and Verma 1983, 1984, Hall 1988, Day et al. 1990). The experimental evidence (Floryan 1991) also shows that the Görtler problem is inherently non-linear, which limits the validity of any linear theory to the initial stages of growth. Accordingly, the Görtler solution, particularly for the eigenfunctions, could be improved with a parabolic marching solution (Spall and Malik 1989) or with non-linear PSE (Herbert 1993, 1997).

With the failure of the linear theory, and the multitude of non-linear paths to transition that are possible, it is doubtful that one would have success applying a non-linear theory without additional guidance and quantitative details from experiments.

The present experiments demonstrate that events which occur in the throat region are key to understanding the effects of surface heating, even in the apparent absence of influence by surface roughness. Therefore, concentration on receptivity to internal and external disturbances in the throat region could present a fruitful area of research with numerical tools. For example, one could do a simple numerical experiment with PSE by inserting a disturbance in the form of streamwise vorticity (e.g. Klebanoff mode) into the layer and seeing how the disturbance damps with and without surface heating. This would be a significant step toward solidifying or rejecting the heuristic arguments presented in Sections 6.1, 6.2, and 6.3 – apart from the "stability" issues in the latter half of the nozzle.

6.4.2 Experimental Measurements

A number of improvements could be made to the existing experimental measurements. The signal-to-noise ratio should be improved by an order of magnitude so that free-stream disturbances can be accurately measured along with boundary layer unsteadiness. This would also allow the experimenter to measure the growth of the instability starting at or upstream of the neutral point. The instrumented overlay used in the present experiments should be eliminated to avoid any uncertainties associated with a modified nozzle surface. Accurate mean-flow measurements should be acquired for the conditions of the present experiment to allow a quantitative interpretation of the DPP recordings presented herein. The mean-flow measurements would also accurately locate the MEP relative to the boundary layer thickness. The disturbance environment should be measured in the subsonic approach, preferably decomposed into acoustic (p'/P) and

vorticity (u'/U) modes. As discussed in detail through the introduction, these disturbances provide the boundary conditions for the stability experiment. Without knowledge of these conditions, one of the major independent variables of the problem is left unspecified, and the applicability and relevance to any other environment is uncertain.

The LST calculations indicate that steady Görtler vortices are likely to occur on the contoured surface. Therefore, it would be beneficial to measure the growth (or absence) of steady perturbations in the spanwise direction. This could be accomplished with mean-flow measurements at fine span-wise increments, and oil-flow techniques.

If a comparison with theory and experiment is required to validate the predictive capabilities of a theory, then a more detailed set of "validation" experiments should be conducted. Saric (1990), Saric (1993), and Haynes et al. (1996), set forth precepts for such experiments.

The effect of heating on the sidewall has also not been tested to date. The sidewall has a highly three-dimensional boundary layer (King and Demetriades 1993, Demetriades et al. 1994, Alcenius et al. 1996, Demetriades et al. 1998) with different stability mechanisms (Alcenius et al. 1996) than the contoured surface. The surface heating technique in a two-dimensional tunnel can only be successful toward increasing $Re_{\Delta x}$ if transition on *all 4 walls* is delayed.

$(Re_{x,T})_{heat}/(Re_{x,T})_{unheat}$	T_w/T_o	Transition Detection	Design Mach No	Nozzle Configuration	Source
>2 (variable x)	1.22 @ x=0	MEP Pitot*	3	2D	Present
1.2 (variable x)	1.13 @ x=0	MEP Pitot*	3	2D	Present
0.5 (variable P_o)	0.67 @ x=?	MEP Hot Wire*	3	2D	MSU-SWT, (Demetriades 1992a)
1.2 (variable P_o)	1.4, uniform	Pitot profile / Radiated signal	5	Axisymmetric	LaRC M5 POC, (Harvey et al 1975)
0.85 (variable P_o)	0.85, @ x/L=0.6	Radiated signal	4	2D	Purdue Ludwieg Tube, (Schneider 1997)

*Measurement recorded on lower contoured surface

Table 6-1. Comparison of heat transfer effect between three facilities.

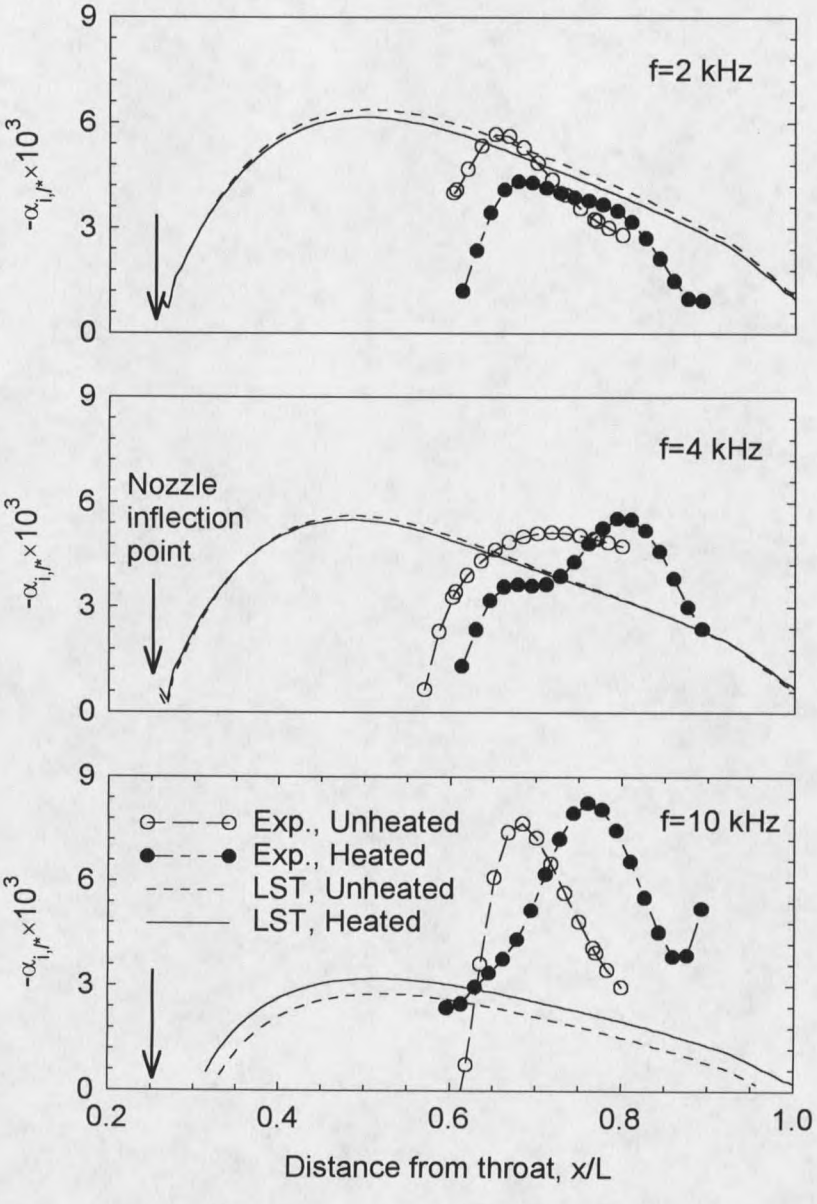

Figure 6-1. Comparison of spatial amplification rates ($-\alpha_{i,f^*}$) between the experiment and linear stability theory (LST) for traveling Görtler modes at $Re'_\infty=5.2\times10^6$/m with and without surface heating. Heated condition is $(T_w/T_o)_{x=0}=1.13$.

CHAPTER 7

CONCLUSIONS

The goal of the present study was to investigate the effects of surface heating on the stability and transition of a supersonic nozzle boundary layer. The study was restricted to the boundary layer on the lower contoured surface in the Mach 3 two-dimensional nozzle of the supersonic wind tunnel at Montana State University. Two different tunnel conditions were chosen to generate two distinct states of the boundary layer with an unheated surface. (a) The first condition was selected as a "stability" case (i.e. pre-transitional) with $Re'_\infty=5.2\times10^6$/m that exhibited unsteady properties leading to transition onset. (b) A higher $Re'_\infty=6.2\times10^6$/m case was selected as a transitional/turbulent case with dense intermittent bursting along the entire nozzle length.

The boundary layer was then heated from the wall to explore changes in the boundary layer stability and transition associated with surface heating. The surface temperature at the nozzle throat was $(T_w/T_o)_{x=0}=1.13$ for the stability case at $Re'_\infty=5.2\times10^6$/m, and $(T_w/T_o)_{x=0}=1.22$ for the transitional case at $Re'_\infty=6.2\times10^6$/m. The stability of the boundary layer for conditions (a) and (b) with and without surface heating was computed with linear stability theory for first-mode Tollmien-Schlichting, and Görtler instabilities. Measured surface temperature distributions were used in the calculations. Unsteady fluctuations were also measured over the latter half of the nozzle

from $0.56<x/L<0.95$, where x is the distance from the throat and L is the total nozzle length. The following conclusions have been drawn from the present work:

The present experiments have shown that the effect of surface heating for the low Reynolds number (stability) case has been to reduce the amplitude of a low frequency disturbance at all streamwise positions. The lower disturbance amplitudes in the latter half of the nozzle appear to come first by a reduction in the disturbance amplitude at $x/L<0.5$, and second by a small decrease in the growth rates from $0.5<x/L<0.7$. Suppression of this low frequency activity caused turbulent bursting to be moved downstream, thereby increasing the extent of laminar flow to nearly the entire nozzle length. When heat was applied, no significant shift in the center frequency of the unsteady oscillations occurred.

At high stagnation pressures, the heating effect was powerful enough to quench a dominant low frequency ($F\times10^4=0.04$, f=2 kHz) oscillation and the turbulence that began at the nozzle throat. This was accomplished with a throat temperature that was only 22% over the stagnation temperature. Surface heating concentrated in the throat reduced the fluctuation magnitudes (wide-band $p_p'_{,rms}/P_o$) at the first measurement station x/L=0.54 by an order of magnitude from 3.3% to 0.35%. For all streamwise positions, the fluctuation levels at $Re'_\infty=6.2\times10^6$/m with heating were the same or even less than those of the heated, $Re'_\infty=5.2\times10^6$/m case. Apparently, the higher heating level compensated, and possibly overcame, the increase in Reynolds number.

Linear stability theory failed to predict transition in the nozzle boundary layer according to an N-factor correlation based on observed transition in other low-

disturbance wind tunnels (as originally shown by King and Demetriades 1993). In comparison to the experiment, the linear stability predictions showed a much smaller effect of heating on the stability of the boundary layer. Heat had a mild stabilizing effect on steady Görtler vortices and a destabilizing effect on unsteady Görtler modes. Though first-mode Tollmien-Schlichting waves were stable until x/L=0.90, the calculations showed that they could be further stabilized at x/L>0.9 by concentrating heating in the nozzle throat. Additionally, the calculations showed that this stabilization was achieved in the presence of a positive heat-flux over the entire nozzle length (x/L<1), and an adiabatic condition beyond the nozzle exit (x/L>1).

Calculations of the mean-flow showed a positive heat flux at all streamwise locations. Therefore, the decrease in unsteady activity could not have come by a "natural cooling" mechanism. Calculations showed that roughness Reynolds numbers decrease with surface heating. However, all Re_k were calculated at less than 0.2, using a measured maximum peak-to-valley height. Therefore, roughness arguments do not appear to explain the observed transition delay either.

Clearly, the experiment and theory have shown at least two different paths to turbulence suppression by heating the surface of a supersonic nozzle. (1) The experiment demonstrates that heat suppresses a bypass mechanism triggered by receptivity events near and possibly upstream of the nozzle throat. Decreasing the "initial conditions" for the stability problem, in turn, causes the transition location to be moved downstream. (2) The computations show that a proper heating distribution can also be used to suppress the growth of linear instabilities in the nozzle if bypass were not present.

The similarity of the two Reynolds number cases (Re'_∞=5.2×10^6/m and 6.2×10^6/m) when heat is applied suggests that heating the nozzle throat has reduced both cases to a stability dominated transition path, compared to a bypass dominated path in the unheated condition. However, this can only be considered speculation without more measurement.

APPENDICES

APPENDIX A

DOCUMENTATION FOR ANALOG TAPE RECORDINGS

DOCUMENTATION FOR ANALOG TAPE RECORDINGS

This appendix contains the documentation for the analog tape recordings for the MEP data reported herein. The recording circuit and conduct of the experiment are documented and described in Chapter 5 (Experimental Measurements). In the following tables, the "Record Number" is composed of the tape number and a recording index, where the recording index starts at 01 and increments by 1 for every continuous interval of valid data (identified by the 20 kHz tone). The corresponding location on the tape is noted with the lineal footage at the start and end of a data record. Information regarding the temperature record is also provided (filename and time at recording).

Tape #239a, MEP recordings

Settings

Recorded by: T. Brogan
Recording date: 4/6/94
Record Speed: 120 ips
CH. 3: DPP Signal (amplified)
CH. 5: y-voltage
CH. 7: Tone (1Vrms @ 20 kHz real time)
Temperature Record: DPP2.DAT (1 - 29)

Tunnel Conditions

P_o: 500 mmHg
T_o : 21 °C
Screen (320 mesh): YES
Nozzle Condition: Unheated
$(T_w)_{x=0}$: 15.5 °C

DPP Conditions

Transducer: Kulite CQ-030-100D
S/N: 419-6-34
DPP Sensitivity: 1.50 μV/mmHg/Vdc (pre-amplified, from manufacturer)
Excitation Voltage: 3.15 VDC (Dry Cell batteries)
DPP Amplification: 3640 V/V
Amplifier: 027307U Differential Amp. + HP 465A

Record Number	Start (ft)	End (ft)	T_{throat} (°C)	Time on T_w Record (min)	DPP Vrms				x (cm)	y (cm)
					Recorded (@120 ips)	Playback (@3.75 ips)	Digital (tot.)*	Digital (clean)**		
239-04	379	501	15.1	8.0	0.36	0.43	0.365	0.351	36.53	0.180
239-05	501	621	15.1	12.0	0.34	0.39	0.336	0.321	35.89	0.170
239-06	621	747	15.1	15.1	0.325	0.38	0.319	0.303	35.26	0.171
239-07	747	867	15.1	17.0	0.31	0.36	0.304	0.287	34.62	0.169
239-08	867	991	15.1	21.0	0.29	0.34	0.286	0.267	33.99	0.165
239-09	991	1115	15.1	25.0	0.28	0.32	0.267	0.247	33.35	0.175
239-10	1115	1237	15.2	30.0	0.265	0.3	0.250	0.228	32.72	0.179
239-11	1237	1369	15.2	36.0	0.25	0.29	0.238	0.215	32.08	0.174
239-12	1369	1498	15.3	39.0	0.24	0.27	0.221	0.196	31.45	0.178
239-13	1498	1627	15.2	41.0	0.225	0.26	0.212	0.185	30.81	0.170
239-14	1627	1750	15.2	45.0	0.22	0.25	0.199	0.171	30.18	0.175
239-15	1750	1888	15.2	47.0	0.21	0.23	0.188	0.158	29.67	0.173
239-16	1888	2007	15.3	53.0	0.21	0.23	0.183	0.152	29.54	0.153
239-17	2007	2147	15.3	56.0	0.2	0.22	0.172	0.138	28.91	0.165
239-18	2147	2274	15.2	60.0	0.195	0.21	0.164	0.129	28.27	0.165
239-19	2274	2405	15.3	70.0	0.18	0.19	0.155	0.117	27.64	0.162
239-20	2405	2537	15.3	73.0	0.185	0.18	0.142	0.099	27.00	0.163
239-21	2537	2658	15.4	77.0	0.175	0.18	0.137	0.092	26.37	0.159
239-22	2658	2778	15.4	91.9	0.17	0.17	0.131	0.083	25.73	0.165
239-23	2778	2901	15.4	96.9	0.165	0.17	0.127	0.077	25.10	0.163
239-24	2901	3022	15.5	101.9	0.165	0.16	0.123	0.071	24.46	0.154
239-25	3022	3142	15.5	104.9	0.16	0.16	0.123	0.068	23.83	0.147
239-26	3142	3272	15.6	110.0	0.16	0.16	0.118	0.062	23.32	0.146
239-27	3272	3392	15.8	115.9	0.16	0.16	0.119	0.061	23.19	0.147
239-28	3392	3518	15.7	120.9	0.16	0.16	0.116	0.059	22.56	0.145
239-29	3518	3646	15.7	124.9	0.16	0.16	0.115	0.055	21.92	0.134

*DPP total signal from .156 kHz to 320 kHz on integrated spectrum

**Record 239-01 subtracted in the square from DPP total digital signal

Table A-1. Documentation for Analog Data Recordings at MEP, Re'_∞=5.2×10^6/m, Unheated nozzle

Tape #239b, MEP recordings

Settings

Recorded by: T. Brogan
Recording date: 4/6/94
Record Speed: 120 ips
CH. 3: DPP Signal (amplified)
CH. 5: y-voltage
CH. 7: Tone (1Vrms @ 20 kHz real time)
Temperature Record: DPP4.DAT

Tunnel Conditions

P_o: 500 mmHg
T_o : 21 °C
Screen (320 mesh): YES
Nozzle Condition: Heated
$(T_w)_{x=0}$: 60 °C

DPP Conditions

Transducer: Kulite CQ-030-100D
S/N: 419-6-34
DPP Sensitivity: 1.50 μV/mmHg/Vdc (pre-amplified, from manufacturer)
Excitation Voltage: 3.15 VDC (Dry Cell batteries)
DPP Amplification: 3640 V/V
Amplifier: 027307U Differential Amp. + HP 465A

Record Number	Start (ft)	End (ft)	T_{throat} (°C)	Time on T_w Record (min)	DPP Vrms				x (cm)	y (cm)
					Recorded (@120 ips)	Playback (@3.75 ips)	Digital (tot.)*	Digital (clean)**		
239-30	3646	3767	60.9	74.0	0.24	0.29	0.232	0.208	36.30	0.106
239-31	3767	3890	61.0	85.0	0.22	0.24	0.198	0.169	35.66	0.157
239-32	3890	4010	60.2	89.0	0.21	0.22	0.176	0.143	35.02	0.170
239-33	4010	4131	61.1	91.9	0.2	0.22	0.175	0.142	34.39	0.170
239-34	4131	4251	61.0	94.9	0.195	0.22	0.171	0.137	33.75	0.173
239-35	4251	4377	60.0	98.9	0.19	0.21	0.165	0.129	33.12	0.171
239-36	4377	4520	60.0	110.0	0.18	0.2	0.155	0.116	32.48	0.154
239-37	4520	4644	60.9	114.9	0.18	0.19	0.150	0.110	31.85	0.171
239-38	4644	4773	60.8	117.9	0.175	0.19	0.141	0.097	31.21	0.169
239-39	4773	4890	63.4	121.9	0.17	0.18	0.136	0.090	30.58	0.170
239-40	4890	5026	61.1	124.9	0.165	0.17	0.130	0.080	29.94	0.172
239-41	5026	5154	60.6	128.9	0.16	0.16	0.125	0.072	29.31	0.175
239-42	5154	5278	61.1	131.9	0.155	0.16	0.123	0.069	28.67	0.169
239-43	5278	5400	61.2	143.9	0.15	0.16	0.119	0.061	28.04	0.175
239-44	5400	5518	61.2	146.9	0.15	0.15	0.115	0.054	27.40	0.170
239-45	5518	5643	60.3	149.9	0.145	0.15	0.117	0.056	26.77	0.162
239-46	5643	5768	61.1	154.9	0.15	0.15	0.112	0.047	26.13	0.169
239-47	5768	5892	61.1	167.9	0.145	0.15	0.113	0.049	25.50	0.159
239-48	5892	6018	60.5	171.9	0.145	0.15	0.111	0.045	24.86	0.162
239-49	6018	6141	61.2	175.8	0.14	0.14	0.109	0.039	24.23	0.169
239-50	6141	6261	60.9	179.8	0.145	0.15	0.110	0.040	23.59	0.161
239-51	6261	6395	61.3	185.8	0.145	0.15	0.110	0.042	22.95	0.155
239-52	6395	6533	61.1	192.8	0.145	0.15	0.110	0.041	22.32	0.169
239-53	6533	6674	60.2	197.8	0.145	0.15	0.110	0.041	21.69	0.155
239-54	6674	6800	60.8	205.8	0.16	0.14	0.097	0.012	22.32	0.327
239-55	6800	6925	60.8	222.8	0.24	0.27	0.217	0.193	36.29	0.149

*DPP total signal from .156 kHz to 320 kHz on integrated spectrum

**Record 239-01 subtracted in the square from DPP total digital signal

Table A-2. Documentation for Analog Data Recordings at MEP, $Re'_{\infty}=5.2\times10^{6}$/m, Heated nozzle, $(T_w/T_o)_{x=0}=1.13$

Record Number	Start (ft)	End (ft)	Conditions	DPP Vrms				x (cm)	y (cm)
				Recorded (@120 ips)	Playback (@3.75 ips)	Digital (tot.)*	Digital (clean)**		
239-01	0	129	No Flow		0.14	0.1022			
239-02	121	256	F/S, UHT, NSCR		0.13	0.0938		36.80	1.47
239-03	256	379	F/S, UHT, SCR		0.13	0.0943		36.80	1.47
239-56	6925	7106	F/S, HT, SCR	0.16	0.13	0.1012		36.30	3.12
239-59	8070	8202	F/S, UHT, SCR	0.16	0.13	0.0986			
239-61	8704	8850	No Flow		0.14	0.104			

*DPP total signal from .156 kHz to 320 kHz on integrated spectrum
**Record 239-01 subtracted in the square from DPP total digital signal

F/S: Free-Stream Measurement.
UHT: Unheated Nozzle
HT: Heated Nozzle (Circulated Ethylene Glycol)
SCR: Screen @ 2-D contraction installed
NSCR: Screen @ 2-D contraction not installed

Table A-3. Documentation for Analog Data Recordings of Electronic and Free-stream Noise, Re'_∞=5.2×10^6/m Heated and Unheated nozzle

Tape #084, MEP recordings

Settings

Recorded by: T. Brogan
Recording date: 4/8/94
Record Speed: 120 ips
CH. 3: DPP Signal (amplified)
CH. 5: y-voltage
CH. 7: Tone (1Vrms @ 20 kHz real time)
Temperature Record: DPP10.DAT

Tunnel Conditions

P_o: 595 mmHg
T_o : 16 °C
Screen (320 mesh): YES
Nozzle Condition: Unheated
$(T_w)_{x=0}$: 12 °C

DPP Conditions

Transducer: Kulite CQ-030-100D
S/N: 419-6-34
DPP Sensitivity: 1.50 μV/mmHg/Vdc (pre-amplified, from manufacturer)
Excitation Voltage: 3.11 VDC (Dry Cell batteries)
DPP Amplification: 3640 V/V
Amplifier: 027307U Differential Amp. + HP 465A

Record Number	Start (ft)	End (ft)	T_{throat} (°C)	Time on T_w Record (min)	DPP Vrms				x (cm)	y (cm)
					Recorded (@120 ips)	Playback (@3.75 ips)	Digital (tot.)*	Digital (clean)**		
084-04	374	501	13.0	0	0.35	0.41	0.351	0.337	36.27	0.230
084-05	501	636	13.0	4	0.345	0.41	0.355	0.340	35.64	0.230
084-06	636	752	12.9	7	0.35	0.41	0.353	0.339	35.26	0.237
084-07	752	876	12.8	12	0.35	0.41	0.352	0.338	35.00	0.231
084-08	876	996	12.7	25	0.34	0.4	0.342	0.327	34.37	0.228
084-09	996	1115	12.5	29	0.34	0.4	0.345	0.331	33.73	0.239
084-10	1115	1240	12.5	35	0.34	0.41	0.353	0.339	33.10	0.229
084-11	1240	1357	12.5	40	0.34	0.4	0.346	0.331	32.46	0.222
084-12	1357	1475	12.1	72	0.34	0.4	0.342	0.327	31.83	0.216
084-13	1475	1598	12.2	75	0.34	0.39	0.340	0.327	31.19	0.211
084-14	1598	1705	12.2	80	0.34	0.4	0.338	0.323	30.56	0.210
084-15	1705	1853	12.2	84	0.34	0.4	0.343	0.329	29.92	0.212
084-16	1853	1986	12.0	87	0.34	0.4	0.343	0.329	29.29	0.215
084-17	1986	2112	12.1	91	0.34	0.41	0.346	0.332	28.65	0.219
084-18	2112	2236	12.0	95	0.335	0.4	0.349	0.334	28.02	0.210
084-19	2236	2357	12.1	100	0.345	0.41	0.348	0.334	27.64	0.201
084-20	2357	2478	12.0	104	0.35	0.41	0.349	0.335	27.38	0.209
084-21	2478	2597	11.9	129	0.35	0.41	0.356	0.342	26.75	0.189
084-22	2597	2717	11.9	133	0.35	0.41	0.359	0.345	26.11	0.191
084-23	2717	2843	11.8	136	0.35	0.42	0.362	0.348	25.48	0.183
084-24	2843	2965	11.8	140	0.36	0.42	0.361	0.348	24.84	0.181
084-25	2965	3092	11.8	143	0.36	0.42	0.366	0.352	24.20	0.175
084-26	3092	3208	11.9	147	0.36	0.42	0.364	0.351	23.57	0.162
084-27	3208	3333	11.9	154	0.36	0.42	0.363	0.349	22.93	0.161
084-28	3333	3333	11.8	157	0.355	0.42	0.359	0.345	22.30	0.155
084-29	3453	3643	11.8	161	0.36	0.42	0.362	0.348	21.67	0.151

*DPP total signal from .156 kHz to 320 kHz on integrated spectrum

**Record 084-03 subtracted in the square from DPP total digital signal

Table A-4. Documentation for Analog Data Recordings at MEP, $Re'_\infty=6.2\times10^6$/m, Unheated nozzle

Record Number	Start (ft)	End (ft)	Conditions	DPP Vrms				x (cm)	y (cm)
				Recorded (@120 ips)	Playback (@3.75 ips)	Digital (tot.)*	Digital (clean)**		
084-01	55	179	No Flow	0.14	0.13	0.0991			
084-02	179	307	F/S, UHT, NSCR	0.14	0.12	0.0973		36.03	2.153
084-03	307	429	F/S, UHT, SCR	0.14	0.13	0.099		36.03	2.153
084-30	3698	3776	F/S, UHT, SCR	0.14	0.12	0.097		28.25	2.696
084-31	3776	3902	No Flow	0.14	0.12	0.1005			

*DPP total signal from .156 kHz to 320 kHz on integrated spectrum
**Record 084-03 subtracted in the square from DPP total digital signal

F/S: Free-Stream Measurement.
UHT: Unheated Nozzle
HT: Heated Nozzle (Circulated Ethylene Glycol)
SCR: Screen @ 2-D contraction installed
NSCR: Screen @ 2-D contraction not installed

Table A-5. Documentation for Analog Data Recordings of Electronic and Free-stream Noise, $Re'_{\infty}=6.2\times10^{6}$/m Unheated nozzle.

Tape #238, MEP recordings

Settings

Recorded by: T. Brogan
Recording date: 4/7/94
Record Speed: 120 ips
CH. 3: DPP Signal (amplified)
CH. 5: y-voltage
CH. 7: Tone (1Vrms @ 20 kHz real time)
Temperature Record: DPP8.DAT (13-20)
DPP9.DAT (21-39)

Tunnel Conditions

P_o: 595 mmHg
T_o : 16 °C
Screen (320 mesh): YES
Nozzle Condition: Heated
$(T_w)_{x=0}$: 80 °C

DPP Conditions

Transducer: Kulite CQ-030-100D
S/N: 419-6-34
DPP Sensitivity: 1.50 μV/mmHg/Vdc (pre-amplified, from manufacturer)
Excitation Voltage: 3.15 VDC (Dry Cell batteries)
DPP Amplification: 3640 V/V
Amplifier: 027307U Differential Amp. + HP 465A

Record Number	Start (ft)	End (ft)	T_{throat} (°C)	Time on T_w Record (min)	DPP Vrms				x (cm)	y (cm)
					Recorded (@120 ips)	Playback (@3.75 ips)	Digital (tot.)*	Digital (clean)**		
238-13	5304	5419	80.8	4.0		0.27	0.223	0.196	36.30	0.210
238-14	5419	5537	79.6	7.0		0.23	0.185	0.150	35.66	0.215
238-15	5537	5655	80.9	11.0		0.22	0.167	0.127	35.02	0.218
238-16	5655	5777	81.0	14.0		0.21	0.156	0.112	34.39	0.226
238-17	5777	7896	80.9	17.0		0.2	0.147	0.099	33.75	0.229
238-18	7896	6019	80.9	20.0		0.19	0.145	0.097	33.11	0.231
238-19	6019	6139	80.4	23.0		0.19	0.145	0.097	32.48	0.232
238-20	6139	6257	79.8	26.7		0.18	0.144	0.095	31.85	0.224
238-21	6257	6398	80.9	9.0	0.19	0.18	0.143	0.095	31.21	0.222
238-22	6398	6524	81.2	14.0	0.2	0.18	0.143	0.093	30.58	0.223
238-23	6524	6649	81.4	17.0	0.185	0.17	0.133	0.077	29.94	0.233
238-24	6649	6766	80.6	22.0	0.18	0.17	0.137	0.084	29.31	0.223
238-25	6766	6890	81.4	27.0	0.18	0.17	0.136	0.082	28.67	0.224
238-26	6890	7014	81.4	31.0		0.16	0.132	0.076	28.04	0.211
238-27	7014	7143	81.4	35.0		0.16	0.129	0.071	27.40	0.215
238-28	7143	7267	81.3	87.9	0.17	0.16	0.123	0.060	26.77	0.215
238-29	7267	7386	81.0	91.9	0.17	0.16	0.122	0.056	26.13	0.228
238-30	7386	7503	81.9	95.9	0.165	0.16	0.120	0.052	25.50	0.225
238-31	7503	7627	81.8	99.9	0.165	0.16	0.120	0.051	24.86	0.220
238-32	7627	7746	81.6	103.3	0.165	0.15	0.120	0.052	24.23	0.223
238-33	7746	7862	80.8	107.9	0.16	0.15	0.116	0.045	23.59	0.222
238-34	7862	7988	82.0	110.9	0.16	0.15	0.113	0.037	23.09	0.236
238-35	7988	8104	81.9	115.9	0.16	0.15	0.107	0.030	22.32	0.246
238-36	8104	8464	81.4	120.9	0.16	0.15	0.113	0.041	21.68	0.190
238-39	8464	8590	81.5	140.9	0.16	0.15	0.117	0.055	23.01	

*DPP total signal from .156 kHz to 320 kHz on integrated spectrum

**Record 238-38 subtracted in the square from DPP total digital signal

Missing values indicate a value that was not recorded during the experiment

Table A-6. Documentation for Analog Data Recordings at MEP, Re'_∞=6.2×10^6/m, Heated nozzle, $(T_w/T_o)_{x=0}$=1.22

Record Number	Start (ft)	End (ft)	Conditions	DPP Vrms				x (cm)	y (cm)
				Recorded (@120 ips)	Playback (@3.75 ips)	Digital (tot.)*	Digital (clean)**		
238-01	0	121	No Flow		0.13	0.1034			
238-02	121	243	F/S, UHT, NSCR		0.13	0.0995		35.94	
238-03	243	369	F/S, UHT, SCR		0.13	0.0993		35.94	
238-37	8222	8344	F/S, HT, SCR	0.16	0.14	0.1022		28.04	2.090
238-38	8344		No Flow	0.16	0.15	0.1082			

*DPP total signal from .156 kHz to 320 kHz on integrated spectrum
**Record 238-38 subtracted in the square from DPP total digital signal

F/S: Free-Stream Measurement.
UHT: Unheated Nozzle
HT: Heated Nozzle (Circulated Ethylene Glycol)
SCR: Screen @ 2-D contraction installed
NSCR: Screen @ 2-D contraction not installed

Table A-7. Documentation for Analog Data Recordings of Electronic and Free-stream Noise, $Re'_{\infty}=6.2\times10^{6}$/m Heated nozzle, $(T_w/T_o)_{x=0}=1.22$.

APPENDIX B

AMPLIFICATION RATE COMPUTATION FROM EXPERIMENTALLY DETERMINED POWER SPECTRA

AMPLIFICATION RATE COMPUTATION FROM EXPERIMENTALLY DETERMINED POWER SPECTRA

Power spectra obtained from experimental measurements contain scatter that presents difficulties when computing spatial derivatives for amplification rates. Even a small amount of scatter in a progression of power spectra can produce completely useless results. A common approach to computing derivatives in data with scatter is to "smooth" the raw data first, then take derivatives from the smoothed data (Demetriades 1992). A difficulty with any smoothing technique is that the technique itself can appear to replace the raw data accurately, but in fact produce misleading results in derivatives of the smoothed data. Accordingly, both the smoothing and differentiation procedures must be subjectively evaluated together. The streamwise progression spectra of pitot pressure fluctuations from the $Re'_{\infty}=5.2\times10^{6}$/m, unheated case is used as the example case in the following discussion. This progression of spectra is shown in Figure B-1.

The most successful technique explored here was to use polynomials obtained by a least-squares-fit to the raw data for smoothing. In order to obtain sufficiently smooth and physically representative polynomial functions, it was necessary to find a balance between the order of the polynomial and the region of data over which the polynomial was fit. To capture the curvature of the raw data, the polynomial needed a minimum order N+2, where N is the number of inflection points of the raw spectrum (ignoring scatter). Beyond this "minimum", the adequacy of the polynomial order was subjectively decided by the analyst. A polynomial degree that was too low would eliminate or mask important

physical phenomena, while a degree that was too high would add unwanted and misleading inflection points. Figures B-2 and B-3 show how the polynomial approximation to a discrete spectrum varied with the polynomial order in the frequency (n_f) and spatial (n_x) domains.

Figure B-4 shows a one-dimensionally smoothed spectrum that was obtained by replacing original power spectra with polynomials in the frequency domain (polynomial order n_f). The polynomials were computed with a least-squares fit to the raw spectrum. Although the spectra generally look much smoother, spatial derivatives computed with finite differences were still erratic since the scatter in the spatial domain was not eliminated. The same technique was also applied to the spatial domain by directly computing polynomials in x from the raw data (Figure B-5). However, representations in the frequency domain were not smooth which produced amplification rates (Figure B-6) that were not continuous in frequency – a result that is physically unrealistic.

A 3-dimensional smoothing operation was also explored by replacing the raw spectra with polynomials in f, then replacing those smoothed spectra with polynomials in the spatial dimension x. Figures B-7 through B-10 show the global variations in both spectrum amplitudes and spatial derivatives due to different n_x and n_f. The principal feature of Figures B-7 through B-10 is that almost imperceptible changes in the spectrum progression cause large differences in the spatial derivatives. Due to the large number of points, very little difference was seen in the frequency domain with different polynomials above n_f=5. However, the variations in $\partial A/\partial x$ with spatial polynomial order n_x were significant over the range n_x=3 to n_x=10, with the largest variations occurring at the edges

of the plots. At n_x=3 there was too much "smoothing" with the polynomials in x, while at n_x=10 there were too many degrees of freedom (DOF) in the polynomial compared to the number of data points.

The current set of spectrum data was smoothed using a 10^{th} degree polynomial (10.2 points/DOF) in the frequency domain, and a 7^{th} degree polynomial in the spatial domain (3.7 points/DOF).

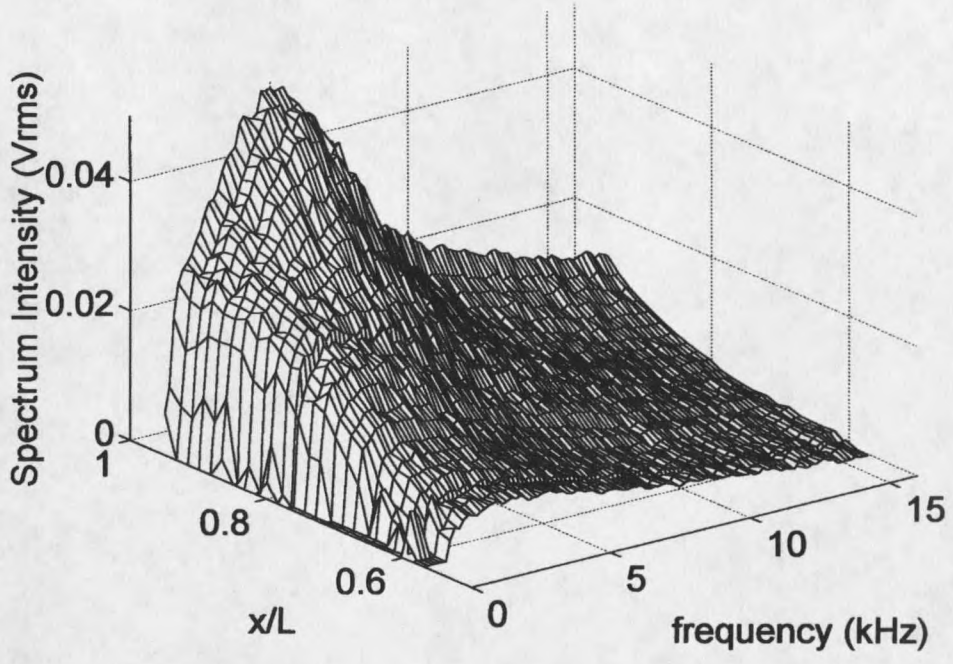

Figure B-1. Example raw spectra progression. $Re'_{\infty}=5.2\times10^{6}$/m, Unheated Nozzle.

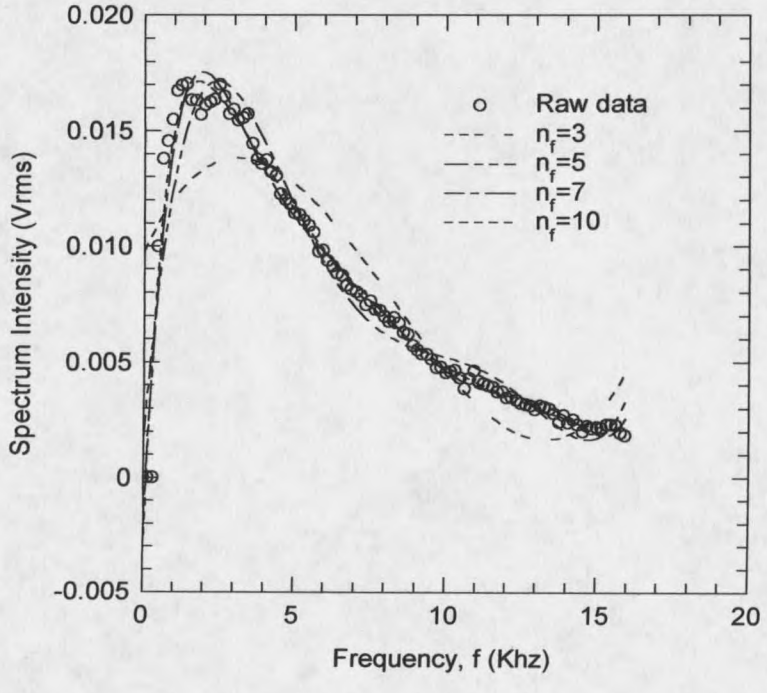

Figure B-2. Variations of a smoothed curve in the frequency domain with polynomial order n_f.

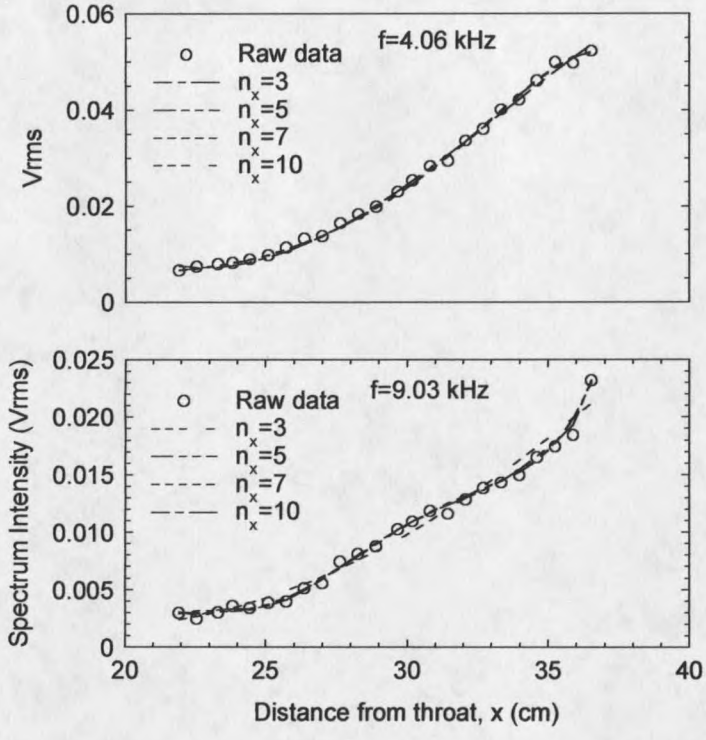

Figure B-3. Variations of a smoothed curve in the spatial domain with polynomial order n_x.

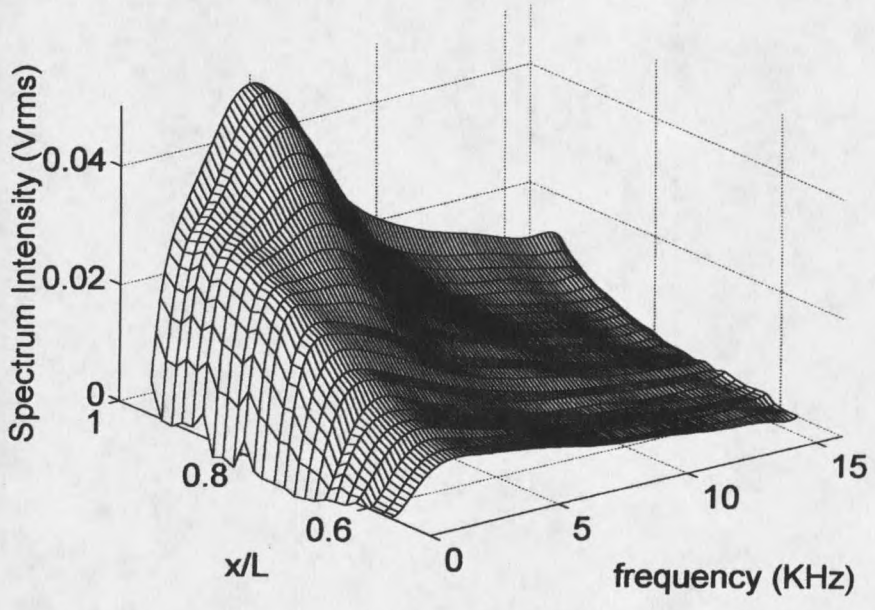

Figure B-4. Spectra progression with smoothing using polynomials (n_f = 10) in the frequency domain only.

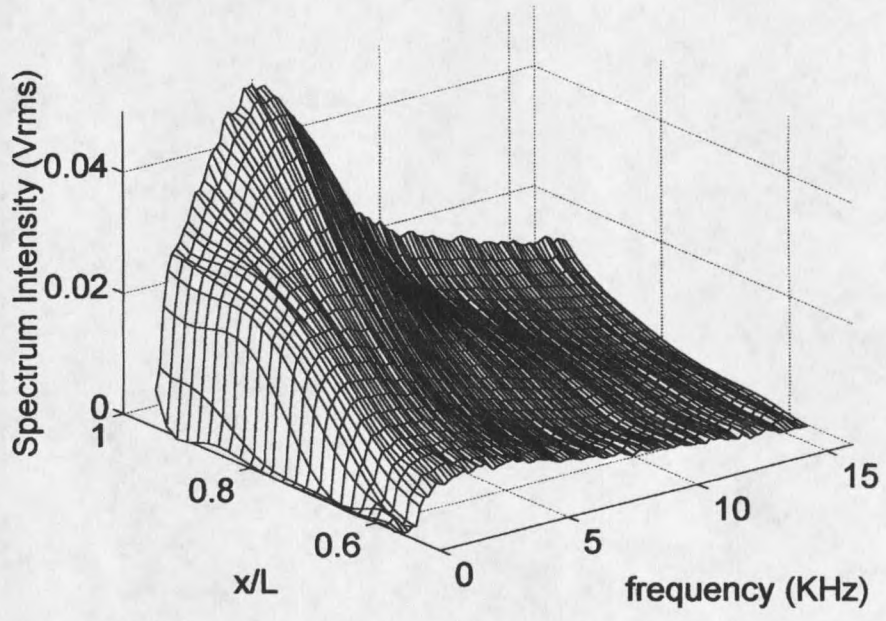

Figure B-5. Spectra progression with smoothing using polynomials (n_x=7) in the spatial domain only.

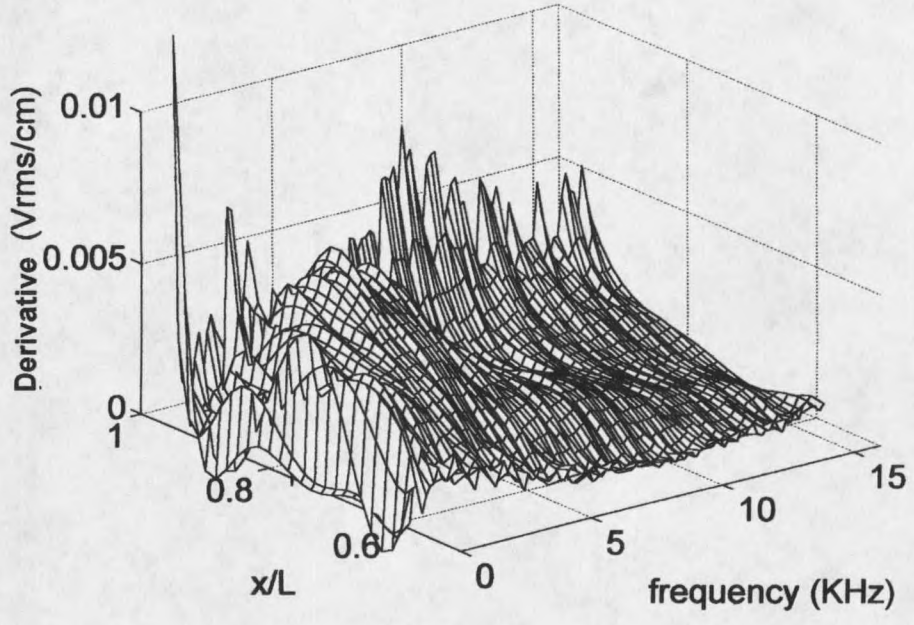

Figure B-6. Spatial derivative $\partial A/\partial x$ computed from spectra smoothed only in the spatial domain (spectra progression in Figure B-5).

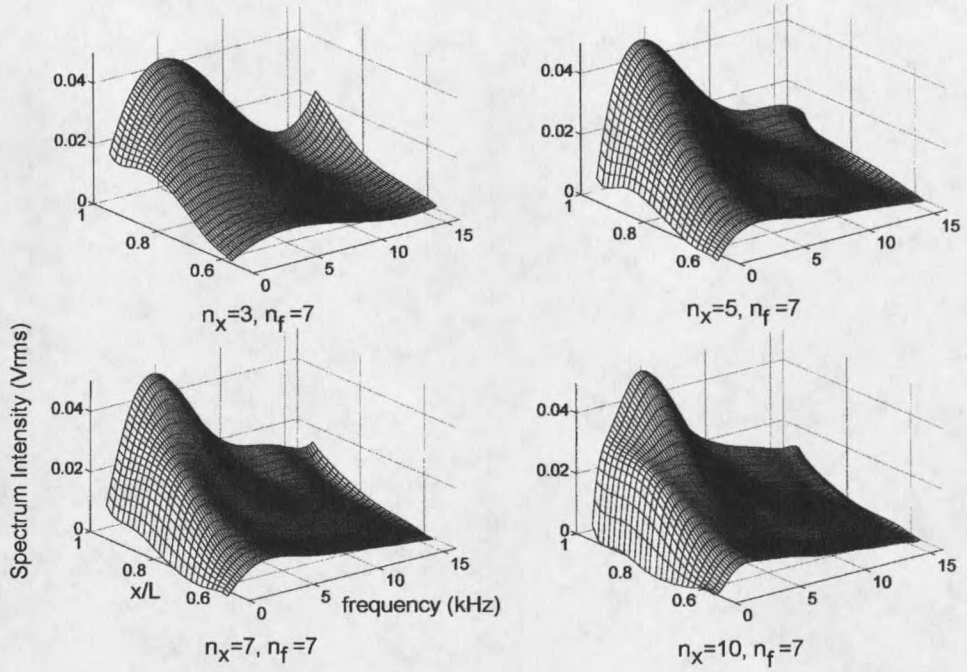

Figure B-7. Global variance of smoothed spectra with different polynomial degrees in frequency domain (n_f).

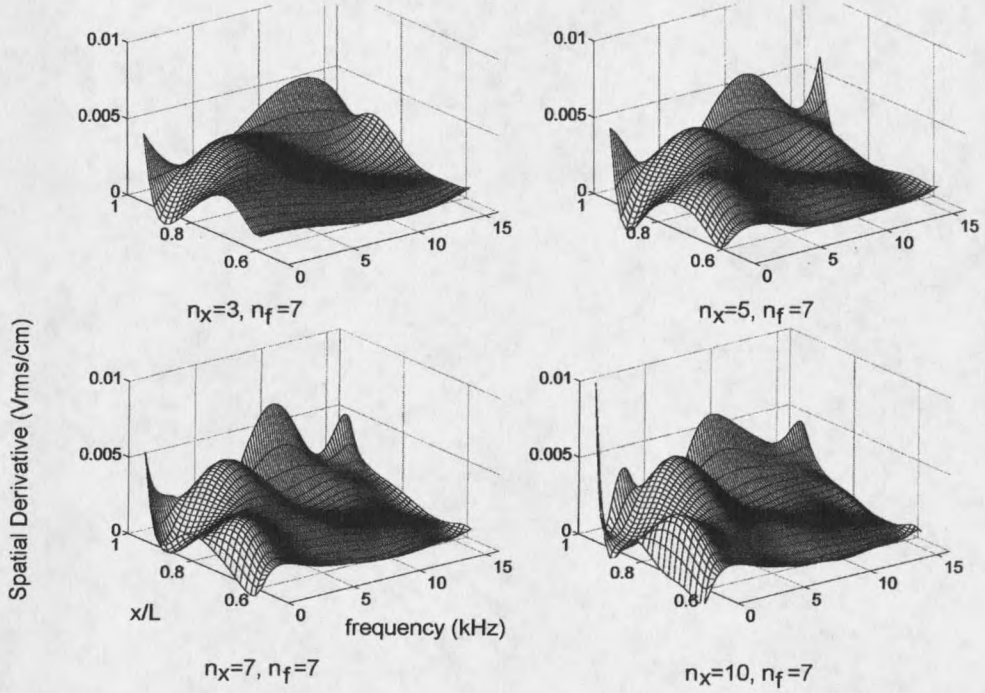

Figure B-8. Global variance of spatial derivatives ($\partial A/\partial x$) with different polynomial degrees in frequency domain (n_f).

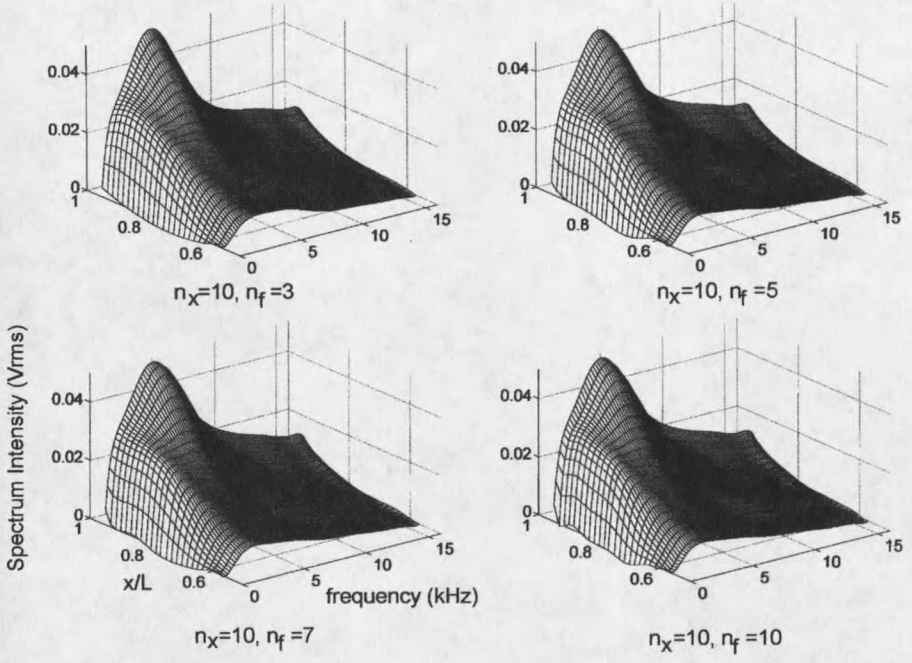

Figure B-9. Global variance of smoothed spectra with different polynomial degrees in spatial domain (n_x).

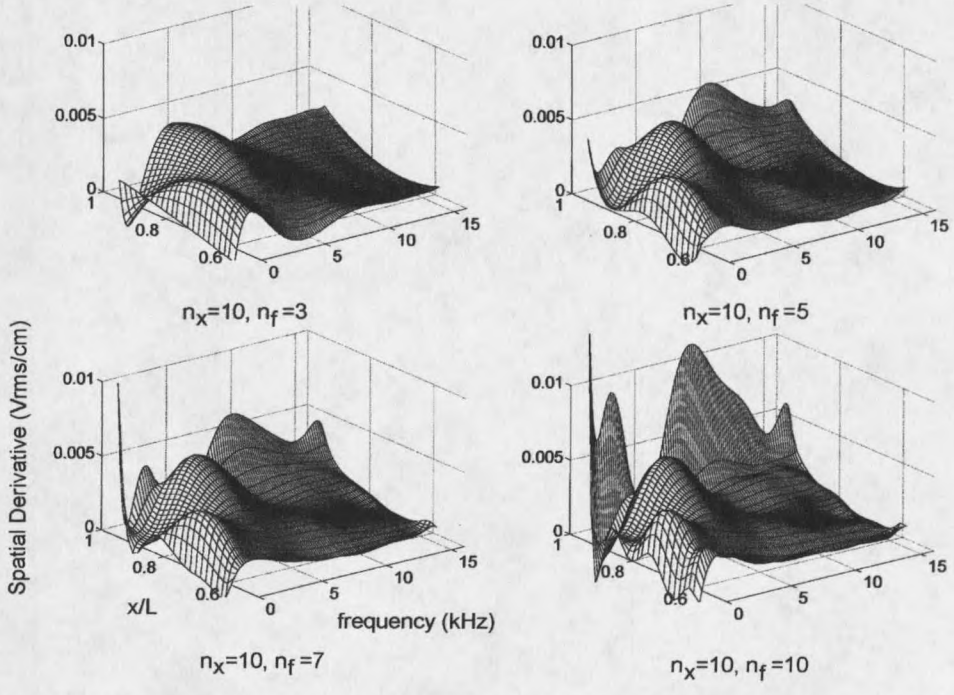

Figure B-10. Global variance of spatial derivatives ($\partial A/\partial x$) with different polynomial degrees in spatial domain (n_x).

APPENDIX C

TURBULENT INTERMITTENCY COMPUTATION USING DIGITAL TECHNIQUES

TURBULENT INTERMITTENCY COMPUTATION USING DIGITAL TECHNIQUES

Transition from a laminar to turbulent flow begins with the formation of discrete turbulent spots that grow and merge with increasing distance in the streamwise direction. If one monitors the instantaneous velocity, or pressure at a point within the transition region, these turbulent spots move past the sensor and show up as a "burst" of turbulence, in an otherwise laminar signal. Further downstream the frequency and size of the turbulent bursts increase, until there is no distinguishable laminar signal within the shear layer and the boundary layer is said to be fully turbulent. A primary feature of turbulence is random, 3-dimensional, high-frequency fluctuations in velocity, pressure, and other thermodynamic properties with amplitudes typically at least an order of magnitude above the "low-frequency" oscillations found in an unstable laminar boundary layer. These high-frequency turbulent fluctuations are superimposed on a time-averaged or a mean flow-field, and travel in fluid packets or eddies whose size can vary continuously from the boundary layer thickness down to the Kolmogorov length scale, $l_k = \left(\nu^3 \delta / U^3\right)^{1/4}$ (Schlichting 1974).

The turbulent intermittency or simply intermittency at a point in the flow is defined as the fraction of time that the flow is turbulent as seen by a stationary sensor in the flow. For example, an intermittency of 1.0 would indicate a measurement of fully turbulent flow, and a value of 0.0 would indicate a completely laminar flow with no turbulent bursting.

Intermittency is often a good statistical indication of the onset and extent of transition in a shear layer, where onset is defined as the point at which bursting first starts to occur. In terms of boundary layer stability, intermittency can also be used as an indication of non-linear effects, though the latter often begin far upstream of intermittent bursting.

The intermittency of a waveform involves the subjective discrimination of which portions are turbulent and which portions are not. Although automated techniques can be and usually are implemented, an algorithm used to discriminate between the instantaneous laminar or turbulent signal invariably involves a set of parameters and threshold values that have been subjectively set by the user. Furthermore, the uniqueness of each electronic circuit (e.g. frequency response, instrument sensitivity) and electronic noise contributors in a given experiment cause the recorded signal to look different from experiment to experiment, regardless of the flow conditions. Most often, the decision of a laminar versus a turbulent signal must be initially made by a visual comparison of the two signal types in a given experiment. From there, fluctuation thresholds and quantitative limits of "high" and "low" frequency oscillations can be established.

There are two classes of techniques commonly used for computing the intermittency of a signal. The first class, which is the more common, involves conditioning the signal and applying some "detector function" $S(\vec{r},t)$ that is sensitive to turbulence, as a function of position $\vec{r}$, and time t. Then based on a specified criterion, the signal over some interval can be identified as laminar or turbulent. Hedley and Keffer (1974) present a review of intermittency computation using a detector function and local discriminator.

The second class uses the probability density of the signal amplitude directly, and has been used with good success for wall mounted sensors that identify turbulent spots by changes in the instantaneous wall shear (Schneider 1995, Hansen and Hoyt 1984, Narasimha 1985). The calculation of a probability density function (PDF) is particularly easy for the wall shear stress since the signal amplitude for a laminar condition is a minimum and the shear stress associated with the core of the turbulent spot is 3 to 5 times larger than that of laminar flow. Very little pre-conditioning is necessary for the original hot-film signal. However, if the PDF technique is to be applied to velocity or some other fluctuating quantity within the boundary layer, pre-conditioning would be necessary. Properties in a laminar and turbulent layer oscillate* about the same mean value; hence, instantaneous amplitude is not sufficient. Other choices for the PDF input could be the modulation width (peak-to-peak voltage) of the signal or a local RMS value.

The technique used in this work follows the first class of methods using a detector function and a threshold criterion. Previous researchers have used a wide range of detector functions, most of them involving a time derivative of one or more flow velocities. The most successful intermittency techniques use more than one component of the instantaneous velocity vector to capitalize on the three-dimensional nature of turbulence. However, in most shear layer measurements, (and is the case here) acquisition of multiple velocity components is not possible due to the large probe size required, and

---

* a strictly laminar boundary layer, by definition has no fluctuations, however, here "fluctuations" in the laminar boundary layer would be instabilities and electronic noise from the recording circuit.

experimental complexity. The choice of $S(\vec{r},t)$ is arbitrary and its purpose is to sensitize the probe signal in some manner to increase the discriminatory capability between a turbulent and non-turbulent signal. It is also usually necessary to incorporate some smoothing over small time intervals into $S(\vec{r},t)$ to eliminate contamination by electronic noise and random dropouts that can incorrectly indicate a laminar signal within a turbulent spot. An indication of local turbulence, $I(\vec{r},t)$, can be computed by subjecting the detector function to a user specified threshold, C, below which, the signal is laminar and above which, the signal is turbulent so that,

$$I(\vec{r},t) = \begin{cases} 1 & S(\vec{r},t) \geq C \quad \text{(turbulent)} \\ 0 & S(\vec{r},t) < C \quad \text{(laminar)} \end{cases} \qquad \textbf{C-1}$$

This random square wave is carried along with the original signal and can be averaged over time to produce an intermittency, γ, as a function of position only.

Turbulence Detection

Two simple detector functions were attempted here to characterize the turbulence intermittency. The first was a simple peak-to-peak (PP) measurement over a specified hold time, t_{hold}, defined as

$$\{S(\vec{r},t_i),\ldots,S(\vec{r},t_i+t_{hold})\} = \max\{v_i,\ldots,v_{i+n_{hold}}\} - \min\{v_i,\ldots,v_{i+n_{hold}}\} \qquad \textbf{C-2}$$

where v_i is the i^{th} voltage sample and n_{hold} is the number of samples in the hold time interval. An indicator for turbulence was then computed using equation C-1. The settings for hold time and threshold level were selected by comparing the indicator function to the original wave-form and choosing combinations of t_{hold} and C, such that the indicator

function graphically matched observed bursts of turbulence. Figures C-1 and C-2 each show the details of the intermittency calculation with a sample waveform using a peak-to-peak detector (equation C-2). As mentioned above, detector functions usually incorporate some type of "smoothing" by either averaging or integrating over some small time interval in order to drop out natural "zeros" contained in the random turbulence signal. The peak-to-peak discriminator does not average, but instead selects the extremum over a set of n_{hold} data points. Zeros within a turbulent signal are simply skipped over, assuming they are within the discriminating interval. Alternatively, any single-spike anomalies associated with the electronic circuit will be picked-up as a turbulent burst over the entire time interval t_{hold}.

The second turbulence detector technique explored here was a mean-square (MS) fluctuating velocity where the mean was acquired over a user-defined hold time, t_{hold}.

$$\{S(\vec{r},t_i),\ldots,S(\vec{r},t_i+t_{hold})\} = \text{mean}\{v_i^{\,2},\ldots,v_{i+n_{hold}}^{\,2}\} \qquad \textbf{C-3}$$

Again, with the indicator function computed by equation C-1. Conceptually, a mean-square detector is more attractive than the peak-to-peak detector, since it incorporates smoothing into the algorithm to allow for the true zeros that can be found within a turbulent signal, and to absorb very short duration anomalies. In an idealized laminar boundary layer, by definition, there are no fluctuations present. In an unstable laminar boundary layer, there are fluctuations within preferred frequency bands. The present experiments showed laminar unstable activity in the range of 0.5 to 15 kHz which contained as much as 95% of the total wide-band rms value. Accordingly it became

necessary to filter this "low-frequency" activity from the recorded signal and apply the MS discriminator to the high-pass filtered signal. The resulting high-frequency "fluctuations" associated with a laminar signal were due to electronic noise in the recording circuit.

Digital Filtering Techniques

Figure C-3 shows a cartoon of the typical characteristics of a high-pass filter compared to an idealized filter. Frequencies for the pass-band and stop-band are normalized relative to the Nyquist frequency f_N (320 kHz for the present experiments). Although the cutoff frequency f_{cut}, was 20 kHz for all intermittency computations presented, the high sampling rate required steep roll-off characteristics relative to f_N, for a transition width ($\Delta f_t/f_N$) on the order of 10^{-2}. All filters converge to the idealized "brick-wall" filter of Figure C-3 for infinite filter orders. However, practicality and CPU time forced compromises in the filter characteristics such as pass-band ripple, stop-band attenuation, and transition width. A thorough discussion of various filter types with their advantages and disadvantages can be found in most digital signal processing text books (Openheim & Schaffer 1965).

The attenuation characteristics of four different filter types (Figure C-4) were computed using MATLAB routines from the Signal Processing Toolbox. In computing the transfer function coefficients for each of the filter cases, the maximum filter order was limited due to numerical problems and computational time. FIR filters typically required impractical filter orders for the requirements of the present work. Here, the transition width was the critical parameter in filter design; compromises were allowed for the pass-

band ripple (R_p) and stop-band ripple (R_s). Accordingly, an elliptic filter provided the most "accurate" filter characteristics for a given filter order. Pass-band ripple was limited to 0.1 dB and the stop-band attenuation of 50 dB. Phase shift between the original and filtered signals was eliminated by filtering the signal in the forward direction, reversing the filtered sequence, and running it back through the filter again. The resulting sequence had precisely zero-phase distortion, and double the specified filter order.

Figures C-5 through C-8 show the stages of the intermittency computation using a mean-square discriminator applied to the filtered signal.

Discussion of the Technique

A graphical comparison between Figures C-2 and C-5, and C-3 and C-6 demonstrates that the mean-square detector picks up the same bursting action as the peak-to-peak detector, but the MS signal is more pronounced in the turbulent regions. Figure C-9 shows plots of the intermittency sensitivity as a function of threshold values for both the MS and PP detector functions. The range of "realistic" intermittency, indicated by the double-headed arrows was determined by graphically comparing the indicator function to the original waveform and deciding on a visual basis whether the laminar and turbulent spots were correctly indicated. Other "objective" techniques have been used by previous researchers, such as choosing the threshold level at the knee (maximum curvature) of the γ-C curve (Hedley and Keefer 1974) or by choosing the intermittency at the intersection of two lines formed by linear trends outside of the correct intermittency range (Kuan and Wang 1990). However, these graphical techniques require a specific shape of the γ-C

curve that is not necessarily common to all measurements in a shear layer (Schneider 1995). It is noted in Figure C-9 that the bands of realistic intermittency for low intermittency values do correspond to a region of maximum local curvature in the γ-C curve. At higher intermittency levels, there is little or no curvature in the γ-C curves.

Table C-1 displays the upper and lower limits for intermittency and threshold values. The PP technique shows a larger variation in the upper and lower limits for different stagnation conditions and streamwise location, while the MS technique is more robust. The wide-band MS electronic noise level with no airflow in the tunnel and in the free-stream was about 0.01 Vms; above 20 kHz, the filtered noise signal was 0.007 Vms. The MS detector consistently shows a good threshold value at about 0.02 Vms, three times that of the signal from a laminar waveform (based on 20 kHz high-pass filtered signals). Figure C-10 shows the MS detector function applied to a wind-off signal. Based on the results of Table C-1, the single threshold of $\mathrm{Vms/Vms_{laminar}} = 3$ for all waveforms appears to produce intermittency estimations within ± 0.05, based on a visual judgement. It is possible that defining the turbulence criterion relative to the electronic noise can provide a consistent comparison of intermittency computation and turbulence detection between other experiments. However, before this hypothesis can be justified, the present results must be compared with experiments using other electronic circuits and recording equipment. Schneider (1995) has reported a good choice of turbulence identification for a shear-stress signal twice that of the laminar value.

Case		Intermittency		MS Threshold		PP Threshold	
(record #)	x/L	Lower	Upper	Lower	Upper	Lower	Upper
1b (10)	0.850	0	0.03	0.018	∞	0.52	∞
1b (7)	0.900	0.08	0.14	0.015	0.023	0.55	0.68
1b (4)	0.949	0.21	0.26	0.019	0.027	0.54	0.65
1c (32)	0.910	0	0.04	0.016	∞	0.58	∞
1c (30)	0.943	0	0.06	0.014	∞	0.54	∞
2a (29)	0.563	0.52	0.57	0.015	0.032	0.44	0.70
2a (20)	0.711	0.58	0.65	0.014	0.032	0.40	0.55
2a (10)	0.860	0.80	0.88	0.014	0.022	0.38	0.54
2a (4)	0.942	0.82	0.90	0.012	0.024	0.43	0.58
2b (35)	0.580	0	0.01	0.014	∞	0.46	∞

Table C-1. Intermittency range and threshold values for selected waveform records.

Much of the error in the intermittency computation does not lie in the technique itself, but the lack of clarity in the extent of a turbulent spot. Figure C-8 shows the PDFs of several of the records in Table C-1, where the PDF, $P(S(\vec{r},t))$ is scaled to satisfy the definition,

$$\int_{-\infty}^{\infty} P(S(\vec{r},t))dS = 1 \qquad \textbf{(C-4)}$$

If a comparison is made between the PDF of a laminar signal such as record 1c-30 versus a signal with large intermittency, like 2a-4, a large overlap is seen that is from a signal that is neither laminar nor turbulent, but somewhere in-between. These in-between regions are characteristics of the "edges" of a turbulent spot. In Schneider's experiment (1995) it was estimated that the probability of measuring a signal from one of these in-between regions was typically about 20%. The decision (visual and/or mathematical) as to how much of this in-between region is deemed turbulent is the largest contributor to differences in intermittency values between various algorithms to calculate intermittency.

Error in intermittency can also be introduced by the level of smoothing from the sampling rate, t_s, and by the hold time, t_{hold}, used in the detector function. Table C-2 shows some characteristic times for the present experiment. If we assume that the Kolmogorov length scale defines the smallest eddy generated within the layer, then ideally, t_s and t_{hold} should be small enough to capture these bursts. However, at large Reynolds numbers, these small eddies coalesce to some degree into fine-scale turbulent structures that have a larger spatial extent on the order of 15 l_k to 35 l_k (Hedley and Keffer 1974). If the smoothing interval were small enough to detect the individual eddies, one may be detecting spectral turbulence, rather than the interfaces of turbulent spots. It can be argued that a lower bound on the smoothing interval can be established as no smaller than the spectral domains of the fine-scale turbulent structures. Essentially, this controversy in establishing a lower bound on a sampling interval lies in the somewhat arbitrary definition of a "turbulent spot". In this work, the conglomerations of fine-scale turbulence have been treated as single turbulent spots, as is done by most researchers, when characterizing intermittency.

Individual record length (4096 digital points)	6.40 msec
Sampling time interval, t_s	1.56 μsec
Hold time, t_{hold}	25 μsec
Oscillation period at dominant instability, T_{us}	250 - 500 μsec
Kolmogorov time, l_k/U	10 μsec

Table C-2. Characteristic time scales

Intermittency is a statistical quantity that requires a sufficient record length to obtain a statistically stationary value. The smoothness of the PDF plots was used as an indication of a sufficient averaging length. All intermittency computations were performed with ensemble average of 100 waveform records, which corresponds to about 2600 - 5100 periods (not contiguous) of the dominant instability that produced the turbulent bursts. Figure C-11 shows the PDFs computed with 100 waveforms vary only fractions of a percent of the full-scale range, and on a linear scale, the plots appear fairly smooth.

Error in the Computing Turbulent Intermittency

Error in the intermittency computation can be estimated with the standard deviation σ of the intermittency values computed for each waveform in a data set (in this case 100 waveforms). Since γ is a statistical parameter, which is constant for a stationary function, σ is primarily a result of the length of the individual waveforms. Thus, if the individual waveforms were longer, it is expected that the standard deviation would be less. Although σ is not a direct measure of the deviation between measured and true intermittency, σ is sensitive to the presence of the "in-between" regions that are neither turbulent nor laminar.

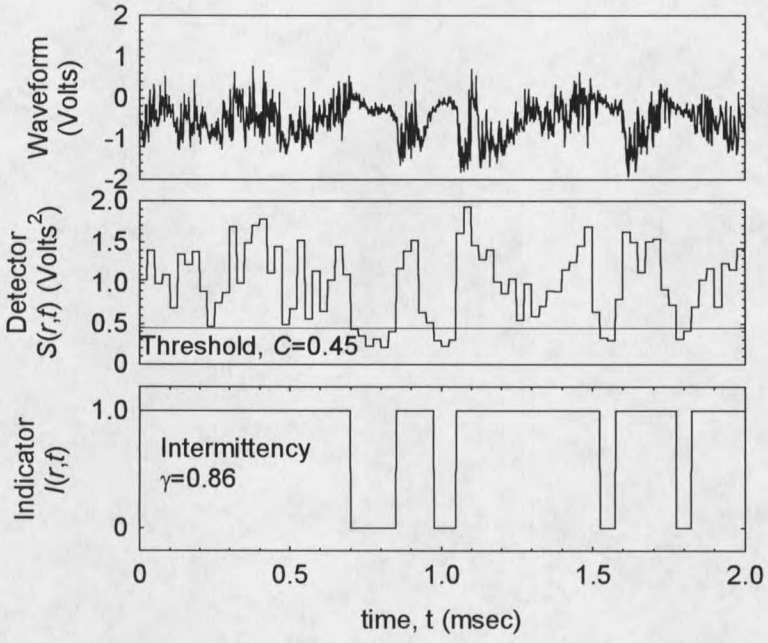

Figure C-1. Intermittency computation using a peak-to-peak detector, P_o=500 mmHg, T_o=21 °C, Unheated Nozzle, x/L=0.949.

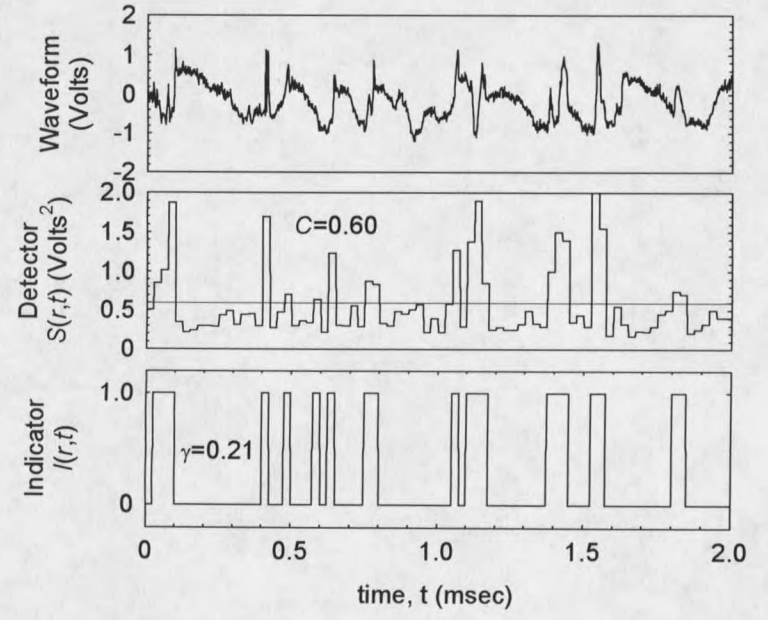

Figure C-2. Intermittency computation using a peak-to-peak detector, P_o=595 mmHg, T_o=16 °C, Unheated Nozzle, x/L=0.942.

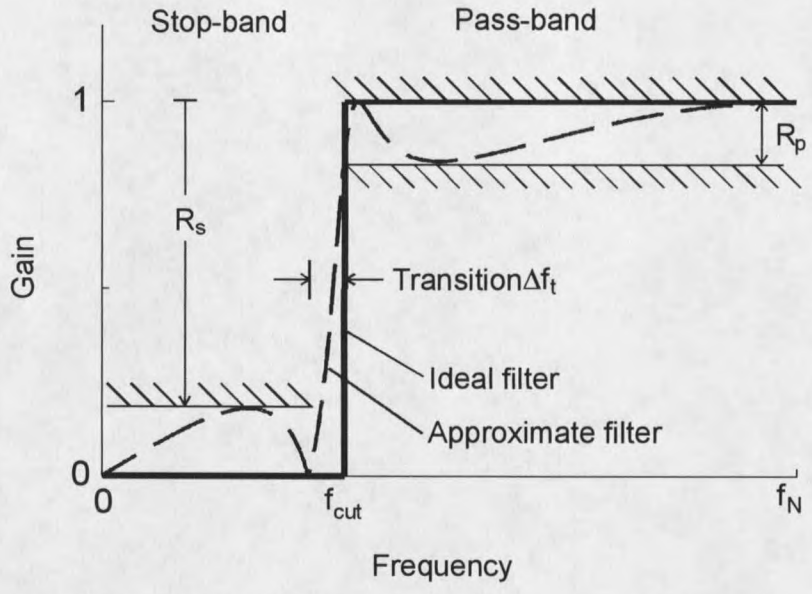

Figure C-3. General digital high-pass filter characteristics.

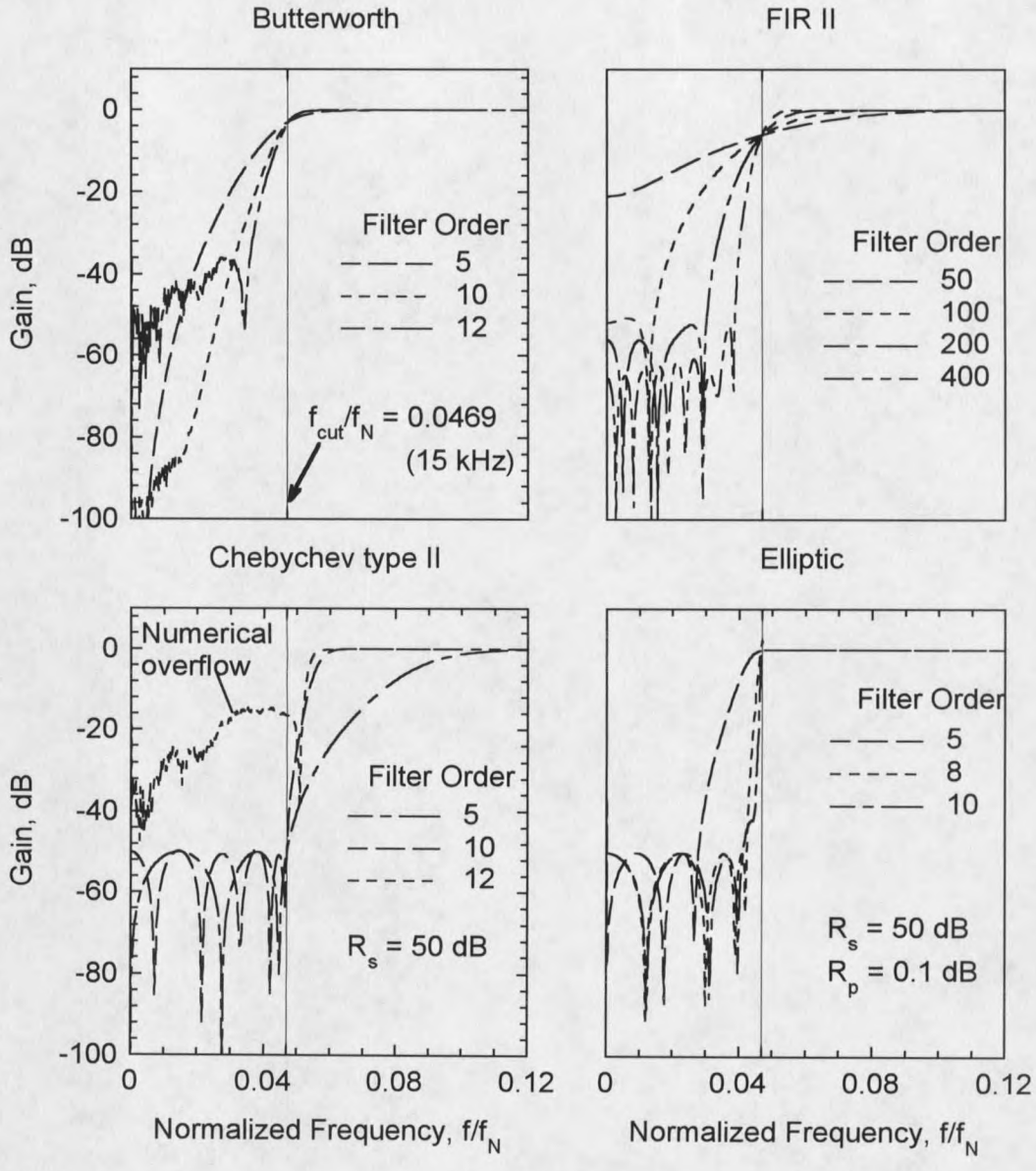

Figure C-4. Attenuation Characteristics of different IIR and FIR filter types. Nyquist frequency f_N=320 kHz, Cutoff frequency, f_{cut}=15 kHz.

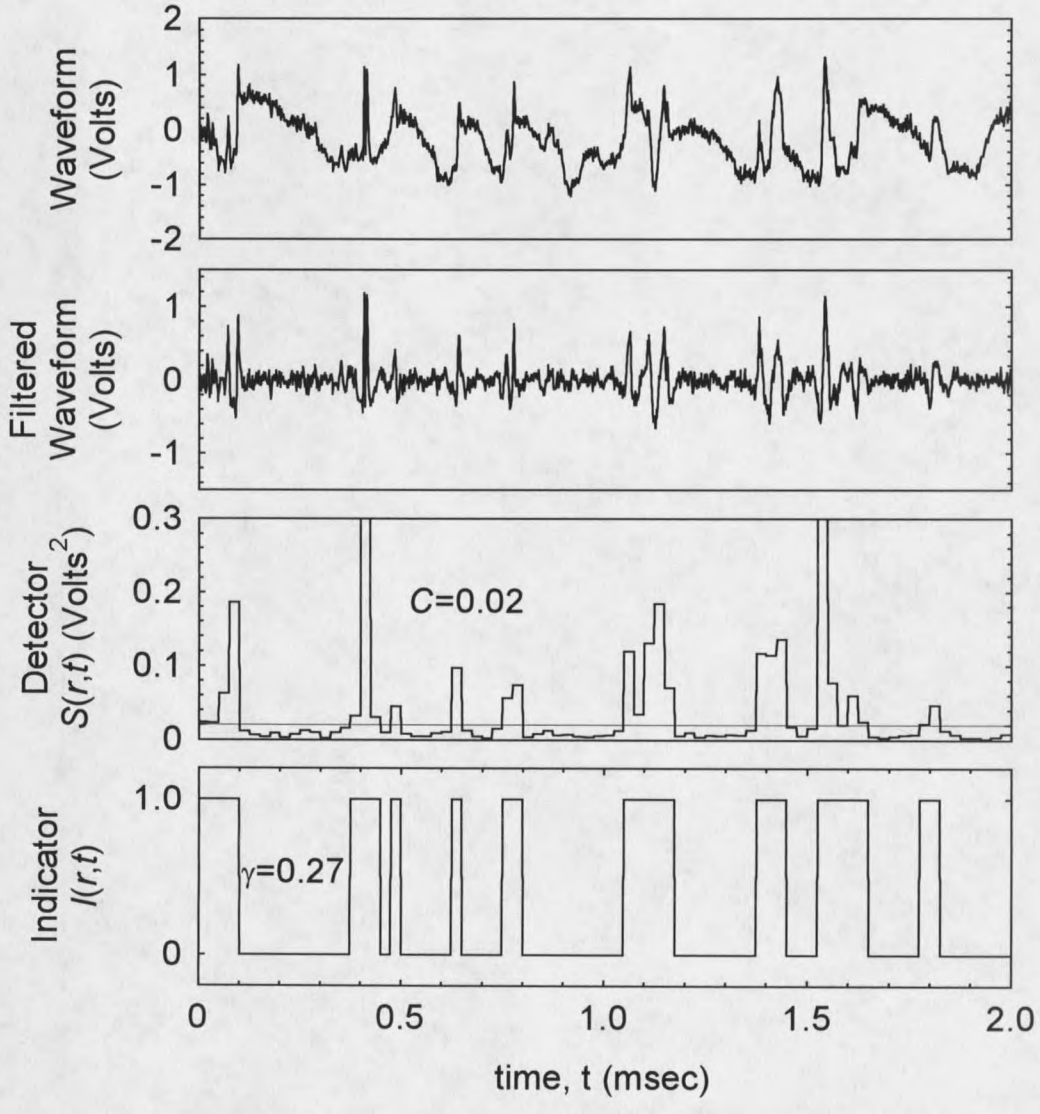

Figure C-5. Intermittency computation using a 20 kHz filtered mean-square detector, P_o=500 mmHg, T_o=21 °C, Unheated Nozzle, x/L=0.949.

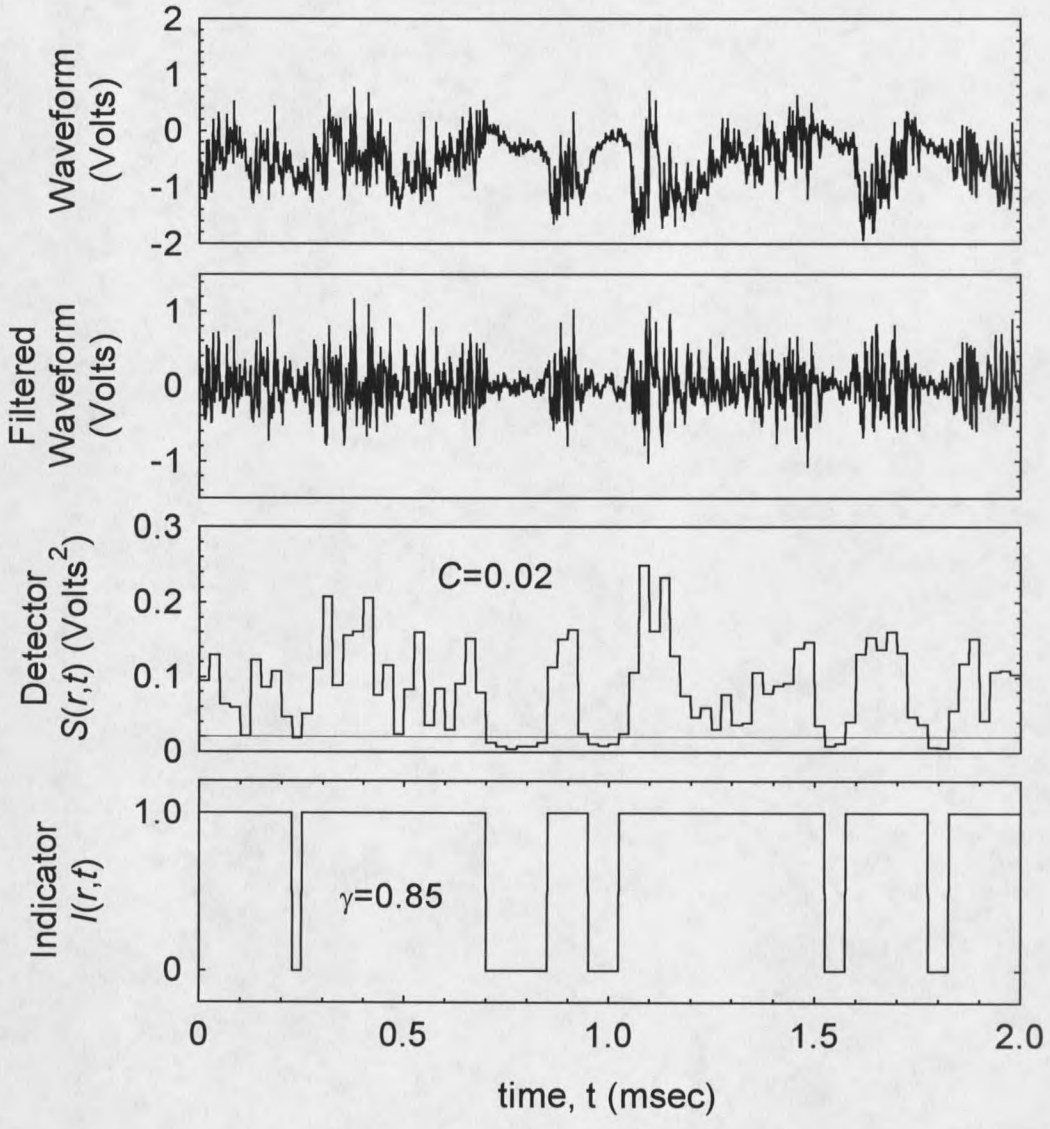

Figure C-6. Intermittency computation using a 20 kHz filtered mean-square detector, P_o=595 mmHg, T_o=16 °C, Unheated Nozzle, x/L=0.942.

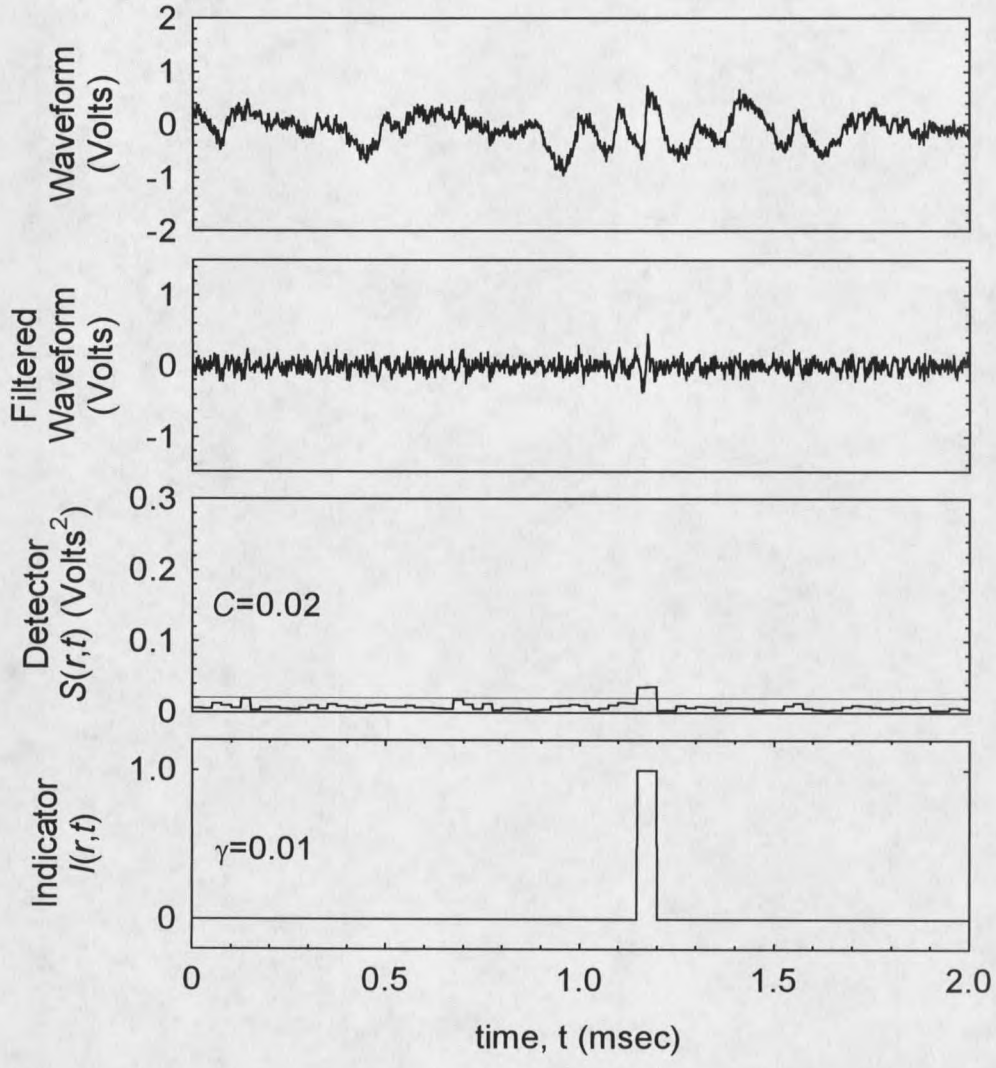

Figure C-7. Intermittency computation using a 20 kHz filtered mean-square detector, P_o=500 mmHg, T_o=21 °C, Heated Nozzle, $(T_w/T_o)_{x=0}$=1.13, x/L=0.949.

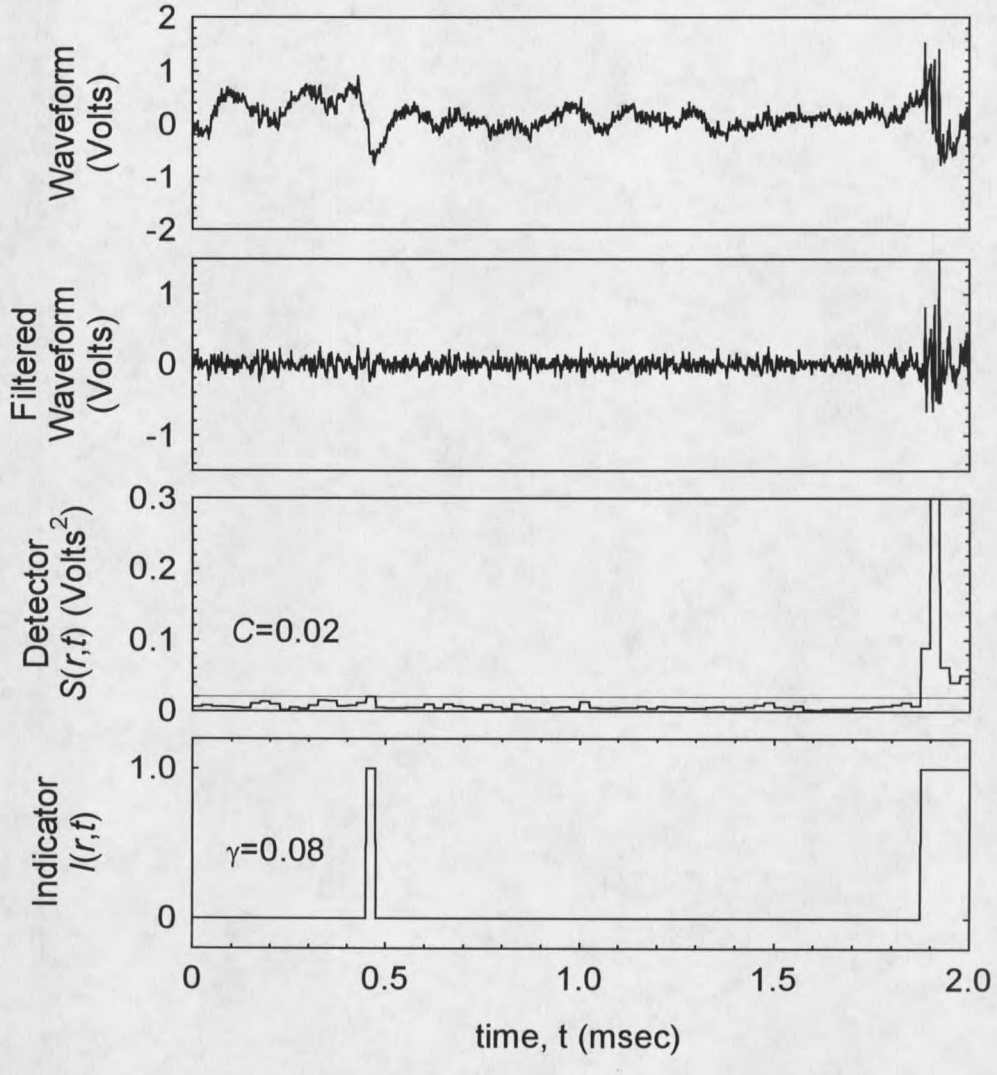

Figure C-8. Intermittency computation using a 20 kHz filtered mean-square detector, P_o=595 mmHg, T_o=16 °C, Heated Nozzle, $(T_w/T_o)_{x=0}$=1.22, x/L=0.943.

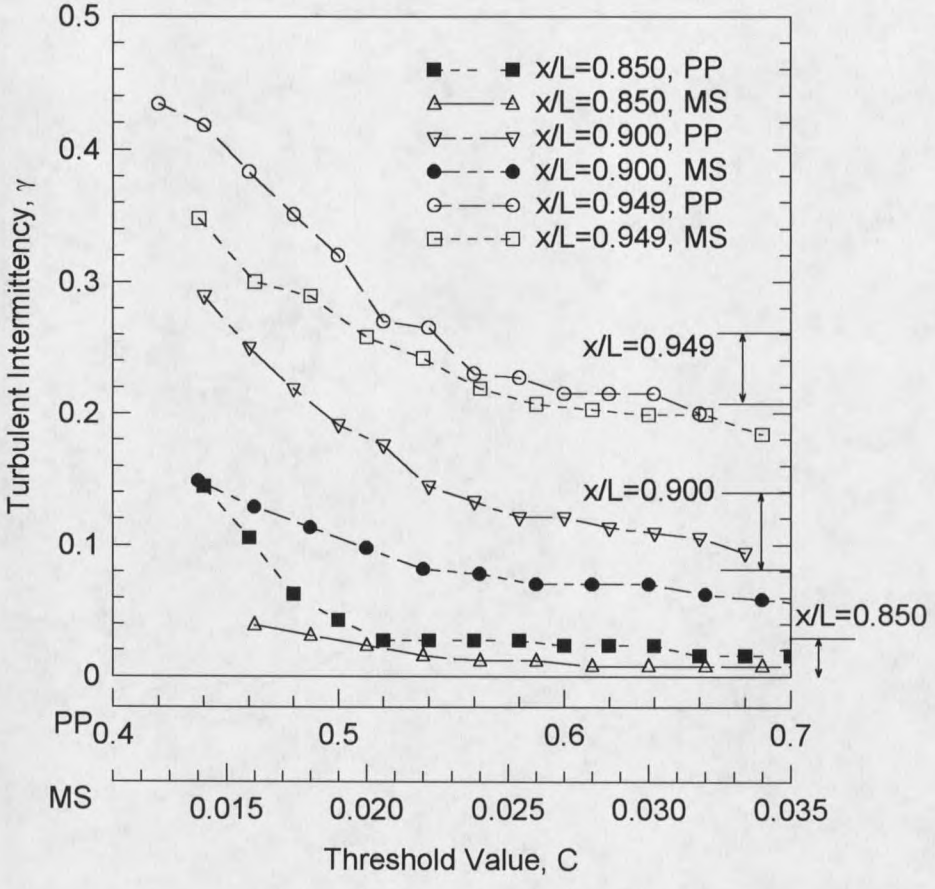

Figure C-9. Intermittency sensitivity to threshold values. Conditions for curves are P_o=500 mmHg, T_o=21 °C, Unheated Nozzle. (PP) Peak-to-peak detector, (MS) Mean-square detector. Arrows indicate range of "realistic" intermittency by visual inspection of the waveforms, detector, and indicator functions.

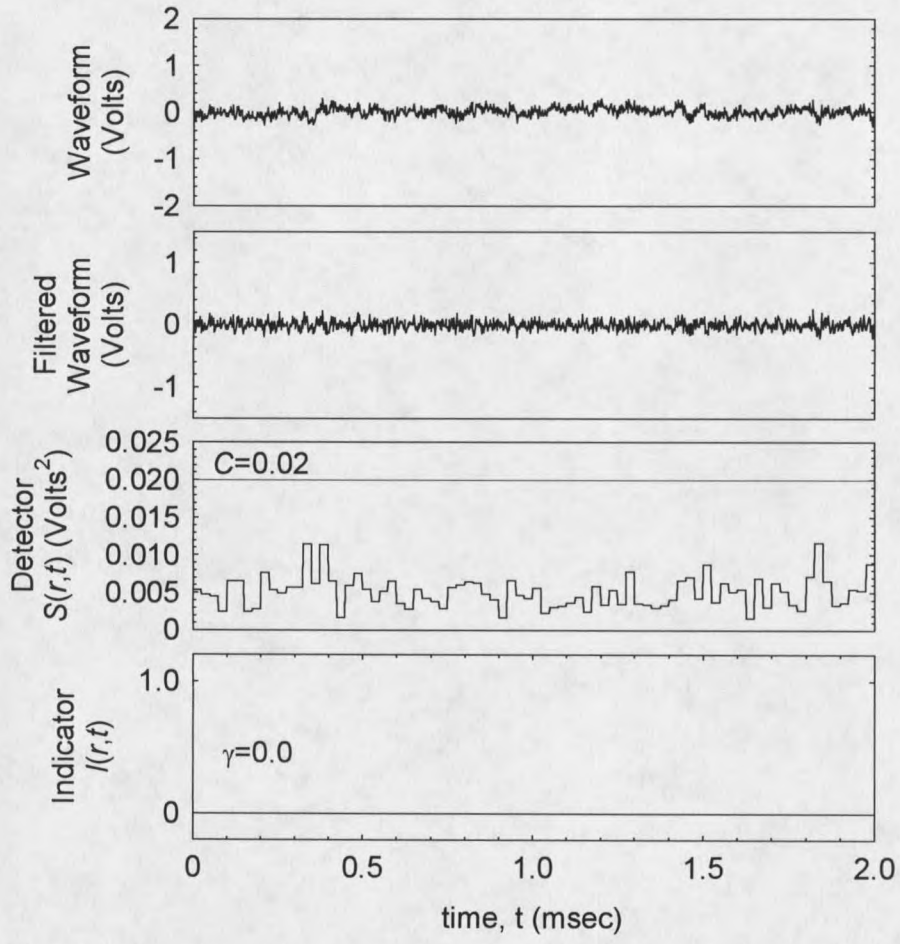

Figure C-10. Filtered mean-square detector function applied to electronic noise recording.

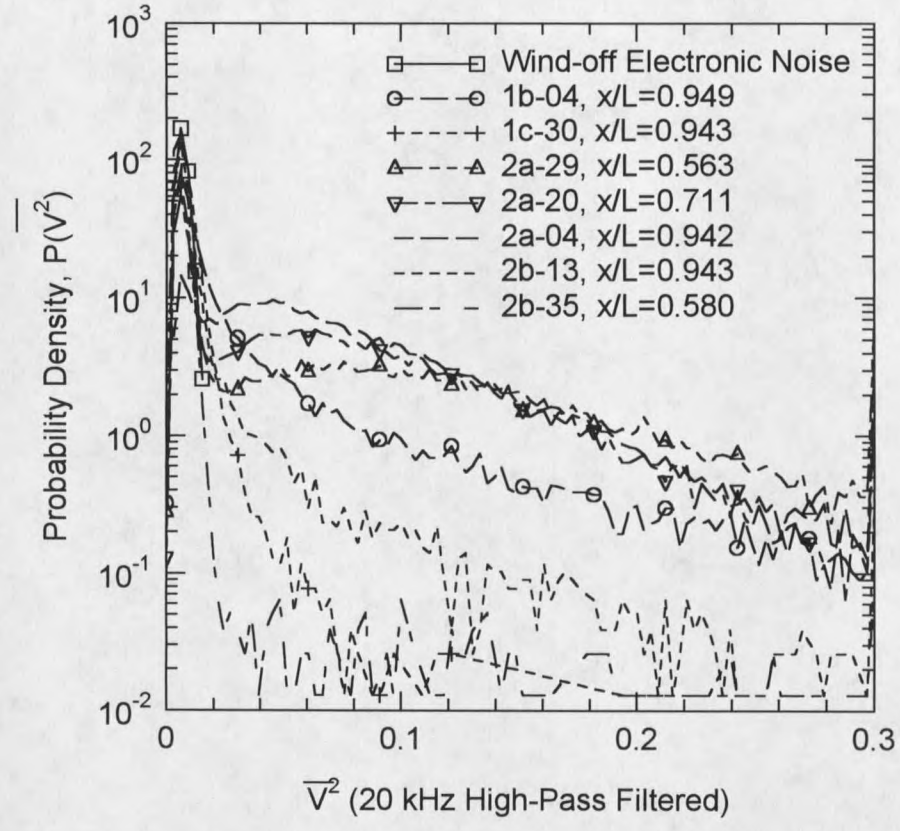

Figure C-11. PDF plots with 100 waveforms averaged.

REFERENCES

REFERENCES

Alcenius, T.J., Schneider, S.P., Beckwith, I.E., White, J.A., Korte, J.J., "Development of Square Nozzles for Supersonic Low-Disturbance Wind Tunnels," *J. of Aircraft*, Vol. 33, No. 6, pp. 1131-1138, December 1996.

Alcenius, T.J., "Development of Square Nozzles for High-Speed, Low-Disturbance Wind Tunnels," *M.S. Thesis*, Dep't. of Aeronautics and Astronautics, Purdue University, December 1994.

Ames Research Staff, "Equations, Tables, and Charts for Compressible Flow," *NACA TR-1135*, 1953.

Arnal, D., "Boundary Layer Transition: Predictions Based on Linear Theory", *Special Course in Transition Modeling*, AGARD Report 793, 1993, Ref. 2.

Beckwith, I.E., "Development of a High-Reynolds Number Quiet Tunnel for Transition Research," *AIAA J.*, Vol. 13, No. 3, March 1975, pp. 300-306.

Beckwith, I.E. and Holley, B. "Gortler Vortices and Transition in Wall Boundary Layers of Two Mach 5 Nozzles," *NASA TP-1869*, August 1981.

Beckwith, I.E., Creel, T.R., Chen, F.-J., and Kendall, J.M., "Free-Stream Noise and Transition Measurements on a Cone in a Mach 3.5 Pilot Low-Disturbance Tunnel", *NASA TP-2180*, September 1983.

Beckwith, I.E., and Miller, C.G, III, "Aerothermodynamics and Transition in High-Speed Wind Tunnels at Nasa Langley," *Annual Review of Fluid Mechanics*, Vol. 22, 1990, pp. 419-439.

Beckwith, I.E., Chen, F.-J., and Malik, M.R., "Design and Fabrication Requirements for Low-Noise Supersonic/Hypersonic Wind Tunnels," AIAA Paper No. 88-0143, 1988.

Beckwith, I.E., Harvey, W.D., Harris, J.E., and Holley, B.B., "Control of Supersonic Wind-Tunnel Noise by Laminarization of Nozzle-Wall Boundary Layers," *NASA TM X-2879*, December 1973.

Berger, S.E., "Experiments on the Relationship Between Shape and Effectiveness for Three-Dimensional Boundary Layer Trips at Supersonic Speeds," *M.S. Thesis*, Dep't. of Mechanical Engineering, Montana State University, May 1988

Böttcher, J. and Wedemeyer, E., "The Flow Downstream of Screens and its Influence on the Flow in the Stagnation Region of Cylindrical Bodies," *J. of Fluid Mechanics*, Vol. 204, 1989, pp. 501-522.

Bradshaw, P., "The Effect of Wind-Tunnel Screens on Nominally Two-Dimensional Boundary Layers," *J. of Fluid Mechanics*, Vol. 22, part 4, 1965, pp. 679-687.

Brogan, T.P., "Effects of Surface Heating on the Laminar Boundary Layer of a Two-Dimensional, Mach 3.0 Wind Tunnel Nozzle," *M.S. Thesis*, Dep't. of Mechanical Engineering, Montana State University, July 1995.

Brogan, T.P. and Demetriades, A., "Effects of Surface Heating on Instabilities in a Supersonic Nozzle Boundary Layer," AIAA Paper No. 98-0779, January 1998a.

Brogan, T.P. and Demetriades, A., "Influence of Sidewall Transition on Measured Free Stream Noise in a Two-Dimensional Supersonic Tunnel", AIAA Paper 98-2614, June 1998b.

Buning, P., et al., "OVERFLOW User's Manual (version 1.7u)," NASA, March 1997.

Chen, F.-J., Malik, M.R., and Beckwith, I.E., "Instabilities and Transition in the Wall Boundary Layers of Low-Disturbance Supersonic Nozzles," AIAA Paper 85-1573, July 1985.

Chen, F.-J., and Malik, M.R., "On the Design of a New Mach 3.5 Quiet Nozzle", In *Instability and Transition*, ed. M.Y. Hussaini and R.G. Hoyt, Vol. II, Springer-Verlag, 1990, pp. 246-257.

Chen, F.-J., Wilkinson, S. P., and Beckwith, I.E., "Gortler Instability and Hypersonic Quiet Nozzle Design," AIAA Paper 91-1648, June 1991.

Chen, F.-J., "Boundary Layer Transition Extent Measurements on a Cone and Flat Plate at Mach 3.5," AIAA Paper 93-0342, January 1993.

Cohen, C.B., and Reshotko, E., "The compressible laminar boundary layer with heat transfer and arbitrary pressure gradient," *NACA TR-1294*, 1956.

Cooper, M., Mayo, E.E., and Julius, J.D., "The influence of Low Wall Temperature on Boundary-Layer Transition and Local Heat Transfer on 2 1-inch-Diameter Hemispheres at a Mach Number of 4.95 and Reynolds Number/Foot of 73.2×10^6," *NASA TN D-391*, 1960.

Creel, T.R., Beckwith, I.E., and Chen, F.-J., "Nozzle Wall Roughness Effects on Free-Stream Noise and Transition in the Pilot Low-Disturbance Tunnel", *NASA TM 86389*, 1985.

Day, H.P., Herbert, T., and Saric, W.S., "Comparing Local and Marching Analysis of Gortler Instability," *AIAA J.*, Vol. 28, No. 6, 1990, pp. 1010-1015.

Demetriades, A., "Roughness Induced Transition on a Blunt Body Simulated by a DeLeval Nozzle Throat," Aeronutronic Rept. U-6496, Newport Beach, Calif., 1977-78. (Work performed under USA-SAMSO Contract F04701-77-C-0113).

Demetriades, A., "Boundary Layer Transition in a Supersonic Nozzle Throat in the Presence of Cooling and Surface Roughness," *MSU-SWT TR 82-01*, Montana State University, August 1981a.

Demetriades, A., "Roughness Effects on Boundary-Layer Transition in a Nozzle Throat," *AIAA J.*, Vol. 19, No. 3, March 1981b, pp. 282-289.

Demetriades, A., "Growth of disturbances in a laminar boundary layer at Mach 3," *Physics of Fluids A*, Vol. 1, No. 2, 1989, pp. 312-317.

Demetriades, A., "Recent Developments in Immersible Sensors for High-Speed Flow Turbulence," ASME FED-Vol. 108, 1991, pp. 35-41.

Demetriades, A., "Cooling and Roughness Effects on Transition on Nozzle Throats and Blunt Bodies," *J. of Spacecraft and Rockets*, Vol. 29, No. 4, 1992a, pp. 432-436.

Demetriades, A., "Experimental Study of a Shear Layer Separating a Mach 8 from a Mach 3 Stream," *MSU-SWT TR 93-01*, Montana State University, December 1992b.

Demetriades, A., Mueller, R.L., Reda, D.C., and King, L.S., "Boundary Layer Studies in a 2-D Supersonic Nozzle For Quiet Tunnel Applications," AIAA Paper 94-2507.

Demetriades, A., "Stabilization of a Nozzle Boundary Layer by Local Surface Heating," *AIAA J.*, Vol 34, no. 12, December 1996, pp. 2490-2495.

Demetriades, A., Brogan, T.P., King, L.S., Reda, D.C., "Experimental and Computational Boundary Layer Studies in a Supersonic Two-Dimensional Nozzle" (Submitted to AIAA J.), 1998.

Deyle, H. and Bippes, H., "Disturbance Growth in an Unstable Three-Dimensional Boundary Layer and Its Dependence on Environmental Conditions," *J. of Fluid Mechanics*, Vol. 316, 1996, pp. 73-113.

Dougherty, N.S. and Fisher, D.F., "Boundary Layer Transition Correlation on a Slender Cone in Wind Tunnels and Flight for Indications of Flow Quality," *AEDC TR-81-26*, February 1982. (also as NASA citation AD A111328)

Dovgal A. V., Levchenko V.Y., and Timofeev V.A., "Boundary Layer Control by a Local Heating of the Wall," *Laminar-Turbulent Transition* (D. Arnal and R. Michel, eds.), Springer-Verlag, Berlin, 1990, pp. 113-121.

El-Hady, N.M., and Verma, A.K., "Growth of Gortler Vortices in Compressible Boundary Layers Along Curved Surfaces", *J. of Engineering and Applied Sciences*, Vol. 2, 1983, pp. 213-238

El-Hady, N.M., and Verma, A.K., "Instability of Compressible Boundary Layers Along Curved Walls with Suction or Cooling", *AIAA J.*, Vol. 22, No. 2, February 1984, pp. 206-213.

Floryan, J.M. and Saric, W.S., "Stability of Gortler Vortices in Boundary Layers," *AIAA J.*, Vol. 20 No. 3, 1981, pp. 316-324.

Floryan, J.M., "On the Gortler Instability of Boundary Layers," *Prog. Aerospace Sciences*, Vol. 28, 1991, pp. 235-271.

Gad-el-Hak, M., "Transition Control," Instability and Transition, Vol. I, Springer-Verlag, 1990, pp. 319-354.

Garg, V.K., Diprima, R.C., "The Effect of Heating on the Stability of Flow Over Concave Walls," *Physics of Fluids*, Vol. 27, No. 4, April 1984, pp. 812-820.

Gaster, M., "On the Effects of Boundary Layer Growth on Flow Stability," *J. of Fluid Mechanics*, Vol. 66, 1974, pp. 465-480.

Goldstein, M.E., Leib, S.J., and Cowley, S.J., "Distortion of a Flat-Plate Boundary Layer by Free-Stream Vorticity Normal to the Plate," *J. of Fluid Mechanics*, Vol. 237, 1992, pp. 232-260.

Hall, P., "Taylor-Gortler Vortices in Fully Developed or Boundary Layer Flows: Linear Theory," *J. of Fluid Mechanics*, Vol. 124, 1982, pp. 475-494.

Hall, P., "The Linear Development of Gortler Vortices in Growing Boundary Layers," *J. of Fluid Mechanics*, Vol. 130, 1983, pp. 41-58.

Hall, P. "The Nonlinear Development of Gortler Vortices in Growing Boundary Layers," *J. of Fluid Mechanics*, Vol. 193, 1988, pp. 243-266.

Hall, P. and Malik, M. "The growth of Gortler vortices in Compressible Boundary Layers," *J. of Engineering Mathematics*, No. 23, January 1989, pp. 239-251.

Hansen, R.J., and Hoyt, J.G., "Laminar-to-Turbulent Transition on a Body of Revolution With an Extended Favorable Pressure Gradient", *Trans. ASME: J. Fluids Engineering*, vol. 106, 1984, pp. 202-210

Harris, J.E. and Blanchard, D.K., "Computer Program for Solving Laminar, Transitional or Turbulent Compressible Boundary-Layer Equations for Two Dimensional and Axisymmetric Flow," *NASA TM 83207*, February 1982.

Harvey, W.D., Stainback, P.C., Anders, J.B., and Cary, A.M., "Nozzle-Wall Boundary Layer Transition and Free Stream Disturbances at Mach 5," *AIAA J.*, Vol 13, no. 3, March 1975a, pp. 307-314.

Harvey, W.D., Cary, A.M., Jr., and Harris, J.E., "Experimental and Numerical Investigation of Boundary Layer Development and Transition on the Walls of a Mach 5 Nozzle," *NASA TN D-7976*, 1975b

Haynes, T.S., Reed, H.L., Saric, W.S., "CFD Validation Issues in Transition Modeling," AIAA Paper 96-2051, June 1996.

Hedley, T., Keffer, J., "Turbulent/non-turbulent Decisions in an intermittent flow", *J. Fluid Mechanics*, vol. 64, 1974, pp. 625-644

Herbert, T., "Parabolized Stability Equations," *Special Course on Progress in Transition Modelling*, AGARD Report 793, 1993, ref. 4.

Herbert, T., "Parabolized Stability Equations," *Annual Review of Fluid Mechanics*, Annual Reviews, Vol. 29, 1997, pp. 245-83.

Herbert, T. and Morkovin, M.V., "Dialogue on Bridging Some Gaps in Stability and Transition Research," In *Laminar-Turbulent Transition*, ed. R. Eppler, H. Fasel, Springer-Verlag, 1980, pp.47-72.

Jespersen, D., Pulliam, T., and Buning, P., "Recent improvements to OVERFLOW," AIAA Paper No. 97-0644, January 1997.

Kazakov, A.V., Kogan, M.N., and Kuparev, V.A., "Optimization of Laminar-Turbulent Transition Delay by Means of Local Heating of the Surface," *Fluid Dynamics*, Vol. 30, No. 4, 1995

Kobayashi, R. and Kohoma, Y., "Taylor Gortler Instability of Compressible Boundary Layers," AIAA J., Vol. 15, No. 12, 1977, pp. 1723-1727.

King, L.S. and Demetriades, A., "Comparisons of Predictions with Measurements for a Quiet Supersonic Tunnel," AIAA Paper 93-0344, January 1993.

King, L.S., Smith, C.A., Davis S.S., "Effect of Transition Location on Airfoil Performance," AIAA Paper 98-2634, June 1998.

Kuan, C., and Wang, T., "Investigation of the intermittent behavior of transitional boundary layer using a conditional averaging technique", *Experimental Thermal and Fluid Science*, vol. 3, 1990, pp. 157-173.

Laufer, J., "Aerodynamic Noise in Supersonic Wind Tunnels," *J. of the Aerospace Sciences*, Vol. 28, No. 9, Sept. 1961, pp. 685-692.

Laufer, J., "Some Statistical Properties of the Pressure Field Radiated by a Turbulent Boundary Layer," *Physics of Fluids*, Vol. 7, No. 8, August 1964, pp. 1191-1197.

Lees, L., "The Stability of the Laminar Boundary Layer in a Compressible Fluid," *NACA TR 876*, September 1946.

Lees, L., "Note on the Stabilizing Effect of Centrifugal Forces on the Laminar Boundary Layer Over Convex Surface," *J. of Aeronautical Sciences*, Vol. 25, No. 6, June 1958.

Mack, L. M., "Boundary Layer Linear Stability Theory", *Special Course on Transition and Stability of Laminar Flow*, AGARD Report 709, March 1984, ref. 3.

Mack, L.M., "Boundary Layer Stability Theory", *JPL Report 900-277*, Rev. A, November 1969.

Mack, L.M., "Linear Stability Theory and the Problem of Supersonic Boundary-Layer Transition," AIAA J., Vol. 13, No. 3, March 1975, pp. 278-289.

Maestrello, L., "Transition Delay and Relaminarization of Turbulent Flow", *Instability and Transition*, ed. M.Y. Hussaini and R.G. Voigt, Vol. I, Springer-Verlag, 1990, pp. 153-159.

Maestrello, L. and Nagabushana, K.A., "Relaminarization of Turbulent Flow on a Flat Plate by Localized Surface Heating," AIAA Paper No 89-0985, 1989.

Malik, M.R., "Prediction and Control of Transition in Supersonic and Hypersonic Boundary Layers", *AIAA J.*, Vol. 27, No. 11, November 1989a, pp. 1487-1493.

Malik, M.R., "e^{MALIK}: A New Spatial Stability Analysis Program for Transition Prediction Using the e^N method," High Technology Corporation, Report No. HTC-8902, March 1989b.

Malik, M.R., "Numerical Methods for Hypersonic Boundary Layer Stability," J. of Computational Physics, Vol. 86, 1990, pp. 376-413.

Malik, M.R., and Hussaini, M.Y., "Numerical Simulation of Interactions Between Gortler Vortices and Tollmien-Schlichting Waves," *J. of Fluid Mechanics*, Vol. 210, 1990b, pp. 183-199.

Malik, M.R. and Poll, I.E., "Effects of Curvature on Three-Dimensional Boundary Layer Stability," *AIAA J.*, Vol. 23, No. 9, September 1985, pp. 1362-1369.

Masad, J. A., Nayfeh A.H., "Laminar Flow Control of Subsonic Boundary Layers by Suction and Heat-Transfer Strips," *Physics of Fluids*, Vol. 4, No. 6, June 1992, pp. 1259-1272.

McCroskey, W.J., "Experimental Investigation of Boundary Layer Transition on a Flat Plate with a Point Heat Source at the Leading Edge," Princeton University Report No. 623, 1962.

McCormack, P.D., Walker, H., and Kelleher, M., "Taylor-Gortler Vortices and Their Effect on Heat Transfer," J. of Heat Transfer, Trans. of the ASME, Vol. 92, pp. 101-112.

Morkovin, M.V., "Fluctuations and Hot-Wire Anemometry in Compressible Flows," AGARD, November 1956.

Morkovin, M. V., "On Supersonic Wind Tunnels With Low Free-Stream Disturbances," *J. of Applied Mechanics*, Tran. ASME, Vol 26, Series E, June 1959, pp. 319-324.

Morkovin, M.V., "Bypass Transition to Turbulence and Research Disiderata," *NASA CP-2386*, 1984, pp. 161-204.

Morkovin, M.V., "On Roughness-Induced Transition: Facts, Views, and Speculations," In *Instability and Transition*, eds. M.Y. Hussaini and R.G. Voigt, Vol. 1, Springer-Verlag, Berlin, 1990, pp. 281-295.

Morkovin, M.V., "Panoramic View of Changes in Vorticity Distribution in Transition Instabilities and Turbulence," *Boundary Layer Stability and Transition to Turbulence*, eds. Reda, D.C, Reed, H.L, and Kobayashi, R., ASME FED-Vol. 114, 1991, pp. 1-12.

Mueller, R., "Boundary Layer Transition on the Nozzle of a Two-Dimensional Mach 3.0 Wind Tunnel," *MS Thesis*, Dept. of Mechanical Engineering, Montana State University, December 1993.

Munro, S. E., "Effects of Elevated Driver-Tube Temperatures on the Extent of Quiet Flow in the Purdue Ludwieg Tube", M.S. Thesis, Dep't. of Aeronautics and Astronautics, Purdue University, December 1996.

Nayfeh, A.H., "Effect of Streamwise Vortices on Tollmien-Schlichting Waves," *J. of Fluid Mechanics*, Vol. 107, pp. 441-453, 1981.

Nayfeh, A.H., and Al-Maaitah, A., "Influence of Gortler vortices on Tollmien-Schlichting Waves," AIAA Paper No. 87-1206, 1987.

Olynick, D. and Tam, T., "Trajectory Based Validation of the Shuttle Heating Environment," *J. of Spacecraft and Rockets*, Vol. 34, No. 2, March-April 1997, pp. 172-181

Oppenheim and Schaffer, *Digital Signal Processing*, Prentice-Hall, 1975.

Ostrander, M.J., Thomas, S.R., and Srinivasan, S., "CFD Simulation of Square Cross-Section, Contoured Nozzle Flows: Comparison with Data," AIAA Paper No. 89-0045, January 1989.

Pate, S., "Effects of Wind Tunnel Disturbances on Boundary-Layer Transition with Emphasis on Radiated Noise: A Review," AIAA Paper No. 80-0431, Mar. 1980.

Pate, S.R., and Schueler, C.J., "Radiated Aerodynamic Noise Effects on Boundary-Layer Transition in Supersonic and Hypersonic Wind Tunnels," *AIAA J.*, Vol. 7, No. 3, March 1969, pp. 450-457.

Pulliam, T., "Efficient Solution Methods for the Navier-Stokes Equations," *Lecture Notes for the von Karman Institute for Fluid Dynamics Lecture Series: Numerical Techniques for Viscous Flow Computation in Turbomachinery Bladings*, von Karman Institute, Brussels, Belgium, January 1986.

Reda, D.C., "Correlation of Nosetip Boundary-Layer Transition Data Measured in Ballistics-Range Experiments," *AIAA J.*, Vol. 19, No. 3, March 1981, pp. 329-339.

Reed, H.L., "Direct Numerical Simulation of Transition: The Spatial Approach", *Special Course on Progress in Transition Modelling*, AGARD Report 793, 1993., ref. 6.

Reed, H. L., Saric, W. S., and Arnal, D., "Linear Stability Theory Applied to Boundary Layers," *Annual Review of Fluid Mechanics*, Annual Reviews, Vol. 28, 1996, pp. 389-428.

Reibert, M.S., and Saric W.S., "Review of Swept-Wing Transition," AIAA Paper No. 97-1816, 1997.

Reshotko, E., "Transition Reversal and Tollmien-Schlichting Instability," *The Physics of Fluids*, Vol. 6, No. 3, March 1963, pp. 335-342.

Reshotko, E., "Progress, Accomplishments and Issues in Transition Research," AIAA Paper 97-1815, June 1997a.

Reshotko, E., "Flow Quality Issues for Large Wind Tunnels," AIAA Paper 97-0225, January 1997b.

Saric, W., "Low-Speed Experiments: Requirements for Stability Measurements", In *Instability and Transition*, (Hussaini, M.Y., and Voigt, R.G., eds.), Vol. 1, Springer-Verlag, Berlin, 1990, pp. 162-172.

Saric, W., "Gortler Vortices," *Annu. Rev. Fluid Mech.*, Vol. 26, 1994, pp. 379-409.

Saric, W., "Physical Description of Boundary-Layer Transition: Experimental Evidence," *Special Course on Progress in Transition Modelling*, AGARD Report 793, 1993, ref. 1.

Saric, W., Carrillio, R.B., and Reibert, M.S., "Leading Edge Roughness as a Transition Control Mechanism," AIAA Paper No. 98-0781, January 1998.

Schlichting, H., *Boundary Layer Theory*, 5th ed., McGraw-Hill, 1979.

Schneider, S.P., "Improved methods for measuring laminar-turbulent intermittency in boundary layers", *Experiments in Fluids*, vol. 18, Feb. 1995, pp. 370-375.

Schneider, S.P., "Laminar-Turbulent Transition in High-Speed Compressible Boundary Layers with Curvature: Controlled Receptivity and Extent-of-Transition Experiments," Final Report, AFOSR Grant F49620-94-1-0067, Purdue University, January 1997.

Schneider, S.P., "Design of a Mach-6 Quiet-flow Wind-Tunnel Nozzle Using the e**N Method for Transition Estimation," AIAA Paper 98-0547, January 1998a.

Schneider, S.P., "Survey of Flight Data for Boundary Layer Transition at Hypersonic and Supersonic Speeds," AIAA Paper 98-0432, January 1998b.

Schnieder, S.P., and Haven, C.E., "Quiet-Flow Ludwieg Tube for High-Speed Transition Research," *AIAA J.*, Vol. 33, No. 4, April 1995, pp. 688-693.

Smith, A.M.O, and Gamberoni, N., "Transition, Pressure Gradient, and Stability Theory," Douglas Aircraft Report ES-26388, 1956. [also in Proc. Ninth Internat. Cong. Appl. Mech., vol. 4, pp. 234-244 (1957)]

Smits, A.J. and Dessauge, J.-P., *Turbulent Shear Layers in Supersonic Flow*, American Institute of Physics, 1996.

Spall, R.E. and Malik, M.R., "Goertler Vortices in Supersonic and Hypersonic Boundary Layers," *Physics of Fluids*, Vol 1, No. 11, November 1989, pp. 1822-1835.

Stainback, P.C., Anders, J.B., Jr., Harvey, W.D., Cary, A.M., Jr., and Harris, J.E., "An Investigation of Boundary Layer Transition on the Wall of a Mach 5 Nozzle," AIAA Paper 74-136, January 1974.

Swearingen, J.D., and Blackwelder, R.F., "The Growth and Breakdown of Streamwise Vortices in the Presence of a Wall," *J. of Fluid Mechanics*, Vol. 182, 1987, pp. 255-290.

Thompson R.A., Hamilton, H.H II, Berry, S.A., Horvath, T.J., and Nowak, R.J., "Hypersonic Boundary-Layer Transition for X-33 Phase II Vehicle," AIAA Paper 98-0867, June 1998

Tritz, T.G., "Measurements of Supersonic Boundary Layer Turbulence with a Dynamic Pitot Probe," *MS Thesis*, Dept. of Mechanical Engineering, Montana State University, December 1990.

Van Driest, E.R., "Evaluation of PANT Transition Roughness Data and Transition Criterion," unpublished memo to SAMSO, Nov. 1975 (Discussed and referenced in Reda, D.C., 1981, *AIAA J.*, Vol. 19, No. 3, pp. 329-339)

Van Ingen, J.L., "A Suggested Semi-Emperical Method for the Calculation of the Boundary Layer Transition Region", Inst. Of Tech., Dept. of Aeronautics and Engrg., Report VTH-74, Delft, Holland.

Wazzan, A.R., Gazley, C. Jr., and Smith A.M.O., "Tollmien-Schlichting Waves and Transition," Prog. in Aerospace Sciences, Vol. 18, No. 2, 1979, pp. 351-392.

Wazzan, A.R., Gazley, C. Jr., and Smith, A.M.O., "H-R_x Method for Predicting Transition," *AIAA J.*, Vol. 19, No. 6, 1981, pp. 810-812.

Wattmuf, J.H., "Detrimental Effects of Almost Immeasurably Small Freestream Nonuniformities Generated by Wind-Tunnel Screens," *AIAA J.*, Vol. 36, No. 3, March 1998, pp. 379-386.

Wesseling, P., "Introduction to Multigrid Methods," *ICASE Report No. 95-11* (also as *NASA CR 195045*), February 1995.

Westin, K.J.A., Boiko, A.V., Klingmann, B.G.B., Kozlov, V.V., and Alfredson, P.H., "Experiments in a Boundary Layer Subjected to Free Stream Turbulence. Part I. Boundary Layer Structure and Receptivity," *J. of Fluid Mechanics*, Vol. 281, 1994, pp. 193-218.

Wilkinson, J.H., *The Algebraic Eigenvalue Problem*, Oxford, 1965.

Wilkinson, S.P., Anders, S.G., Chen, F.-J., White, J.A., "Status of NASA Langley Quiet Flow Facility Developments", AIAA Paper 94-2498, June 1994.

Wilkinson, S.P., "A Review of Hypersonic Boundary Layer Stability Experiments in a Quiet Mach 6 Wind Tunnel," AIAA Paper 97-1819, June 1997.

Wolf, S.W.D., Laub, J.A., and King, L.S., "Flow Characteristics of the NASA-Ames Laminar Flow Supersonic Wind Tunnel for Mach 1.6 Operation," AIAA Paper 94-2502, June 1994.

Wolf, S.W.D. and Laub, J.A., "Low-Disturbance Flow Measurements in the NASA-Ames Laminar Flow Supersonic Wind Tunnel," AIAA Paper 96-2189, June 1996.